THE SHOCK AND VIBRATION BULLETIN

Part 4
Prediction and Experimental Techniques,
Isolation and Damping

JUNE 1973

A Publication of
THE SHOCK AND VIBRATION
INFORMATION CENTER
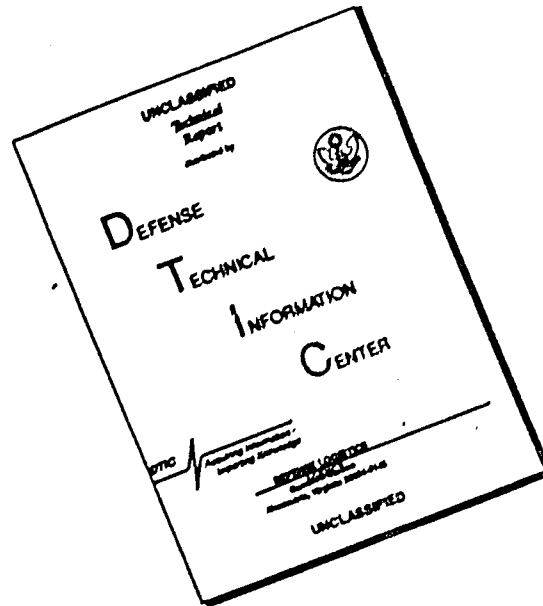Naval Research Laboratory, Washington, D.C.

Office of
The Director of Defense
Research and Engineering

82 03 26 071

DISCLAIMER NOTICE

DEFENSE
TECHNICAL
INFORMATION
CENTER

THIS DOCUMENT IS BEST QUALITY AVAILABLE. THE COPY FURNISHED TO DTIC CONTAINED A SIGNIFICANT NUMBER OF PAGES WHICH DO NOT REPRODUCE LEGIBLY.

SYMPOSIUM MANAGEMENT

THE SHOCK AND VIBRATION INFORMATION CENTER

Robert O. Belsheim, Director
Henry C. Pusey, Coordinator
Edward H. Schell, Coordinator
Rudolph H. Volin, Coordinator

Bulletin Production

Graphic Arts Branch, Technical Information Division,
Naval Research Laboratory

THE
SHOCK AND VIBRATION
BULLETIN

JUNE 1973

A Publication of
**THE SHOCK AND VIBRATION
INFORMATION CENTER**
Naval Research Laboratory, Washington, D.C.

The 43rd Symposium on Shock and Vibration was
held at the Asilomar Conference Grounds, Pacific
Grove, California, on 5-7 December 1972. The U.S.
Army, Fort Ord, was host.

Office of
The Director of Defense
Research and Engineering

CONTENTS

PART 4

Prediction and Experimental Techniques

Isolation and Damping

PAPERS APPEARING IN PART 1

Shock Testing

PAPERS APPEARING IN PART 2

Structural Analysis

PREDICTION AND
EXPERIMENTAL TECHNIQUES

A SIMPLIFIED NONLINEAR METHOD FOR ESTIMATING
THE FATIGUE LIFE OF ACOUSTICALLY
EXCITED PANELS

M. B. McGrath, P. J. Jones, S. R. Tomer
Martin Marietta Corporation
Denver, Colorado

Present methods for calculating the fatigue life of panels subjected to
short duration, high intensity random acoustic excitation have been shown
to compute expected fatigue life much shorter than that demonstrated by
tests. A simple method based on the "single mode approach" is presented
which includes nonlinear effects of membrane stresses due to large dis-
placements and an improved description of the low cycle/high stress portion
of the standard S/N curve. A simple, economical computer program imple-
menting this method is included and comparisons of analytical predictions
and test results are presented.

INTRODUCTION

Skin panels of aerospace vehicles are of-
ten exposed to high intensity, short duration
random acoustic noise. Prediction of the
fatigue life of such panels has, in general,
relied on the linear "single mode approach"
coupled with Miner's cumulative damage rule.
This design tool, either analytical or in the
form of design charts, severly under estimates
the fatigue life for ring frame, stringer type
panels which are designed for short duration,
high intensity acoustic excitation.

The parameters effecting the fatigue life
prediction of panels subjected to acoustic ex-
citation were investigated in an attempt to
obtain better correlation between simple ana-
lytical techniques and existing test data. The
parameters studied were boundary condition,
curvature effects, preload, temperature, fun-
damental frequency, damping, variation of input
acoustic excitation, membrane effects and S/N
data interpretation. Of these the last two
were found to have a significant effect for
metallic ring frame, stringer panels designed
to survive high intensity acoustic excitation
for short durations.

This paper presents an extension of the
"single mode approach" to include the effects
of nonlinear response associated with large
displacements and an improved method of using
conventional S/N data. A simple computer pro-
gram implementing this method is described and
a listing is included. The results of a sample
problem using both the linear and nonlinear

method are compared to test data where excellent
agreement with the nonlinear method is obtained.

LINEAR METHOD

The fatigue life of a panel exposed to
acoustic excitation depends on the stress his-
tory and the tolerance of the material to the
accumulated damage. The approach used for cal-
culating the fatigue life of a panel is to
determine the stress levels and the distribu-
tion of the stress due to the acoustic excita-
tion. Using this "stress history" the accumu-
lated damage is calculated based on a damage
model and conventional S/N data. When the
damage reaches a certain value, the panel is
assumed to have fatigued and the time to fail-
ure is calculated based on the known response
frequency. The method requires knowing the
stress level, stress distribution, panel fre-
quency, damage model, S/N data and excitation
power spectrum.

The linear "single mode approach" (1, 2,
3) for calculating the stress in panels sub-
jected to random acoustic excitation is com-
monly used and relies on the following assump-
tions: 1) the panel response is primarily in
the fundamental mode, 2) the acoustic excita-
tion is fully correlated over the panel, 3) the
input pressure spectral density is essentially
constant around the fundamental frequency, and
4) the mode of vibration is the same as the
deflected shape for a uniform pressure. In
addition to these general assumptions, the
boundary condition of riveted panels is

1

generally assumed to be fixed.

The equation based on the single mode assumption for computing RMS Stress, $\bar{\sigma}$, is

$$\bar{\sigma} = \sqrt{\frac{\pi}{2} f_n Q S_p} \; K_o \qquad (1)$$

where f_n = panel natural frequency, S_p = pressure spectral density, Q = dynamic amplification factor, and K_o = maximum stress for a uniform pressure of unit magnitude. The linear method further assumes that the stress peaks have a Rayleigh Distribution and uses conventional S/N data to calculate the damage accumulation. Miner's rule is commonly used which assumes that the damage is linearly accumulated based on a ratio of actual cycles used at a given stress level to the total number of cycles to failure at that stress level as obtained from S/N data. When the response displacements and stresses are small, test data has indicated that the Rayleigh Distribution and cumulative damage rule give reasonable estimates of the fatigue life.

NONLINEAR EFFECTS

However, when thin panels are exposed to high intensity random acoustic excitation, the panel may respond with large displacements. For displacements beyond the linear range membrane stresses are induced that cause the panel to be stiffer than predicted by the linear theory and consequently the actual stresses are less than predicted by the linear theory. Test data for such cases have verified that the stress peaks have a distribution skewed from a Rayleigh curve, (4). Since the stress levels are less the damage accumulated will be less than predicted by the linear theory and the panel will survive more cycles to failure. The nonlinear effect actually prolongs the fatigue life of a panel and the linear calculations can be overly conservative.

A second problem can result in using Miner's cumulative damage rule for large stresses since the common S/N data must be extrapolated into the low cycle/high stress region of the S/N curve. The ordinary extrapolation for the linear method is made to the static ultimate stress value for one-half cycle. However, reference (5) indicates that a better estimate of the true ultimate for low cycle fatigue can be made by extrapolating the S/N data on a log-log plot to the one-half cycle point. This extrapolation results in a much higher value of ultimate stress than the static ultimate and when used in the accumulated damage calculations results in a less conservative estimate for the low cycle fatigue of a panel.

APPROACH

The approach proposed to calculate fatigue life of panels exposed to high intensity acoustic excitation is based on extending the linear single mode approach to account for the two effects discussed above. The large displacement effect is accounted for by assuming that the fluctuating pressure peaks (not stress peaks) follow a Rayleigh distribution and calculating the corresponding stress distribution using nonlinear plate equations that include the effect of large displacements. (The non-linear effect on panel fundamental frequency and damping is not included). This calculation produces a skewed stress distribution which is used in Miners damage rule with the S/N data to estimate the fatigue life. The second effect is accounted for by using a log-log extrapolation to the low cycle region on conventionally available high cycle S/N data.

The basic steps of the linear method are well established and can be performed by hand calculations or implemented on a digital computer. The extension to include the two effects is best discussed in terms of the individual steps of the calculations which the following describes. The method has been implemented on a computer program and is listed in the appendix.

1) Compute Natural Frequency

The formulas used in the program for computing the panel natural frequency were taken from reference (6). The program assumed clamped boundary conditions.

2) Compute RMS Pressure

The RMS pressure, P_{RMS}, is calculated using the equation

$$P_{RMS} = \sqrt{\pi/2 \; f_n Q S_p} \qquad (2)$$

where the terms are defined previously. The acoustic spectrum is input to the program in 1/3-octave values and the program interpolates based on straight lines on a linear (db) log (frequency) curve. The pressure spectral density values are computed assuming the calculated panel natural frequency is the center frequency of a 1/3-octave band. The relation of center frequency to 1/3-octave bandwidth is described below:

$$\frac{f_H}{f_L} = 1.2589 \qquad (3)$$

where f_L = lower frequency and f_H = higher frequency of the 1/3 octave band. Also

$$f_C^2 = f_H \, f_L \qquad (4)$$

where f_C = the center frequency (in this case, the natural frequency of the panel). Using this relationship, it can be shown that the bandwidth (BW) can be expressed as

$$BW = f_H - f_L = 0.23 \, f_C \qquad (5)$$

The program selects the range on the input acoustic curve that encompasses the natural frequency as shown in the sketch:

Frequency (log)
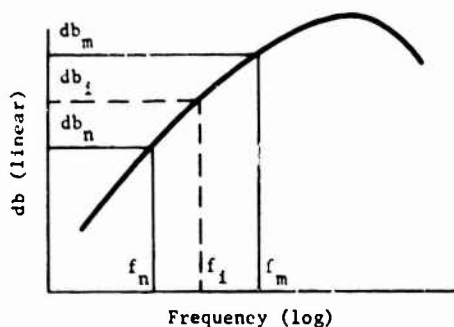
The db level at $f_i (db_i)$ is then computed as

$$db_i = \left[\frac{db_m - db_n}{\log_{10} f_m/f_n} \right] \log_{10} f_i/f_n + db_n$$

The pressure spectral density (Sp) used in equation (2) can be expressed as

$$Sp = \frac{(2.9 \times 10^{-9} \, psi)}{0.235 \, f_j} \, 10^{db_i/10} \qquad (7)$$

3) Compute Stress Values

Formulas used for computation of the bending and membrane stress and displacement were taken from (7). The only modification to the basic equations was an allowance to compute maximum static stress based on a maximum fiber distance (fiber distance of panel thickness divided by 2 used in basic equations).

4) Interpolate S/N Data

The S/N curve supplied is interpolated based on straight lines on a log-log curve. For example, assume the following input S/N curve:

Cycles (log)
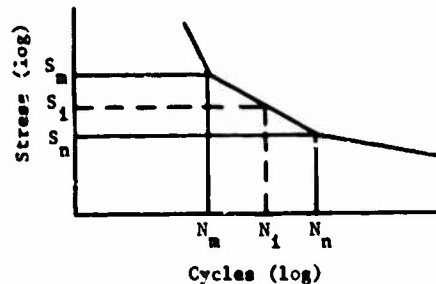
The program selects the range on the curve based on S_i, which, for this case, would be S_n to S_m, and computes N_i based on

$$\log_{10} N_i = \left[\frac{\log_{10} (N_m/N_n)}{\log_{10} (S_m/S_n)} \right] \log_{10}(S_i/S_n)$$
$$+ \log_{10} N_n \qquad (8)$$

if the computed value on N_i is less than 0.5 indicating a stress level near the ultimate stress, the program uses $N_i = 0.5$.

5) Calculate Damage

The program computes fatigue life based on the cumulative damage criteria:

$$D_m = \sum \frac{n_x}{N_x} = 1.0 \text{ at failure} \qquad (9)$$

where n_x and N_x are applied and allowable cycles at a given stress level. Assuming a Rayleigh distribution of peaks, the probability of occurrence of a pressure peak at sigma level x is

$$P(x) = x \exp\left(-\frac{x}{2}\right) \qquad (10)$$

where $P(x)$ equals fraction of the total number of cycles. The pressure peak is then equaled to stress levels using membrane and bending theory. Essentially, the pressure peaks follow a Rayleigh distribution, but because of nonlinear membrane effects, the stress distribution is not Rayleigh. It can be shown that the number of random cycles to failure is

$$N_R = \frac{1}{\displaystyle\int_0^\infty \frac{P_{(x)} \, dx}{N_x}}$$

3

This equation is the basis for the fatigue-life computation. The program performs a numerical integration on

$$\int_0^\infty \frac{P_x\ dx}{N_x} \qquad (12)$$

using sigma values (x) from 0.2 to 5.0 with dx = 0.2. With the value of N_R, the time to failure (t_f) is computed as

$$t_f = f_n \cdot N_R \qquad (13)$$

The listing of the program is given in the appendix. The run time per case is approximately 2 seconds. The computer program input consists of panel geometry and structural properties, 1/3-octave acoustic spectrum, and material S/N data. The output includes panel natural frequency, pressure spectrum density, rms pressure and displacement, cycles to failure, time to failure, and a damage table. The input format includes the option to repeat information from the previous case and change one input parameter at a time. The format of the input is shown in Table I.

Table I

PROGRAM INPUT DATA

Input	Format
1. NCASE = Number of cases	I5
2. ICK = Code for repeating panel data (repeat if ICK = 0 must not be 0 for 1st case)	I5
3. ES, EL, T, E, R, WT, Q, D = Short side, long side, thickness, modulus of elasticity, Poisson's ration, weight per unit area, amplification factor, distance to extreme fiber. (Will use previous data if ICK = 0.)	10X, 3E17.8, E15.8
4. JCK, DBINC = Code for repeating acoustic data if equals 0 (if not, JCK equals number of input points on acoustic curves), DBINC incremental db value to be added to initial input curve (this allows for increasing the original 1/3-Octave acoustic curve without repeating the input data).	I5, 5X, E17.8
5. PSD (J,1), PSD (J,2) J=1,JCK PSD (J,1) = Frequency PSD (J,2) = db value (will use previous data plus DBINC if JCK = 0)	10X, 2E17.8
6. KCK, SNINC = Code for repeating SN data if KCK equals 0 (if not, KCK number of input points on SN curve), SNINC incremental number to be multiplied times the initial input curve (this allows for increasing the initial SN curve without repeating input data).	I5, 5X, E17.8
7. SN (K,1), SN (K,2) K=1,KCK SN (K,1) = Stress SN (K,2) = Number of cycles (will use previous data times SNINC if KCK = 0) If NCASE equals 1, this is the last input. For next case go to 2 and repeat.	10X, 2E17.8

4

TEST VERIFICATION RESULTS

The method described in this paper and the computer program were verified through comparison with test results available from previous acoustic tests. The results are compared for twelve panels from two different tests and are summarized in Table II. The tests were performed on two Titan II 10 foot diameter skirt sections of .040" thick aluminum skin riveted to vertical longerons and horizontal frames, the spacing of which defines the panel sizes. The acoustic overall sound pressure levels (OASPL) were 163.5 and 164.5 db and the input spectrum and response frequency of the panels were measured. (The acoustic spectrum is required to be input to the program to determine the one-third octave level in the region of the natural frequency.) The excitation was applied in bursts lasting for 30 seconds for the 164.5 db level and for 120 seconds for the 163.5 db level test. Cracks were noted in the panel sections and the test completed when all 6 panels exhibited a crack.

In the first set of panels in Table II, the failures occured from 210 to 360 seconds. The number of cycles to failure range from 2.4 to 4.2 x 10^4 cycles which is in the lower range where S/N data is commonly measured. This panel configuration was analyzed using both the linear and non-linear methods (the linear method also used the log-log extrapolation of the S/N data) and the non-linear method predicts a result that is in the range of failure and conservative. The linear method with log-log S/N extrapolation predicts a time to failure that is conservative by two orders of magnitude. The linear method with an extrapolation to the static ultimate stress predicts that failure will result in 1.4 cycles or .012 seconds. The linear method for this case is not reasonable since the answer requires a stress well into the non-linear range to produce failure.

The second set of panels failed from 840 to 1500 seconds or in 6.6 x 10^4 to 1.2 x 10^5 cycles. The predictions were again both conservative.

Table II

COMPARISON OF TEST AND ANALYSIS RESULTS FOR FATIGUE LIFE OF PANELS

Test Parameters				Test Results	Analysis Results			
					Linear (Log-Log S/N)		Non-Linear	
Panel Type and Geometry	Material	Input Acoustics	Frequency (Hz)	Time to Failure	Frequency (Hz)	Time to Failure (sec)	Frequency (Hz)	Time to Failure (sec)
6 Panels of Missile Skirt, Longeron/ Frame Construction 8.7x21.5 x.04"	2014-T6 Aluminum	164.5 db OASPL	118	6 Panels: 210 to 360 Seconds	120	3.8	120	170
6 Panels of Missile Skirt, Longeron/ Frame Construction 11.9x15.6 x.040	2014-T6 Aluminum	163.5 db OASPL	78	6 Panels: 840 to 1500 Seconds	79	17	79	470

CONCLUSIONS

An extension of the widely used "single mode method" for estimating fatigue life of panels subjected to random acoustic excitation has been developed. The basic changes involve a first order correction to include non-linear (membrane) effects on stress computation and a improved description of low cycle/high stress S/N data. Excellent agreement with test data for metallic frames, stringer panels was obtained using the modified method and with the method that incorporates only the S/N data extrapolation technique. However, the test results were for failures in the 10^4 cycle range where the large deflections are less pronounced. In fact, the proposed method will approach the linear method above the 10^6 cycle range. For panels configurations where large deflection would occur (less than 10^3 cycles) the proposed method would be most applicable. The safest approach is to use both methods described above and compare the cycles to failure and base the judgement on the order of magnitude numbers. In any analytical prediction of fatigue, the answer can only be used as an order of magnitude estimate and the actual configuration should be verified by test if the estimate is at all questionable.

REFERENCES

1. Miles, J. W., "On Structural Fatigue Under Random Loading", the Journal of Aeronautical Sciences, Vol 21, No. 11, pp 753-762, November, 1954.

2. Rudder, Fred F., Jr., "Acoustic Fatigue of Aircraft Structural Component Assemblies", AFFDL-TR-71-107, Lockheed-Georgia Company, February 1972.

3. Kuchta, B. J., Howell, L. J., and Sealey, D. M., "Determination of Methods for Establishing Space Shuttle Load Spectra", NASA CR-112033.

4. Eshleman, A. L., Jr., and Van Dyke, J. D. Jr., "A Rational Method of Analysis of Matrix Methods of Acoustically Loaded Structure for Prediction of Sonic Fatigue Strength", Acoustical Fatigue in Aerospace Structures, edited by Trapp, Walter J. and Forney, Donald M. Jr., Syracuse University Press 1958.

5. Raske, D. T. and Morrow, J. D., "Mechanics of Materials in Low Cycle Fatigue Testing", Manual of Low Cycle Fatigue Testing, ASTM STP 465, American Society for Testing and Materials, 1969, pp 1-25.

6. Warburton, C. B., "The Vibration of Rectangular Plates", Proc. Inst. Mech. Eng., Ser. A, Vol 168, No. 12, 1954, pp 371-384.

7. Roark, Ramond J., Formulas for Stress and Strain, McGraw-Hill Book Company, 4th Edition, pp 244-250.

NPAR COMPUTER PROGRAM LISTING

```
      PROGRAM NPAR(INPUT,OUTPUT,TAPE5=INPUT,TAPE6=OUTPUT)
C
C NPAR = NONLINEAR PANEL ACOUSTIC RESPONSE
C
C     PROGRAM COMPUTES FATIQUE LIFE OF FLAT ISOTROPIC PANELS
C     SUBJECTEO TO ACOUSTIC EXCITATION
C     COMBINATION OF BENDING AND MEMBRANE THEORY(LARGE OEFL.)
C     CLAMPED PANELS ONLY IFIX=2
C
C     ANALYSIS USES SINGLE MOOE APPROACH AND MINER CUMULATIVE
C     DAMAGE CRITERIA
C
C     PAUL JONES 4/72
C
      DIMENSION PSO(20,2),ALAOB(11),BTAOB(11),COEF(11),
     *          AL(2,11),BT(2,11),AOB(2),SN(20,2)
C
      OATA XG/1.506/
      DATA XH/1.248/
      DATA XJ/1.248/
      OATA YG/1.506/
      OATA YH/1.248/
      OATA YJ/1.248/
      OATA AL/0.,0.,.165,.28,.25,.51,.59,.825,.80,1.07,.95,1.24,
     *     1.08,1.40,1.19,1.50,1.28,1.63,1.38,1.72,1.54,1.86/
      DATA BT/0.,0.,3.8,5.75,6.90,11.12,14.7,20.30,21.0,27.3,26.5,35.0,
     *     31.5,41.0,36.2,47.0,40.4,52.5,45.0,57.6,53.5,67.0/
      OATA AOB/1.,1.5/
      OATA COEF/0.,12.5,25.,50.,75.,100.,125.,150.,175.,200.,250./
C
 1001 FORMAT(I5,5X,3E17.8)
 1002 FORMAT(10X,3E17.8,E15.8)
 1003 FORMAT(/,5X,40HNAT FREQ OUT OF BOUNDS OF INPUT SPECTRUM)
 1004 FORMAT(10X,2E17.8)
 1005 FORMAT(/,5X,30HPANEL NATURAL FREQUENCY EQUALS,2X,1E15.8)
 1006 FORMAT(/,5X,32HPRESSURE SPECTRAL OENSITY EQUALS,2X,1E15.8)
 1009 FORMAT(/,5X,19HRMS PRESSURE EQUALS,2X,1E15.8)
 1010 FORMAT(/,5X,23HRMS OISPLACEMENT EQUALS,2X,1E15.8)
 1011 FORMAT(/,5X,32HCYCLES TO FAILURE (DM=1.) EQUALS,2X,1E15.8)
 1012 FORMAT(/,5X,15HTIME TO FAILURE,2X,1E15.8,2X,7HSECONDS)
 1013 FORMAT(1H1,//,23HOUTPUT OATA CASE NUMBER,2X,I5)
 2002 FORMAT(10X,3E17.8)
 2000 FORMAT(/,5X,24HCUMMULATIVE DAMAGE TABLE)
 2001 FORMAT(/,14X,9HSIGMA (X),11X,9HSTRESS X ,9X,4HP(X),13X,4HN(X),
     *11X,9HP(X)/N(X))
 3000 FORMAT(/,5X,10HINPUT DATA)
 3001 FORMAT(13X,13HSHORT SIOE = ,1F15.8,14H ,LONG SIDE = ,1F15.8)
 3002 FORMAT(13X,12HTHICKNESS = ,1F15.8,20H ,MODULUS OF ELAS = ,
     *1E15.8)
 3003 FORMAT(13X,17HPOISSIONS RATIO = ,1F15.8,16H ,WEIGHT/AREA = ,
     *1F15.8)
 3004 FORMAT(13X,21HAMPLIFICATION FACT = ,1F15.8,13H ,FIX CODE = ,I5)
 3005 FORMAT(13X,10HOB INCR = ,1F15.8,24H ,SN INCR = ,1F15.8)
C
C
C READ NUMBER OF CASES
      READ(5,1001)NCASES
C
      OO 99 I=1,NCASES
      WRITE(6,1013) I
```

```
C LENGTH OF SHORT EDGE,LENGTH OF LONG EDGE,THICKNESS,MODULUS OF ELASTICITY,
C POISSONS RATIO,WEIGHT PER UNIT AREA,DAMPING(Q),DISTANCE TO EXT. FIBER
C READ STRUCTURAL PANEL DATA (USE PREVIOUS DATA IF ICK=0)
      READ(5,1001)ICK,FREQ
      IF(ICK.EQ.0) GO TO 10
      READ(5,1002)ES,EL,T,E,R,WT,Q,D
      IFIX=2
C
C READ INPUT ACOUSTIC SPECTRUM (USE PREVIOUS DATA IF JCK=0)
C SPECTRUM MUST COVER EXPECTED PANEL RESONANT FREQUENCY
C READ INPUT ACOUSTIC SPECTRUM (USE PREVIOUS DATA IF JCK=0)
C SPECTRUM MUST COVER EXPECTED PANEL RESONANT FREQUENCY
C 1/3 OCTAVE LEVELS DB VS. FREQ (LINEAR,LOG)
C JCK EQUALS NUMBER OF POINTS ON INPUT SPECTRUM
C
C DBINC EQUALS INCREASE(DECREASE)OVER INITIAL 1/3 OCTAVE CURVE.
C DBINC = 0 FOR FIRST CASE. IF JCK NOT EQUAL TO ZERO (CASE 2,ETC)
C THEN DBINC SHOULD BE ZERO.
C
   10 READ(5,1001)JCK,DBINC
      IF(JCK.NE.0)KCJ=JCK
      IF(JCK.EQ.0) GO TO 15
      READ(5,1004)((PSD(J,1),PSD(J,2)),J=1,JCK)
C
C READ INPUT CONVENTIONAL S-N DATA (USE PREVIOUS,DATA IF KCK=0)
C STRAIGHT LINES ON LOG-LOG PLOT    STRESS-N (LOW STRESS FIRST)
C KCK EQUALS NUMBER OF POINTS ON SN CURVE
C
C SNINC EQUALS INCREASE (DECREASE) OVER INITIAL S-N CURVE.  SNINC = 1.
C FOR FIRST CASE.  NUMBER OF CYCLES = NUMBER OF CYCLES INITIALLY *SNINC
C
   15 READ(5,1001)KCK,SNINC
      IF(KCK.NE.0)KKC=KCK
      IF(KCK.EQ.0) GO TO 16
      READ(5,1004)((SN(J,1),SN(J,2)),J=1,KCK)
C
C WRITE OUT INPUT DATA
   16 WRITE(6,3000)
      WRITE(6,3001) ES,EL
      WRITE(6,3002) T,E
      WRITE(6,3003) R,WT
      WRITE(6,3004) Q,IFIX
      WRITE(6,3005) DBINC,SNINC
C
C COMPUTE NATURAL FREQUENCY OF PANEL
C
      IF (FREQ .GT. 0.0) GO TO 18
      FPR2=XG**4+(YG*EL/ES)**4+(2.*(EL/ES)**2)*
     * (R*XH*YH+(1.-R)*XJ*YJ)
      FPR=FPR2**.5
      FREQ=(FPR*(T**1.5)*3.1416/EL**2)*((E*8.042/(WT*(1.-R**2)))**.5)
C
C INTERPOLATE INPUT ACOUSTIC DATA OBTAIN PRESSURE SPECTRAL
C DENSITY VALUE AT NATURAL FREQUENCY - LINEAR INTERPOLATION
C
   18 ICK=KCJ-1
   20 DO 30 K=1,ICK
      FR1=PSD(K,1)
      FR2=PSD(K+1,1)
```

8

```
          IF(FREQ.GE.FR1.AND.FREQ.LE.FR2) GO TO 35
       30 CONTINUE
          WRITE(6,1003)
          GO TO 99
       35 ALP=ALOG10(PSD(K+1,1)/PSD(K,1))
          ALPHA=ALOG10(FREQ/PSD(K,1))
          DBPAL=(PSD(K+1,2)-PSD(K,2))/ALP
          DB=DBPAL*ALPHA+PSD(K,2)+ DBINC
          BW=.235*FREQ
          PSI2=(8.58E-18)*(10.**(DB/10.'))
          PS=PSI2/BW
C
C INTERPOLATE DISPLACEMENT AND STRESS COEFFICIENTS
C FOR A/B RATIO
C
          RATIO=EL/ES
          AB1=AOB(1)
          AB2=AOB(2)
          DO 45 J=1,11
          N=J
          IF(RATIO.GT.AB2) GO TO 40
          BTAOB(N)=(((BT(2,N)-BT(1,N))/(AB2-AB1))*(RATIO-AB1))+
         *           BT(1,N)
          ALAOB(N)=(((AL(2,N)-AL(1,N))/(AB2-AB1))*(RATIO-AB1))+
         *           AL(1,N)
          GO TO 45
       40 BTAOB(N)=BT(2,N)
          ALAOB(N)=AL(2,N)
       45 CONTINUE
C
C COMPUTE RMS PRESSURE AND DISPLACEMENT
C
          RMSPR=(1.57*FREQ*PS*Q)**.5
          COEFF=(RMSPR*(ES**4))/(E*(T**4))
          DO 46 J=1,10
          CO1=COEF(J)
          CO2=COEF(J+1)
          N=J
          IF(COEFF.GE.CO1.AND.COEFF.LE.CO2) GO TO 47
       46 CONTINUE
       47 ALPHA=(((ALAOB(N+1)-ALAOB(N))/(CO2-CO1))*(COEFF-CO1))+
         *           ALAOB(N)
          RMSDS=ALPHA*T
C
C COMPUTE FATIQUE LIFE OF PANEL
C ASSUME RAYLEIGH DISTRIBUTION OF PRESSURE PEAKS
C
          WRITE(6,2000)
          WRITE(6,2001)
          DELTAS=.2
          SIGMA=0.0
          SUM=0.0
          II=KKC-1
          DO 65 K=1,25
          SNF1=SN(1,1)
          SIGMA=SIGMA+DELTAS
          PROBS=SIGMA*EXP(-SIGMA**2./2.)
          SIGPR=SIGMA*RMSPR
          COEFF=(SIGPR*(ES**4))/(E*(T**4))
          DO 48 J=1,10
          CO1=COEF(J)
```

9

```
      CO2=COEF(J+1)
      N=J
      IF(COEFF.GE.CO1.AND.COEFF.LE.CO2) GO TO 49
   48 CONTINUE
   49 BETA=(((BTAOB(N+1)-BTAOB(N))/(CO2-CO1))*(COEFF-CO1))+
     *          BTAOB(N)
      SIGST=BETA*(E*(T**2)/(ES**2))
      IF(SIGST.LE.SNF1) GO TO 55
      DO 50 J=1,II
      N=J
      SNF1=SN(J,1)
      SNF2=SN(J+1,1)
      IF(SIGST.GE.SNF1.AND.SIGST.LE.SNF2) GO TO 60
   50 CONTINUE
      GO TO 60
   55 N=1
   60 ALP=(ALOG10(SN(N+1,2)/SN(N,2)))/(ALOG10(SN(N+1,1)/SN(N,1)))
      TLOGN=(ALP*(ALOG10(SIGST/SN(N,1))))+ALOG10(SN(N,2))
      IF (SNINC .EQ. 0.) SNINC=1.0
      TN=10.**TLOGN*SNINC
      IF(TN.LT..5)TN=.5
      PON=PROBS/TN
      WRITE(6,2002)SIGMA,SIGST,PROBS,TN,PON
   65 SUM=SUM+PON*DELTAS
      FLCY=1./SUM
      TFL=FLCY/FREQ
C
C PRINT DATA
C
      WRITE(6,1005) FREQ
      WRITE(6,1006) PS
      WRITE(6,1009) RMSPR
      WRITE(6,1010) RMSOS
      WRITE(6,1011) FLCY
      WRITE(6,1012) TFL
   99 CONTINUE
      END
```

STUDIES ON THE DYNAMIC IMPACT OF JET ENGINE BLADES

C. T. Sun[1] and R. L. Sierakowski[2]
National Research Council Senior Research Associates
Air Force Materials Laboratory
Wright Patterson Air Force Base, Ohio

The foreign object damage of jet engine fan and compressor blades is studied considering the flexure-torsion vibrations of a discretized mass model. A transient vibration problem is solved with initial velocity conditions used to simulate the dynamic loading conditions. A parametric study of numerical results of bending and torsional vibration of titanium and boron-aluminum blades is presented and discussed in detail.

INTRODUCTION

As a consequence of improving the performance of jet engine systems, the introduction of high performance composite type materials for jet engine fan compressor blade applications has been considered. The potential use of such materials introduces a wide variety of challenging new technological problems ranging from blade fabrication techniques to examining mechanical properties changes occurring during use in varied environments. One area of principal concern relates to the response of such blade materials when subjected to dynamic loadings caused by ingestion of stones, ice balls and birds. Such impact type loadings are classified under the general area of foreign object damage with such objects creating localized or far removed failures. Localized damage is usually of the cratering or penetration type while that produced at far removed locations is usually the result of dynamic overstress or wave interaction.

Some recent analytical studies related to the wave surface shape and speed during impact of composite plate materials have been discussed in [1]. In addition, some limited experimental studies on the impact resistance and fracture of plate type composites have been discussed in [2-4].

Less consideration has been focused on obtaining data on the magnitude of the dynamic stresses produced during impact on blade materials. In order to understand and evaluate potential candidate materials to withstand impact damage, it is desirable to develop characterization techniques to identify important material response parameters. Such data is needed to systematize and classify testing techniques to reproduce and evaluate candidate materials.

In the present investigation four types of compressor blade materials have been studied including stainless steel, titanium, boron-aluminum, and graphite-epoxy. Numerical results for the first and second natural bending frequencies, tip displacement, and maximum flexural stress are presented as a function of engine speed Ω, and the first torsional frequency, maximum angle of twist, and maximum torsional stress as a function of a geometrical parameter c considering a fixed strike velocity. A response comparison between a

---

1. On leave of absence from Iowa State University.
2. Present address: Department of Engineering Science and Mechanics, University of Florida.

11

geometrically similar boron-aluminum and
titanium blade is discussed.

ANALYSIS

For initial study, an examination of the
dynamic response of blades subjected to
impacting objects of sizeable mass relative to
the blade mass is considered. The discrete
mass model developed takes into account com-
bined bending, torsion and centrifugal loading
and is formulated using Lagrangian mechanics.

An overall view of a typical fan blade
assembly is shown in Figure 1 and a schematic
of the geometric configuration used in the
analytical formulation is shown in Figure 2.

Figure 2. Schematic of Fan
or Compressor Blade

Figure 1. Overall View of Fan Assembly[*]

For model purposes the blade has been con-
sidered to be a cantilever beam with lumped
masses placed at selected spanwise stations.
A further division of the mass distribution
along the blade chord has been made to account
for eccentricity between the blade center of
gravity and elastic axis.[**] The geometrical
notation used is shown in Figure 3. The kinetic
and potential energies for the homogeneous
blade configuration as shown in Figure 3 and
defined in terms of the generalized coordinates
y_i and ϕ_i are given below:

Figure 3. Geometrical Beam Notation

[**] One approximate method to determine the
chordwise mass to be placed at elastic axis
and center of gravity, respectively, is to
use a weighted mass distribution and the
percentage of the static moment about geo-
metrical profile of the chord.

[*] Courtesy of United Aircraft Corporation

12

$$T = \frac{1}{2} \sum_{i=1}^{n} m_{e.a.}^{(i)} (\dot{y}_i + L_i \Omega)^2 + \frac{1}{2} \sum_{i=1}^{n} m_{c.g.}^{(i)} (\dot{y}_i$$

$$+ e_i \dot{\phi}_i + L_i \Omega)^2 \tag{1}$$

$$V = \frac{1}{2} \sum_{i=1}^{n} \sum_{j=1}^{n} k_{ij} y_i y_j + \frac{1}{2} \sum_{i=1}^{n} \sum_{j=1}^{n} h_{ij} \phi_i \phi_j$$

$$+ \frac{1}{2} \sum_{i=1}^{n} m_{c.g.}^{(i)} \Omega^2 L_i^2 \left(\frac{y_i + L_i}{L_i}\right)^2 \cos^{-1} \frac{L_i}{(e_i^2 + L_i^2)^{1/2}} \tag{2}$$

The last term in (2) represents the contribution of centrifugal force due to engine rotation.

In the present analysis, the influence of damping has been neglected. The governing equations of motion are then obtained using Lagrangian mechanics.

$$\frac{d}{dt}\left(\frac{\partial L}{\partial \dot{q}_k}\right) - \frac{\partial L}{\partial q_k} = 0 \tag{3}$$

Since, for the blade geometries considered, the shear center is very close to the centroid of the blade, (i.e., e_i is very close to zero) the flexural-torsion coupling is small and each of the motions has been considered independently. In this case, y_i and ϕ_i in (1) become uncoupled. The kinetic energy T can then be expressed as

$$T = \frac{1}{2} \sum_{i=1}^{n} m_1^{(i)} (\dot{y}_i + L_i \Omega)^2 + \frac{1}{2} \sum_{i=1}^{n} m_2^{(i)} c_i^2 \dot{\phi}_i^2 \tag{4}$$

In equation (4) it is to be noted that a pseudo geometrical dimension c_i has been included. This has been incorporated in order to calculate uncoupled torsional vibrations. (See Figure 4.)

A typical equation of motion for bending is then given by

$$m^{(i)} \ddot{y}_i + \sum_{j=1}^{n} k_{ij} y_j + m^{(i)} y_i \Omega^2 = 0 \tag{5}$$

and for torsion by

$$m_2^{(i)} c_i^2 \ddot{\phi}_i + \sum_{j=1}^{n} h_{ij} \phi_j = 0 \tag{6}$$

Equation (6) shows that the engine speed Ω has no effect on torsional vibration. This fact is nearly true when the coupling effect between bending and torsion is very small. Considering harmonic motion the eigenvalues and eigenvectors for the system are obtained by setting the determinant of equations (5) and (6) equal to zero separately.

$$\left| \bar{k}_{ij} - \omega^2 \delta_{ij} \right| = 0 \tag{7}$$

for bending and

$$\left| \bar{h}_{ij} - \omega^2 \delta_{ij} \right| = 0 \tag{8}$$

for torsion. In equations (7) and (8) the m_i, Ω and c_i have been incorporated into the $\bar{k}_{ij}$ and $\bar{h}_{ij}$ for convenience. Equations (7) and (8) represent the standard eigenvalue problem.

Once the eigenvalues and eigenvectors have been obtained, the transient vibration problem can be studied. In the present analysis, the impact event has been incorporated as an
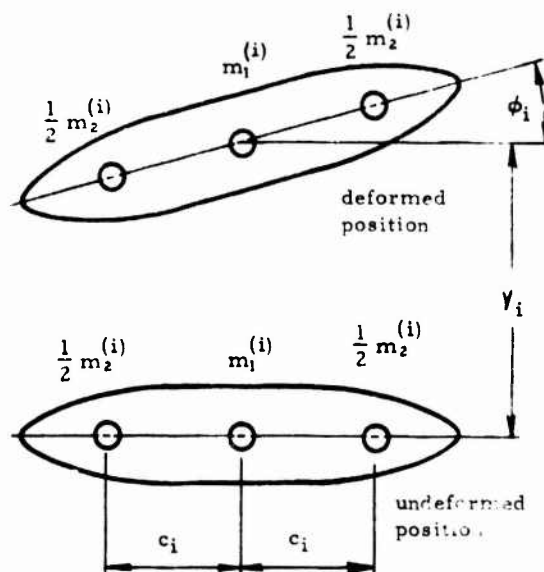
Figure 4. Cross Section of Symmetric Uncoupled Bending-Torsion Geometry

13

initial condition. The general solution is thus given by [5]:

$$\{y\} = \sum_{s=1}^{n} [P]_s \{y(0)\} \cos \omega_s t$$

$$+ \sum_{s=1}^{n} [P]_s \{\dot{y}(0)\} \frac{\sin \omega_s t}{\omega_s}$$

(9)

where

$$[P]_s = \frac{\{\phi_s\} \{\phi_s\}^T [m]}{[\phi_s]^T [m] [\phi_s]}$$

(10)

In Equation (10), $\{\phi_s\}$, a column matrix, represents the sth column of the modal matrix $[\phi]$ and $[\phi_s]^T$ is the transpose of $[\phi_s]$. In addition, an upper bound response has been calculated by taking the maximum values of the trigonometric functions and assuming these to occur simultaneously.

RESULTS AND DISCUSSION

Although several materials have been examined, data obtained for two of the blade materials considered have been presented graphically in Figures 5-10. The two materials represented are titanium and boron-aluminum with the geometrical and physical properties of titanium and boron-aluminum blades being given in Tables 1 and 2, respectively. It is noted that the area moments of inertia for both blades are not constants along the span, and this fact has been incorporated in evaluating the bending stiffness coefficients k_{ij}.

For the cases considered, object impact has been introduced into the results through an initial velocity condition. In the present studies a single impact velocity of 100 ft/sec. has been introduced as a reference, recognizing that results for higher velocities can be obtained by scaling the reference results. In the present analysis a Rayleigh distribution for the lumped masses has been used in conjunction with a variable geometry blade profile.

In Figure 5 the uncoupled bending frequencies are plotted versus engine speed Ω for the two materials. It is noted that the stiffer boron-aluminum blade has a natural frequency in first bending approximately three times greater than that of the titanium blade.

Figure 6 shows the blade tip displacement as measured from the elastic axis as a function of Ω. It can be seen that the tip displacement for titanium blades as a function of engine speed is greater than the corresponding boron aluminum. This results in the root bending stresses shown in Figure 7 plotted versus engine operating speed. For the impact situation considered, (100 ft./sec.) the magnitude of the stresses shown appear insufficient to cause failure; however, upward scaling of the impact velocity would result in correspondingly higher stresses, resulting in blade failure. For the case of torsional impact, that is, when chordwise eccentricity exists between the center of gravity and elastic axis, calculated results for uncoupled torsional frequency, torsional stresses and angle of twist are presented in Figures 8, 9, and 10, respectively. The torsional stresses have been calculated on the basis of an assumed narrow rectangular chordwise blade profile based upon an average spanwise angular displacement. Since there is lack of theoretical and experimental guidance regarding the magnitude and location of the lumped mass $m_2^{(i)}$ along the chord, two sets of data for the two materials studied are shown and compared. The first case assumes that 60% of the mass is at the blade center gravity while the second case assumes a 30% distribution. In each case we introduce a parameter c to indicate the chordwise location of $m_2^{(i)}$ relative to the elastic axis. The torsional natural frequency torsional stresses and angle of twist calculated for these chordwise mass distributions are presented in Figures 8, 9, and 10 as a function of c for titanium and boron-aluminum blades. As expected, when the values of c and $m_2^{(i)}$ increase the torsional stresses and the angle of twist increase while the natural frequencies decrease.

CONCLUDING REMARKS

Based upon the investigation of titanium and boron-aluminum blades, it is observed that the effect of engine speed Ω is insignificant on the resulting blade stress. This observation is particularly true for the boron-aluminum blade, which is stiffer than the titanium blade. In general, the influence of engine rotation is to stiffen the blade. However, this influence decreases as the blade stiffness increases.

It can be seen from Figures 8-10 that the values of c and η play a very important role in torsional vibration. As c and/or η increase the torsional stiffness of the blade tends to

decrease. A reasonable value of c or η can be determined experimentally. The torsional mode of vibration, however, is less significant than the corresponding bending modes.

Finally, due to the light weight and high strength of the boron-aluminum, its response characteristics are superior to the corresponding titanium blade.

ACKNOWLEDGEMENT

Figure 6. Maximum Displacement as a Function of Rotor Speed

Figure 5. Bending Natural Frequencies as a Function of Rotor Speed
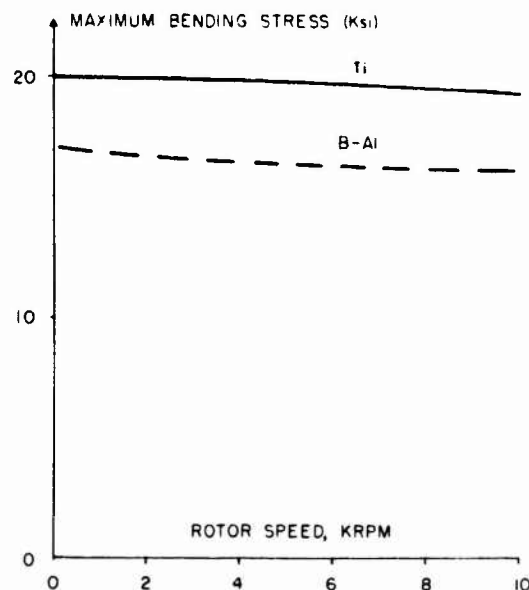
Figure 7. Maximum Bending Stress as a Function of Rotor Speed

15
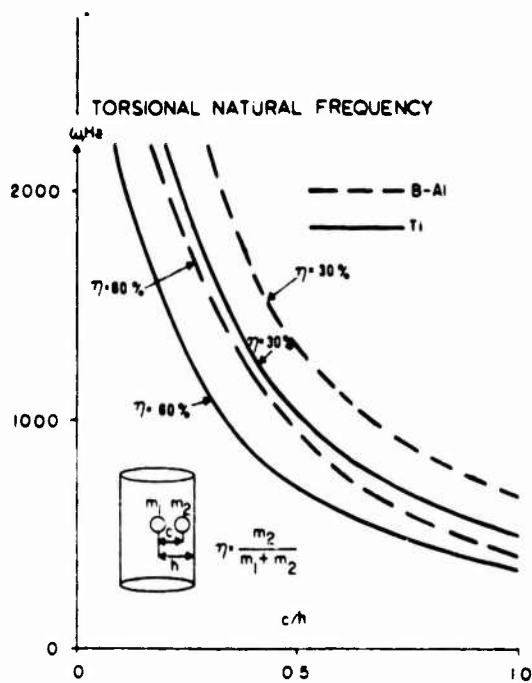
Figure 8. Torsional Natural Frequency as a Function of c/h
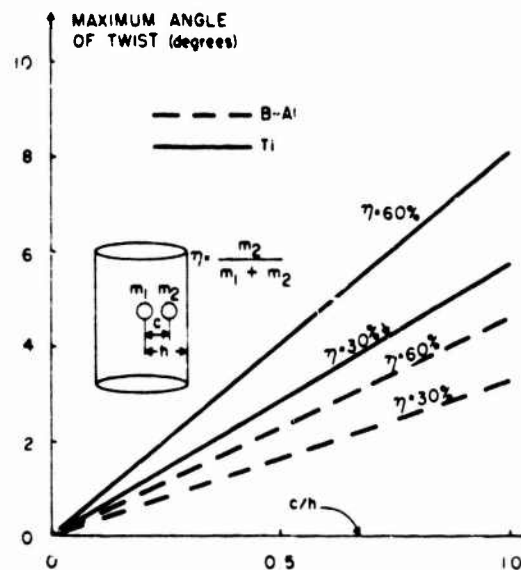
Figure 10. Maximum Angle of Twist as a Function of c/h
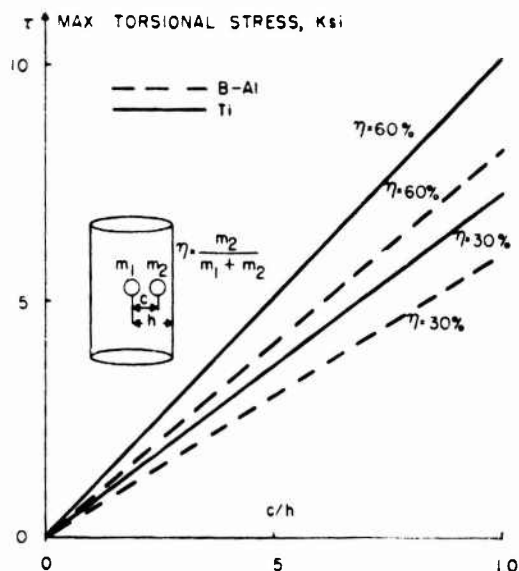
Figure 9. Maximum Torsional Stress as a Function of c/h

16

TABLE 1.   TITANIUM BLADE

Spanwise Station	1	2	3	4	5	6
$m^{(i)} \left(\frac{\text{lb}}{\text{in}} \sec^2 \right)$	$.276 \times 10^{-3}$	$.580 \times 10^{-3}$	$.609 \times 10^{-3}$	$.614 \times 10^{-3}$	$.686 \times 10^{-3}$	$.834 \times 10^{-3}$
L_i (in.)	12	10	8	6	4	2
Area Moment of Inertia (in.^{4})	1.26×10^{-3}	1.54×10^{-3}	2.874×10^{-3}	2.080×10^{-3}	4.400×10^{-3}	10.020×10^{-3}

$E = 16 \times 10^6$ psi

Average chord length = 4 in.

Average thickness = 1/4 in.

$G = 6.4 \times 10^6$ psi

Span length = 12 in.

17

TABLE II. BORON-ALUMINUM BLADE

Spanwise Station	1	2	3	4	5	6
$m^{(i)}\left(\dfrac{lb}{in}\,sec^2\right)$	$.294 \times 10^{-4}$	$.646 \times 10^{-4}$	$.841 \times 10^{-4}$	$.956 \times 10^{-4}$	$.932 \times 10^{-4}$	$.720 \times 10^{-4}$
L_i (in.)	9.2	7.6	6.2	4.8	3.4	2.7
Area Moment of Inertia (in.^{4})	1.146×10^{-4}	2.456×10^{-4}	4.224×10^{-4}	6.713×10^{-4}	10.02×10^{-4}	11.98×10^{-4}

Spanwise Station	7	8	9
$m^{(i)}\left(\dfrac{lb}{in}\,sec^2\right)$	$.618 \times 10^{-4}$	$.653 \times 10^{-4}$	$.660 \times 10^{-4}$
L_i (in.)	2.0	1.3	0.6
Area Moment of Inertia (in.^{4})	14.16×10^{-4}	16.47×10^{-4}	18.88×10^{-4}

$E = 36 \times 10^6$ psi

Chord length = 2.228 in.

Average thickness = 1/8 in.

$G = 8.5 \times 10^6$ psi

Span length = 9.2 in.

REFERENCES

1. F. C. Moon, "Wave Surfaces Due to Impact on Anisotropic Plates", Journal of Composite Materials, Vol. 5, 1972, p. 62.

2. B. P. Gupta and N. Davids, "Penetration Experiments with Fiberglass Reinforced Plastics", Experimental Mechanics, Vol. 6, 1966, p. 455.

3. A. Worzesien, "Improving the Impact Resistance of Glass-Fibre Composites", Composites Technology, Vol. 3, 1972, p. 172.

4. R. L. Sierakowski, G. E. Nevill, Jr., C. A. Ross, and E. R. Jones, Studies on the Dynamic Fracture Characteristics of Composites, Tech. Report AFATL-TR-72-44, March, 1972.

5. S. H. Crandall, "Numerical Methods of Analysis", Shock and Vibration Handbook, Vol. 2, 1961, 28-19, McGraw-Hill Book Company.

NOMENCLATURE

Symbol	Definition
Ω	Engine operating speed
ω	Blade natural frequency
$m_1^{(i)}$	Segment of lumped mass located along blade elastic axis
$m_2^{(i)}$	Segment of lumped mass located at chordwise c.g. of blade
$m_{e.a.}$	Chordwise lumped mass at elastic axis
$m_{c.g.}$	Chordwise lumped mass at center of gravity
$m^{(i)}$	Total mass lumped at each station $= m_1^{(i)} + m_2^{(i)} = m_{e.a.} + m_{c.g.}$
y_i	Vertical deflection at i^{th} blade spanwise station measured to the elastic axis
ϕ_i	Blade twist at i^{th} blade spanwise station measured to the elastic axis

Symbol	Definition
L_i	Spanwise distance between lumped mass locations to the root of blade
e_i	Chordwise distance between shear center and c.g. at spanwise station i
c_i	Chordwise pseudo distance introduced for an off center mass to incorporate torsion effects
η_i	$\dfrac{m_2^{(i)}}{m^{(i)}}$
h	Half chord length
h_{ij}	Blade torsional rigidity
k_{ij}	Blade flexural rigidity
T	Kinetic energy of blade system
V	Potential energy of blade system
$C.F.$	Centrifugal force

DISCUSSION

Mr. Doepker (Babcock and Wilcox Co.): What was the relative impact properties of the graphite epoxy blade versus the fiberglass blade? Was the fiberglass superior from an impact standpoint?

Mr. Sun: I think the graphite epoxy was superior.

Mr. Doepker: Did you perform any analysis to optimize the ply layups of those materials?

Mr. Sun: The lamination effect will be the third stage.

A TIME DOMAIN MODAL VIBRATION TEST TECHNIQUE

S.R. Ibrahim, Graduate Student
The University of Calgary
Department of Mechanical Engineering
Calgary, Alberta, Canada

and

E.C. Mikulcik, Associate Professor
The University of Calgary
Department of Mechanical Engineering
Calgary, Alberta, Canada

A technique using the free response to determine a mathematical model of a structure is developed. Vibration parameters are then determined from this model. Simulated responses from both lumped and distributed parameter systems demonstrate that this technique produces excellent results, even in the presence of closely spaced natural frequencies and high damping, when frequency domain methods fail.

INTRODUCTION

Modal vibration testing is carried out to determine, experimentally, the natural frequencies and the associated principal modes and damping factors of structures. Such tests are often performed either to verify or to determine mathematical models of the system being tested.

Techniques that are presently used in vibration tests [1-11]* may be classified as 'frequency domain' methods. Vibration parameter data is extracted from frequency response information (i.e. from frequency domain 'numbers') obtained directly from sine wave testing, or from Fourier analysis of random or transient test results [12-16]. It is usually necessary to assume that the structure being tested has light damping, and that the modes are sufficiently separated in frequency so that a single degree of freedom approximation is adequate at the resonant frequencies. This aspect of frequency response techniques is discussed in references [2,17,18], where it is shown that the application of frequency domain methods to structures which do not comply with these assumptions may lead to serious errors in the test results.

_____

* Numbers in brackets designate references at end of paper.

This paper describes the theory of a technique in which a 'time domain', rather than a frequency domain model of the test structure is obtained. The structure may be driven or not driven; the undriven case is simpler, and is the one described here. Vibration parameters of the structure are obtained directly from the time domain model without the necessity for assumptions concerning the degree of damping or the spacing of natural frequencies.

Simulated experimental data for a two degree of freedom spring-mass-damper system is used to compare this technique with frequency response methods. This comparison of results based on 'exact experimental data' serves to point out that large errors are possible when using frequency response methods for systems having closely spaced natural frequencies, especially in the presence of considerable damping, even when the experimental data is excellent. It also shows that, under the same circumstances, the time domain technique produces excellent results because there are no assumptions involved in the procedure of determining vibration parameters from the time domain model.

The possibility of using a lumped parameter model for obtaining vibration information about a distributed parameter system is explored. It is shown that the number of measurement stations located on the test

structure should, in theory, be equal to the number of modes excited in the test response. Validity is demonstrated by using simulated data for a pinned-pinned beam to identify four modes, assuming four measurement stations on the beam.

THE TIME DOMAIN MODEL

A lumped parameter linear model is assumed to describe the system to be tested. The general equation of motion for the system is [20-22]

$$\underline{M} \ddot{\underline{y}} + \underline{C} \dot{\underline{y}} + \underline{K} \underline{y} = \underline{f} \text{ *} . \tag{1}$$

$\underline{M}$, $\underline{C}$ and $\underline{K}$ are the mass, damping, and stiffness matrices respectively; $\underline{y}$ and $\underline{f}$ are the displacement and forcing function vectors.

The time domain model chosen to represent the system for vibration study is equation (1) rewritten in the following state variable form:

$$\begin{bmatrix} \dot{\underline{y}} \\ \ddot{\underline{y}} \end{bmatrix} = \begin{bmatrix} \underline{o} & \underline{1} \\ -\underline{M}^{-1}\underline{K} & -\underline{M}^{-1}\underline{C} \end{bmatrix} \begin{bmatrix} \underline{y} \\ \dot{\underline{y}} \end{bmatrix} + \begin{bmatrix} \underline{o} \\ \underline{M}^{-1} \end{bmatrix} \underline{f} \tag{2}$$

or

$$\dot{\underline{x}} = \underline{A} \underline{x} + \underline{B} \underline{f} \tag{3}$$

where

$$\underline{x} = \begin{bmatrix} \underline{y} \\ \dot{\underline{y}} \end{bmatrix} ,$$

$$\underline{A} = \begin{bmatrix} \underline{o} & \underline{I} \\ -\underline{M}^{-1}\underline{K} & -\underline{M}^{-1}\underline{C} \end{bmatrix} ,$$

and

$$\underline{B} = \begin{bmatrix} \underline{o} \\ \underline{M}^{-1} \end{bmatrix} ,$$

The eigenvalues of $\underline{A}$ are the roots of the system's characteristic equation [19], hence the system is completely characterized by $\underline{A}$. The matrix $\underline{B}$ determines the system's response to a particular forcing function $\underline{f}$. This means that $\underline{B}$ need not be known in order to determine the vibration parameters of the system, hence a vibration test method may be based on the free response only. Such a test method would be easier to implement

---
* Matrices are indicated by underlined capital letters; vectors are indicated by underlined lower case letters.

since the need to obtain and deal with excitation records would be eliminated. The technique described in this paper is based on the determination of $\underline{A}$ using the free response governed by

$$\dot{\underline{x}} = \underline{A} \underline{x} \tag{4}$$

For a system of n lumped masses, $\underline{A}$ is of dimension 2n x 2n. Equation (2) shows that the upper half of $\underline{A}$ is [$\underline{o}$ $\underline{I}$], hence n x 2n, or $2n^2$ elements of $\underline{A}$ need be determined in order to characterize the system completely.

The $2n^2$ unknown elements of $\underline{A}$ are determined by noting that at any instant of time, t_i, equation (4) specifies that the following relationship must hold between the accelerations, velocities, and displacements of the lumped masses:

$$\dot{\underline{x}}_i = \underline{A} \underline{x}_i \tag{5}$$

If the accelerations, velocities, and displacements of the n lumped masses are measured and therefore known at t_i, then equation (5) represents 2n scalar equations in the elements of $\underline{A}$. The equations which correspond to the upper half of $\underline{A}$ are identities; the other n equations are linear non-homogeneous in the $2n^2$ unknown elements of $\underline{A}$. Writing equation (5) at 2n different time instants $t_1, t_2 \ldots t_{2n}$ results in $2n^2$ linear non-homogeneous equations in the unknown elements of $\underline{A}$, hence $\underline{A}$ can be completely determined. It is convenient to write these $2n^2$ equations together with $2n^2$ equations corresponding to the upper half of $\underline{A}$ in the following form:

$$[\dot{\underline{x}}_1 \ \dot{\underline{x}}_2 \ \cdots \ \dot{\underline{x}}_{2n}] = \underline{A} [\underline{x}_1 \ \underline{x}_2 \ \cdots \underline{x}_{2n}] \tag{6}$$

or

$$\dot{\underline{X}} = \underline{A} \underline{X} , \tag{7}$$

whence,

$$\underline{A} = \dot{\underline{X}} \underline{X}^{-1}$$

Equation (7) can be solved for $\underline{A}$ because all the elements of $\dot{\underline{X}}$ and $\underline{X}$ can be obtained from measured response data. The responses at all coordinates of the n degree of freedom system must be recorded and digitized at 2n different instants in time, giving 2n different displacement vectors, 2n corresponding velocity vectors, and 2n corresponding acceleration vectors.

In order that the identified $\underline{A}$ matrix represent the n degree of freedom system, all n modes must contribute to the response information used for identification.

22

VIBRATION PARAMETERS FROM THE A-MATRIX

The relation of the vibration parameters to $\underline{A}$ becomes apparent by assuming a solution of the form

$$\underline{x} = \underline{\psi}\, e^{\lambda t} \tag{8}$$

for equation (4). Substitution of this solution into equation (4) results in the following eigenvalue problem:

$$\lambda\, \underline{\psi} = \underline{A}\, \underline{\psi} \tag{9}$$

Hence it follows that the eigenvalues, or characteristic roots, of $\underline{A}$ give information about the system's natural fequencies and damping factors, and the eigenvectors are the damped principal modes of vibration. Real eigenvalues correspond to overdamped modes of vibration, while eigenvalues corresponding to modes for which the damping is less than critical are complex of the general form $\lambda_j = a_j + ib_j$. The damped and undamped natural frequencies, and the damping ratio associated with the j-th mode are given by

$$\omega_{dj} = b_j \tag{10}$$

$$\omega_{nj} = \sqrt{a_j^2 + b_j^2} \tag{11}$$

$$\eta_j = \frac{a_j}{\sqrt{a_j^2 + b_j^2}} \tag{12}$$

Complex eigenvalues occur in conjugate pairs, with corresponding complex conjugate eigenvectors. Each pair of complex eigenvalues corresponds to a single natural frequency and damping ratio, and the associated pair of complex conjugate eigenvectors corresponds to a single real mode shape.

The undamped principal modes of vibration may be determined using equation (9) by setting $\underline{M}^{-1}\underline{C} = 0$ in the $\underline{A}$ matrix.

RESULTS FOR A TWO DEGREE OF FREEDOM SYSTEM

The technique discussed in the preceeding sections, and various frequency response methods, are applied here to system response data which is simulated on the digital computer. It is shown that, even with excellent experimental data, the basic assumptions made in the theory of the frequency response methods can lead to serious errors in the results for systems having close natural frequencies, especially in the presence of considerable damping. The results obtained using the time domain technique are consistently good.

The system that is used as the structure under test is shown in Figure 1. Results for the following two cases are presented in detail:

Case 1: highly damped system with well spaced undamped natural frequencies

Case 2: lightly damped system, with closely spaced undamped natural frequencies

In addition, results are noted for comparison purposes for the following two additional cases:

Case 3: lightly damped system with well spaced undamped natural frequencies

Case 4: highly damped system with closely spaced undamped natural frequencies

The system parameters corresponding to the four cases considered are listed in Table 1, and the theoretical vibration parameters are presented in Table 2. It is of interest to note that damped modes for less than critical damping are complex, indicating that the two masses of the system do not move exactly in or out of phase if the system is vibrating in such a mode.

Frequency Response Methods

The frequency response for each case was calculated by applying an impulse input to the system and then calculating the transfer matrix over the frequency range from 0 to 30 HZ at intervals of 0.05 HZ. The following quantities were calculated for use in applying the various frequency response methods:

X_{ij}, the in-phase component of the amplitude at coordinate i due to a harmonic force at coordinate j.

Y_{ij}, the quadrature component of the amplitude at coordinate i due to a harmonic force at coordinate j.

A_{ij}, the modulus of the amplitude at coordinate i due to a harmonic force at coordinate j.

R_{ij}, the rate of change of arc length with respect to frequency on the complex receptance plot (X_{ij} versus Y_{ij}).

Z_{ij}, the impedance of coordinate i due to a driving harmonic force at coordinate j.

The frequency response methods employed are the following:

1) The peak amplitude method [1]

The natural frequencies are assumed to correspond to the peaks in the plots of A_{ij} versus the driving frequency.

23

2) The quadrature response method [2]

The driving frequency is assumed to be equal to a natural frequency when the in-phase component of the response, X_{ij}, is zero. This corresponds to a 90 degree phase difference between the forcing function and the response.

3) The maximum quadrature component method [2]

Resonances are assumed to correspond to maxima in the quadrature component, Y_{ij}, of the response. This is the component which is 90 degrees out of phase with the forcing function.

4) The Kennedy and Pancu Technique [3]

Natural frequencies are assumed to correspond to maxima of R_{ij}, the rate of change of arc length of the complex receptance plot with respect to driving frequency.

5) The mechanical impedance method [5]

Natural frequencies are assumed to correspond to minima of the plots of impedance versus the driving frequency.

Frequency response plots for each of the above methods are shown in Figures 2 to 8 for cases 1 and 2; the natural frequencies determined for all four cases are listed in Table 3. These results show that case 3 is the only case for which two natural frequencies were detected. The results for this case show considerable scatter with varying degree of accuracy for each method used. The principal modes for case 3 using peak amplitude method were found to be (1,0.93) and (1,-0.832). The errors in these modes are 8.25% and 12.9% as compared to the theoretical damped modes, and 7% and 17.8% as compared to the theoretical undamped modes.

Time Domain Method

Time response data for the four cases was obtained by numerically integrating the equations of motion using the initial conditions

$$y_1(o) = 1 \quad ; \quad \dot{y}_1(o) = 0$$

$$y_2(o) = 3 \quad ; \quad \dot{y}_2(o) = 0$$

The response matrices $\dot{X}$ and X were obtained using four response vectors containing response information at $t = 0.0, 0.02, 0.04, 0.06$ sec. The vibration parameters obtained from the eigenvalues and eigenvectors of the identified A matrices, calculated using the method of A.N. Krylov [23] are presented in Table 4. The percentage error in the identified vibration parameters are also listed in Table 4. Since there are no approximations involved in extracting

vibration data from the time domain model, these errors are due to computation errors derived in the numerical integration of the time responses, and in the calculation of the eigenvalues and eigenvectors of the A matrices.

DISTRIBUTED PARAMETER SYSTEMS

All physical structures posess distributed mass, elasticity and damping. Such structures, referred to as continuous systems or distributed parameter systems, are described by partial differential equations and they theoretically contain an infinite number of degrees of freedom and hence an infinite number of frequencies and modes of vibration. In practice, however, the frequency range of interest contains only a finite number of these frequencies. It is shown here that the time domain method of vibration testing based on lumped parameter systems, as described in this paper can be used to obtain vibration parameters of distributed systems when it is considered that only a finite number of modes contribute to the response.

The free response of n points, or stations, on a linear elastic distributed parameter structure in which n modes are excited is

$$\underline{p} = \sum_{i=1}^{2n} R_i \underline{\psi}_i e^{\lambda_i t} \tag{13}$$

where $\underline{p}$ is the vector whose elements are the displacements of the n stations, R_i are constants, $\underline{\psi}_i$ are the complex modal vectors, and λ_i are the characteristic roots. Let it be assumed that there exists a hypothetical lumped parameter system with n masses which move in exactly the same manner as the n points of the distributed structure. The response of this hypothetical lumped system is, then,

$$\underline{y} = \sum_{i=1}^{2n} R_i \psi_i e^{\lambda_i t} \tag{14}$$

If this response is used to identify the vibration parameters of the hypothetical n degree of freedom lumped parameter system, then, the parameters so determined are also those of the n modes excited.

In summary, it can be stated that the time domain method described in this paper may be applied to distributed structures if the number of measuring points on the structure equals the number of modes which contribute to the measured response of the structure. The response measurements obtained are then used in the same manner as for the lumped parameter case.

Results for a Pinned-Pinned Beam

In this section, computed response data for a uniform beam with viscous damping is used to identify the first four frequencies and mode shapes of a beam. The parameters of the beam are as follows:

Young's modulus (E)	30×10^6	lb/in^2
Viscous damping constant (c)	0.5	$lb \cdot sec/in^2$
Length (L)	24	in.
Width (b)	3	in.
Thickness (h)	0.5	in.

The equation of motion of the beam is

$$EI \frac{\partial^4 y}{\partial x^4} + c \frac{\partial y}{\partial t} + \frac{\rho A}{g} \frac{\partial^2 y}{\partial t^2} = 0 \qquad (15)$$

Equation (15) was solved for simply supported end conditions, with initial conditions chosen so that only the first four modes were present in the response. Displacement, velocity, and acceleration responses at four stations, located at distances of L/8, 3L/8, 5L/8 and 7L/8 from one end, were calculated for each one-thousandth of a second from 0.001 sec to 0.009 sec. These responses were used to construct $\underline{X}$ and $\underline{\dot{X}}$ response matrices which, in turn, were used to determine the $\underline{A}$ matrix, from which the vibration parameters of the beam, at the four stations, were obtained. These parameters together with the theoretical ones, are listed in Table 5. The results show that the identified values are essentially exact except for computer round-off errors.

CONCLUSIONS AND REMARKS

A time domain vibration technique which can identify both lumped and distributed parameter systems is described. The method entails the development of a time domain model of the system from free vibration test data, followed by calculation of the system's vibration parameters using the model. There are no approximations involved in obtaining the vibration parameters, so if the vibration test data is sufficiently accurate to produce a good model, the method will give good results even for structures having high damping and close natural frequencies. This paper describes only the theory of the technique; the practicality of applying it to real structures is the subject of further research by the authors.

REFERENCES

1. Bishop, R.E.D. and G.M.L. Gladwell, "An Investigation into the Theory of Resonance Testing," Phil. Trans. A1963, 255, (No. 1055), pp. 241.

2. Pendered, J.W., "Theoretical Investigation into the Effects of Close Natural Frequencies in Resonance Testing," Journal Mechanical Engineering Science, 1965, Vol. 7, No. 4, pp. 372.

3. Kennedy, Charles C. and C.D.P. Pancu, "Use of Vectors in Vibration Measurement and Analysis," Journal of the Aeronautical Sciences, 1947, Vol. 14, No. 11, pp. 603.

4. Stahl, C.V. Jr., "Phase Separation Technique for Ground Vibration Testing," Aerospace Engineering, July 1962.

5. Hunter, N.F. Jr. and J.V. Otts, "The Measurement of Mechanical Impedance and its use in Vibration Testing," The Shock and Vibration Bulletin, Bulletin 42, Part 1, January 1972.

6. Lewis, R.C. and O.L. Wrisley, "A System for the Excitation of Pure Natural Modes of Complex Structures," Journal of Aerospace Sciences, Vol. 17, No. 11, November 1950.

7. Trail-Nash, R.W., "On the Excitation of Pure Natural Modes in Aircraft Resonance Testing," Journal of Aerospace Sciences, Vol. 25, 1958, pp. 775.

8. Smith, Strether, and A.A. Woods Jr., "A Multi-Driver Admittance Technique for Vibration Testing," The Shock and Vibration Bulletin, Bulletin 42, Part 3, January 1972.

9. Raney, J.P., "Identification of Complex Structures Using Near Resonance Testing," The Shock and Vibration Bulletin, Bulletin 38, Part 2, August 1968.

10. Flannelly, William G., Joseph H. McGravy and Alex Berman, "A Theory of Identification of the Parameters in the Equation of Motion of A Structure Through Dynamic Testing," Symposium on Structural Dynamics, University of Technology, Loughborough, England, March 1970.

11. Dale, Bruce O. and Reymond Cohen, "Multi-parameter Identification in Linear Continuous Vibratory Systems," Journal of Dynamic Systems, Measurements and Control, March 1971.

12. Favour, John D., Maclom C. Mitchell, and Norman L. Olson, "Transient Test Techniques for Mechanical Impedance and Modal Survey Testing," The Shock and Vibration Bulletin, Bulletin 42, Part 1, January 1972.

13. White, R.G., "Evaluation of Dynamic Characteristics of Structures by Transient Testing," Symposium on Structural Dynamics, University of Technology, Loughborough, England, March 1970.

14. Clarkson, B.L. and C.A. Mercer, "Use of Cross-Corrolation in Studying the Response of Lightly Damped Structures to Random Forces," AIAA Journal, Vol. 3, No. 12, December 1965.

15. Otts, John V. and Norman F. Hunter, Jr., "Random Force Vibration Testing," The Shock and Vibration Bulletin, Bulletin 38, Part 2, August 1968.

16. Christiansen, Robert G. and Wallace W. Parmenter, An Experimental Technique for Determining Vibration Modes of Structures with Quasi-Stationary Random Forcing Function," The Shock and Vibration Bulletin, Bulletin 42, Part 4, January 1972.

17. Pendered, J.W. and R.E.D. Bishop, "A Critical Introduction to Some Industrial Resonance Testing Techniques," Journal Mechanical Engineering Science, 1963, Vol. 5, No. 4, pp. 345.

18. Young, Joseph P. and Frank J. On, "Mathematical Modeling via Direct Use of Vibration Data," Society of Automotive Engineers, Paper No. 690615, National Aeronautic and Space Engineering and Manufacturing Meeting, Los Angeles, California, October 1969.

19. Takahashi, Y., M.J. Rabins and D.M. Auslander, Control, Addison-Wesley Publishing Company, 1970.

20. Bishop, R.E.D., "The Treatment of Damping Forces in Vibration Theory", Journal o^ Royal Aeronautical Society," Vol. 59, November 1955.

21. Lancaster, P., "Free Vibration and Hystretic Damping," Journal of Royal Aeronautical Society, Vol. 64, p. 229, 1960.

22. Bishop, R.E.D., The Matrix Analysis of Vibration, Cambridge University Press, England, 1965.

23. Faddeva, N.V., Computational Methods of Linear Algebra, Dove Publications Inc., N.Y., 1959.

TABLE 1

PARAMETERS OF THE TWO DEGREE OF FREEDOM SYSTEM

Case	Masses (lb)		Stiffnesses (lb/in)			Damping Coefficients (lb.sec/in)		
	M_1	M_2	k_1	k_2	k_3	C_1	C_2	C_3
1	10.0	10.0	100.0	50.0	100.0	3.0	2.0	1.0
2	10.0	10.0	100.0	1.0	100.0	0.3	0.2	0.1
3	10.0	10.0	100.0	50.0	100.0	0.3	0.2	0.1
4	10.0	10.0	100.0	1.0	100.0	3.0	2.0	1.0

TABLE 2

THEORETICAL VIBRATION PARAMETERS OF THE TWO DEGREE OF FREEDOM SYSTEM

Case	Mode No.	Damped			Undamped	
		Frequency (HZ)	Principal Mode (y_2/y_1)	Damping Factor	Frequency (HZ)	Principal Mode (y_2/y_1)
1	1	--	-0.2719	1.3583	9.8585	1.0000
	2	8.5918	1.6589+i0.3327	0.5579	13.9420	-1.0000
	3	--	-0.5809	1.3583	--	--
2	1	9.7674	-0.6149+i0.0221	0.1912	9.8585	1.0000
	2	9.8489	1.6159+i0.0584	0.0546	9.9566	-1.0000
3	1	9.8582	1.0155+i0.1229	0.0617	9.8585	1.0000
	2	13.7944	-0.9494+i0.1620	0.1316	13.9420	-1.0000
4	1	--	-0.6100	1.9143	9.8585	1.0000
	2	8.2621	1.6212+i0.0049	0.5465	9.9566	-1.0000
	3	--	-0.6174	1.9143	--	--
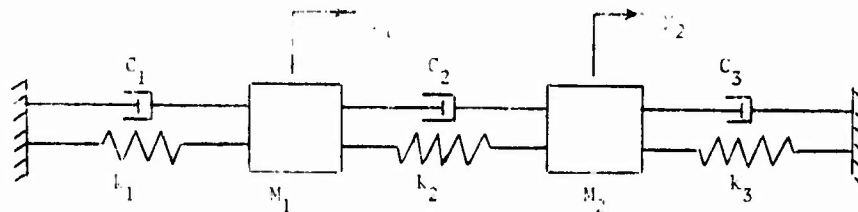
FIGURE 1   TWO DEGREE OF FREEDOM SYSTEM

27

TABLE 3

NATURAL FREQUENCIES FROM FREQUENCY RESPONSE METHODS

Case	Mode No.	Peak Amplitude		Quadrature Component		Max. Quadrature Component		Kennedy and Pancu		Mechanical Impedance		Theoretical	
		at M_1	at M_2	at M_1	at M_2	at M_1	at M_2	at M_1	at M_2	at M_1	at M_2	Damped	Undamped
1	1	--	--	--	--	--	--	--	--	--	--	--	9.8585
	2	--	.200	10.025	9.425	7.175	8.600	--	8.150	9.625	10.250	8.5918	13.9420
2	1	9.850	.350	9.850	9.875	9.850	9.850	9.750	9.650	9.850	9.850	9.7674	9.8585
	2	--	--	--	--	--	--	--	--	--	--	9.8489	9.9566
3	1	9.775	9.900	9.875	9.875	9.825	9.850	10.05	9.75	9.825	9.925	9.8585	9.8585
	2	14.22	--	--	14.95	13.925	13.875	14.000	13.50	14.425	--	13.7911	13.9420
4	1	--	--	--	--	--	--	--	--	--	--	--	9.8585
	2	--	9.925	9.875	9.875	6.8	8.825	7.150	8.20	9.850	9.850	8.3621	9.9566

TABLE 4

IDENTIFIED VIBRATION PARAMETERS FOR THE FOUR CASES OF THE TWO DEGREE OF FREEDOM SYSTEM

Case	Mode No.	Damped			Undamped	
		Frequency (Hz) and Error (%)	Principal Mode (y_2/y_1) and Error (%)	Damping Factor and Error (%)	Frequency (Hz) and Error (%)	Principal Mode (y_2/y_1) and Error (%)
1	1	--	-0.2721 (0.0645)	1.3593 (0.0736)	9.8581 (0.0040)	1.0007 (0.0752)
	2	8.5917 (0.0011)	1.6591+i0.3326 (0.0094)*	0.5576 (0.0537)	13.9515 (0.0681)	-1.0010 (0.1)
	3	--	-0.5819 (0.1856)	1.3593 (0.0736)	--	--
2	1	9.7678 (0.0040)	-0.6177+i0.0254 (0.0145)	0.1913 (0.0523)	9.8537 (0.0486)	1.0085 (0.85)
	2	9.8486 (0.0030)	1.6165+i0.0580 (0.0338)	0.0546 (0.0000)	9.9574 (0.0080)	-1.0247 (2.4700)
3	1	9.8582 (0.0000)	1.0154+i0.1230 (0.0109)	0.0617 (0.0000)	9.8585 (0.0000)	0.9999 (0.0100)
	2	13.7941 (0.0021)	-0.9494+i0.1620 (0.0023)	0.1316 (0.0000)	13.9418 (0.0014)	-1.0000 (0.0000)
4	1	--	-0.6101 (0.0145)	1.9130 (0.0679)	9.8581 (0.0040)	0.9970 (0.3000)
	2	8.2620	1.6211+i0.0050 (0.0037)	0.5465 (0.0000)	9.9563 (0.0030)	-1.0159 (1.59)
	3	--	-0.6177 (0.0548)	1.9130 (0.0679)	--	--

* Error in the magnitude

TABLE 5

THEORETICAL AND IDENTIFIED VIBRATION PARAMETERS OF THE PINNED-PINNED BEAM

VIBRATION PARAMETERS	MODE NO.			
	1	2	3	4
ω_n (rad/sec.)	498.9834	1995.9339	4490.8513	7983.7356
ω_d (rad/sec.)	444.7936	1983.0798	4485.1532	7980.5324
Damping Factor	0.4532	0.1133	0.0504	0.0283
Mode* y_2/y_1 Shape (damped y_3/y_1 and (undamped) y_4/y_1	2.4142 2.4142 1.0000	1.0000 -1.0000 -1.0000	-0.4142 -0.4142 1.0000	-1.0000 1.0000 -1.0000
ω_n (rad/sec.)	498.9834	1995.9317	4490.9127	7983.8540
ω_d (rad/sec.)	444.7973	1983.0789	4485.2129	7980.6467
Damping Factor	0.4532	0.1133	0.0503	0.0283
Damped* y_2/y_1 Mode Shape y_3/y_1 y_4/y_1	2.4141-i0.0000 2.4141-i0.0000 1.0000+i0.0000	1.0000+i0.0000 -1.0000+i0.0000 -1.0000-i0.0000	-0.4142+i0.0000 -0.4141-i0.0000 0.9999+i0.0000	-1.0000+i0.0000 1.0000-i0.0000 1.0000+i0.0000
Undamped* y_2/y_1 Mode Shape y_3/y_1 y_4/y_1	2.4142 2.4142 1.0000	1.0000 -1.0000 -1.0000	-0.4142 -0.4141 0.9999	-1.0000 1.0000 1.0000

* Mode shapes give the relative deflections at locations $y_1 = L/8$, $y_2 = 3L/8$, $y_3 = 5L/8$

and $y_4 = 7L/8$

Case 1:
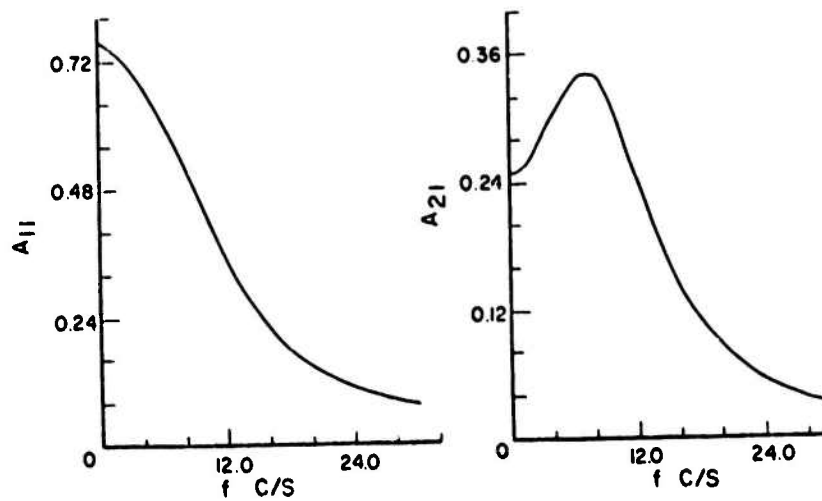
Case 2:
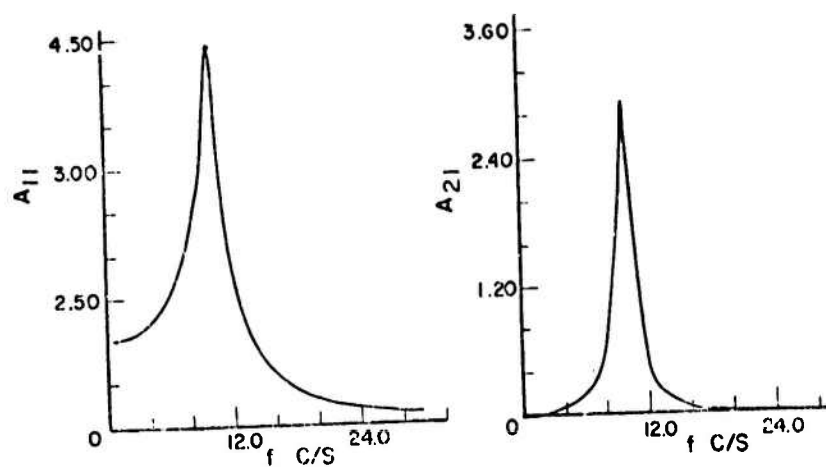
FIGURE 2   AMPLITUDE VERSUS FREQUENCY
(Cases 1 and 2)

31
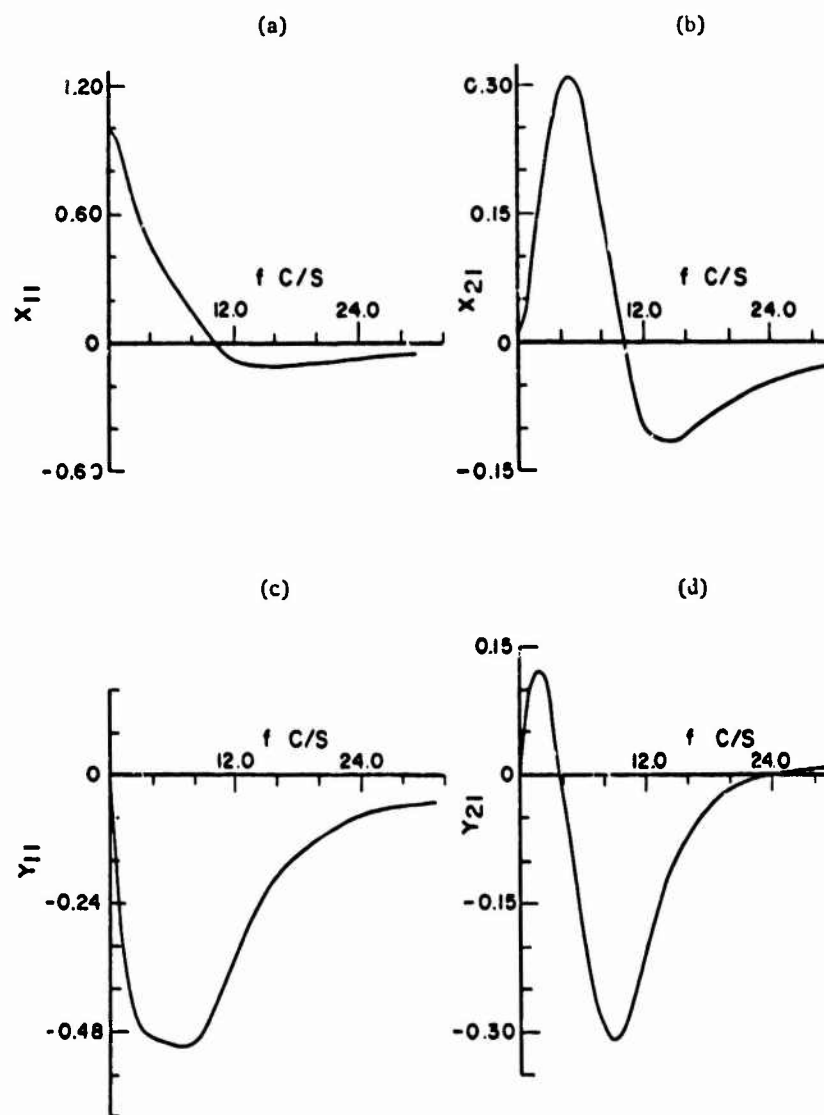
FIGURE 3   IN-PHASE AND QUADRATURE COMPONENTS VERSUS FREQUENCY
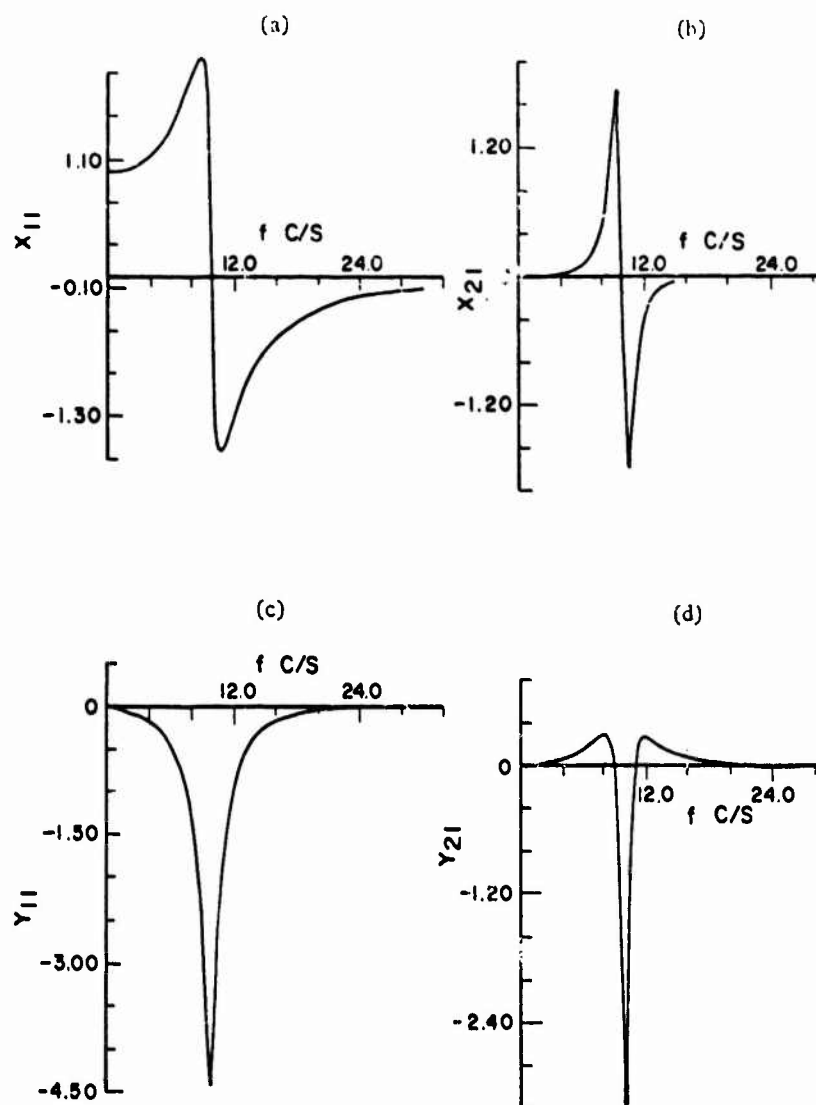
(Case 1)

FIGURE 4   IN-PHASE AND QUADRATURE COMPONENTS VERSUS FREQUENCY

(Case 2)

33
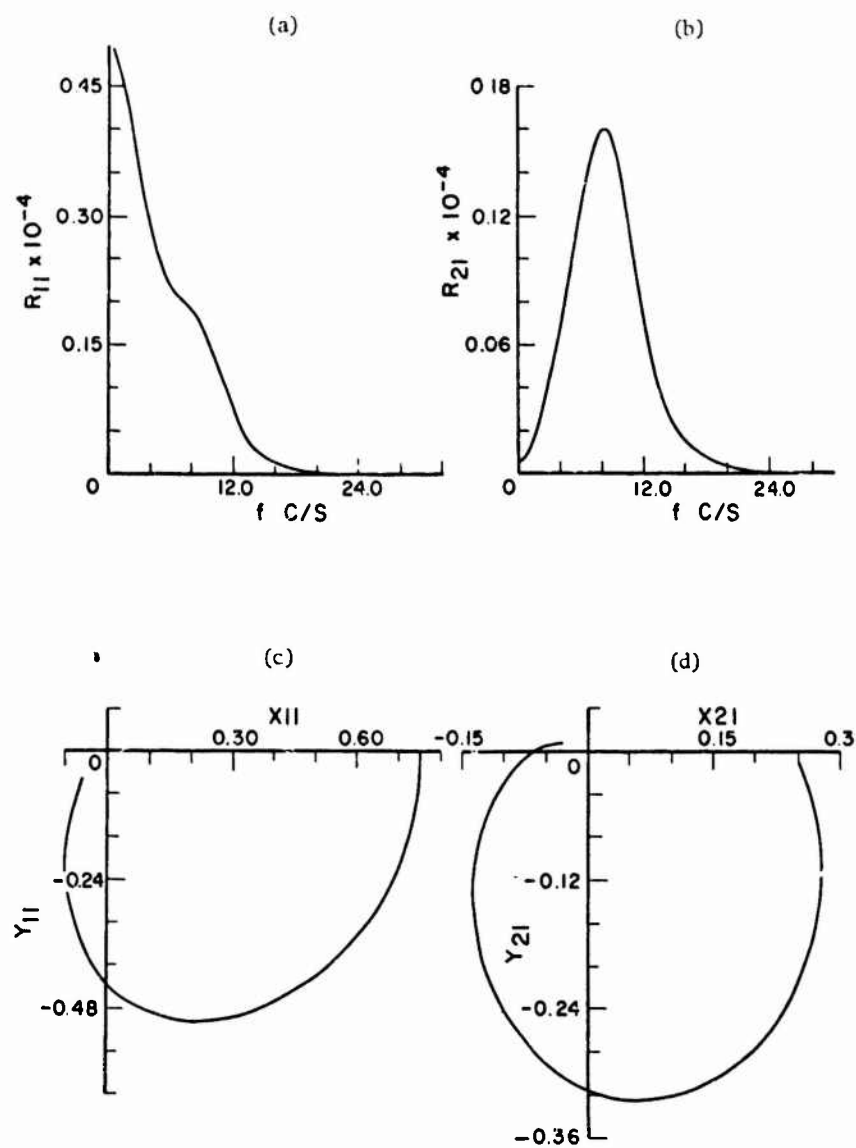
FIGURE 5   KENNEDY AND PANCU PLOTS

(Case 1)

34
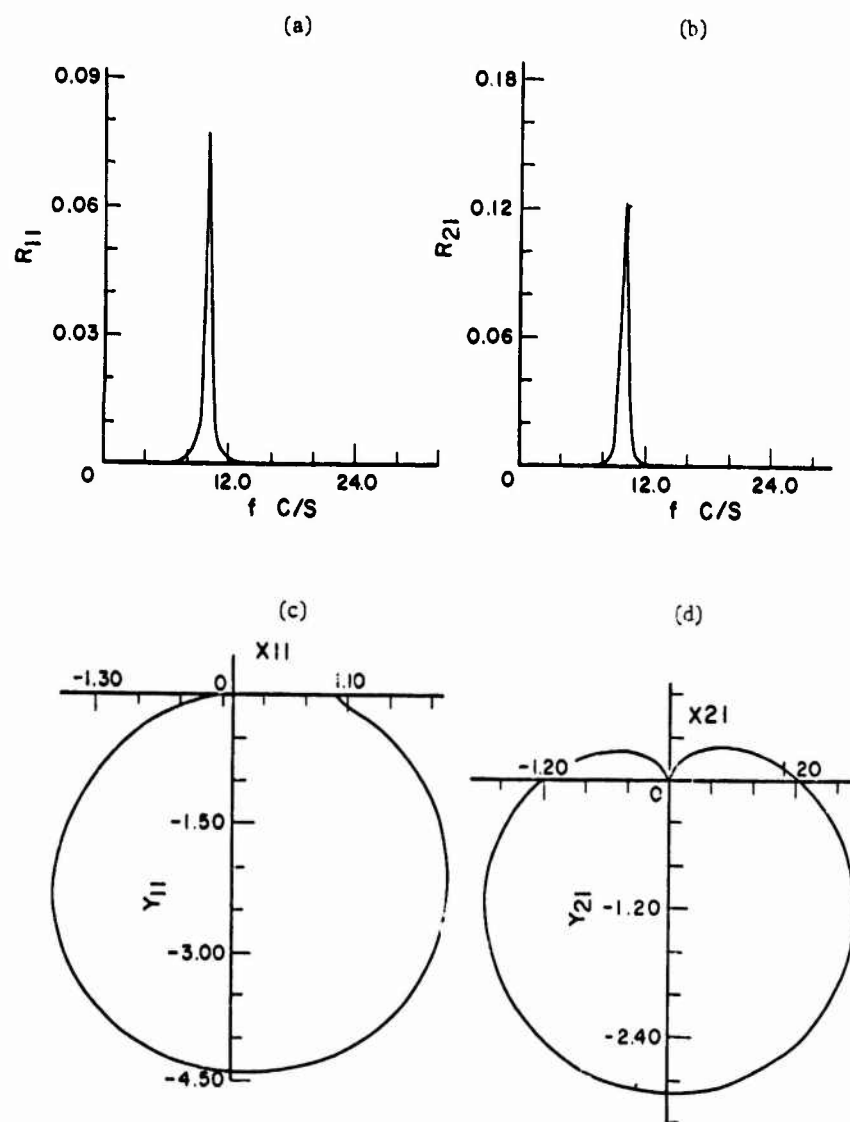
FIGURE 6   KENNEDY AND PANCU PLOTS

(Case 2)

35
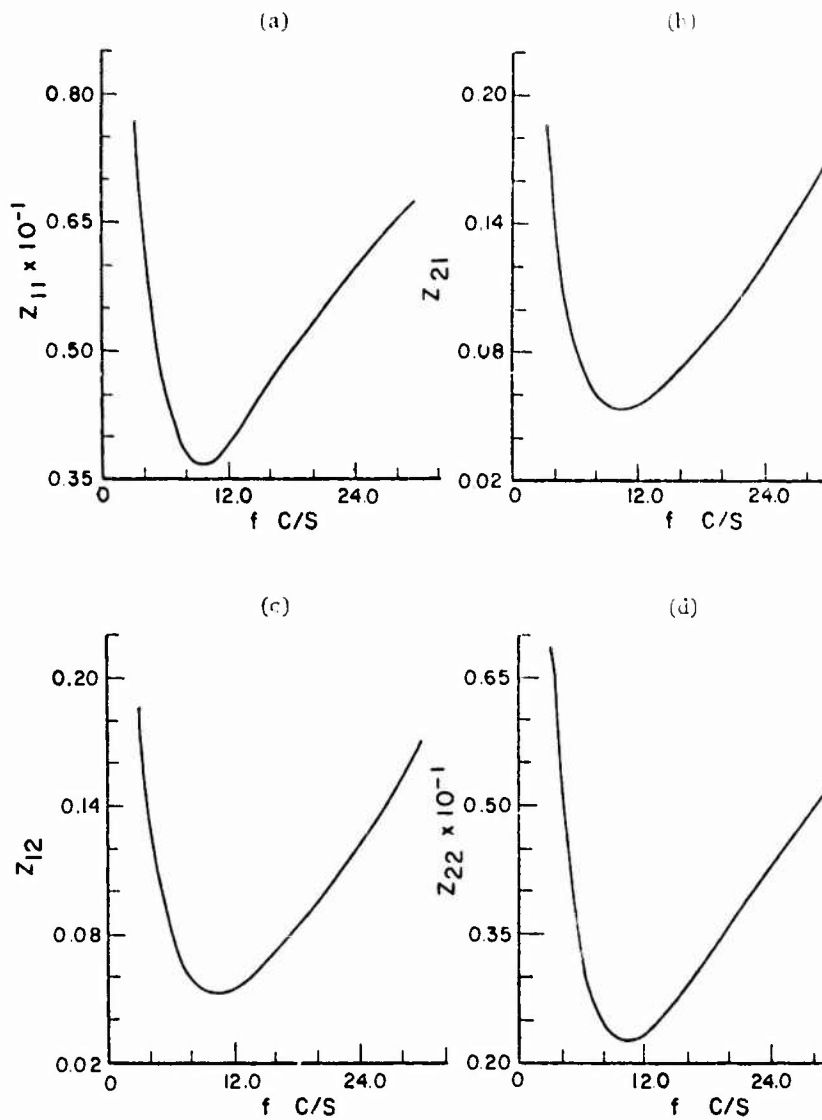
FIGURE 7   MECHANICAL IMPEDANCE VERSUS FREQUENCY

(Case 1)
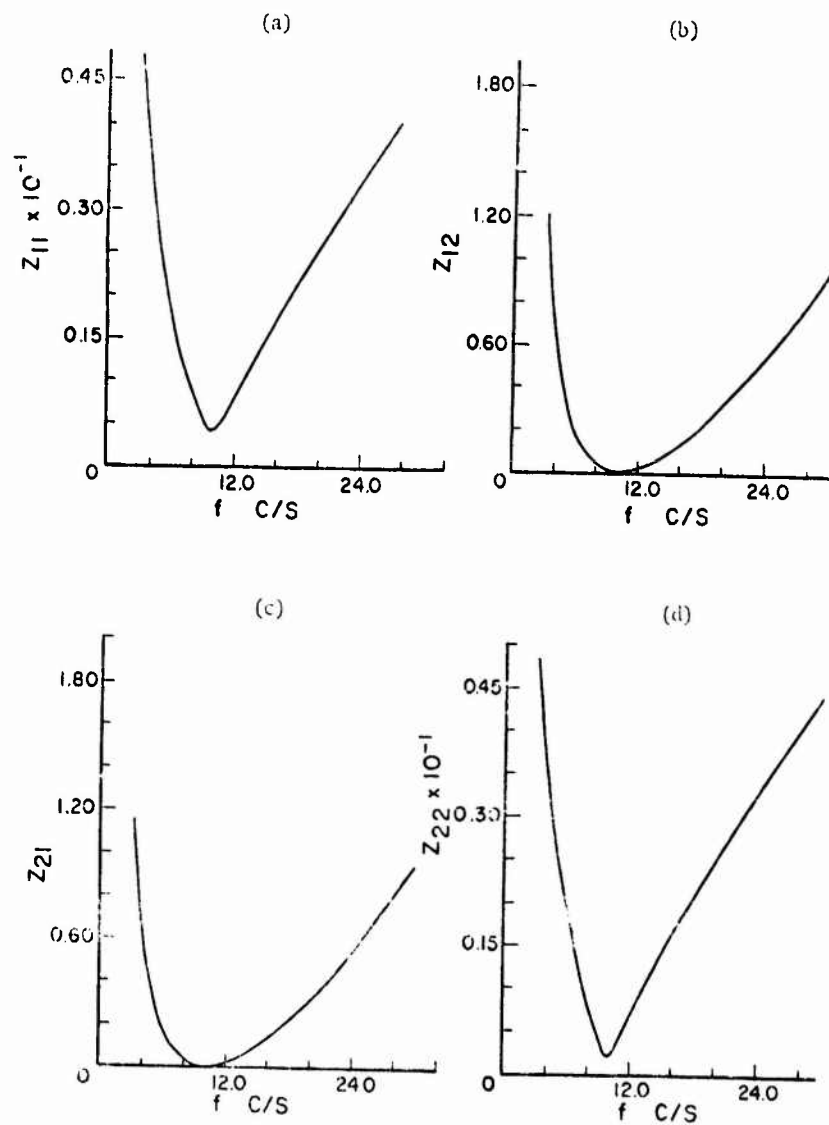
FIGURE 8   MECHANICAL IMPEDANCE VERSUS FREQUENCY

(Case 2)

37

NATURAL FREQUENCIES AND DAMPING OF FULL-SCALE
HYDROFOILS BY "PLUCK TEST" METHODS (U)

James R. Peoples
Naval Ship Research and Development Center
Bethesda, Maryland

(U) A series of tests using simple transient techniques were conducted on the hydrofoil ship, USS PLAINVIEW (AGEH-1). The objective of these tests was to study the structural dynamic characteristics of the hydrofoil strut-foil system. The first three strut foil natural frequencies were found and their damping factors estimated. Several hull natural frequencies were also identified. The test methods, instrumentation and results are discussed.

INTRODUCTION

(U) Flutter of the strut-foil system is one of the main considerations in the design of the AGEH (hydrofoil research ship). Safe operation of the ship depends upon validation of design calculations. Table 1 lists the principal dimensions of the AGEH and the general arrangement of the ship is shown in Figure 1. A one-eighth structurally scaled model of the AGEH main strut-foil system was built[1] by Southwest Research Institute and tested by the Naval Ship Research and Development Center (NSRDC).* Flutter analysis was also made at NSRDC† on this model using model parameters. The results of the model flutter calculations agreed well with the model tests. The full scale flutter calculations , however, indicated a higher flutter speed than that which would be obtained by scaling the experimental flutter speed of the model up to its full scale value. This prompted a need to conduct tests to determine the full-scale vibration characteristics so as to properly evaluate the structural parameters of the full-scale strut-foil system and their relation to the model. Several approaches had been considered for exciting the system so that natural frequencies and mode shapes could be measured. However, the "pluck" approach was considered the most feasible in terms of time and cost for the information the tests would yield. The data obtained from these tests would also be useful in establishing the scaling factor for flutter speed between model and full-scale strut-foil systems.

TABLE 1
AGEH Characteristics

HULL CHARACTERISTICS	
LENGTH, OVERALL - FEET	212
LENGTH BETWEEN PERPENDICULARS - FEET	206
BREADTH, HULL - FEET	40.3
MAXIMUM BREADTH, FOIL DOWN - FEET	70.8
DISPLACEMENT, FULL LOAD - LONG TONS	320
DISPLACEMENT DURING TESTS - LONG TONS	250
FULL LOAD DRAFT, FOILS UP - FEET	6.4
FULL LOAD DRAFT, FOILS DOWN - FEET	25
HULL MATERIAL	5456 ALUMINUM

MAIN STRUT CHARACTERISTICS	
OVERALL STRUT LENGTH - FEET	28.5
STRUT CORD LENGTH - FEET	11.75
FOIL SPAN LENGTH, TIP TO TIP - FEET	26
WEIGHT OF EACH STRUT-FOIL ASSEMBLY - LONG TONS	21
MATERIAL	HY50/100 STEEL

PRELIMINARY STUDIES AND CALCULATIONS

(U) Calculations performed at NSRDC‡ indicated that the first three natural frequencies of the full-scale AGEH

---

* D. Cieslowski conducted the tests in 1968.

† Y. Liu performed the flutter calculations.

‡ J. Caspar and Y. Liu performed the full-scale strut-foil natural frequency calculations.
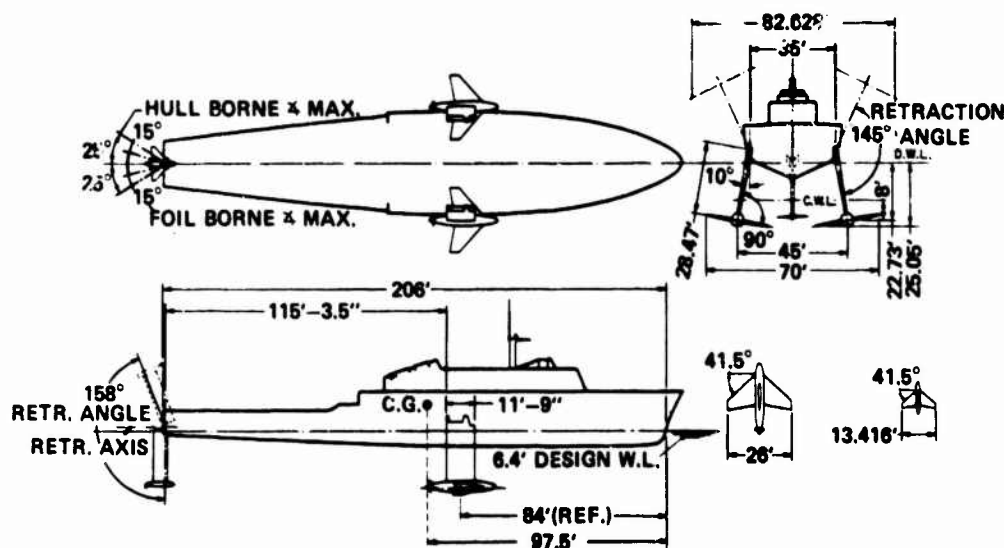
Figure 1 – PLAINVIEW (AG(EH)-1) General Arrangements

main strut-foil system should occur at 1.3 Hz, 3.5 Hz, and 4.5 Hz. The first natural frequency is predominantly associated with a strut bending mode. The second frequency is of prime interest because it is associated with torsional deformations of the strut. Strut-foil systems of the AGEH type generally flutter in this mode. The third mode consists of a combination of various bending and torsion deformations of the strut-foil system.

(U) In support of the "Pluck" tests, calculations were made to determine the natural frequencies of the hull in the vertical and horizontal bending modes. These calculations were done using a 19-section finite-element beam with the General Bending Response Code Computer program at NSRDC.[2] The calculations were done for hullborne, light-load conditions. The added mass of the water was considered in all appropriate cases. Since the hull was constrained in the horizontal direction by the test setups, a calculation was done for this condition. A value of 5.8×10^4 pounds per inch was estimated to be the effective stiffness of the constraining cables. The results of these calculations are shown in Table 2.

TEST SETUP

(U) The tests were conducted in a zero-speed hull-borne condition with the foils fully submerged, during the period from 12 to 24 February 1970 at Puget Sound Naval Shipyard, Bremerton, Washington. Figure 2 shows the overall test setup for exciting the main strut torsion mode. The AGEH was held in place between two piers by a system of cables and the load applied to the strut through a bridle and pulley arrangement. The purpose of this arrangement was to minimize loading other than torque on the strut.

TABLE 2
Measured and Calculated Hull Frequencies

VERTICAL			
MODE	MEASURED FREQUENCY Hz	MEASURED DAMPING σ/σ_c PERCENT	CALCULATED FREQUENCY Hz
1	1.51	2.4	1.75
2	3.75	3.3	3.51
3	5.51	1.5	5.55
4	7.5	---	7.55
5	5.5	---	5.50

ATHWARTSHIP			
MODE	MEASURED FREQUENCY Hz	CALCULATED FREQUENCY Hz WITHOUT CONSTRAINTS	CALCULATED FREQUENCY Hz WITH CONSTRAINTS
1	5.5	5.25	5.31
2	10.0	5.52	10.25

(U) Figure 3 gives a view of the main foil and the method of applying the load to the foil. A load was placed on the foil 122 inches from the pod centerline, producing an initial torque in the strut. A standard nylon rigging strap, with pads to spread the load on the trailing edge of the foil, was used to apply the load to the strut-foil system. The load was suddenly released by cutting the cable with a standard cable cutter Type 1SE173, manufactured by Atlas Chemical Industries, Inc., capable of cutting up to 1/2 inch of standard steel cable. The strut-foil system was allowed to vibrate freely, and the resulting acceleration response was

40
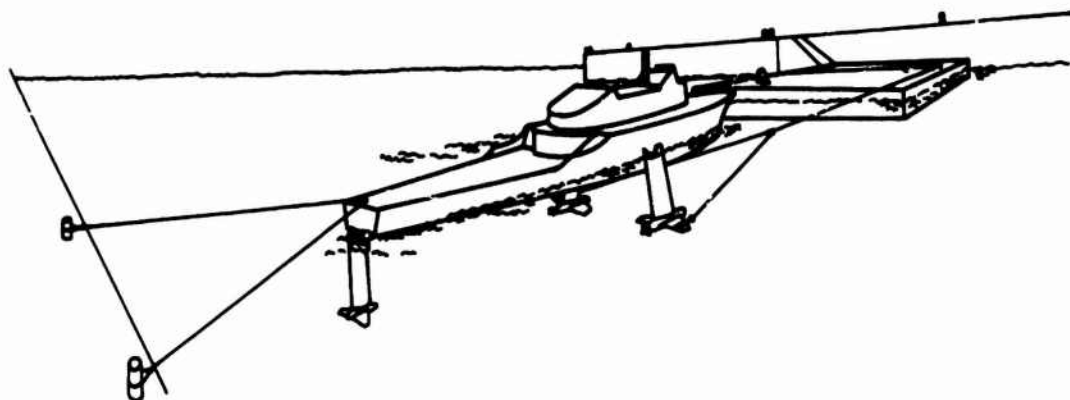
Figure 2 - Overall Test Configuration
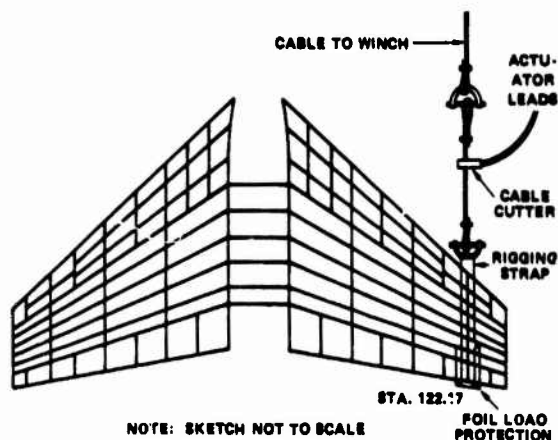
NOTE: SKETCH NOT TO SCALE

Figure 3 - Foil-Loading Method - Torsion

Figure 4 - Main Strut-Loading Method - Bending

measured and analyzed to obtain the natural frequencies. The maximum load placed on the foil in this configuration was 10,000 pounds.

(U) The setup shown in Figure 3 will produce a torque on the strut. In order to excite bending modes of the strut, the method shown in Figure 4 was used. The maximum load applied in this configuration was 4,000 pounds.

(U) Table 3 outlines the tests that were performed. In order to insure that the hull and strut-foil structure was not damaged by applying the loads, the load was applied in increments, and strain gages near the strut downlock (the linkage near the root of the strut which locks the strut to the hull, maximum bending moment and torque would occur at this location) and on the hull were monitored throughout the test.

TABLE 3
Tests Conducted

RUN	CABLE TENSION (LB.)	NOTES
1	2000	
2	4000	MAIN
3	8000	1. STRUT RIGGED FOR TORSIONAL EXCITATION.
4	4000	
5	10000	
6	2000	MAIN 1. STRUT RIGGED FOR BENDING EXCITATION.
7	--	2. IN RUN NO. 7 A MEASUREMENT OF THE AMBIENT NOISE WAS CONDUCTED
8	4000	WITHOUT TENSION ON THE CABLE.
9	10000	MAIN 1. STRUT RIGGED FOR TORSIONAL EXCITATION.
10	4000	1. TAIL STRUT TEST - TORSIONAL EXCITATION.
11	4000	2. RUNS 10 AND 11 WERE CONDUCTED WITH THE RUDDER HYDRAULICS ACT-
12	4000	IVE, RUN 12 HYDRAULICS INACTIVE.

41

TEST INSTRUMENTATION

(U) Accelerations of the strut-foil system were measured, using Kistler Type 305T servo accelerometers and their associated signal conditioners. All measurements were recorded on magnetic tape and oscillograph paper. Real-time spectrum analysis was performed by a Honeywell/Saicor SAI-21 real-time analysis system. Figure 5 shows a block diagram of the on line instrumentation used during these tests.

(U) The location and orientation of the accelerometers on the main strut-foil system and hull are shown in Figure 6. Gages at these selected locations were used to determine the modes of vibration of the strut-foil system and the motions of the hull. Torsion of the strut is measured at location 1A and 1B. Locations 2 and 7 measure strut bending, while vertical foil bending is measured at locations 3 and 4. Strut bending and torsion are measured by the gages at locations 5 and 6. Gages at locations 8 and 9 measure the rigid body motions of the hull in yaw and roll. The locations on the stern at 10, 11, and 12 measure the vibration response of the hull.

(U) Strain gages were installed on the strut at the downlock and were monitored during the tests. Two channels, one torsional and one bending, of strain data from the starboard strut were recorded on magnetic tape. Strain gages at the same locations on the port strut were monitored on the ship instrumentation system. This system which is separate from the instrumentation described above is provided as an integral part of the ship equipment to measure various operational parameters.

— ACCELEROMETER LOCATIONS
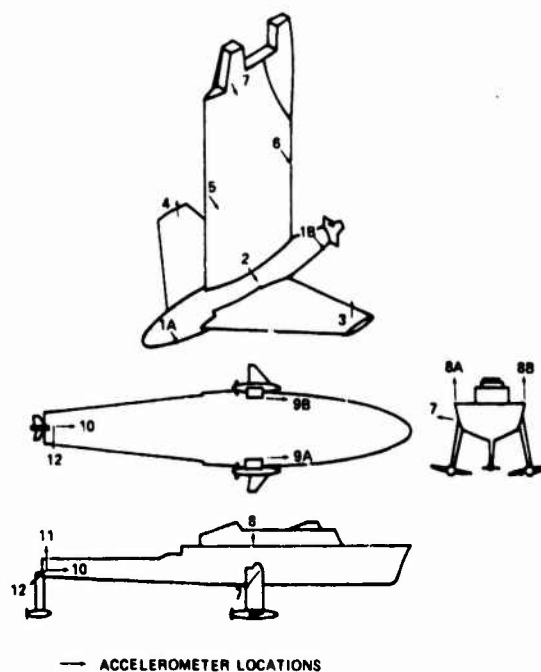
Figure 6 – Accelerometer Locations and Orientation Main Strut-Foil System
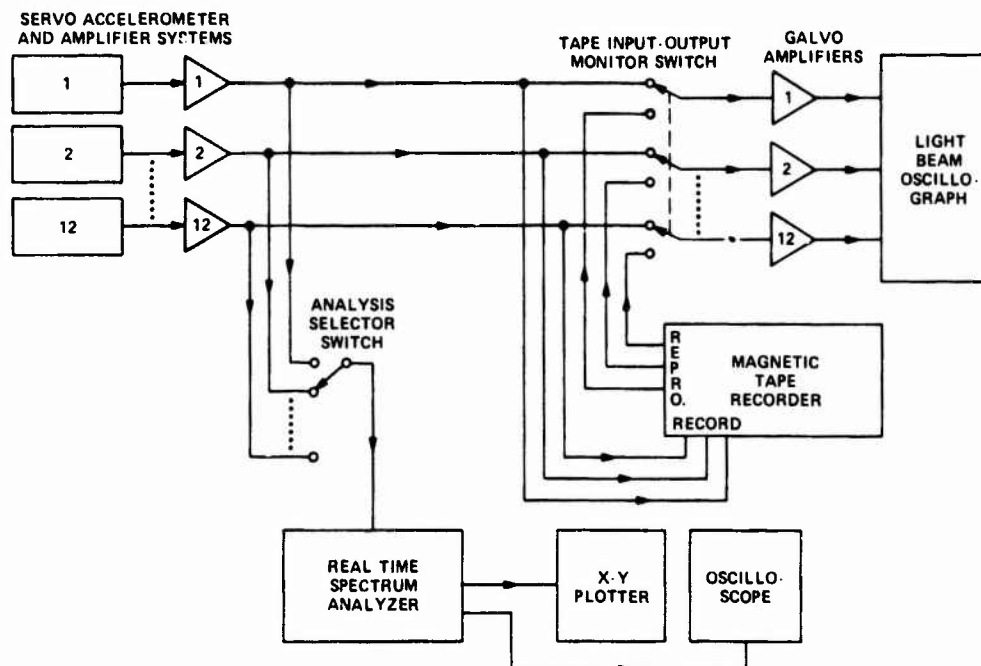
Figure 5 – On Line Instrumentation Block Diagram

42

DATA ANALYSIS

(U) Channels 1 and 2 of Runs 8 and 9 were chosen for detailed analysis. These runs represent the best data collected on the main strut-foil system. All instrumentation systems were active during these runs, and maximum initial load levels were used. Attenuator and gain settings were optimized, based upon the experience gained from previous tests. Channel 1 is a combination of two accelerometers on the forward and aft extremes of the pod, equidistant from the midchord of the strut. The output of the aft gage, 1B, was subtracted from forward gage, 1A, to give a signal proportional to the torsional motion of the strut. Channel 2 is a recording of the output of accelerometer 2 which was placed on the bottom of the strut at midchord. This gage is, therefore, sensitive to transverse motion at the lower frequencies. Of these motions, bending should be predominant. In Run 8 the initial load was placed so as to excite predominantly bending motion, and Run 9 was arranged to excite predominantly torsional motions.

(U) Data on Channels 1 and 2 were spectrum analyzed. The linear spectra of 20 second samples of these data are shown in Figures 7 and 8. In these figures all gains have been normalized, and the output of Channel 1 has been divided by a factor of 2 so that the Channel 1 spectra represent the acceleration of the end of the pod due to torsion of the strut.

(U) Figures 9 and 10 are a linear spectrum analyses of a 20-second sample of the vertical acceleration response of the stern on Channel 11 during Runs 11 and 9. Figure 11 is a spectrum of the output of accelerometer 12 which is the response of the stern in the athwartship direction during Run 9.

Figure 8 – Main Strut Torsional and Bending Response Spectrum, Torsional Initial Load
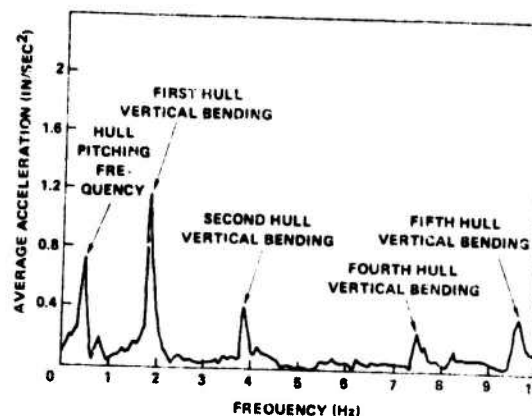
Figure 9 – Hull Stern Vertical Response Spectrum, Run 9

Figure 7 – Main Strut Torsional and Bending Response Spectrum, Bending Initial Load
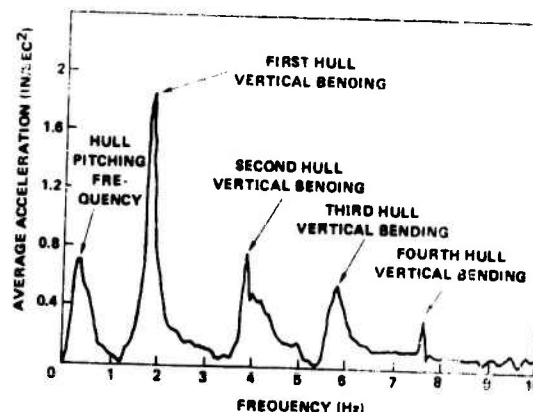
Figure 10 – Hull Stern Vertical Response Spectrum, Run 11

43
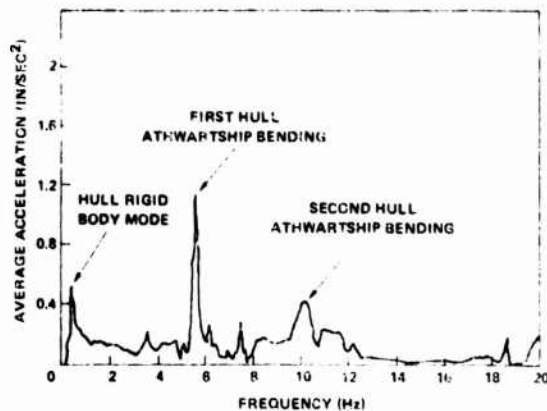
Figure 11 – Hull Stern Athwartship Response
Spectrum, Run 9

(U) The spectra in Figures 7 through 11 were obtained using a GR/Time Data 1923C FFT Analysis system. The spectra are obtained by calculating the auto spectrum and taking the square root of the magnitude of each spectral point.

(U) To obtain exact measurements of the frequencies and damping present in the data, several channels of selected runs were recorded on a magnetic tape loop and were then reversed and played back through filters in reverse time. The center frequency of the filter was tuned to suspected natural frequencies and was fine tuned to the point where maximum filter output was obtained. The bandwidth was kept sufficiently wide, a minimum of 10 percent of the center frequency, to avoid adverse effects on the data due to the filter fill time. The filter output was then recorded on string oscillograph paper and the frequency was visually counted. The results of these analyses are presented in Tables 2 and 4.

TABLE 4
Measured and Calculated Natural Frequencies and
Measured Damping Values of
Main Strut-Foil System

MODE	MEASURED FREQUENCY Hz	MEASURED DAMPING c/c_c PERCENT	CALCULATED FREQUENCY Hz
1	1.37	4.7	1.3
2	4.2	9.0	3.5
3	4.85	1.9	4.5

(U) The filtered output was also used to measure the damping present in the structure. The methods described in Reference 3 were used to make the damping analysis. The filter output is recorded on a string oscillograph display and each oscillation is measured. These
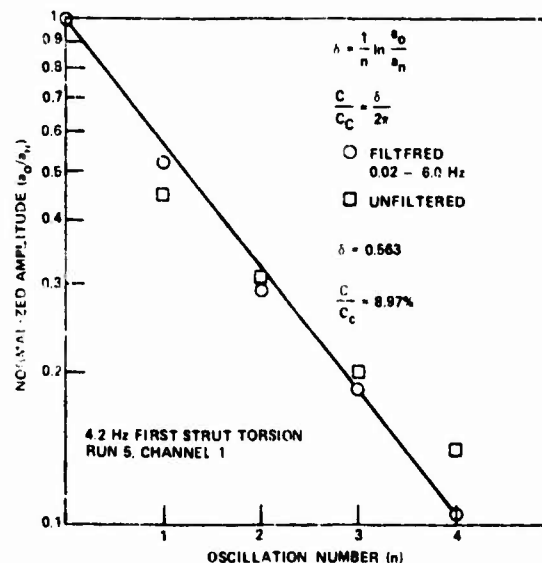
Figure 12 – Typical Damping Analysis

measurements are plotted on semilogrithmic paper. From this plot an estimate of the decay rate may be obtained. Figure 12 contains a typical analysis. Tables 2 and 4 present the results of all damping analyses.

DISCUSSION

Main Strut-Foil

(U) The first three natural frequencies of the main strut were excited in Run 8 in which a bending initial load was applied. In Figure 7 the strut torsional response (Channel 1, Run 8) shows strong resonant peaks at approximately 4.2 and 4.9 Hz. The spectrum for the bending response, Channel 2, contains peaks at 1.3, 1.8, and 4.9 Hz. The amplitude of the torsional response spectra at 4.2 Hz is about five times the bending response at 4.2 Hz. The strong peak at 1.3 Hz in the bending data is not shown in the torsional data. The peak in the strut-bending data at 1.8 Hz is due to a hull vertical mode. The mode was strongly excited in this run because the struts are located near a hull antinode for this mode. The hull vertical motion causes a bending motion to be induced in the strut. Both response spectra contain peaks at 4.9 Hz. These data indicate that 1.3 Hz is predominantly a bending mode, 4.2 Hz is predominantly a torsional mode and 4.9 Hz is a combination of the two motions.

(U) Further indication of the contribution of the strut characteristics to the first three modes can be seen in Run 9 (Figure 8) in which a torsional initial load was applied. These spectra of the responses during Run 9 contain peaks at 4.2 and 4.9 Hz in both Channels 1 and 2 and very little response at other frequencies. The torsional response (Channel 1) at 4.2 Hz is heavily predominant.

44

The average torsional acceleration is five times larger than the average bending acceleration response (Channel 2) at 4.2 Hz. These data indicates a heavy dependence of the 4.2 Hz mode on the torsional properties of the strut.

(U) The 1.3 Hz mode was not excited by torsional excitation. This confirms that the torsional characteristics of the strut have little effect on the first mode and that it is almost a pure bending mode.

(U) Figures 7 and 8 show that the 4.9 Hz mode was excited by both bending and torsional excitation. This is a heavily coupled mode and it is difficult to tell from the data whether bending or torsion predominates.

(U) The main strut-foil data as shown in Figures 7 and 8 are summarized in Table 4. The calculated natural frequencies are included for comparison.

Hull

(U) Five hull vertical frequencies were clearly excited by the pluck of the strut-foil system in Runs 9 and 11 as shown by the results in Figures 9 and 10. The loading method used during these runs had the effect of applying a large moment in the vertical plane at the stern. The resulting response was by far the easiest from which to obtain frequencies. A comparison of the calculated and measured vertical natural frequencies (Table 2) shows very good agreement.

(U) The hull was not excited very well in athwartship bending during any run. This was expected since the loads were all applied in a general fore-and-aft direction. Run 9 represents the best data collected in the athwartship direction.

(U) Figure 11 shows peaks in the hull-stern athwart-whip response during Run 9 and 5.6 and 10.0 Hz. A comparison of the frequencies obtained from the horizontal response of the hull stern in Run 9 and the calculated natural frequencies is shown in Table 2. The data show frequencies which fall between the constrained and unconstrained calculated natural frequencies. This indicates that the cables were not as effective in the horizontal direction as had been assumed.

Damping

(U) The measured damping values for the first and third main-strut modes shown in Table 4 seem to be within a normal range of values. The value of 9.0 percent for the second mode is unusually high. The first and third modes are heavily dependent on the bending characteristics of the strut. The second mode is predominantly torsional.

(U) One possible cause of the high damping in the second mode is that the strut skin is bolted to the main-strength member of the strut. It is possible that the skin

plating contributes a large amount of sliding friction when torsional motions are induced.

(U) The measured damping of the hull shown in Table 2 falls between 1.6 and 3.2 percent of critical for the first three vertical modes. These values are considered to be within the normal range of values for aluminum-hull structures.

CONCLUSIONS

(U) The first three measured natural frequencies of the main strut foil system are 1.3, 4.2, and 4.9 Hz. Damping values for these three modes are 4.7, 9.0, and 1.9 percent of critical, respectively. These frequencies vary somewhat from the calculated frequencies of 1.3, 3.5, and 4.5 Hz but are considered in reasonably good agreement for the purpose of flutter analysis. Although the damping values are reasonable for structures of this type, the second mode value of 9.0 percent seems somewhat high.

(U) Good agreement exists between the hull calculations in the vertical and athwartship bending directions and the measurements for these modes. The measured damping for the hull vibration modes seems reasonable for aluminum structures.

(U) The method of testing, as described in this paper, is an inexpensive means of obtaining useful information concerning the dynamic characteristics of hydrofoil strut-foil systems. The method can be used to study the frequencies and damping of such systems. Mode shape determination would require an extensive instrumentative and data analysis effort. It is felt therefore that a vibration generator test is the best method of determining mode shapes.

REFERENCES

1. Ransleben, G. E., Jr., "Description of a One-Eighth Scale Flutter Model of the Main Hydrofoil Assembly of the AG(EH) 800 Hydrofoil Research Ship," Southwest Research Institute Technical Report, (Dec 1966).

2. Cuthill, E. H. and F. M. Henderson, "Description and Usage of General Bending Response Code," David Taylor Model Basin Report 925, (Jul 1965).

3. Alma, H. F. and W. P. Foster, "Damping Values of Naval Ships Obtained from Impulse Loadings," The Shock and Vibration Bulletin, No. 40, (Dec 1969).

Mr. Gelef (TRW Systems): I was very surprised that you were able to get the damping from the log decrement when you have the problem of several modes excited at the same time. When you try to look at one at a time through a filter, the effects of the filters tend to contaminate the effects of the damping. How did you do it?

Mr. Peoples: Well, in general that's true. During some of the testing with the struts we excited almost a pure torsional mode so we didn't have modal interference on some of the other runs, not the … that I showed here. There was suffici… …ead in the hull frequencies so that one could filter with a wide enough bandwidth to avoid any problem. We didn't even have to reverse these in time. Frequently, you can reverse the date in time, run it backwards through the filter and thereby minimize the filter effects that way. However, in this case that wasn't even necessary. The filter bandwidths were wide enough that it didn't make any difference.

Mr. Gelef: I would like to call your attention to a paper* that Professor Cronin and I presented two years ago at the Shock and Vibration Symposium which did some curve fitting in the frequency domain and enables one to get the damping with whatever accuracy you want. We just finished using this program on a lunar test module and it worked very nicely.

Mr. Peoples: I have read your paper and used your method. It is very good.

* Shock and Vibration Bulletin No. 41, Part 7, Page 9.

46

ON THE THEORY AND PRACTICE OF STRUCTURAL
RESONANCE TESTING

Chen-Chou Ni
Applied Mechanics Branch
Ocean Technology Division
Naval Research Laboratory

An application oriented treatment of structural resonance testing
has been developed. The analyses are based on possible dynamic
boundary conditions encountered, or experienced in real testing en-
vironments. For each dynamic boundary condition, a governing equa-
tion or equations are derived from basic physical and mathematical
principles. These equations contain information providing analytical
bases for testing techniques as well as interpretation of experimental
results. Laboratory tests on a steel beam with three simple supports
were performed according to each derived technique. Results agree
very well and demonstrate their independence of choice of test tech-
niques. The theoretically predicted possible deficiency in revealing
physical information from the tests were also observed. The clarifica-
tion of such a deficiency is made possible by data analysis suggested by
one of the techniques.

NOMENCLATURE

[ ] Square matrix

( ) Non-square matrix

{ } Column matrix

⌐⌐ Row matrix

[M] Mass matrix

[K] Stiffness matrix

[Z] Mechanical impedance matrix

$[Z^p]$ Mechanical impedance matrix of the principal substructure

$[Z^b]$ Mechanical impedance matrix of the base substructure

$[Z^s]$ Mechanical impedance matrix of the support substructure

$[\mathfrak{M}]$ Mechanical mobility matrix

$\left(\sum_{s}^{p} \right)$ Coupling matrix of the pth and sth substructures

{C} Constant column matrix

$Z_{\nu\mu}$ Cofactor of the impedance de-terminant associated with the impedance element $z_{\mu\nu}$

$\ddot{q}$ Generalized acceleration

$\dot{q}$ Generalized velocity

q Generalized displacement

$f_\nu(t)$ Generalized force associated with the νth generalized coordi-nate

$\bar{f}_\nu$ Generalized force amplitude associated with the νth general-ized coordinate

$q_{\mu\nu}, \dot{q}_{\mu\nu}, \ddot{q}_{\mu\nu}$ The μth response due to the νth force input of the generalized displacement, velocity, and ac-celeration respectively

47

$\bar{q}_{\mu\nu}, \dot{\bar{q}}_{\mu\nu}, \ddot{\bar{q}}_{\mu\nu}$ The amplitude of the μth response due to the νth force input of the generalized displacement, velocity, and acceleration respectively

ω Exciting frequency

$\theta_{\mu\nu}$ Relative phase of the μth generalized displacement response with respect to the νth applied force

$\phi_{\mu\nu}$ Relative phase of the μth generalized velocity response with respect to the νth applied force

$m_{\mu\nu}$ Mobility element of the μth row and νth column

$|[\ ]|$ The determinant of a square matrix

C_β, C_ν Constants

$\Omega(m_{\mu\nu};\omega)$ Mobility function

$\psi(m_{\mu\nu};\omega)$ Resonance function

INTRODUCTION

The natural frequencies of a mechanical system, in many ways, play an important role in engineering. The basic theory of small oscillation has been established and well documented for more than a century. Direct application of such a theory for practical purposes often presents difficulties, especially for complicated structures. Suppose we are given a structure with statically fixed constraints and asked to find its natural frequencies. This is the usual way normally a practical engineer or test engineer receives his assignment. One way to find the true natural frequencies of a given structure is by resonance testing. As we all know that structural natural frequency is a boundary value problem. The natural frequencies measured are closely related to its support conditions. Test results obtained under different dynamic support conditions correspond to different structures. Therefore, without positive control of the support movement or without having the knowledge of the motion of the supports during the test, correct interpretation of the test data become difficult to say the least. It is evident that a practical engineer faces a more complicated problem than the conceived theoretical one which naturally takes the given statically fixed constraints as the dynamic boundary condition of the structure.

Theoretical treatment as such yields insufficient information to guide a proper resonance test unless the supports are truly remaining stationary through the test. Unfortunately, it is quite often not the case. Realizing this fact, test engineers have made efforts to overcome such practical difficulties by using specially designed fixtures to simulate a dynamic boundary condition equivalent to the given statically fixed constraints. As the state of art, the current practice in fixture design is rather empirical than analytical. Tremendous experiences in testing is a necessity in order to achieve a suitable design for each particular case. Even so, for comparatively large structures, fixture design become forbidding both economically and technically.

In this paper, an attempt to bridge this traditional gap between theory and practice was made. As a result of this effort, an application oriented treatment of structural resonance testing has been evolved. This treatment will provide the practical engineers alternative ways to conduct structural resonance testing under various possible testing boundary conditions.

Equation of Motion

Some important definitions and mathematical formalism pertaining to this work are briefly reviewed. The equations of motion of an n degree-of-freedom, undamped,* linear time-invariant lumped mass system in configuration space has the general form

$$[M]\ \{\ddot{q}\} + [K]\ \{q\} = \{f(t)\}\ . \qquad (1)$$

Consider a single applied sinusoidal force

$$f_\nu(t) = \bar{f}_\nu \sin \omega t . \qquad (2)$$

The steady state solution of equation (1) with the applied force in equation (2) is

$$q_{\mu\nu} = \bar{q}_{\mu\nu} \sin(\omega t + \theta_{\mu\nu}) \qquad (3)$$

where $\theta_{\mu\nu}$ is the relative phase of the μth generalized displacement response with respect to the νth applied force. For undamped systems, equation (3) becomes

$$q_{\mu\nu} = \bar{q}_{\mu\nu} \cos \theta_{\mu\nu} \sin \omega t \qquad (4)$$

$$\theta_{\mu\nu} = 0,\ \text{or}\ \pi$$

---

*This treatment is valid for structures with small damping [3].

and the spatial part of equation (1) becomes

$$(-\omega^2 [M] + [K]) \{\bar{q}_{\mu\nu} \cos \phi_{\mu\nu}\} = \begin{Bmatrix} 0 \\ \cdot \\ \cdot \\ \bar{f}_\nu \\ \cdot \\ 0 \end{Bmatrix} \quad (5)$$

or

$$\left(-\omega [M] + \frac{1}{\omega} [K]\right) \{\bar{q}_{\mu\nu} \sin \phi_{\mu\nu}\} = \begin{Bmatrix} 0 \\ \cdot \\ \cdot \\ \bar{f}_\nu \\ \cdot \\ 0 \end{Bmatrix} \quad (6)$$

where

$$\omega \bar{q}_{\mu\nu} \cos \theta_{\mu\nu} = \bar{q}_{\mu\nu} \sin \phi_{\mu\nu} , \quad \phi_{\mu\nu} = \frac{\pi}{2} + \theta_{\mu\nu}$$

for steady states. The angle $\phi_{\mu\nu}$ here is the relative phase of the μth generalized velocity response with respect to the νth force. The square matrix operator in equation (6)

$$-\omega [M] + \frac{1}{\omega} [K] = [Z] \quad (7)$$

is defined as the mechanical impedance matrix.

For a nondegenerate system, the impedance matrix has a rank of n and its inverse exists

$$[Z] [Z]^{-1} = [Z]^{-1} [Z] = [I] . \quad (8)$$

By a linear transformation, equation (6) can be written as

$$\{\bar{q}_{\mu\nu} \sin \phi_{\mu\nu}\} = [\mathfrak{M}] \begin{Bmatrix} 0 \\ \cdot \\ \bar{f}_\nu \\ \cdot \\ 0 \end{Bmatrix} \quad (9)$$

where

$$[\mathfrak{M}] = [Z]^{-1} \quad (10)$$

is defined as the mechanical mobility matrix of the system.

From equation (9), the elements of the mechanical mobility matrix

$$m_{\mu\nu} = \frac{\bar{q}_{\mu\nu} \sin \phi_{\mu\nu}}{\bar{f}_\nu} \quad (11)$$

can be determined by measuring the generalized velocity and force amplitudes and the relative phase between them. Each force application enables us to determine one column vector of the mobility matrix provided that the corresponding spatial response vector is measured. Equation (10) shows that the elements of the mobility matrix can be expressed in terms of cofactors of the impedance determinant and the impedance determinant itself as

$$m_{\mu\nu} = \frac{Z_{\mu\nu}}{|[Z]|} . \quad (12)$$

It is evident, from equation (7) and (10), the mobility elements are functions of the exciting frequency alone for a given structure. In other words, the mobility elements are invariant physical quantities of the dynamic structure with respect to space and time.

For multiple force inputs with a single exciting frequency, Eq. (6) and (9) become

$$[Z] \left\{\sum_\nu \bar{q}_{\mu\nu} \sin \phi_{\mu\nu}\right\} = \begin{Bmatrix} \bar{f}_1 \\ \cdot \\ \cdot \\ \bar{f}_\nu \\ \cdot \\ \bar{f}_n \end{Bmatrix} \quad (13)$$

and

$$\left\{\sum_\nu \bar{q}_{\mu\nu} \sin \phi_{\mu\nu}\right\} = [\mathfrak{M}] \begin{Bmatrix} \bar{f}_1 \\ \cdot \\ \cdot \\ \bar{f}_\nu \\ \cdot \\ \bar{f}_n \end{Bmatrix} . \quad (14)$$

Where the force components represent the spatial distribution of the total force vector. In this particular case, all the force components are assumed in phase. This assumption does not represent a general situation but a sufficient special consideration of our interest.

49

In general, structures under study are most likely coupled to their neighboring structures. A correct mathematical model which can be used to analyze its response to an external force input must take the total structure involved into consideration. For the convenience of discussion in the forthcoming analyses, the following nomenclature of the structures are adopted.

Total structure: The spatial extent of the dynamic influence due to the external force.

Principal substructure: The structure whose dynamic response behavior is to be determined.

Support substructure: The substructure composed of the common constraints or the connecting parts of the principal and the base substructure.

Base substructure: The remaining part of the total structure other than the principal and the support substructures.

According to the above subdivision, equations (6) and (9) can always be arranged to have the partitioned form

$$
\begin{bmatrix}
[Z^P] & (\Sigma_S^P) & (0) \\
(\Sigma_P^S) & [Z^S] & (\Sigma_B^S) \\
(0) & (\Sigma_S^B) & [Z^B]
\end{bmatrix}
\begin{Bmatrix}
\{\bar{\dot{q}}_{\alpha\nu}^P \sin\phi_{\alpha\nu}\} \\
\{\bar{\dot{q}}_{\beta\nu}^S \sin\phi_{\beta\nu}\} \\
\{\bar{\dot{q}}_{\gamma\nu}^B \sin\phi_{\gamma\nu}\}
\end{Bmatrix}
=
\begin{Bmatrix}
\{0\} \\
\{\,\} \\
\{\bar{f}_\nu\}
\end{Bmatrix}
\quad (15)
$$

and

$$
\begin{Bmatrix}
\{\bar{\dot{q}}_{\alpha\nu}^P \sin\phi_{\alpha\nu}\} \\
\{\bar{\dot{q}}_{\beta\nu}^S \sin\phi_{\beta\nu}\} \\
\{\bar{\dot{q}}_{\gamma\nu}^B \sin\phi_{\gamma\nu}\}
\end{Bmatrix}
=
\begin{bmatrix}
m_{11} & \cdots & m_{1n} \\
\vdots & & \vdots \\
m_{n1} & \cdots & m_{nn}
\end{bmatrix}
\begin{Bmatrix}
\{0\} \\
\{\,\} \\
\{\bar{f}_\nu\}
\end{Bmatrix}
\quad (16)
$$

respectively.

By definition, there is no direct coupling between the principal substructure and the base substructure. The submatrices on the diagonal of the impedance matrix are the impedance matrices of the substructures. The off-diagonal matrices, in general nonsquare, represent the coupling mechanisms between adjacent substructures. The generalized velocity and applied force vectors or column matrices are partitioned accordingly. Here, each substructure, although written in a lumped mass model form, will be kept intact throughout the mathematical manipulation.

Theoretical Background of
Resonance Testing

Suppose the total structure considered is composed of an ℓ degree-of-freedom principal substructure, an $m-\ell$ degree-of-freedom support substructure, and an $n-m$ degree-of-freedom base substructure. Methods used for determining the natural frequencies of composite structures and substructures can be categorized according to their dynamic boundary conditions.

Case 1. Unconstrained structure: The principal substructure is freely suspended. There exists no support and base substructures. Equation (15) and (16) become

$$
[Z^P] \{\bar{\dot{q}}_{\alpha\nu}^P \sin\phi_{\alpha\nu}\} =
\begin{Bmatrix}
0 \\
\vdots \\
\bar{f}_\nu^P \\
\vdots \\
0
\end{Bmatrix}, \quad \alpha, \nu = 1, 2, \cdots \ell
\quad (17)
$$

and

$$
\bar{\dot{q}}_{\alpha\nu}^P \sin\phi_{\alpha\nu}\} = [\mathfrak{M}]
\begin{Bmatrix}
0 \\
\vdots \\
\bar{f}_\nu^P \\
\vdots \\
0
\end{Bmatrix}.
\quad (18)
$$

The corresponding mobility elements are

$$
m_{\alpha\nu}^P = \frac{\bar{\dot{q}}_{\alpha\nu}^P \sin\phi_{\alpha\nu}}{\bar{f}_\nu^P} = \frac{Z_{\alpha\nu}^P}{|[Z^P]|}
\quad (19)
$$

and the components of the generalized velocity responses are

50

$$\bar{q}^P_{\alpha\nu} \sin\phi_{\alpha\nu} = \frac{Z^P_{\alpha\nu}}{|[Z^P]|} \; \bar{f}^P_\nu . \qquad (20)$$

Equation (20) shows

$$\bar{q}^P_{\alpha\nu} \longrightarrow \infty \quad \text{when} \quad |[Z^P]| = 0$$

i.e., with the response sensor mounted on any part of the principal substructure (or the total structure in this case) and a force applied at any where on the structure, the monitored response amplitude will show peaks at the natural frequencies of the structure corresponding to $|[Z^P]| = 0$. Ambiguity may arise when the particular cofactor $Z^P_{\alpha\nu}$ becomes very small at the resonance frequencies. Since the cofactor $Z^P_{\alpha\nu}$ depends on where the response and applied force are located, such ambiguity may be eliminated by changing the locations of the response sensor and the force application. Unfortunately there is no simple rule to follow.

Case 2. Fixed Constraints in Space: The principal substructure is rigidly mounted on an infinite impedance support substructure for all exciting frequencies (within the range of interest). The dynamic boundary condition for this case are either

a.
$$\{\bar{q}^S_{\beta\nu} \sin\phi_{\beta\nu}\} = \{0\}$$
$$\qquad (21)$$
$$\{\bar{q}^B_{\gamma\nu} \sin\phi_{\gamma\nu}\} = \{0\}$$

or

b.
$$\{\bar{q}^S_{\beta\nu} \sin\phi_{\beta\nu}\} = \{0\}$$
$$\qquad (22)$$
$$\{\bar{q}^B_{\gamma\nu} \sin\phi_{\gamma\nu}\} \neq \{0\} .$$

With the force applied on the principal substructure, equation (15) can be written as

$$[Z^P] \; \{\bar{q}^P_{\alpha\nu} \sin\phi_{\alpha\nu}\} = \begin{Bmatrix} 0 \\ \cdot \\ \cdot \\ \cdot \\ \bar{f}^P_\nu \\ \cdot \\ 0 \end{Bmatrix} \qquad (23)$$

and

$$[Z^P] \; \{\bar{q}^P_{\alpha\nu} \sin\phi_{\alpha\nu}\} = \begin{Bmatrix} 0 \\ \cdot \\ \cdot \\ \cdot \\ \bar{f}_\nu \\ \cdot \\ 0 \end{Bmatrix} \qquad (24)$$

$$\left(\sum_s^P\right)\{\bar{q}_{\alpha\nu} \sin\phi_{\alpha\nu}\} + \left(\sum_B^S\right)\{\bar{q}^B_{\gamma\nu} \sin\theta_{\gamma\nu}\} = \{0\}$$

$$[Z^B] \; \{\bar{q}^B_{\gamma\nu} \sin\phi_{\gamma\nu}\} = \{0\}$$

for subcases "a" and "b" respective.y. The subcase "a" corresponds to the fact that the principal substructure is the to'al structure and the subcase "b" represents the inner resonance phenomenon if a solution exists. In either case, the spatial equation of motion of the principal substructure

$$[Z^P] \; \{\bar{q}^P_{\alpha\nu} \sin\phi_{\alpha\nu}\} = \begin{Bmatrix} 0 \\ \cdot \\ \cdot \\ \cdot \\ \bar{f}^P_\nu \\ \cdot \\ 0 \end{Bmatrix} \qquad (25)$$

must be satisfied. It is noticed that equation (25) has the same form of equation (17) except that the principal substructures referred to in these two cases are not the same. If the same structure is considered, the rank of the impedance matrix $[Z^P]$ in equation (25) equals to the rank of the impedance matrix in equation (17) minus the degree-of-freedom of the support substructure, which is rigidly constrained by mounting. The natural frequencies measured in this case are so called fixed-base natural frequencies. It is expected that the dynamic boundary conditions are intimately associated with the natural frequencies measured. By the same reasoning given in case 1, we have

$$\bar{q}^P_{\alpha\nu} \sin\phi_{\alpha\nu} = \frac{Z^P_{\alpha\nu}}{|[Z^P]|} \cdot \bar{f}^P_\nu \qquad (26)$$

similarly

$$\bar{q}^P_{\alpha\nu} \longrightarrow \infty \quad \text{when} \quad |[Z^P]| = 0 .$$

The fixed-base natural frequencies corresponding to $|[Z^P]| = 0$ may be revealed by vibration

test in a manner described in case 1. Similar ambiguities may also arise for the same reason.

Case 3. Rigid Body Motion of the Constraints as a Whole: When the support, or base and support, substructures are in motion, any force applied to the principal substructure does not yield information about the fixed-base natural frequencies of the principal substructure [1]. Therefore, in the treatment of case 3, force application to the principal substructure is avoided. The dynamic boundary condition for this case is

$$\{\bar{q}^*_{\beta\nu} \sin\phi_{\beta\nu}\} = \{C_\beta\} \qquad (27)$$

where $\{C_\beta\}$ is a constant column matrix; $\beta = \ell + 1, \ell + 2, \ldots, m$ for all frequencies within the range of interest. Then with the applied force either on the support substructure or on the base substructure, if the direct excitation were possible, equation (15) becomes

$$\begin{bmatrix} [Z^P] & \left(\sum_s^P\right) & (0) \\ \left(\sum_P^S\right) & [Z^S] & \left(\sum_B^S\right) \\ (0) & \left(\sum_s^B\right) & [Z^B] \end{bmatrix} \begin{Bmatrix} \{\bar{q}^P_{\alpha\nu} \sin\phi_{\alpha\nu}\} \\ \{ C_\beta \} \\ \{\bar{q}^B_{\gamma\nu} \sin\phi_{\gamma\nu}\} \end{Bmatrix} = \begin{Bmatrix} \begin{Bmatrix} 0 \\ \vdots \\ \cdot \end{Bmatrix} \\ \begin{Bmatrix} \cdot \\ \vdots \\ \bar{f}^{SB}_\nu \\ \vdots \\ 0 \end{Bmatrix} \end{Bmatrix} \qquad (28)$$

where the support substructure response vector can have at most six independent components.

To examine the physical possibility of such an excitation, we recall equation (16) and consider a single sinusoidal force input with constant amplitude

$$\begin{Bmatrix} \{\bar{q}^P_{\alpha\nu} \sin\phi_{\alpha\nu}\} \\ \{ C_\beta \} \\ \{\bar{q}^S_{\gamma\nu} \sin\phi_{\gamma\nu}\} \end{Bmatrix} = \begin{Bmatrix} m_{1\nu} & \bar{f}^{SB}_\nu \\ \vdots \\ m_{n\nu} & \bar{f}^{SB}_\nu \end{Bmatrix} \qquad (29)$$

Then the corresponding dynamic boundary condition in equation (27) becomes

$$\{C_\beta\} = \begin{Bmatrix} m_{\ell+1\nu} & f^{SB}_\nu \\ \vdots \\ m_{m\nu} & f^{SB}_\nu \end{Bmatrix} . \qquad (30)$$

Since the mobility elements are functions of exciting frequencies, equation (30) can not be satisfied over an arbitrary frequency range. Physically, this means that we are no longer able to use a single steady state sinusoidal force to perform the resonance test. Therefore, the basic idea for a direct excitation of the resonance modes at the fixed-base natural frequencies of the principal substructure in this case has to be different from the previous cases. In fact, the popularly used shake table test technique is of this kind. It is done by designing the mounting fixture in such a way that the fixture or the support substructure responds like a rigid body within the interested frequency range, and instead of controlling a constant level sinusoidal force input, a time dependent force amplitude is controlled by a feedback system. The feedback signal is from a response sensor mounted on the fixture. In essence, it is a support substructure response controlled test at a prescribed level. The corresponding spatial equation of motion of the principal substructure, under the special provision above, can be written as

$$[Z^P] \{\bar{q}^P_{\alpha\nu} \sin\phi_{\alpha\nu}\} = \{C_\nu\} \qquad (31)$$

or

$$\{\bar{q}^P_{\alpha\nu} \sin\phi_{\alpha\nu}\} = [\mathbb{M}^P] \{C_\nu\} \qquad (32)$$

where

$$\{C_\nu\} = \sum_s^P \{C_\beta\}$$

From equations (12) and (32), the individual generalized velocity response becomes

$$\bar{q}^P_{\alpha\nu} \sin\phi_{\alpha\nu} = \frac{\lfloor Z^P_{\alpha\nu} \rfloor \{C_\nu\}}{|[Z^P]|} . \qquad (33)$$

Again by following the same argument and response measurement given in Case 1 and Case 2, i.e.,

$$\bar{q}^P_{\alpha\nu} \rightarrow \infty \quad \text{when} \quad |[Z^P]| = 0$$

the fixed-base natural frequencies of the principal substructure are determined by a conventional shake table test. As one can see from the numerator on the right side of equation (33), more involved ambiguities may arise for situations when

$$\lfloor Z^p_{\alpha\nu} \rfloor \{ C_\nu \}$$

becomes very small at the resonance modes.

The resonance testing methods analyzed heretofore are quite popular in engineering practice and laboratory experiment, when the dynamic support condition can be simulated. The analytical results derived from considerations of dynamic boundary conditions provide not only information about how and what to measure but also better understanding of the physical aspects of the information obtained from testing.

Case 4. Elastically Coupled Substructures: When the substructures involved are elastically coupled, theoretical analysis shows that a direct excitation of the resonance modes of a principal substructure at its fixed-base natural frequencies are possible if the following necessary restrictions are being satisfied [3] and [4].

Restriction I   No force applied on the principal substructure.

Restriction II   No. of force applications $\geq$ no. of the degree-of-freedom of the support substructure.

The first restriction can be fulfilled without difficulty. The second restriction requires multiple force input. Such force input is technically uncontrollable because there is no rational way to select a desirable set of forces without solving the problem analytically first [5]. By trial and error approach, the probability of having accidental success of such a choice of forces is very remote.

A new semianalytical method, which indirectly derives the resonance modes of these type of substructures has been developed [3] and experimentally validated [4]. A condensed version of these two was published elsewhere [6]. For the completeness of this treatment, the vital part of the theory is described in the following:

The dynamic boundary condition for the excitation of a resonance mode at one of the fixed-base natural frequencies of the principal substructure requires

$$\{ \bar{q}^s_{\beta\nu} \sin \phi_{\beta\nu} \} = \{ 0 \} \tag{34}$$

With the restrictions given above, equation (9) becomes

$$\begin{Bmatrix} \{ \bar{q}^p_{\alpha\nu} \sin \phi_{\alpha\nu} \} \\ \{ \quad 0 \quad \} \\ \{ \bar{q}^R_{\gamma\nu} \sin \phi_{\gamma\nu} \} \end{Bmatrix} = \begin{bmatrix} m_{11} & & m_{1n} \\ & & \\ & & \\ m_m & & m_m \end{bmatrix} \begin{Bmatrix} \{ 0 \\ \vdots \} \\ \{ \vdots \} \\ \langle \bar{f}^{SB}_\nu \rangle \\ \vdots \\ 0 \end{Bmatrix} \tag{35}$$

Consider the simplest case of restriction II. By physically limiting the number of force applications to the number of degree-of-freedom of the support substructure, then equation (34) can be written

$$\begin{bmatrix} m_{\xi\nu} & \cdots & \\ & \vdots & \\ & \vdots & \\ & \vdots & \\ & \vdots & \\ m_{q\nu} & \cdots & \end{bmatrix} \{ \bar{f}^{SB}_\nu \} = \{ 0 \}, \quad \begin{array}{l} \ell + 1 \leqslant \xi \leqslant n \\[4pt] m \leqslant \eta \leqslant n . \end{array} \tag{36}$$

Where the square mobility submatrix in equation (36) is composed of any combination of $m-\ell$ columns of the mobility submatrix pertaining to the support response vector. The double superscripts sB of the force components designate the application points of the forces being limited within the support and base substructure. Nontrivial solutions of equation (36) exist if

$$\begin{vmatrix} m_{\ell+1\nu} & - & - & - & - & - \\ & & \vdots & & \\ & & \vdots & & \\ & & \vdots & & \\ m_{\mu\nu} & - & - & \vdots & - & - \end{vmatrix} = 0 = \Omega(m_{\mu\nu}; \omega) . \tag{37}$$

Theoretically, it means the sets of forces exist to satisfy the given boundary condition in equation (34) at the frequencies determined by the secular equation (37). We define this determinant as the mobility function $\Omega(m_{\mu\nu}; \omega)$. Mathematically we have reduced a multiple dimension vector problem in equation (34) to a one variable scalar function, a polynomial of the exciting frequency in equation (37). The physical significance of this mathematical step is evident by the following: first, in general, the excitation of a resonance mode of the principal substructure at one of its fixed-base natural

53

frequencies is technically uncontrollable for a non-degenerate structure; therefore, equation (36) is of little practical value [5]. Second, since the mobility elements containing the inherent dynamic properties of the total structure are functions of exciting frequency alone, certainly one can take advantage of its measurableness and construct a mobility function which is defined as the left-side of equation (37) artificially. This is done by applying one controlled sinusoidal force at a time, totally $n-\ell$ times, to measure the responses of the support substructure. The required mobility elements in equation (37) are then calculated in accordance with equation (11). By judicious variation of the exciting frequency, the mobility function $\Omega(m_{\mu\nu}; \omega)$ enables us to trace out the solutions of the secular equation (37) graphically.

It becomes clear, since the mobility function defined in equation (37) depends on the relative phase among the forces by a constant multiplier. Such multiplier will not alter the solution of the secular equation (37). Therefore it is our liberty to consider the simplest case by choosing zero phase for all force components. This explains the generality of the expression in equations (13), (14), and (35). Any solution yielded from the mobility function must satisfy equation (14) of the total structure. The explicit relation between the mobility function and the fixed-base natural frequencies of the principal substructure was established through equation (8) and (14) in the partitioned form

$$
\begin{bmatrix} [Z^P] & \left(\Sigma_S^P\right) & (0) \\ \left(\Sigma_P^S\right) & [Z^S] & \left(\Sigma_B^S\right) \\ (0) & \left(\Sigma_S^B\right) & [Z^B] \end{bmatrix} \begin{bmatrix} \\ \mathfrak{M} \\ \\ \end{bmatrix} = \begin{bmatrix} [I] & (0) & (0) \\ (0) & [I] & (0) \\ (0) & (0) & [I] \end{bmatrix} . \quad (38)
$$

Then the mobility matrix in equation (38) is replaced by a nonsingular matrix as suggested by the mobility function in equation (37). There are many ways to choose this nonsingular matrix depending on the force application. Since the exact locations of the applied forces are irrelevant so far as the determination of the fixed-base natural frequencies of the principal substructure is concerned although the mobility elements involved in the square mobility submatrix in equation (36) will be different [3]. Therefore, a set of forces applied on the support substructure is considered in this case without losing its generality. Equation (38) becomes

$$
\begin{bmatrix} [Z^P] & \left(\Sigma_S^P\right) & (0) \\ \left(\Sigma_P^S\right) & [Z^S] & \left(\Sigma_B^S\right) \\ (0) & \left(\Sigma_S^B\right) & [Z^B] \end{bmatrix} \begin{bmatrix} [I] & \begin{pmatrix} m_{1\ell+1} & \cdot & \cdot \\ \cdot & \cdot & \cdot \\ \cdot & \cdot & \cdot \end{pmatrix} & (0) \\ (0) & [\Omega] & (0) \\ (0) & \begin{pmatrix} \cdot & \cdot & \cdot \\ \cdot & \cdot & m_{nm} \end{pmatrix} & [I] \end{bmatrix}
$$

$$ (39) $$

$$
= \begin{bmatrix} [Z^P] & (0) & (0) \\ \left(\Sigma_P^S\right) & [I] & \left(\Sigma_B^S\right) \\ (0) & (0) & [Z^B] \end{bmatrix}
$$

Taking the determinant of both sides of equation (39) and applying LaPlace's expansion, we have

$$ |[Z]| \cdot |[\Omega]| = |[Z^P]| \cdot |[Z^B]| \quad (40) $$

or

$$ \Omega(m_{\mu\nu}; \omega) = \frac{|[Z^P]| \cdot |[Z^B]|}{|[Z]|} \quad (41) $$

where $|[\Omega]| = \Omega(m_{\mu\nu}; \omega)$.

Equation (41) shows explicitly that the mobility function does contain information of the fixed-base natural frequencies of the principal substructure, $|[Z^P]| = 0$, but also the fixed-base natural frequencies of the base substructure, $|[Z^B]| = 0$, and the natural frequencies of the total structure, $|[Z]| = 0$. In order to identify the fixed-base natural frequencies of the principal substructure, another mobility function is constructed to eliminate the extraneous information involved in the mobility function in equation (41). Suppose an additional shaking force is applied at one location on the principal substructure, then by following the same procedure of deriving equation (41), the corresponding mobility function is

$$\Omega'(m_{\mu\nu};\omega) = \begin{bmatrix} m_{tt} & \cdots & \cdots & m_{tm} \\ & & & \\ \cdot & m_{\ell+1\ell+1} & \cdots & m_{\ell+1m} \\ \cdot & \cdot & & \cdot \\ \cdot & \cdot & & \cdot \\ \cdot & \cdot & & \cdot \\ m_{mt} & m_{m\ell+1} & \cdots & m_{mm} \end{bmatrix} \quad (42)$$

$$= \frac{|[Z'^P]| \cdot |[Z^B]|}{|[Z]|} \ .$$

Comparing equation (41) and (42), the only difference found is the impedance determinant of the principal substructure. The impedance determinats $|[Z^B]|$ and $|[Z]|$ remain unchanged. This fact suggests a way to exclude the extraneous informations by taking the ratio of these two mobility functions. A resonance function is defined as

$$\psi(m_{\mu\nu};\omega) = \left\| \frac{\Omega'(m_{\mu\nu};\omega)}{\Omega(m_{\mu\nu};\omega)} \right\| = \left\| \frac{|[Z'^P]|}{|[Z^P]|} \right\| . \quad (43)$$

Here a double line designates absolute value. The absolute values are chosen so that the graphical representation of the resonance function conforms to the conventional concept of "resonance peak." For a real structure, $[Z'^P]$ is finite for a finite exciting frequency, thus, the singularities of the resonance function $\psi(m_{\mu\nu};\omega)$ corresponding to $|[Z^P]| = 0$ give the identity of the fixed-base natural frequencies of the principal substructure.

It is noted that the resonance function is not defined when

$$|[Z^B]| = 0 \quad \text{and} \quad |[Z]| = 0$$

although the analytical form in equation (43) shows that the resonance function is independent of the impedance determinants $|[Z^B]|$ and $|[Z]|$. The reason is that we are not measuring the impedance elements but the mobility elements indirectly through force and response measurements according to equation (11). It is then evident from equation (43) that when $|[Z^B]| = 0$ and $|[Z]| = 0$, the resonance function $\psi(m_{\mu\nu};\omega)$ becomes 0/0 and ∞/∞, respectively. Such induced ambiguities can be eliminated by data analysis and present no real probl^ [4].

By examining the special functions defined in equation (37), (42), and (43), the fixed-base

natural frequencies can be concluded with assurance.

Experimental Results

Experimental results of vibrational tests according to different boundary conditions and the test setups of the substructures involved in each case are shown in Figure 1 through 7. A simple principal substructure was chosen for the purpose of demonstration of the resonance test techniques implied by the theoretical analysis. The principal substructure used consists of a four feet long, two inch by one inch in cross-section, rectangular steel beam with three simple supports at the quarter points along its length. Test for case 1 was not performed because the geometric boundary condition of the test beam does not belong to this case. The test for a structure truly floating can be done by suspending the test structure at one location and applying force at the same location. Figure 1 shows the test result of case 2.
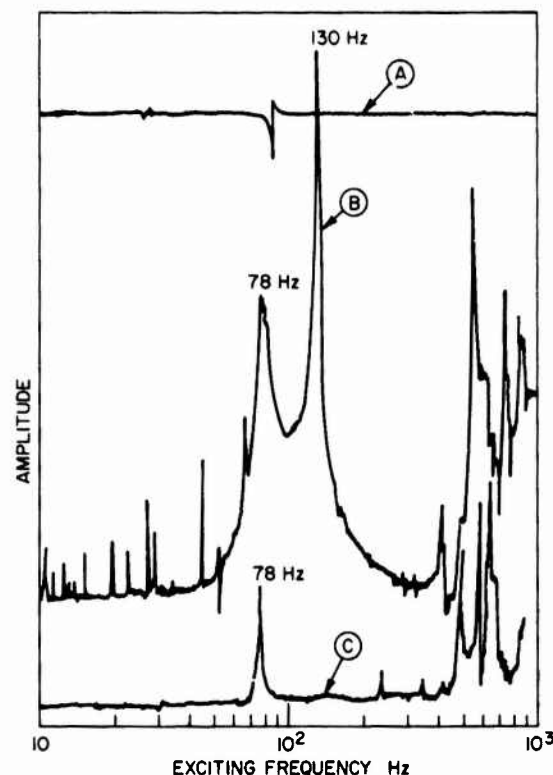
Fig. 1 - Case 2: Fixed constraints in space. (A) Controlled force level. (B) Monitored response signal from the tip of the beam. (C) Monitored response signal from the mounting table.
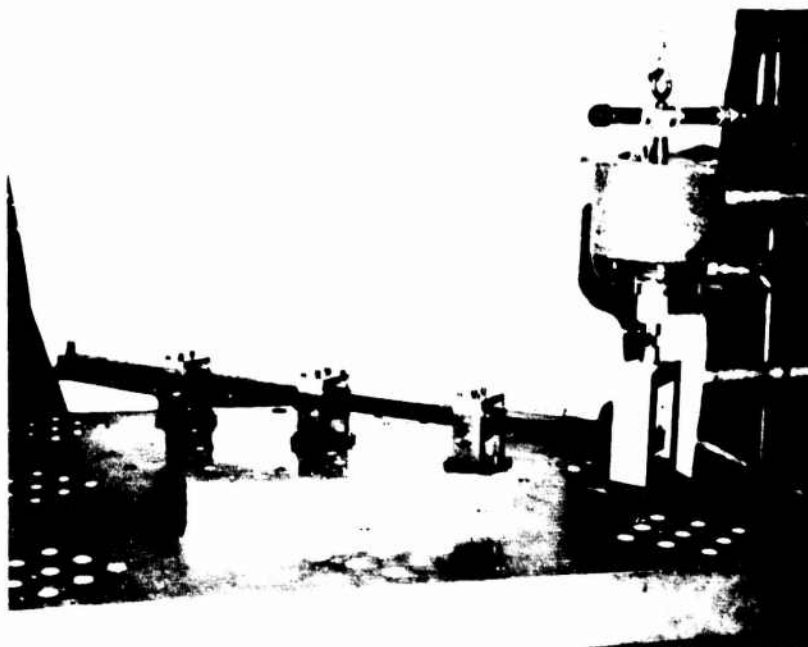
Fig. 2 - The experimental lay-out of the resonance test of the beam with fixed constraints in space. (Case 2)
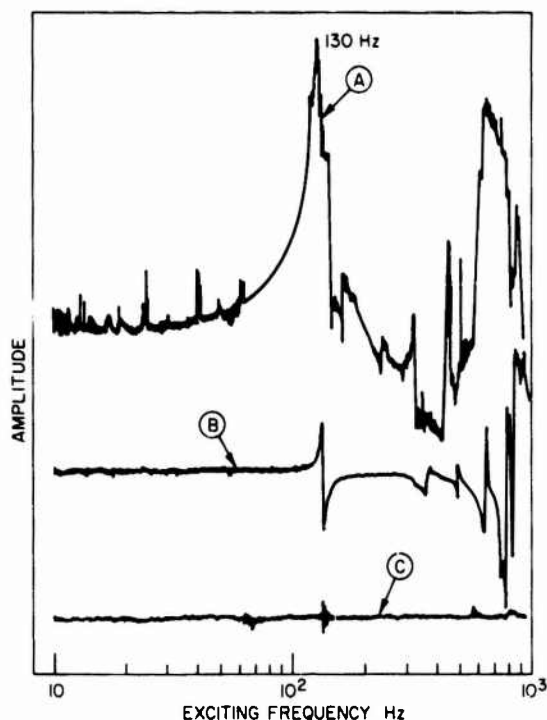
Fig. 3 - Case 3: Rigid body motion of the constraints as a whole. (A) Monitored response signal from the tip of the beam. (B) Monitored response signal from the shake table. (C) Controlled shake table response level.

The curves (A), (B), and (C) were monitored signals from the corresponding sensors shown in Figure 2. These three sensors are the minimum requirement for the identification of the resonance peaks at the fixed-base natural frequencies of the test beam. Curve (A) is the controlled force level. Curve (C) tells that any information beyond the exciting frequency about 400 Hz is not reliable because of the moving of the base substructure itself. Within the frequency range 10 ~ 400 Hz, curve (B) shows two resonance peaks. One is at the frequency of 78 Hz and the other 130 Hz. It is evident from curve (C) that the resonance peak at the frequency of 78 Hz does not belong to the test beam with fixed constraint boundary condition but belong to a more extensive structure including the test beam. Therefore, within the effective frequency range, only one resonance peak at the frequency of 130 Hz is detected despite the fact that two fixed-base natural frequencies of the beam exist inside that frequency range. Figure 3 shows the test result of case 3. The curves (A), (B), and (C) were monitored signals from the corresponding sensors shown in Figure 4. Curve (C) represents the controlled response level of the shake table. Curve (B) indicates that within the frequency range 10 ~ 300 Hz, the shake table moves like a rigid body. Beyond the exciting frequency of 300 Hz, the fixed constraints boundary condition of the test beam is no longer fulfilled. Consequently,

56

Fig. 4 - The experimental lay-out of the resonance test of the beam with it's supports moving as a rigid body. (Case 3)

the information revealed in curve Ⓑ beyond that frequency are not reliable to conclude the fixed-base natural frequencies of the test beam. Curve Ⓐ, within the effective frequency range, shows one peak at the frequency of 130 Hz and an ill-defined shoulder at the exciting frequency around 140 Hz. Figure 5 and 6 show the concluded results of case 4 with the force applications being at the supports as shown in Figure 7. In Figure 5, the resonance function is plotted against the exciting frequency. Like the results obtained from other techniques, only one resonance peak was observed at the exciting frequency of 125 Hz. An additional peak appeared at 140 Hz in the absolute value of the reciprocal of the mobility function versus exciting frequency plotting in Figure 6. By method of deduction [4], we were able to conclude that the two peaks in Figure 6 are the fixed-base natural frequencies of the test beam within the frequency range of 100-200 Hz.

The experimental results as well as the calculated theoretical values of the fixed-base natural frequencies of the lowest two modes of the continuous test beam are summarized in Table I.

Discussion

Table I shows that there are discrepancies in results among the different methods. A

TABLE I

SUMMARY OF RESULTS

•••• A beam with three supports at its quarter points ••••
(Test Frequency Range 100-200 Hz)

		Fixed-base Natural Frequencies in Hz	
		f_1	f_2
Classical Beam Solution		138	148
Case 1		..	..
Case 2		130	..
Case 3		130	..
Case 4	$\Psi\,(\mathfrak{m}_{\mu\nu};\,\omega)\;vs\;\omega$	125	..
	$\Omega\,(\mathfrak{m}_{\mu\nu};\,\omega)^{-1}\;vs\;\omega$	125	140

discrepancy of less than five percent is noticed among the results from the experimental techniques, while amounts to ten to fifteen percent between the experimentally measured values and the calculated theoretical ones. The most probable causes of these discrepancies are believed to be of two main reasons. The first is the induced deficiency inherited in the test techniques of case 2 and 3 explained in the main text. The second is the difficulty to have an exact duplication, or simulation of the dynamic boundary condition as the idealized one for all different test setups. Since the natural

57
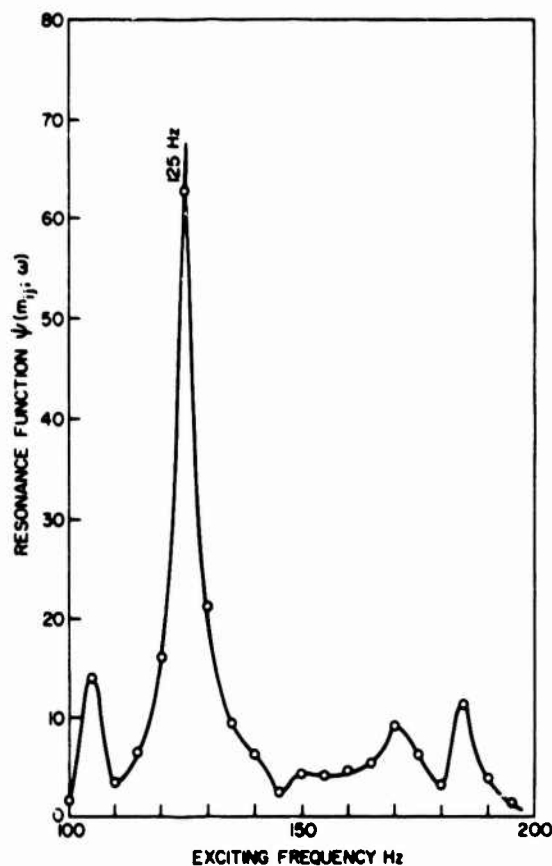
Fig. 5 - The resonance function-exciting
frequency plot resulted from a semi-
analytical resonance test on the beam
elastically coupled with it's neighboring
substructures. (Case 4)

Fig. 6 - The mobility function-exciting
frequency plot resulted from a semi-
analytical resonance test on the beam
elastically coupled with it's neighbor-
ing substructures. (Case 4)

frequencies obtained are intimately related to
the dynamic boundary condition imposed on the
principal substructure under test, such small
shifts in frequency are expected if precise dy-
namic boundary condition can not be main-
tained. In general, the results are considered
in very good agreement except those missing
information listed in Table I for case 2 and 3.
In either case, one of the two frequencies was
not detected. Experimental measurements
show little evidence that this missing informa-
tion is due to the sweeping speed of the force
input. It is likely because of the inherited am-
biguity of the test methods. The advantage of
the test methods used in the case 2 and 3 are
comparative simplicity and directness. Their
drawback is the possibility of revealing incom-
plete information.

The test method of case 4 is of special
value and importance because it is the only
reliable method at the present time to acquire
the fixed-base natural frequencies of a princi-
pal substructure in situ or in laboratory. Es-
pecially, for large structures, sweeping vibra-
tional tests described in case 2 and 3 are
practically impossible. Although the semi-
analytical procedure in the method of case 4
requires simple data analysis to draw conclu-
sion from the test, its correct answers are
certainly worth the effort even for a small
simple structure.

ACKNOWLEDGMENT
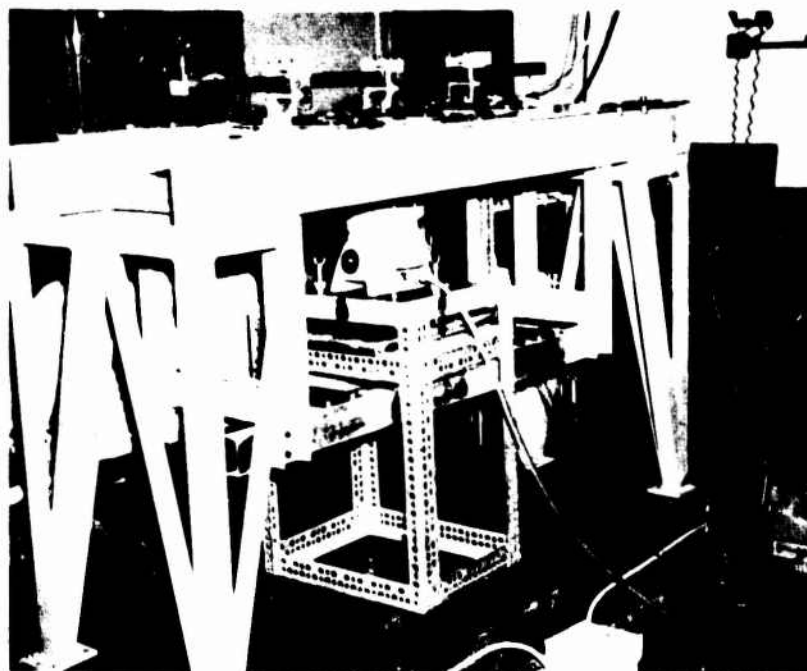
Fig. 7 - The experimental lay-out of the semianalytical
resonance test. (Case 4)

REFERENCES

[1] Petak, L.P. and Kaplan, R.E., "Resonance
Testing in the Determination of Fixed-Base
Natural Frequencies of Shipboard Equip-
ment," NRL Report 6176, December 15,
1964.

[2] Petak, L.P. and O'Hara, G.J., "Determina-
tion of Fixed Base Natural Frequencies of
Dual Foundation Shipboard Equipments by
Shake Tests," NRL Report 6461, August 23,
1966.

[3] Ni, C. and Skop, R.A., "Determination of
Fixed-Base Natural Frequencies of
Multiple-Foundation Mechanical Systems
by Shake Test," NRL Report 7300, Novem-
ber 17, 1971.

[4] Ni, Chen-Chou and Layher, James P.,
"Determination of Fixed-Base Natural
Frequencies of a Composite Structure or
Substructures," — Experiment and Appli-
cation —. NRL Report 7362, December 30,
1971.

[5] Bishop, R.E.D. and Gladwell, G.M.L., "An
Investigation into the Theory of Resonance
Testing," Phil. Tran. Roy. Trans. Roy.
Soc., London 255, 241-280, Jan. 1963.

[6] Ni, C. Skop, R.A. and Layher, J.P.,"
Determination of Fixed-Base Natural
Frequencies of a Composite Structure or
Substructures," Shock and Vibration
Bulletin, No. 42-Part 5, Jan. 1972.

ELEVATION OF GRANULAR MATERIAL BY VIBRATION

Mario Paz
Professor, Civil Engineering Department
University of Louisville
Louisville, Kentucky

and

Vicharn Vivekaphirat
Graduate Student, Civil Engineering Department
University of Louisville
Louisville, Kentucky

Experiments conducted recently in the USSR have shown that
granular material may be conveyed vertically by a suitable
apparatus vibrating torsionally and axially at two synchron-
ized frequencies. This paper describes mathematically the
conveying action of this type of vibrating elevator and also
presents a new conception of a vibrating elevator opera-ed
at a single frequency.

INTRODUCTION

Conveying material by vibration
in the horizontal direction is accom-
plished in its simplest form by a
trough supported by springs at an
angle and by a driving mechanism which
produces harmonic motion. A mathe-
matical analysis of the conveying
action is given by Paz [1]. In that
paper it is shown that the frictional
force developed between the material
and the trough gives the necessary
impulses to produce the conveying
action.

This basic idea has also been
extended to vibrating elevators of a
type having a spiral trough or pipe
mounted on shock absorbers. A vibra-
tory drive imparts helical oscillations
to the trough, causing the material to
move up the spiral trough or pipe.
These existing vibratory elevators
have a disadvantage in that they do not
combine high capacity with adequate
compactness. The effective cross-
sectional area is limited since the
spiral pipe cannot be set at an angle
exceeding the angle of friction for
materials in the pipe. The ideal solu-
tion for the problem would be a machine
that could convey material by vibra-
tion in the vertical direction. An
ingenious machine of this type has been
invented in the USSR and patented in
England by Brumberg [2]. The invention

consists of an apparatus having
two concentric cylindrical tubes with
a number of radial partitions. The
assembly is driven axially in the ver-
tical direction at the same time that
it is vibrated torsionally. The
rectilinear vibratory motion is
synchronized at a frequency twice
the value of torsional frequency im-
parted to the system, as determined
by the equations

$$Y = A_y \cos (2\omega t + \alpha) \qquad (1)$$

and

$$\phi = \phi_o \cos \omega t \qquad (2)$$

where A_y and ϕ_o = amplitudes of
oscillations

ω = torsional frequency

t = time

α = phase angle

To avoid the undesirable require-
ment of providing the vibrating eleva-
tor described with two oscillatory
frequencies and means for their correct
synchronization, an arrangement is con-
ceived which requires a single fre-
quency for elevating materials by
vibration. This arrangement can be
described better with the aid of
Fig. 1, which shows a diagram of the

61

vertical cross-section of the elevator tube, and Fig. 2, which shows a transverse cross-section on line I - I of Fig. 1. The vibrating conveyor consists of two cylindrical shells of different diameters assembled together so that they are coaxial. Channels are formed by subdividing the annular space between the shells with radial partitions. This assembly is mounted on a system of inclined springs and stabilizing bars to allow for a desired helical motion of the tube. The drive mechanism could consist either of motor driving eccentric weights or of a direct drive acting through an eccentric shaft. Either of these drives will impart to the tube the desired helical harmonic motion. The annular tube has a number of internal rectilinear channels parallel to the longitudinal axis of the tube. The inner opposite walls of the radial partition are finished so that the surfaces differ from each other in regard to their frictional properties. One of these surfaces is lined with a rough, highly frictional material, while the other is kept as smooth as possible. During operation the torsional component of the motion pushes the material alternately against the rough and smooth surfaces of the radial partitions. At the same time during the upward motion the frictional forces developed between the rough surfaces and material drag the material vertically producing the conveying action. When the motion is reversed downward, the material is pressed against the smooth surfaces and, ideally, the component of its motion in the vertical direction is not affected.

In this paper an analysis of the conveying action for the dual-frequency vibrating elevator is presented. The analysis is accomplished by describing mathematically the trajectory of the conveyed material during one cycle of oscillation of the elevator. From this study several operating characteristics such as the conveying speed may be determined. Also the analysis presented may be used to study the effect of the various parameters involved in the conveying action and to optimize the design of these vibrating elevators.

DUAL-FREQUENCY SYNCHRONIZED ELEVATOR

The dual-frequency sychronized elevator is given simultaneously an axial and a torsional vibratory motion described respectively by Eqs. (1) and (2). Multiplication of Eq. (2) by the radius R at the point of contact of the material on the radial partition gives the equation for the transverse motion of this point as
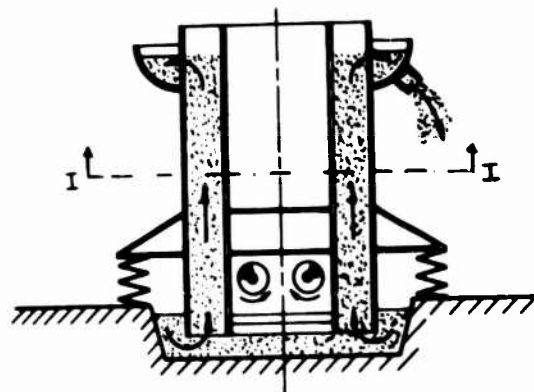
Figure 1

Vertical cross-sectional view of the vibrating elevator.
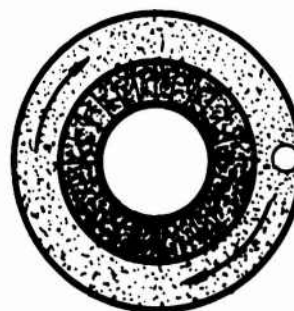
Figure 2

Transverse cross-sectional view of the vibrating elevator.

$$X = \phi_o \, R \cos \omega t \qquad (3)$$

The velocity and acceleration components of this point on the radial partition are given respectively by

$$\dot{X} = -\phi_o \, R \, \omega \sin \omega t \qquad (4)$$

$$\dot{Y} = -2A_y \, \omega \sin (2\omega t + \alpha) \qquad (5)$$

and

$$\ddot{X} = -\phi_o \, R \, \omega^2 \cos \omega t \qquad (6)$$

$$\ddot{Y} = -4A_y \, \omega^2 \cos (2\omega t + \alpha) \qquad (7)$$

The starting point of the analysis is to solve the equation of motion for a particle of material in the condition of impending motion; that is, the condition at which the frictional forces developed at the interface between material and the radial partition has reached the maximum value. Fig. 3 shows the free body diagram of a particle of material at this condition.
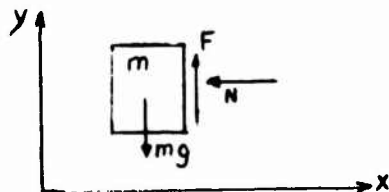
Fig. 3. Free Body diagram particle of material.

Application of Newton's law of motion to the particle in Fig. 3 gives

$$-N = m\ddot{x} \qquad (8)$$

$$F-mg = m\ddot{y} \qquad (9)$$

where $\ddot{x}$ and $\ddot{y}$ are the acceleration components of the particle, F and N the frictional and normal forces respectively, and m the mass of the particle. At impending condition the frictional force is related to the normal force by

$$F = \mu N \qquad (10)$$

where μ is the Coulomb friction coefficient.

At this condition the particle has the same motion as the point of contact on the radial partition; that is, $\ddot{x} = \ddot{X}$ and $\ddot{y} = \ddot{Y}$. Combining Eqs. (8), (9) and (10) results in the following equation:

$$g-4A_y\omega^2\cos(2\omega t+\alpha)-\mu\phi_o R\omega^2\cos\omega t = 0 \qquad (11)$$

The smallest positive root t_1 of Eq.(11) gives the time at which impending motion takes place. After time t_1 the material, acted upon by frictional and normal forces, moves attached to the radial partition. As the elevator decelerates in its vertical motion, it reaches a point at which the frictional forces developed at the interface are insufficient to give the material the same deceleration. Consequently, at this point the material starts to slide vertically relative to the motion of the radial partition. The time t_2 corresponding to this point of the cycle

is obtained from the solution of Eq. (12) which is the same as Eq. (11), except for the reversal of sign of its last term to account for the reversal in the direction of the frictional force, now acting downward on the particle.

$$g-4A_y\omega^2\cos(2\omega t+\alpha)+\mu\phi_o R\omega^2\cos\omega t = 0 (12)$$

The material remains in contact with the radial partition until the torsional acceleration of the elevator reverses its sign ($\omega_t = \pi/2$). During this interval, from time t_2 to time t_3, the material slides vertically on the surface of the radial partition. Its vertical motion is governed by the equation

$$m\ddot{y} = -mg-\mu m\phi_o R\omega^2\cos\omega t \qquad (13)$$

which may be readily integrated for the interval t_2-t_3.

After time t_3 the material loses contact with the radial partition; it is acted upon only by gravitational forces, and consequently the horizontal component of its velocity remains unchanged. The vertical component for the motion of the particle during the time interval between separation of the radial partition and recontact with the opposite radial partition is given by

$$y-y_3 = \dot{y}_3(t-t_3)-\frac{1}{2}g(t-t_3)^2 \qquad (14)$$

where y_3 is the vertical displacement of the material at time t_3. The material strikes the opposite radial partition at time t_4 which is obtained by solving the equation

$$D_1+\phi_o R\cos\omega t = \dot{X}_3(t_4-t_3) \qquad (15)$$

where D_1 is the mean free space between radial partitions. For design purposes this free distance between partitions is computed from Eq. (15) with the condition

$$\omega t_4 = \pi \qquad (16)$$

Under the assumption of perfectly plastic impact, the material will remain in contact with the opposite radial partition after time t_4, although sliding along the vertical direction. Finally, the action of frictional forces in the interface material-radial partition will equalize the velocities at impending condition. This condition is given by Eq. (17) which is similar to Eq. (11) except for a change in the sign of the last term due to the reverse direction of the normal force now developed on the material by the action of opposite

radial partition.

$$g - 4A_y \omega^2 \cos(2\omega t + \alpha) + \mu \phi_o R \omega^2 \cos \omega t = 0 \tag{17}$$

Solution of Eq. (17) in terms of ωt is equal to the solution of Eq. (11) plus π, that is,

$$\omega t_5 = \omega t_1 + \pi \tag{18}$$

This description completes half of the cycle in the motion of the elevator. The other half of the cycle is symmetric for the dual-frequency synchronized elevator.

EXAMPLE

A numerical example is given to illustrate the calculations involved in the dynamic analysis of the material lifted by vibration. The design parameters used for the example are as follows:

Amplitude torsional oscillation:
ϕ_o = 0.8 degrees.

Amplitude axial oscillation:
A_y = 1.5 mm.

Frequency torsional oscillation:
ω = 25 c.p.s.

Frequency axial oscillation:
2ω = 50 c.p.s.

Mean radius of concentric cylinders: R = 375 mm.

Mean distance between radial partitions: D = 50.0 mm.

Coulomb friction coefficient:
μ = 0.5.

Phase angle: α = 220°.

The conveying speed (V_s) is computed from the resulting displacement in one cycle of Table I as follows:

$$V_s = \frac{\text{Total Displacement in Cycle}}{\text{Period}}$$

$$V_s = \frac{2 \times 4.729}{0.04} = 240 \ \frac{mm}{sec}$$

The conveying speed of 240 mm/sec determined in this example compares favorably with the conveying of actual horizontal vibratory conveyors. Nevertheless, experimental results obtained in the USSR indicate a much lower value of 80 mm/sec for the conveying speed. In the comparison of these results it is necessary to observe that all the numerical values for the parameters used in the example are the same as those used in the experiments, except the coefficient of friction which was not indicate by the investigators in Russia.

CONCLUSIONS

The motion of material elevated by vibration has been analyzed and determined under some simplified assumptions. The most important assumptions are: (a) the analysis is restricted to a single particle of material; (b) the impact between material and radial partition of the elevator is considered to be perfectly plastic; and (c) the motion of the vibrating elevator is assumed to be unaffected by the material. Further study of the dual-frequency synchronized elevator as well as the study of the single frequency elevator, along the lines presented, will be necessary to establish practical design criteria for these elevators.

Table I. Vertical displacement of material particle during one cycle of the dual-frequency synchronized elevator motion.

Angle	Time	Coord. point on elevator		Coord. particle		Displacement
ωt (degree)	t (millisec)	X (mm)	Y (mm)	x (mm)	y (mm)	Δy (mm)
14.5	1.60	5.083	-0.537	5.083	-0.537	
37.0	4.10	4.195	+0.611	4.195	+0.611	1.148
90.0	10.00	0.000	+1.150	0.000	+2.345	1.734
180.0	20.00	-8.250	-1.150	-8.250	+3.945	1.600
194.5	21.60	-8.082	-0.537	-8.082	+4.192	0.247
Displacement in half a cycle					=	4.729

REFERENCES

[1] Paz, M., Conveying Speed of
Vibrating Equipment, Publication
No. 64-WA/MH-1, ASME 1965.

[2] Brumberg, R. M., Trostanetsky,
L. M., and Khlebnihov.
Apparatus for Conveying Materials,
The Patent Office, WC2AlAY, London,
United Kingdom 1971.

NOMEMCLATURE

A_y = amplitude axial oscillation

D = mean distance between radial
partitions

F = frictional force

g = acceleration of gravity

m = mass of material

N = normal force

R = mean radius of concentric
cylinders

t = time

V_s = conveying velocity

X,Y = coordinates point of elevator

$\dot{X},\dot{Y}$ = velocity components of point on
elevator

$\ddot{X},\ddot{Y}$ = acceleration components of point
on elevator

x,y = coordinates of material

$\dot{x},\dot{y}$ = velocity component of material

$\ddot{x},\ddot{y}$ = acceleration component of material

α = phase angle

ϕ_2 = amplitude torsional oscillation

μ = Coulomb coefficient of friction

ω = torsional frequency

ISOLATION AND DAMPING

GROUND TESTS OF AN ACTIVE VIBRATION ISOLATION

SYSTEM FOR A FULL-SCALE HELICOPTER

Brantley R. Hanks and William J. Snyder

NASA Langley Research Center
Hampton, Virginia

Ground-based vibration tests were conducted on an electrohydraulic active vibration isolation system developed for vertical isolation of either the pilot's seat or the entire cabin of a research helicopter. This system utilizes two narrow frequency-band isolation notches which can be tuned electronically to desired lifting rotor vibration frequencies and thereby provide more than 90 percent vibration reduction in the isolated structure at these frequencies. Tests verified the performance of the system although low fuselage structural stiffness degraded overall performance. System performance was also affected by the rate of input frequency change.

INTRODUCTION

Among modern-day aircraft, the helicopter imposes probably the most severe vibration environment on man and equipment. In addition to being subjected to random low-frequency turbulence, the helicopter and its passengers also encounter higher frequency inputs not usually found in conventional aircraft. As each blade on the lifting rotor traverses a full circle, it undergoes differential drag, lift, and control forces resulting in high-force vibratory inputs to the transmission and fuselage below. These inputs occur at discrete frequencies, the blade passage frequency and its harmonics, and generally increase in magnitude as airspeed increases. Their frequencies, usually ranging from about 10 to 50 Hz, and directions depend on many factors including rotor speed, number of blades, blade design, and hub/control system design. Also, rotor unbalance can produce an additional input at the lifting rotor rotation frequency, usually about 5 to 8 Hz.

Passive isolation of these inputs is difficult because isolated components undergo high normal accelerations in maneuvers of the helicopter which cause excessive static deflection of ordinary spring isolators. Several advanced isolation techniques for use in helicopters are being evaluated throughout this country (e.g., [1] and [2]) and some are being successfully used [3] and [4]. However, no universal system has been developed as yet because of the wide variety of helicopters, rotor systems, and vibration directions and frequencies.

One candidate isolation system, active isolation, has the potential of providing considerable flexibility in isolation performance, with no static deflection, at the expense of some complexity, cost, and power penalties. Active isolation systems, systems which use feedback-controlled, powered actuators to reduce the transfer of vibration, have been studied analytically for a variety of applications (e.g., [5], [6], and [7]) including helicopters [8]. Laboratory hardware studies have demonstrated effectiveness of the technique [9],

[10], and [11]. Although some sophisticated hardware systems are now being developed (e.g., [12]), the physical implementation and evaluation of active systems in actual vehicles has not progressed rapidly.

This paper will present results from vibration tests on an electrohydraulic active isolation system developed for the NASA Langley Research Center and the USAAMRDL, Langley Directorate, by Barry Wright Corporation. The system was designed to isolate either the cabin or the pilot's seat of a high-performance hingeless rotor helicopter. Vibration tests on the system installed in a helicopter were conducted in the NASA Langley Structural Dynamics Research Laboratory and vehicle responses compared with and without isolation. The ultimate objective of the program is to subjectively evaluate pilot reactions during flight tests to cabin isolation as compared with the less expensive seat isolation.

RESEARCH HELICOPTER

The test vehicle for the active isolation program is the XH-51N helicopter shown in Figure 1. The XH-51N, described in Reference [13], is an experimental helicopter employing a three-bladed hingeless-rotor system. Early flight testing of the military versions of the aircraft revealed a severe vibration problem. This problem was alleviated by incorporating a passive vibration isolation system where the entire cabin of the vehicle was separated from the fuselage and mounted on a spring having a natural frequency at approximately 3 Hz.

During NASA flight testing the nonisolated configuration was partially duplicated by locking out the spring. Cabin vibrations versus airspeed measured during these tests are shown in Figure 2. Levels higher than 1g at 18 Hz, the blade passage frequency, are encountered during transition from hover to forward flight. The vibration level decreases initially following transition but the continuous increase in level with airspeed resulted

67

in a limit of 110 knots at 0.7g although the design top airspeed of the vehicle is in excess of 150 knots. Improvement was substantial in level flight with the isolated cabin operating. This improvement is indicated by data in Figure 3, where cabin levels were almost negligible at 18 Hz. In maneuvers, however, the passive isolation system creates a new problem. The cabin spring has a spring constant of approximately 2100 N/cm (1200 lbf/in.); this spring constant combines with a cabin weight of 2100 N to give a resultant deflection rate of 2.54 cm per g (1 in./g). The limits of travel for the spring are ±0.64 cm (±0.25 in.). As indicated in Figure 4, the cabin spring apparently begins impacting on the stop at about 0.25g resulting in an increased vibration level over level flight. As the normal acceleration is increased further, the cabin spring bottoms solidly and the cabin and fuselage act as if rigidly connected with isolation returning as the aircraft returns to level flight. In addition, a second problem results from coupling of the 3-Hz spring resonance with pilot control motions limiting the maximum airspeed to about 130 knots because of a tendency toward pilot-induced oscillations above this speed [14].

Upon review of these problems, it was decided that this vehicle provided a unique opportunity for applying active isolation concepts with a potential threefold benefit. First, the useful speed range of the vehicle could possibly be increased by almost 20 percent; second, active isolation for helicopter environments could be evaluated in a full-scale vehicle system; and third, the general subjective problem of whether pilot isolation alone, as compared to total cabin isolation, will sufficiently improve a pilot's performance and subjective reaction to a vehicle could be studied.

SYSTEM DESIGN

Design Concept and Requirements

A sketch of the XH-51 helicopter showing the isolated cabin mount configuration is shown in Figure 5. Basically, the cabin is supported under its center of gravity by a single vertical isolator spring which is, in turn, mounted to a cantilevered structure extending forward from the fuselage. Pitch and lateral restraint are provided by hinged straps at the back and bottom of the cabin. In this study, two systems were developed: a cabin isolator and a pilot's seat isolator. The approach to actively isolating the cabin was simply to replace the spring with a hydraulic servoactuator operated by a hydraulic power supply and a control electronics package mounted inside the cabin. For the seat isolation system, the original pilot seat was modified to be supported by an actuator using the same hydraulic and control circuitry as the cabin isolator. Both systems were designed so as to fit in available space with minimum vehicle modifications — a rather severe constraint but necessary because of costs of vehicle structural modifications.

Design and fabrication of the active isolation systems was performed by Barry Wright Corporation. Complete design details are contained in the contractor report [15]. As an aid to understanding system operation, a brief overview of the design is presented in the following sections. The system design was subject to the following specifications:

1. At least 90 percent reduction of isolated-mass vertical vibrations at the blade passage frequency and at one or two additional frequencies as necessary and feasible.

2. Insensitivity to rotor speed variation up to ±10 percent.

3. Maximum vertical dynamic deflections ±0.63 cm (±1/4 in.).

4. Zero static deflection during maneuver accelerations up to 2-1/2g.

5. Fail-safe and flight-qualified design.

Loads to be isolated were 600 Kg (1320 lbm) for the cabin and 175 Kg (385 lbm) for the seat out of a total flight weight of approximately 1910 Kg (4200 lbm).

Servocontrol System

Servocontrol system design concepts were developed and checked out using a simple lumped-mass analog computer model shown in Figure 6. One pitch and four vertical degrees of freedom were included. Masses and moment arms were chosen to yield approximate dynamic characteristics of the real vehicle. This model exhibited cabin-vertical/fuselage-pitch coupled resonance at about 14.5 Hz necessitating the design of an isolation system which provided a high degree of isolation at rotor input frequencies but which remained essentially rigid at this resonance. Simultaneously, the system had to provide isolation over a bandwidth equal to ±10 percent of the primary input frequencies (e.g., 16.2 Hz to 19.8 Hz for the 18-Hz input to compensate for rotor speed variation). The use of a notch system (one which isolates over very narrow frequency bands only) was decided upon. The notches would track (i.e., automatically change their nominal center frequency) in order to compensate for rotor speed variation. Two notches were used, one at 18 Hz and one additional which could be set at either 36 Hz or 6 Hz by making a minor electronics change.

A simplified block diagram of the isolator control system developed to meet the design requirements is shown in Figure 7. The system consists of a hydraulic servoactuator which is, in turn, controlled by position and acceleration feedback. The position loop has an upper frequency cutoff of 3 Hz which enables it to maintain a preset static position of the actuator but minimizes interference with the acceleration control at higher frequencies. The acceleration loop uses quadratic feedback control [10] which has very high gain when the accelerometer input frequency equals the notch frequency with low gain at other frequencies.

In simplified form, the notch open-loop transfer function for a single notch can be written as

$$\frac{\text{Output}}{\text{Input}} = -\frac{K_b \dfrac{\omega^2}{\omega_n^2}}{\left(1 - \dfrac{\omega}{\omega_n}\right)^2 \left(1 - \dfrac{\omega^2}{\omega_n^2}\right)}$$

where K_b is the product of all broad-band gains, ω_n is the notch frequency, and ω is the input

68

frequency. For this system, K_b was designed to be approximately 0.5 and the total closed-loop response reduces to approximately

$$\frac{\text{Output}}{\text{Input}} = \frac{1 - \frac{\omega^2}{\omega_n^2}}{1 + 0.3j \frac{\omega}{\omega_n} - \frac{\omega^2}{\omega_n^2}}$$

At frequencies well above and below ω_n, the transfer function is one. Bandwidth of operation is controlled by both K_b and damping and was designed to provide 90 percent isolation over approximately 1 percent of the notch center frequency.

Notch Frequency Control

The frequency control systems shown in the block diagram of Figure 7 contain two basic control operations. One is a frequency tracking control which varies the notch center frequency as the rotor tachometer frequency varies about the preset notch frequency. The other is a phase-lock control which compensates for tachometer inaccuracy. This system senses the frequency difference by comparing phase between the incoming accelerometer signal and the notch frequency and changes the notch frequency as needed. The phase-lock system was designed to be operational over a range of ±3 percent of the tachometer signal.

HARDWARE

Actuator Systems

Figure 8 shows the cabin actuator system. The cabin actuator system is a compact 152-mm (6-in.) long package containing the actuator, servovalve, and control accelerometer. It fits directly in the space allocated for the original spring with only a few mounting bracket changes.

The seat actuator system, shown in Figure 9, is more complex than that of the cabin. Since the helicopter contained no structure or space for mounting the actuator directly under the seat/pilot center of gravity, it was necessary to mount it at the back of the seat (producing an undesirable but unavoidable moment about the center of gravity). The seat is mounted on four bearings which move on fixed bearing rods attached to the seat support structure. The actuator is similar to the cabin actuator. It is mounted at the lower center of the seat back and attached to the seat frame on one side and the support structure on the other. The control accelerometer is mounted to the seat frame near the actuator. The actuator and accelerometer are canted at a 1/6-rad (10° angle) resulting in a small loss of vertical effectiveness.

Both actuators use unequal piston areas on the top and bottom of the piston to compensate for the static load being supported. The actuators are the sole supporting link in the vertical direction.

Hydraulic Power Supply

The hydraulic system used to supply fluid flow to the actuators is of simple basic design. An engine-driven pump supplies up to 190 ml/sec (3 gpm)

flow at 105 Kg/cm^2 (1500 psi) from a reservoir directly to the servoactuator with an accumulator in the line. From the actuator, the fluid passes through a 4.4-Kw (15 000 Btu/hr) fan-cooled heat exchanger and then returns to the reservoir. Appropriate filters, temperature and pressure sensors, and automatic shutoff valves are included to insure fail-safe operation. A separate electrically driven pump is available to replace the engine-driven one in laboratory tests.

All components of the hydraulic power supply system, with the exceptions of the pumps and the heat exchanger, are located in a single package behind the pilot's seat, as shown in Figure 10. The flight pump is mounted on the engine, the ground-test pump is separate of the helicopter, and the heat exchanger is located in the transmission compartment door. No attempt was made at making the cabin-mounted hydraulics package compact; and hence, it could be reduced in size if necessary. Also, integration of the system into the helicopter hydraulic system design would further reduce space requirements.

Control Electronics

The control electronics circuitry consists of seven plug-in circuit boards mounted in a commercially available box. This package is mounted on a shelf above the hydraulic power supply components behind the pilot's seat, as shown in Figure 10. It contains adjustable notch frequency and gain controls on the front as well as the actuator static position control. It also contains a series of failure-mode indicator lights which aid the operator in determining the cause for any system failure. As in the hydraulic system, this package could be greatly reduced in size if necessary.

Fail-Safe Design

In addition to hydraulic system monitoring and shutoff devices to prevent clogged filters and pressure and temperature overloads, the entire control system and the actuators were designed to be fail safe. The actuators contain steel bearings which are normally held free of the actuator piston by hydraulic pressure. If a pressure loss occurs, they are pushed by springs into slots in the piston to catch and hold it mechanically. A series of logic circuits shuts down the system if preset acceleration, velocity, or displacement levels are exceeded. Finally, a remote shutoff switch is provided at the pilot's station for emergency purposes. All components were designed and tested according to military specifications for flight hardware.

Weight Considerations

The total weight of the hardware including hydraulic fluid adds about 50 Kg (110 lbm) to the flight weight. Much of this weight (16 Kg (35 lbm)) is in the seat mount modifications and could be reduced with design effort. Also, excess weight could be trimmed in the mounting hardware for the hydraulics and control packages. If incorporated in the initial design of a vehicle this size, it is estimated that a similar active isolation system would probably add no more than 27 Kg (60 lbm). These weights do not include penalties associated

with required changes in structure to accommodate system (such as separating cabin from fuselage).

GROUND VIBRATION TESTS

Test Setup

In order to tune the isolation systems, verify their stability for flight tests, and evaluate any isolator/structural interaction problems, a series of vibration tests were conducted in the laboratory. The systems were mounted in a stripped-down XH-51 fuselage, no longer used for flight. Several structural differences in this fuselage, as compared to the flight vehicle, prevented exact duplication of the flight vehicle. However, it is believed that this series of tests adequately provided information necessary to allow safe flight tests to be conducted.

The helicopter mounted in the test setup is shown in Figure 11. The vehicle was elastically suspended at the hub with a 1-Hz natural frequency support system. A ±13-mm (±1/2-in.) stroke hydraulic shaker was attached to the rotor hub and elastically suspended separately from the helicopter as shown in Figure 12. Vertical accelerations of the shaker mass were maintained to provide an approximate constant force input. Two types of sinusoidal input tests were conducted: discrete-frequency tests in which the input frequency was increased manually in incremental steps, and continuous sweep tests in which a constant frequency increase rate was automatically maintained. Vertical and lateral motions of the vehicle were monitored at 22 positions on the vehicle structure.

Missing components of the vehicle such as the engine and tail rotor were replaced with ballast weights. The seats were loaded with 18 Kg (40 lbm) weights mounted on foam rubber such that a 4-Hz natural frequency, 0.3-damping factor system was achieved. Full flight weight of the vehicle was not simulated, however, since fuel and electronic equipment weights were omitted.

DISCUSSION OF RESULTS

A summary of test configurations, conditions, and types is shown in Figure 13. Two types of tests were conducted: discrete frequency and continuous sweep. Also, acceleration data were recorded from the isolator control accelerometer and from accelerometers mounted on the vehicle structure. The entire vehicle response when an isolator was in operation differed from that which occurred with no isolation. In order to include the effects of vehicle dynamics, all data will be presented in terms of ratios of output acceleration to shaker mass acceleration (referred to as transfer functions) and in terms of ratios of isolated to nonisolated transfer functions (referred to as isolator performance).

Cabin Isolator Tests

System Checkout on Analog Computer. Before mounting the cabin isolation system on the helicopter, performance of the control system design was checked by the manufacturer using the analog computer simulation of the vehicle (Fig. 6). Results of these tests, which were discrete frequency tests, are shown in Figure 14 for the 18-Hz isolation

notch. Isolator performance is shown as a function of frequency for three operational modes: (1) the 18-Hz fixed notch, (2) the 18-Hz phase-locked notch, and (3) the 18-Hz tracking notch. The control system performed well, providing better than 98 percent isolation in all modes and tracking ±2 Hz in the track mode. The phase-locked system effectively widened the bandwidth of the fixed notch, increasing it by about a factor of 3 at the 90-percent level.

Discrete-Frequency Laboratory Tests. A series of evaluation tests were conducted on the cabin isolator installed in the vehicle in which constant shaker-acceleration, discrete-frequency steps were input to the vehicle. For this series of tests, three fixed notches were studied: 6, 18, and 36 Hz. Figure 15 shows isolator performance for these tests as monitored at the isolator control accelerometer. More than 90 percent isolation was obtained at all notch frequencies.

Continuous-Sweep Laboratory Tests. The majority of the laboratory test data was obtained in controlled, continuous-sweep tests using 18 Hz and 36 Hz notches only. Isolator performance measured on the cabin floor at the cabin center of gravity rather than at the control accelerometer in order to obtain more realistic performance information. The transfer function of the cabin is compared in Figure 16 for the 18-Hz and 36-Hz tracking notch modes and the nonisolation mode. With no isolation, a rather large amplification occurs at 18.6 Hz. This is thought to be due to a cabin/fuselage relative pitch resonance although instrumentation was insufficient to define it exactly. This type mode was not included in the analytical model. With the isolator in operation, however, a significant reduction in vibration occurs across the tracking band from approximately 17 to 19.5 Hz and the amplification peak is completely eliminated. A peak occurs at each end of the tracking band as the tracking tachometer signal is manually switched in and out of operation. This represents an abnormal condition since in a helicopter the frequency varies up and down about the nominal. Although the isolation system was switched in at 16 Hz, it did not start operating until 17 Hz were reached; and it continued to provide some isolation for 1 Hz beyond the point at which it was switched out. The frequency sweep rate was a nominal 1/4 decade per minute or about 1 Hz every 2 seconds at this frequency.

The 18-Hz tracking notch provided about 75 percent vibration reduction at 18 Hz in this test and 93 percent at the 18.6-Hz peak. The 36-Hz notch, which was tracking from 32 Hz to 40 Hz, provided only 37 percent reduction at best, at about 34 Hz and increased the vibration by a factor of 3 over the unisolated case at about 38 Hz. This was the best performance provided by the 36-Hz notch in the continuous-sweep tests. The fixed notch resulted in the same vibration as the non-isolated case at 36 Hz and the phase-locked notch could not be stabilized.

Isolator performance for the various modes of operation in the sweep tests are compared for the 18-Hz notch in Figure 17. The best performance, 93 percent reduction, is obtained with the tracking notch whereas the phase-locked and fixed notches provide 80 percent and 72 percent reduction,

respectively. However, peak reduction in all cases occurs at 18.6 Hz, the amplification peak of Figure 16. At 18 Hz, the system is just becoming effective, whereas it had provided over   ercent reduction in discrete-frequency tests. .   comparing results from the continuous-sweep tests with the discrete-frequency tests, it appears that if a notch type active isolation system must work at some finite sweep rate, as it may in a helicopter, continuous-sweep tests must be conducted to evaluate its true performance.

Structural Considerations. In the laboratory tests, some effort was made to determine the effects of isolation of the cabin on the responses of the rest of the vehicle structure. Vehicle vertical response along its length is shown in Figure 18 for the 18-Hz isolated and nonisolated conditions. The shaded symbols are the cabin center-of-gravity responses. With the isolator operating, response differs on the fuselage directly under the cabin from that inside the cabin resulting in two data points at the same location. In this test, about 75 percent reduction in cabin center-of-gravity vibration was obtained. A penalty for this isolation is paid, however, in that elsewhere vibration amplification increases significantly, particularly in the nose and along the tail boom. In designing future active isolation systems for flexible vehicles, care must be taken in selecting location and control points to prevent the isolator from shifting an overall vehicle resonance to a hazardous frequency.

Figure 19 shows cabin floor vibrations when the cabin is isolated at 18 and 36 Hz in fixed frequency tests. Accelerations on the cabin floor underneath the seats are compared to the cabin center-of-gravity accelerations. These data and the nose vibration data of Figure 18 indicate that cabin floor flexibility decreases the effective isolation considerably. Total cabin isolation could possibly be improved by either using multiple actuators or using an averaging system with multiple control accelerometers and electronic compensation for cabin flexibility.

Seat Isolator Tests

Discrete-Frequency Tests. Performance of the seat isolation system in the helicopter was evaluated for three fixed-notch frequencies — 6 Hz, 18 Hz, and 36 Hz — in discrete-frequency step tests similar to those conducted on the cabin. Results are presented in Figure 20 where isolator performance, as measured by the control accelerometer, is shown as a function of frequency. Better than 93 percent isolation is obtained at 6 Hz and 18 Hz and almost 98 percent was obtained at 36 Hz. Slight amplification occurs before and after each notch.

As in the cabin tests, the seat was not completely free of all vibration because of lateral and longitudinal vibrations caused by nonvertical inputs at the floor. Also, the offset center of gravity of the isolated mass resulted in a rocking motion about the seat attachment points.

Continuous-Sweep Tests. Continuous-sweep tests were conducted on the seat in the vehicle to evaluate notch frequency tracking controls. Only the isolation notches at 18 Hz and 36 Hz were evaluated. The acceleration transfer function of the seat at

the actuator attachment point is shown in Figure 21 for the tracking notch isolation and nonisolation modes of operation. In the 18-Hz tracking (from 16 to 20 Hz) isolation mode, the amplification peak is reduced by about 84 percent, not as much as for the cabin. Across the bandwidth, average reduction is about 80 percent. In the 36-Hz tracking notch mode, the isolator provided better than 90 percent isolation over most of the 32 to 40 Hz band.

A comparison of isolator performance for the three isolation modes at 18 Hz is shown in Figure 22. Unlike the cabin data, the best isolation at 18 Hz is exhibited by the fixed notch. The phase-lock and tracking notches increase the bandwidth at the expense of some isolator effectiveness. Although no data are shown, the fixed notch performed well at 36 Hz providing a peak isolation effectiveness of 95 percent. This indicates that the seat system is somewhat less sensitive to tracking rate than the cabin system, possibly because of the smaller actuator size. As in the cabin tests, the 36-Hz phase-lock notch could not be stabilized with the seat mounted in the helicopter.

CONCLUSIONS AND RECOMMENDATIONS

Narrow-band active isolation systems capable of isolating either the pilot's seat or the entire cabin of a full-scale helicopter were tested. These tests were conducted in the laboratory on the systems mounted in the helicopter. The following conclusions and recommendations resulted:

1. Active isolation techniques can effectively reduce helicopter cabin response to rotor inputs even near resonances. Narrow-band isolation systems which track input frequency provide good isolation for a varying rotor speed environment.

2. Active vibration isolation of a large portion of a structure can significantly change the vibration characteristics of the unisolated portion. Development of any such active vibration isolation system should include elastic response studies of the entire vehicle.

3. Active isolator performance can be seriously degraded by isolated structure flexibility. The use of multiple actuators or multiple control accelerometers located over the isolated structure with electronic compensation for the structure should be investigated to overcome this difficulty.

4. Continuous-sweep tests must be used to adequately describe the performance of an active isolation system which must operate in a changing frequency environment.

REFERENCES

[1] Robert Jones, "An Analytical and Model Test Research Study on the Kaman Antiresonant Vibration Isolator," USAAVLABS Technical Report 68-42, Nov. 1968.

[2] James D. Cronkhite, "Helicopter Fuselage Vibration Response Analysis Using the Hybrid Computer," Shock and Vibrations Bulletin No. 41, Part 7, 1971.

[3] D. L. Kidd, R. W. Balke, W. F. Wilson, and R. K. Wernicke, "Recent Advances in Helicopter Vibration Control," Proceedings of the 26th Annual Forum of the American Helicopter Society, June 1970.

[4] D. P. Shipman, J. A. White, and J. D. Cronkhite, "Fuselage Nodalization," Proceedings of the 28th Annual Forum of the American Helicopter Society, May 1972.

[5] Peter C. Calcaterra, Richard D. Cavanaugh, and Dale W. Schubert, "Study of Active Vibration Isolation for Severe Ground Transportation Environments," NASA CR-1454, Nov. 1969.

[6] Igor L. Paul, and Erich K. Bender, "Active Vibration Isolator and Active Vehicle Suspension," Report PB 173-648 (Dept. of Transportation Contract No. C-85-65), MID, Nov. 1966.

[7] J. D. Leatherwood, "Analog Analysis of the Heave Response and Control of a Plenum-Type Air-Cushion Vehicle," NASA TN D-6257, April 1971.

[8] Peter C. Calcaterra, and Dale W. Schubert, "Isolation of Helicopter Rotor-Induced Vibrations Using Active Elements," Shock and Vibrations Bulletin No. 37, Part 6, Jan. 1968.

[9] Jack D. Leatherwood, and Grayson V. Dixon, "Active Vibration Isolation for Flexible Payloads," Proceedings of the Institute of Environmental Sciences 14th Annual Technical Meeting and Equipment Exposition, St. Louis, Missouri, April 29-May 1, 1968.

[10] Jerome E. Ruzicka, and Dale W. Schubert, "Recent Advances in Electrohydraulic Vibration Isolation," Shock and Vibrations Bulletin No. 3, Part 4, April 1969.

[11] Peter C. Calcaterra, "Active Vibration Isolation for Aircraft Seating," Sound and Vibration, pp. 18-23, March 1972.

[12] L. Pulgrano, "Tracked Air Cushion Research Vehicle/Guideway Dynamic Analysis," DOT Contract No. FR-00005, March 1971.

[13] William J. Snyder, "A Summary of Rotor Hub Bending Moments Encountered by a High Performance Hingeless-Rotor Helicopter During Nap-of-the-Earth Maneuvers," NASA TN D-4574, May 1968.

[14] Sherman A. Clevenson, William J. Snyder, and John J. Catherines, "Preliminary Study of Effect of Vibration on Aircraft Ride Quality," NASA SP-270, pp. 335-345, May 1971.

[15] Rush E. Allen, and Peter C. Calcaterra, "Design, Fabrication, and Testing of Two Electrohydraulic Vibration Isolation Systems for Helicopter Environments," NASA CR-112052, April 1972.
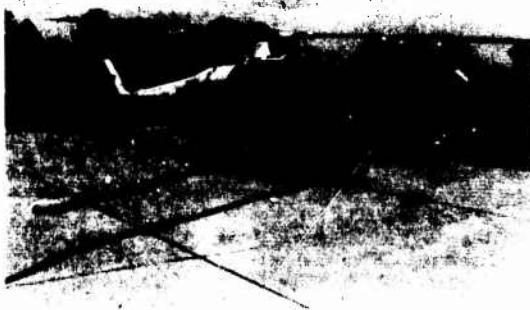
Figure 1.   XH-51N hingeless-rotor research helicopter.
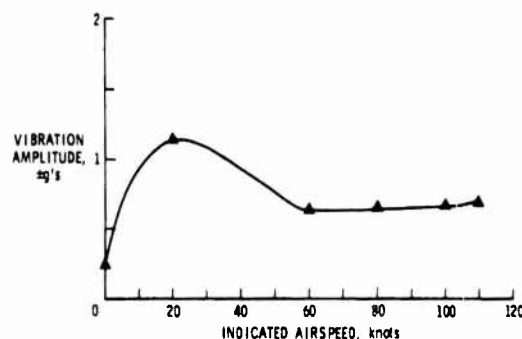
Figure 2.   XH-51N 18 Hz vertical vibrations at pilot's station in flight with unisolated cabin.
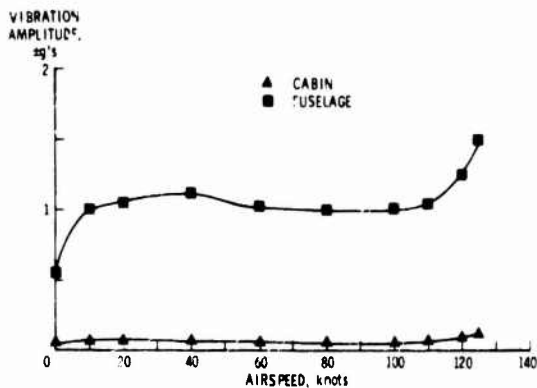
Figure 3. XH-51N 18 Hz vertical vibrations in flight with spring mounted cabin. (Measurement points approximately above and below spring.)
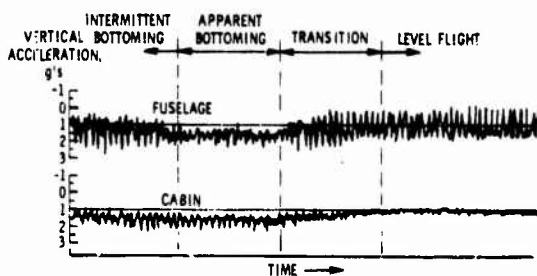
Figure 4. XH-51N vertical vibrations in tight turn maneuver with spring mounted cabin. (Measured approximately above and below spring.)
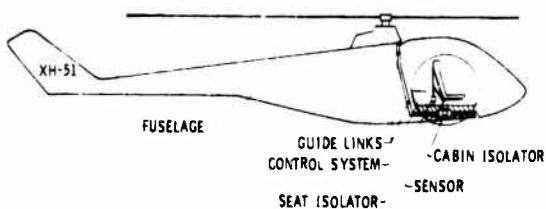
Figure 5. Sketch showing helicopter cabin isolation and seat isolation configurations.
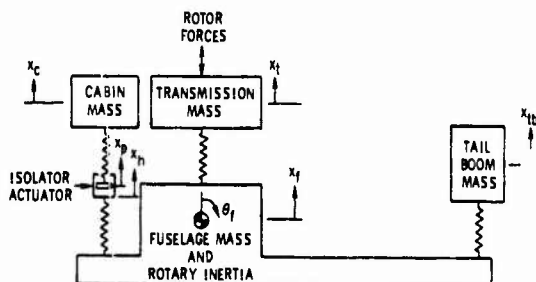
Figure 6. Model used in analog computer simulation for cabin isolator design.
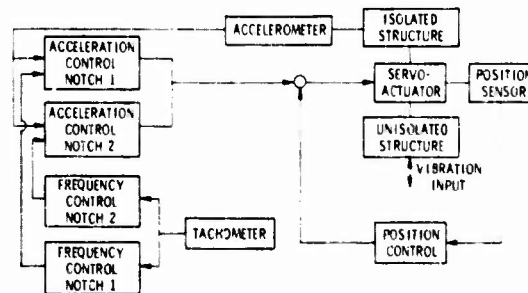
Figure 7. Block diagram of active isolator system.

Figure 8. Servoactuator for helicopter cabin isolation system.
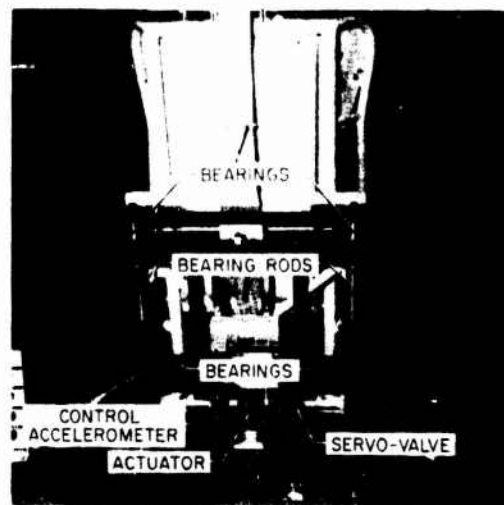
Figure 9. Actively isolated pilot seat hardware.

73
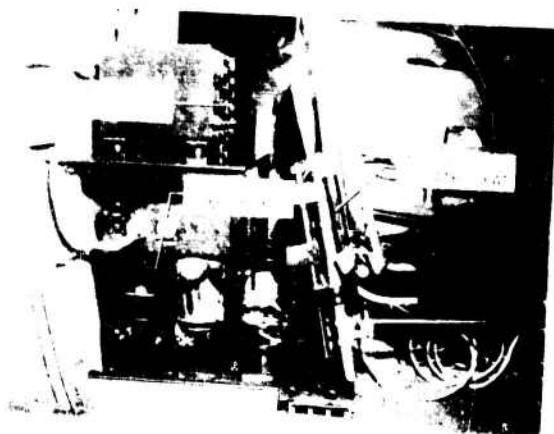
Figure 10. Isolated seat and associated equipment mounted in helicopter.

Figure 11. Stripped-down helicopter mounted in shake test rig.
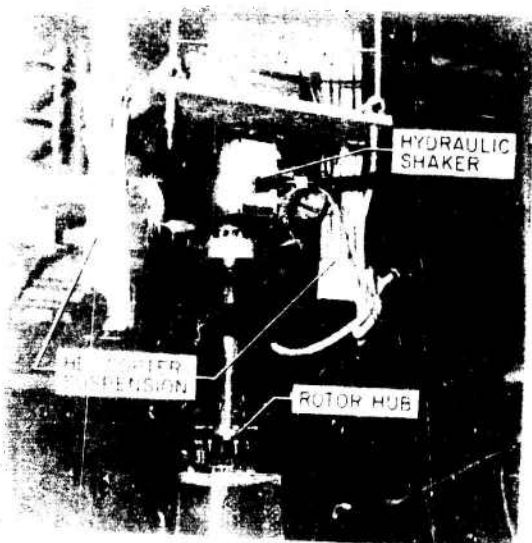
Figure 12. Shaker suspension apparatus.

OPERATIONAL MODE	FIXED-NOTCH			PHASE-LOCKED NOTCH			TRACKING NOTCH		
NOTCH FREQUENCY	6 Hz	18 Hz	36 Hz	6 Hz	18 Hz	36 Hz	6 Hz	18 Hz	36 Hz
CABIN ISOLATOR	D	D, S	D, S		S			S	S
SEAT ISOLATOR	D	D, S	D, S		S			S	S

D   DISCRETE FREQUENCY TESTS
S   CONTINUOUS SWEEP TESTS

Figure 13. Summary of isolator test conditions and types.
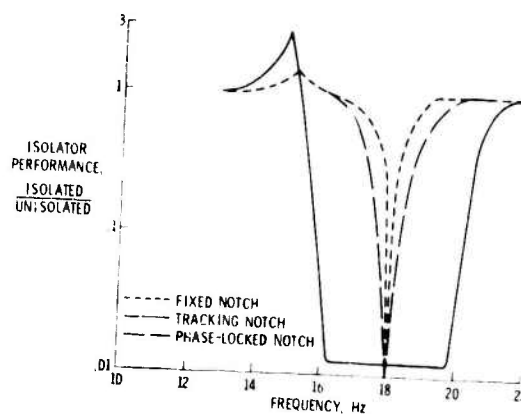
Figure 14. Cabin isolator control system performance on analog computer model of helicopter.
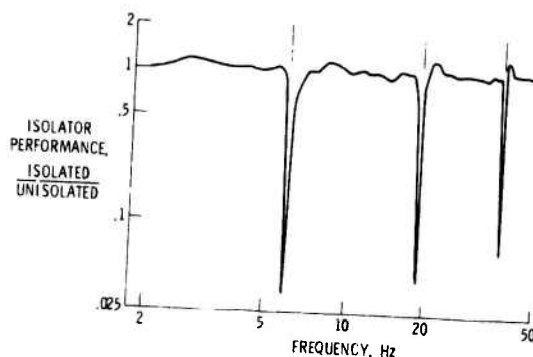
Figure 15. Cabin isolator performance in discrete-frequency tests.

74
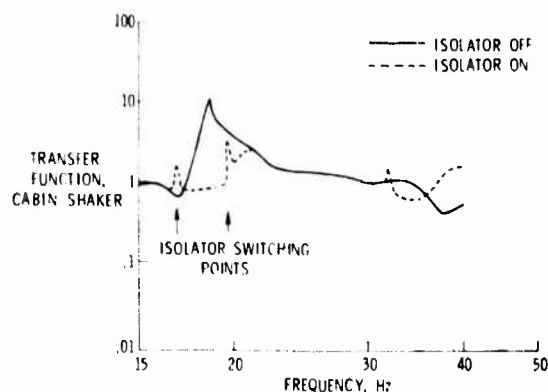
Figure 16. Comparison of isolated and unisolated cabin transfer functions for 18 Hz and 36 Hz tracking notches in continuous-sweep tests.

Figure 19. Effect of cabin floor flexibility on isolator performance.

Figure 17. Cabin isolator performance for three different operational modes in continuous-sweep tests.
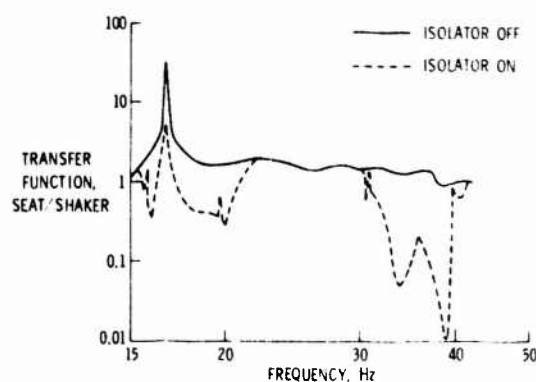
Figure 20. Comparison of isolated and unisolated seat transfer functions for 18 Hz and 36 Hz tracking notches in continuous sweep tests.

Figure 18. Comparison of vehicle response at 18 Hz with and without active cabin isolation.
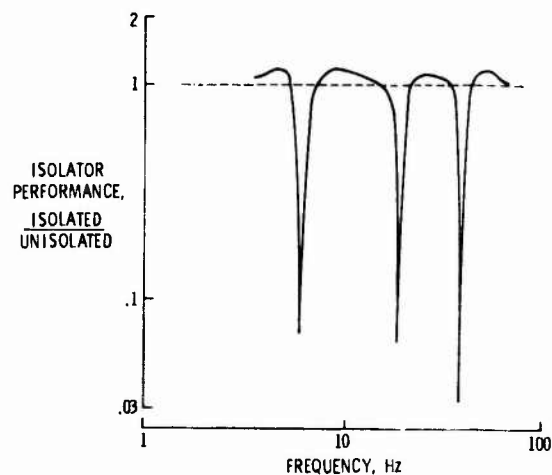
Figure 21. Seat isolator performance for fixed-notch operational mode in discrete-frequency tests.
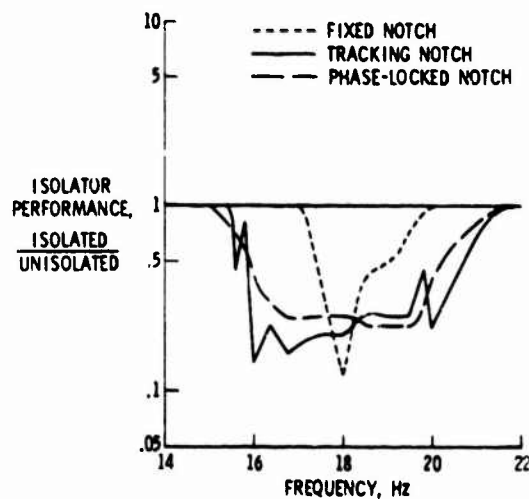
Figure 22. Seat isolator performance for three different operational modes in continuous-sweep tests.

DISCUSSION

Mr. Dickerson (Motorola): What conclusions, if any, did you draw concerning the ability of the pilot to function with relative motion between his torso and head at his control stick and his instruments?

Mr. Hanks: These were only the results of ground tests. Flight tests have not been conducted yet. The isolation system is being installed in the flight vehicle now and we hope by the first of the year to be able to run these subjective tests with pilots.

Mr. Snowdon (Pennsylvania State University): What amount of additional mass are you introducing to control either the vibration of the cabin or the whole craft? Can you quote a percentage?

Mr. Hanks: You mean the weight of the isolation system itself?

Mr. Snowdon: Yes, how do the additional components compare as a percentage of the mass of the cabin, for example.

Mr. Hanks: With respect to the mass of the cabin it is about ten percent. As I mentioned earlier, this is not necessary. Perhaps the weight could be cut fifty percent over what we did, not to mention volume. If it was included in the initial design of a helicopter so you could take advantage of hydraulic systems on the helicopter, it could be cut down even further. One thing that is not included in that estimate is the effect of cutting apart the cabin to begin with, which adds weight. In this particular case the cabin was already cut apart so we didn't add weight from that, but it was different from what would be in a normal helicopter.

A FULL-SCALE EXPERIMENTAL STUDY OF HELICOPTER ROTOR ISOLATION*

Robert Jones

Kaman Aerospace Corporation
Bloomfield, Connecticut

The full-scale experiments were performed on a Kaman UH-2 helicopter fuselage isolated from a simulated rotor and transmission utilizing the Dynamic Antiresonant Vibration Isolator (DAVI). Results of this experimental study on a 6500-pound helicopter show that rotor isolation is feasible. Excellent reduction of vibration throughout the fuselage was obtained at the predominant excitation frequency (n-per-rev). This was accomplished with low static deflection, minimum weight penalty, and small relative vibratory deflections between the rotor and fuselage.

INTRODUCTION

Through company and government sponsored research, great advancements have been made in rotary-wing analysis and design. Even so, major vibration problems still exist in present-day helicopters. These vibration problems not only increased the development time of rotary-wing aircraft and are a source of pilot fatigue, but in all probability are the cause of lower rotary-wing availability due to higher maintenance and lower reliability.

The major source of these vibration problems is the rotor induced shears and moments. The nature of these shears and moments is such as to produce an input at the hub at a frequency that is an integral multiple of the number of blades in the rotor system. The predominant frequency of excitation is the "nth" harmonic of an n-bladed rotor; i.e., for a two-bladed helicopter, the predominant frequency is two-per-rev. These rotor-induced shears and moments produce high-level, low frequency vibration in the fuselage.

One approach to reduce rotary-wing vibration levels is rotor isolation or the isolation of the fuselage from the rotor-induced shears and moments. Rotor isolation is not new. Conventional passive isolation is used in some present-day helicopters to isolate the in-plane shears. However, these soft isolation systems cannot be used for vertical isolation because of the large static deflection and the excessive deflection encountered during maneuvers. Research in rotor isolation has continued for many years. In the earlier published research studies (Refs. 1, 2, and 3) active systems were studied and recommended for vertical isolation.

More recently, due to the increased knowledge in the state of the art of both active and passive vibration systems, Eustis Directorate, Fort Eustis, Virginia, sponsored research to determine the analytical feasibility of rotor isolation. The results of this research are reported in Refs. 4 and 5. In Ref. 5, passive rotor isolation was shown to be analytically feasible utilizing the Kaman Dynamic Antiresonant Vibration Isolator (DAVI).

The DAVI is a passive isolator that provides a high degree of isolation at low frequency with very low static deflection. At the antiresonance of the DAVI, inertia forces cancel spring forces, producing nearly zero transmissibility across the DAVI. The antiresonant frequency is independent of the isolated mass.

This paper discusses the results obtained on an experimental feasibility program of rotor isolation conducted on a full-scale helicopter. This program was conducted on a Kaman UH-2 helicopter in which the fuselage was isolated from the rotor by a DAVI isolation system. The rotor and transmission were simulated by an upper body with proper weight and inertial characteristics.

DAVI BACKGROUND

The Dynamic Antiresonant Vibration Isolator (DAVI) is a passive isolator and is based on inertia coupling at the tuned or antiresonant frequency of the DAVI. Figure 1a shows a schematic of a unidirectional DAVI. It is seen from this schematic that a spring is attached between the isolated weight and the base, as in a conventional isolator. The inertia bar is attached to the isolated weight by a pivot and attached to the base by the non-isolated pivot. At the antiresonant frequency, the inertia force at the isolated pivot from the inertia bar cancels forces from the spring and produces nearly 100 percent isolation.
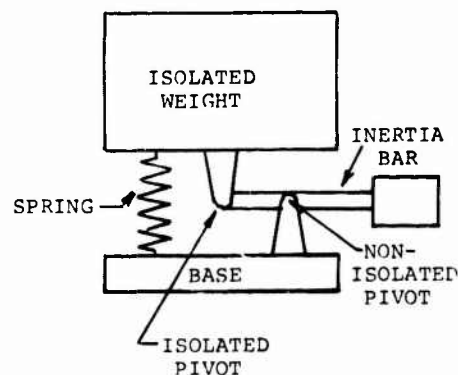
Figure 1b shows a schematic of a three-dimensional DAVI. The 3D DAVI has two inertia bars. The unidirectional inertia bar works in the vertical direction to provide vertical isolation. The two-dimensional inertia bar works in both the longitudinal and lateral directions and provides isolation in the in-plane directions of the springs. Thus, DAVI isolation is obtained in all three directions.

Because of inertial coupling, the DAVI has several unique features that cannot be achieved by conventional passive isolation. These features are:

(1) Nearly 100 percent isolation at the tuned frequency;

(2) Isolation at its tuned frequency is independent of the isolated mass; and

(3) Low frequency isolation with low static deflection.

The feasibility of the DAVI has been proven through several years of company and Eustis Directorate, U.S. Army Air Mobility Research and Development Laboratory sponsorship. Refs. 6, 7, and 8 show the results of this research. This research included analysis, laboratory testing and flight testing of a DAVI isolated platform.

(a) Unidirectional
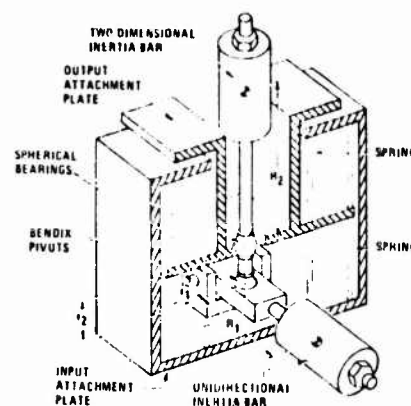
(b) Three-Dimensional

Figure 1. Schematic of the DAVI

Figure 2 shows typical DAVI transmissibility curves as compared to a conventional isolator. These results show that the isolated mass did not affect the antiresonant frequency of the DAVI at 10 Hertz and that excellent isolation is obtained. Furthermore, when comparing the 150-pound conventional isolation system with the 150-pound DAVI isolation system, the conventional system is essentially in resonance at the antiresonant frequency of the DAVI. The spring rates of both systems are identical. The natural frequency of the 150-pound DAVI system is much lower than the conventional system natural frequency because the effective mass of the inertia bar (much greater than its actual mass) adds to the isolated mass and reduces the natural frequency of the system.

Since the helicopter is an essentially constant frequency vehicle, the DAVI, because of its low static deflection and antiresonant characteristics is an ideal isolator for rotor isolation. Therefore, a full scale experimental program to determine the feasibility of rotor isolation using the DAVI was initiated.

FULL SCALE EXPERIMENTAL ROTOR ISOLATION

Design

A full-scale experimental rotor isolation program was conducted on a UH-2 helicopter at a gross weight of 6500 pounds, modified to incorporate a four point three-dimensional DAVI isolation system. The rotor and transmission were simulated by appropriate weight and inertial characteristics.

Figure 3 shows a three-view drawing of the three-dimensional DAVI. The unidirectional inertia bar couples with motion along the vertical axis of the preloaded vertical springs and utilizes rod end bearings as the hinge for the rotor or input pivot. The fuselage or isolated pivot of the unidirectional inertia bar is a spherical bearing. For motions of this unidirectional inertia bar, the weight of the two-dimensional inertia bar adds to the isolated weight or fuselage.

The two-dimensional inertia bar couples with the in-plane motions of the spring and utilizes spherical bearings for both the fuselage or isolated and rotor or input pivots. The rotor or input pivot of the two-dimensional inertia bar and the fuselage or isolated pivot of the unidirectional inertia bar is a common pivot. For
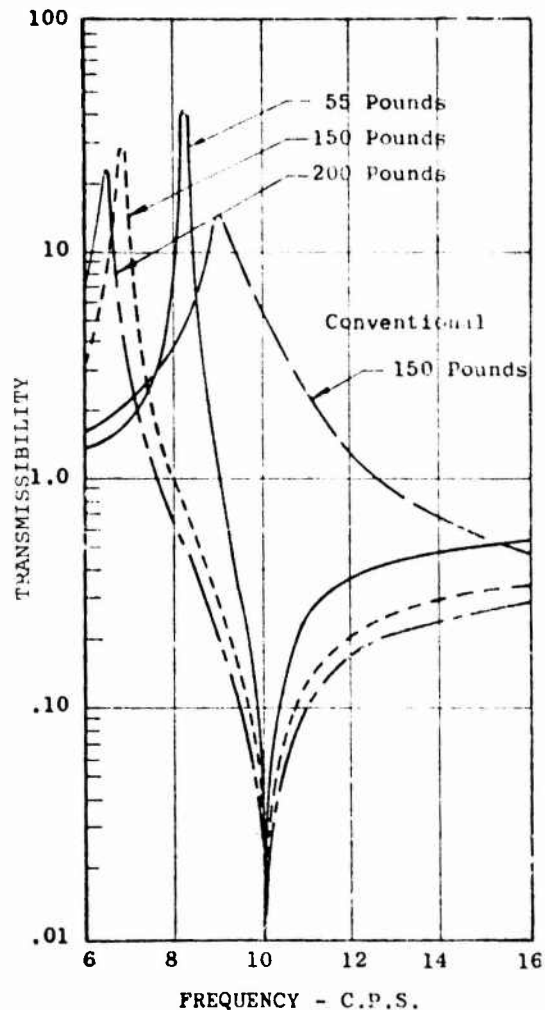
Figure 2.   Typical DAVI
            Transmissibility
            Curve

motions of the two-dimensional inertia bar, the weight of the unidirectional bar adds to the rotor weight.

To reduce internal coupling in the DAVI, the fuselage or isolated pivot of the unidirectional inertia bar is on the vertical elastic axis of the spring system and the isolated pivot of the two-dimensional inertia bar is on the in-plane elastic axis of the spring system.

Table I gives the physical parameters of the individual DAVIs used in this program.

Two different weights of the in-plane inertia bar are required, since the DAVIs were designed for a range of anti-resonance frequencies from 9 to 22 Hertz.

79
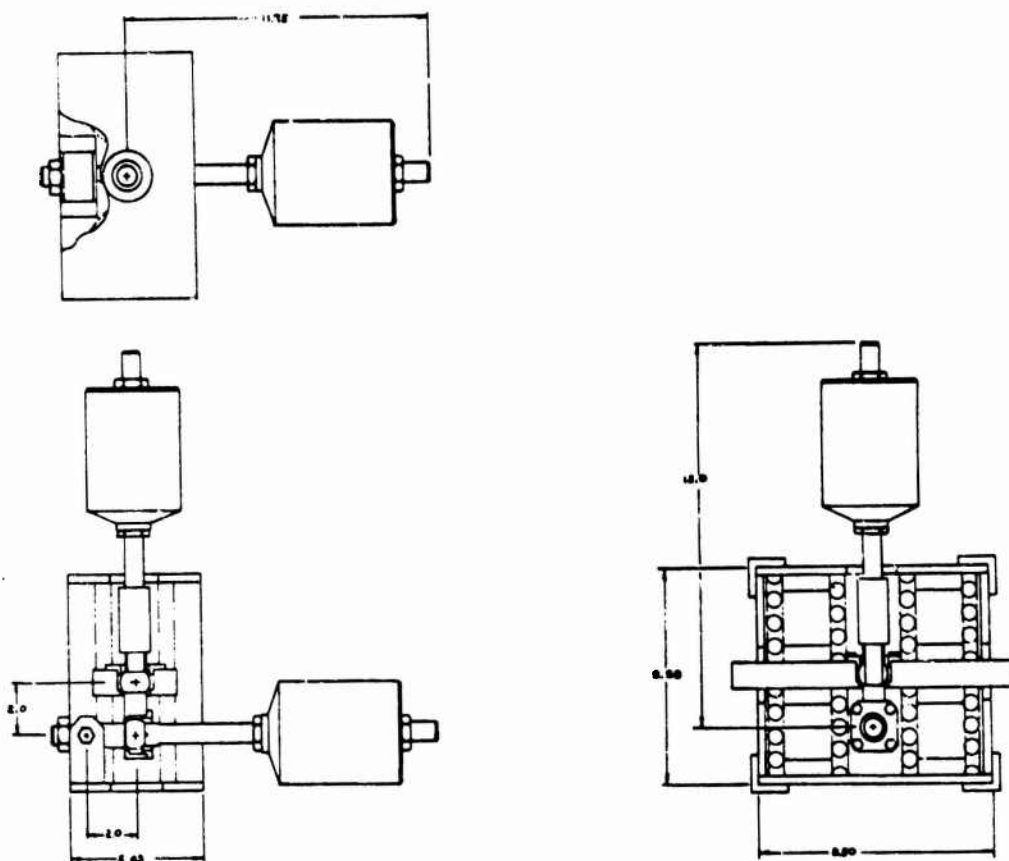
Figure 3. Three-View of the Three-Dimensional DAVI

TABLE I. PHYSICAL PARAMETERS OF DAVI

Spring Rate (Lb/In.)		Pivot Distance	Inertia Bar Weight (Lb)	
Vertical	In-Plane	r (In.)	Vertical	In-Plane
15,780	17,480	2	17.5	14.0; 17.5

To determine the proper position and weight for the movable weight of the inertia bars for the full-scale testing, the DAVIs were individually tested to determine the antiresonance frequency from 9 to 22 Hertz. Figure 4 gives the results of this testing. It is seen from these results that one DAVI inertia bar weight of 17.5 pounds can be use for the unidirectional inertia bar. Depending upon the antiresonance frequency desired, either 17.5 pounds or 14.0 pounds must be used on the two-dimensional inertia bar.

The upper body of the test vehicle was a simulation of the rotor and transmission weight and inertia of a 6500-pound helicopter. Figure 5 shows a plan and profile view of the simulated rotor and transmission. Included as part of the upper body was the electromagnetic shaker used for the excitation. The two reasons for including the shaker in the upper body were that the shaker weighed 760 pounds and was a major part of the weight of the upper body and it was not necessary to construct a large test structure to support the shaker. Because of the weight of the shaker and the fact that the shaker must be rotated to obtain the proper direction of excitation, a simple design was incorporated in the upper body to float the 760 pound shaker on a cushion of air for in-plane rotation. This design

80

allowed one man to rotate the shaker 90 degrees with no major disassembly required.

The fuselage was then suspended from the simulated rotor and transmission by the three-dimensional DAVI isolation system as shown in Figure 6. Figure 6 also shows the location of the instrumentation. The test vehicle was instrumented with ten accelerometers, three of which were located at approximately the center of gravity of the helicopter to pick up the vertical, lateral and longitudinal accelerations. Three accelerometers were located at station 400 to pick up the vertical, lateral and longitudinal accelerations. Three accelerometers were located at station 50 to pick up the vertical, lateral and longitudinal accelerations. One accelerometer was located at approximately the hub waterline and station to record the upper body acceleration in the direction of excitation.

Figure 4. Variation in Antiresonant Frequency With Position of Inertia Bar Weight

PLAN VIEW

PROFILE VIEW
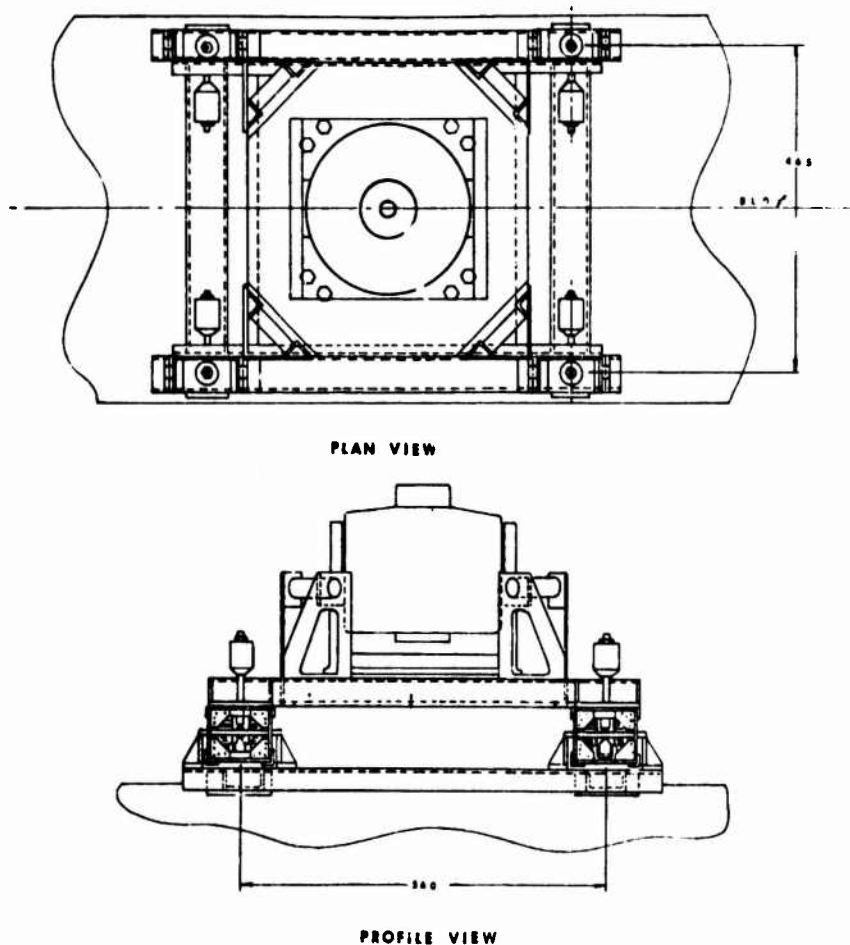
Figure 5. Simulated Rotor and Transmission
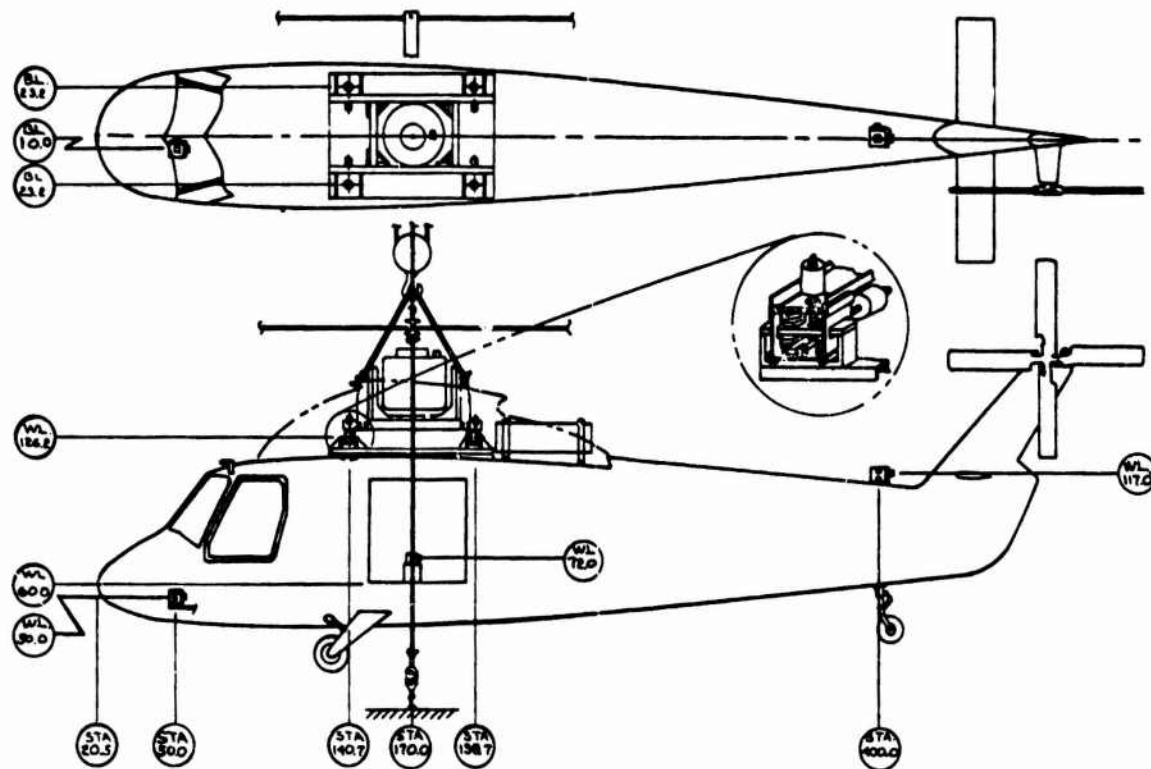
Figure 6. Accelerometer Locations

Twelve linear potentiometers were located across the three-dimensional DAVI mounts. Three potentiometers were used at each mount to measure relative deflection between the upper body (rotor and transmission) and the fuselage in the vertical, lateral and longitudinal directions. A force transducer was installed between the shaker armature and the reaction beam to measure the force output of the electromagnetic shaker.

Test Set-Up and Procedure

The Kaman static test bay was used as the facility to conduct the full-scale experimental tests for rotor isolation. To simulate free-flight conditions, the simulated rotor and transmission was suspended from a 10-ton hoist by a soft bungee chord system. The natural frequencies were low as compared to the excitation frequencies of interest, and therefore, the DAVI isolated aircraft simulated free flight. Figure 7 is a schematic of the suspension system.

Since the electromagnetic shaker is part of the upper body weight, a system was designed to react all of the shaker

excitation forces through tension in standard straps. This system is also shown schematically in Figure 7. The straps run from load reaction beams on the static test frame to smaller reaction beams to which the shaker armature attaches. The reaction straps are tensioned by commercial turnbuckles, and the straps are never allowed to be in compression.

The weight of the small reaction beams is relieved by cable suspension from the frame overhead structure. For vertical excitation, the shaker armature is connected to the vertical reaction beam; for lateral excitation, the shaker is pivoted about its lateral axis and connected to the lateral reaction beam; for fore and aft excitation, the shaker is rotated 90 degrees using the air suspension system and is connected to the fore and aft reaction beam.

Figure 8 shows the test vehicle in the static test bay area.

82
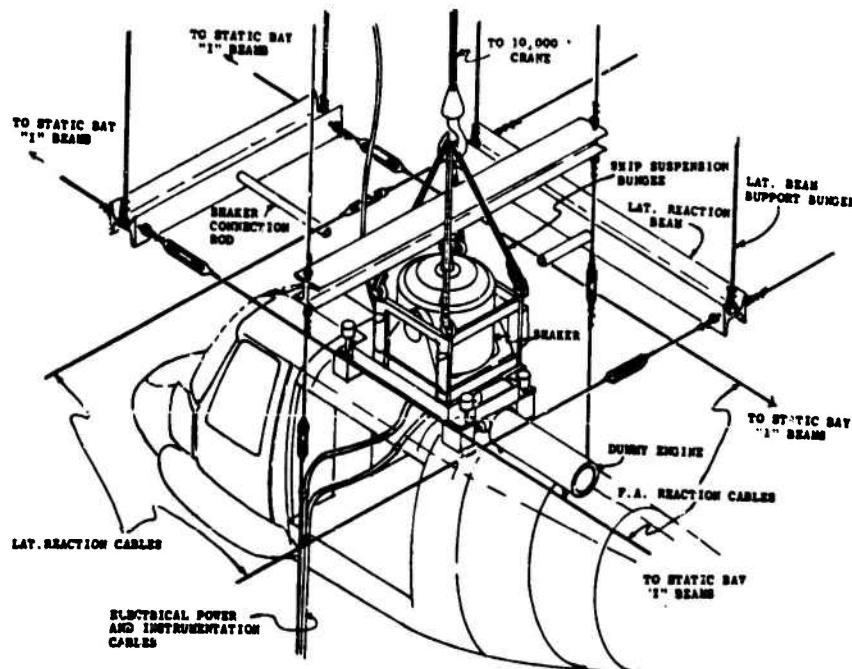
Figure 7. Schematic of the Suspension
and Reaction System
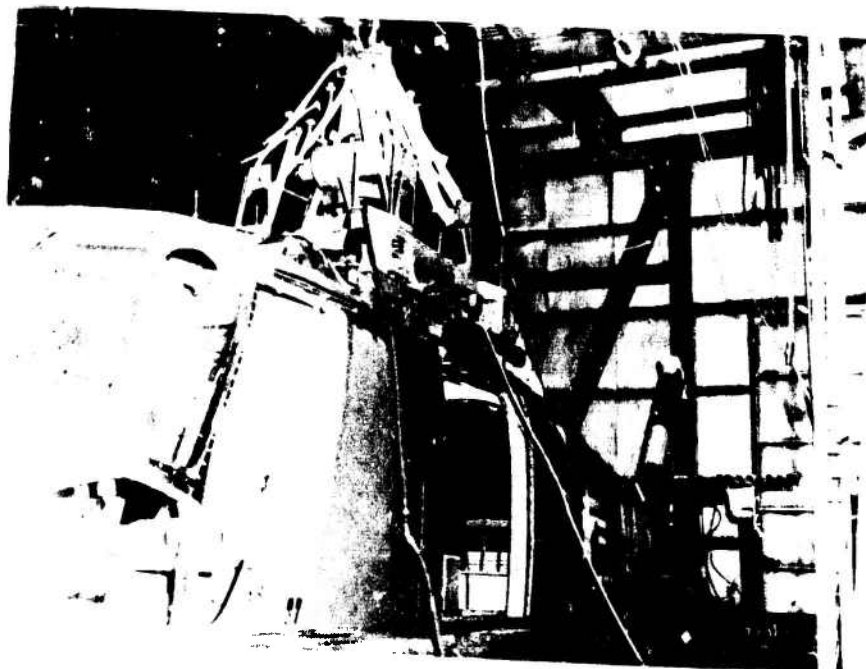
Figure 8. Test Vehicle in the Static Test Bay

Tests were conducted for three directions of vibratory input at the hub on the non-isolated vehicle and then for the isolated vehicle. Tests on the isolated helicopter were conducted for two-bladed, three-bladed, and four-bladed rotor configurations. These rotor configurations were simulated by proper tuning of the DAVI isolation system to the predominant excitation frequency of the rotor system.

The tests were first conducted on the non-isolated vehicle to obtain a base for comparison of results on the isolated vehicle and also to determine a force level in at least one direction of excitation sufficient to produce a minimum of +0.2 g level of acceleration at either the nose (station 50) or the c.g. (station 170) of the helicopter. It was determined that a longitudinal excitation force level of +250 pounds was sufficient to produce the desired acceleration levels at 14.7 Hertz (n/rev of the three-bladed configuration and at 19.8 Hertz (n/rev of the four-bladed configuration). However, at 10.8 Hertz (n/rev of the two-bladed configuration), an excitation force of +500 pounds was required to produce the desired acceleration levels; therefore, two series of non-isolated tests were run: one series up to 45 Hertz at +250 pounds for the three- and four-bladed configurations and one series up to 25 Hertz at +500 pounds for the two-bladed configuration.

Using the excitation force level of +250 pounds, a frequency survey was made on the non-isolated vehicle from 5 Hertz to 45 Hertz in approximately 1-Hertz increments. At the predominant excitation frequencies of 1/rev, n/rev, and 2n/rev and natural frequencies, data at smaller increments were taken. The force level was reduced at frequencies where excessive vibration occurred such as at the natural frequencies. However, for plotting purposes, the data were corrected to a +250-pound excitation force assuming a linear structure and response. This procedure was followed for the +500-pound excitation force except that the vibration survey was made from 5 Hertz to 25 Hertz.

For the isolated vehicle, the DAVI was tuned to the appropriate n/rev frequency, and a vibration survey was made with the same force level. For the four-bladed configuration, the survey was made from 5 Hertz to 45 Hertz; for the three-bladed configuration, the survey was made from 5 Hertz to 35 Hertz; and for the two-bladed configuration, the survey was made from 5 Hertz to 25 Hertz.

Test Results

Figures 9, 10 and 11 show typical time histories of the responses obtained in these tests at the tuned frequency of the DAVI. These figures are the results for the tests made for the simulated three-bladed rotor in which the DAVIs were tuned to 14.7 Hertz.

Figures 9 and 10 show the results for the vertical and longitudinal directions of excitation at the hub. In comparing the results obtained for the non-isolated vehicle to the DAVI isolated vehicle, excellent reduction in vibration is obtained. It is seen that the vibration levels throughout the DAVI isolated fuselage have been reduced. It should be further noted that in Figure 10, a greater magnitude of longitudinal force was used in the DAVI isolation test than in the non-isolated test, so that a greater reduction in vibration level was achieved than is indicated by these responses. It is also seen in these figures that the hub response, although not isolated, is less for the DAVI isolated system than for the non-isolated system.

NON-ISOLATED		DAVI ISOLATION
	INPUT VERTICAL FORCE AT HUB	
	RESPONSE HUB VERTICAL	
	TAIL VERTICAL	
	NOSE VERTICAL	
	CABIN VERTICAL	
	NOSE LATERAL	
	CABIN LATERAL	
	CABIN F & A	
	TAIL LATERAL	
	NOSE F & A	
	TAIL F & A	
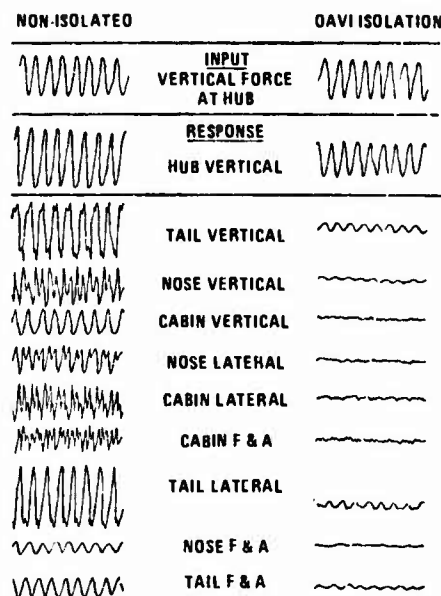
Figure 9.   Time History for Vertical Excitation at Tuned Frequency of the DAVI

84
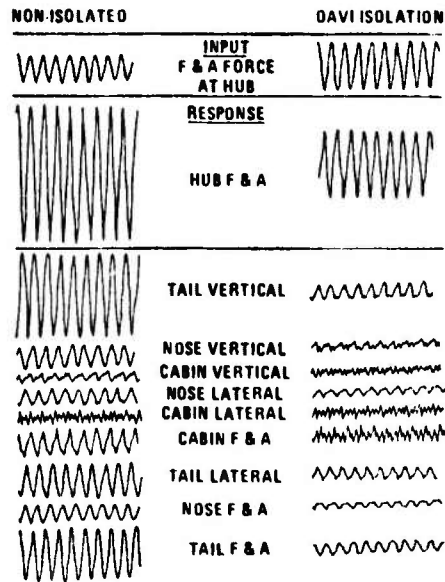
Figure 10. Time History for F&A Excitation at Tuned Frequency of the DAVI
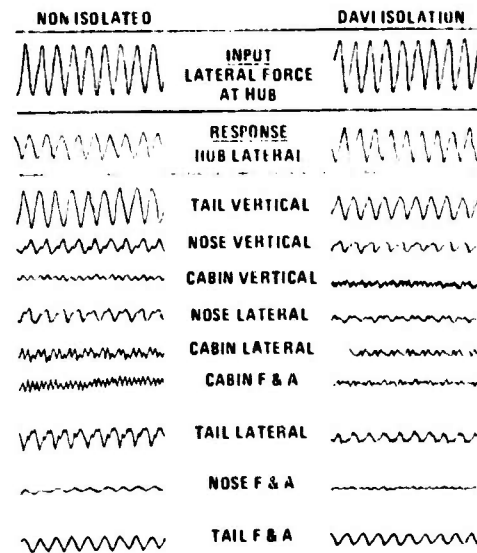
Figure 11. Time History for Lateral Excitation at Tuned Frequency of the DAVI

Figure 11 shows the responses obtained for the lateral direction of excitation. The reduction in vibration in this direction for the DAVI isolated system was not as great as in the other directions of excitation. However, in this direction, vibration levels were low for both the non-isolated and the isolated helicopters. Even at these low vibration levels, isolation was achieved at most locations of the fuselage.

Figure 12 shows the bandwidth obtained over a frequency range from 14 Hertz to 16 Hertz. The solid lines and dashed lines show the response of the non-isolated and DAVI isolated configuration, respectively. These results are for the same magnitude of excitation force at the hub and show the vertical response for a vertical excitation, the lateral response for a lateral excitation and the fore and aft response for a fore and aft excitation. Excellent vibration mitigation was obtained throughout the fuselage and over the entire frequency bandwidth.

Table II shows the average responses of the non-isolated and isolated vehicle at the predominant N/rev of all configurations tested for the nine transducer locations on the fuselage. The average responses were obtained for three levels of vibration on the non-

isolated helicopter; less than $+0.05g$, between $+0.05g$ and $+0.10g$, and greater than $+0.10g$. It is seen from this table that for all levels of vibration, a reduction of vibration occurred for the isolated cases. The isolation system was the most effective at the highest response range for which the lowest transmissibility was obtained. In comparing the average results of the high response range of the non-isolated helicopter to the isolated helicopter for all directions of excitation, it is seen that for the three- and four-bladed configurations, essentially 80 percent isolation was obtained. For the two-bladed rotor configuration, over 50 percent isolation was obtained.

The DAVI system was designed very stiff and the static deflection was less than 0.10 inch. The natural frequencies of the system were all between one-per-rev of the rotor and n-per-rev of the configuration being tested. Therefore little or no amplification occurred at the one-per-rev excitation. Also, because the DAVI system was stiff, the relative deflection between the upper body and lower body was small.

Table III shows the relative deflection obtained in the isolation system for the three rotor configurations tested. The largest relative deflection for the vertical and longitudinal
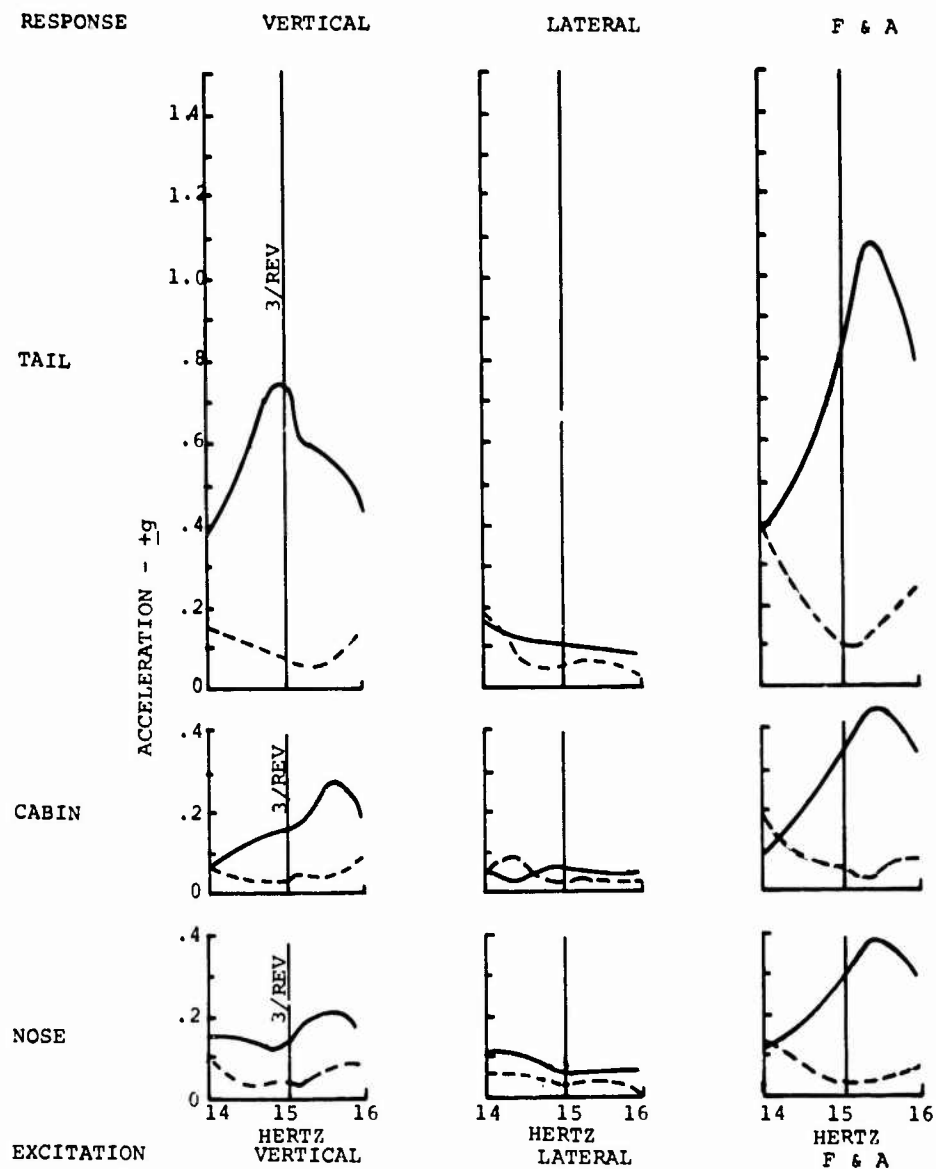
Figure 12.   Bandwidth of the DAVI Isolation System

TABLE II. RANGE OF RESPONSES AT THE PREDOMINANT ROTOR EXCITATION N/REV												

Vertical Excitation

Response Range (±g)	4-Bladed Rotor Avg Response (±g)				3-Bladed Rotor Avg Response (±g)				2-Bladed Rotor Avg Response (±g)			
	N*	Non-Iso	Iso	Tφ	N*	Non-Iso	Iso	Tφ	N*	Non-Iso	Iso	Tφ
<.05	0	-	-	-	0	-	-	-	3	.026	.025	.95
.05-.10	3	.0773	.016	.21	3	.086	.019	.22	5	.0596	.0404	.68
>.10	6	.253	.022	.09	6	.335	.040	.12	1	.152	.064	.42

Longitudinal Excitation

	N*	Non-Iso	Iso	Tφ	N*	Non-Iso	Iso	Tφ	N*	Non-Iso	Iso	Tφ
<.05	3	.0327	.02	.61	0	-	-	-	3	.039	.023	.60
.05-.10	0	-	-	-	2	.066	.0385	.57	2	.061	.030	.50
>.10	6	.1948	.0418	.21	7	.4889	.0993	.20	4	.262	.137	.52

Lateral Excitation

	N*	Non-Iso	Iso	Tφ	N*	Non-Iso	Iso	Tφ	N*	Non-Iso	Iso	Tφ
<.05	1	.029	.010	.34	3	.02	.021	1.05	4	.026	.019	.731
.05-.10	7	.0601	.035	.58	4	.0803	.0507	.63	3	.0827	.068	.82
>.10	1	.161	.064	.40	2	.1865	.1335	.71	2	.1165	.026	.22

All Directions of Excitation

	N*	Non-Iso	Iso	Tφ	N*	Non-Iso	Iso	Tφ	N*	Non-Iso	Iso	Tφ
>.10	13	.2191	.0344	.16	15	.3870	.0801	.21	7	.2047	.0949	.46

*N - Number of recordings of nonisolated response in each response range listed
in column one. (Total number of recording cannot exceed nine.)
φT - Transmissibility; ratio isolated/nonisolated response.

TABLE III. VERTICAL RELATIVE DEFLECTION IN THE DAVI ISOLATION SYSTEM FOR THE PREDOMINANT EXCITATION FREQUENCY			

Vertical Excitation

DAVI Location	Relative Deflection (±in.)		
	4-Bladed Rotor	3-Bladed Rotor	2-Bladed Rotor
Left Fwd	.0068	.0121	.0171
Right Fwd	.0083	.0162	.0094
Right Aft	.0006	.0106	.0212
Left Aft	.0077	.0156	.0040

Longitudinal Excitation

Left Fwd	.0072	.0156	.0125
Right Fwd	.0042	.0131	.0320
Right Aft	.0006	.0078	.0264
Left Aft	.0040	.0210	.0026

Lateral Excitation

Left Fwd	.0150	.0120	.0081
Right Fwd	.0110	.0076	.0069
Right Aft	.0084	.0046	.0036
Left Aft	.0114	.0056	.0034

directions of excitation were +.0212 inch and +.0320 inch, respectively. These deflections are well within the design limits of present-day couplings.

Weight

The objective of this program was to demonstrate the feasibility of rotor isolation using the DAVI concept. For this test program, a three-dimensional DAVI isolation system incorporating four DAVIs of a single size suitable for installation in either a 6500-pound or 10,000-pound helicopter was designed. Isolator parameters were not optimized for either gross weight or any one rotor configuration. Consequently, optimization for performance or minimum weight was not attempted.

The four DAVIs used in this program neglecting the weight of the movable weights on the inertia bar rods, weighed a total of 136 pounds or 1.36 percent of the gross weight of a 10,000-pound helicopter. For the four-bladed configuration tested, the weight of the movable weights on the inertia bar rods of each DAVI was a total of 17.5 pounds. Thus, the total system weighed 2.06 percent of the gross weight of a 10,000-pound helicopter. Therefore, for a 10,000-pound helicopter with design refinements can be designed for less than 2 percent of the gross weight.

CONCLUSIONS

This full-scale experimental study has demonstrated that rotor isolation is feasible using the passive DAVI isolation system.

1. Rotor isolation with the Kaman DAVI is feasible.

2. Vibration levels at the n-per-rev excitation frequency can be reduced to one-fifth to one-tenth the present values encountered.

3. Rotor isolation is feasible with 0.10-inch or less static deflection in the helicopter isolation system.

4. Rotor isolation can be achieved with a very stiff system without adversely affecting the one-per-rev characteristics.

5. Reduction of vibration can be achieved throughout the complete fuselage structure.

6. A rotor isolation system can be designed for 2 percent or less of the gross weight and with normal structural stiffness design.

7. The natural frequencies of the system can be designed to be above one-per-rev, and therefore the possibility of mechanical instability occurring in flight is eliminated.

8. The vibratory relative deflection within the isolation system is small and within the conventional coupling and shaft design limitations now in use.

9. Rotor isolation will not necessarily increase the vibratory levels on the upper body or rotor.

REFERENCES

1. C.E. Theobald, Jr., and R. Jones, "Isolation of Helicopter Rotor Vibratory Forces From the Fuselage", Wright Air Development Center Tech. Rept. 57-404, Sept. 1957.

2. C.E. Crede, and R.D. Cavanaugh, Barry Controls, and H.N. Abramson, Southwest Research Inst., "Feasibility Study of an Active Vibration Isolator for a Helicopter Rotor" Wright Air Development Center Tech. Rept. 58-163, 1958.

3. L.E. Smollen, P. Marshall, and R. Gabel, "A Servo Controlled Rotor Vibration Isolation System for the Reduction of Helicopter Vibration", IAS Paper No. 62-34, Jan. 1962.

4. P.C. Calcaterra, and D.W. Schubert, "Isolation of Helicopter Rotor-Induced Vibrations Using Active Elements", USAAVLABS Tech. Rept. 69-8, June 1969.

5. E.P. Schuett, "Passive Helicopter Isolation Using the Kaman Dynamic Antiresonant Vibration Isolator (DAVI)", USAAVLABS Tech. Rept. 68-46, Dec. 1968.

6. R.C. Anderson, and M.F. Smith, "A Study of the Kaman Dynamic Antiresonant Vibration Isolator (DAVI)", USAAVLABS Tech. Rept. 65-75, Jan. 1966.

7. R. Jones, "An Analytical and Model Test Research Study on the Kaman Dynamic Antiresonant Vibration Isolator (DAVI)", USAAVLABS Tech. Rept. 68-42, Nov. 1968.

8. R. Jones, "Flight Test Results of a DAVI Isolated Platform", USAAVLABS Tech. Rept. 70-57, Nov. 1970.

DISCUSSION

Mr. Allen (Lord Kinematics): Do you have any feeling as to whether the energy in the hub is going to increase? Is it going to be effected by the isolation system?

Mr. Jones: Its going to be effected. Whether it's going to be adversely or beneficially effected is difficult to answer. If I do a rigid body analysis on the system, there is no doubt that I will get increased hub motions over a non-isolated vehicle. However, if we involve structural dynamics of the system, and that is what we had here, we get less hub motion in some areas and greater motion in others. I personally don't think that it's going to be a detrimental effect because many helicopters today use rotor isolation. Bell Helicopter, for example, always isolate theirs for in-plane, so they have a lot of hub motion. We can't say that their helicopters are poor from the aspect of having rotor isolation and low hub impedance in the in-plane direction.

Mr. Henks (NASA Langley Research Center): What was the resonant frequency of the reaction beams that you drove your shaker against?

Mr. Jones: I really can't answer that. They didn't seem to affect the results. I will say that many times the building seemed to be shaking quite a bit, if you went to look at that aspect.

Mr. Henks: I was just wondering if they might be considered something like a rotor mass also.

Mr. Jones: Of course, we were measuring the force between the reaction system and what was being introduced to the system and we were correcting from that force. Having measured the force, I think we should be getting the correct impedance.

DECOUPLING THE THREE TRANSLATIONAL MODES FROM THE THREE ROTATIONAL MODES OF A RIGID BODY SUPPORTED BY FOUR CORNER-LOCATED ISOLATORS

Thomas F. Derby
BARRY DIVISION
Barry Wright Corporation
Watertown, Massachusetts

This paper presents the condition for decoupling translation from rotation for a configuration in which the isolators are located at the corners of a rectangle in a horizontal plane. The center of gravity of the equipment is located arbitrarily with respect to the center of the rectangular pattern of the isolators. A computer program is presented that obtains the orientation of the isolators necessary for decoupling as well as the decoupled natural frequencies. For the special case where the C.G. is above the center of the isolator's rectangular pattern, the same results are presented graphically by a wide range of parameter values.

NOMENCLATURE

Scalers

$A \quad = \quad a/c$

$a \quad = \quad$ distance (See Figure 1)

$B \quad = \quad b/c$

$b \quad = \quad$ distance (See Figure 1)

$C_{\varphi_i}, C_{\theta_i}, C_{\gamma_i} =$ Cosine of φ_i, θ_i, and γ_i, respectively

$c \quad = \quad$ distance (See Figure 1)

$D \quad = \quad d/c$

$d \quad = \quad$ distance (See Figure 1)

$E \quad = \quad e/c$

$e \quad = \quad$ distance (See Figure 1)

$f_i (i = 1$ to $3) =$ natural frequency in X_i direction

$f_a \quad = \quad \sqrt{4k_a/m} \ /2\pi =$ fictitious natural frequency of the mass on four isolators in the axial direction

$k_a \quad = \quad$ axial stiffness of an isolator

$k_r \quad = \quad$ radial stiffness of an isolator

$m \quad = \quad$ mass of rigid body

$p \quad = \quad$ constant of proportionality between damping and stiffness matrices

$S_i (i = 1$ to $16) =$ summations (See Eqs. 52 to (67)

$S_{\varphi_i}, S_{\theta_i}, S_{\gamma_i} =$ Sine of φ_i, θ_i, and γ_i, respectively

$T_\theta, T_\gamma =$ tangent of θ and γ, respectively

$\gamma_i (i = 1$ to $4) =$ angles (See Figure 1)

91

γ = γ_i (i = 1 to 4) when all angles are equal

φ_i (i = 1 to 4) = angles (See Figure 3)

θ_i (i = 1 to 4) = angles (See Figure 1)

θ = θ_i (i = 1 to 4) when all angles are equal

υ = $(f_n/f_a)^2$

σ = k_a/k_r

ω_n = natural frequency (rad/sec)

ω_a = $2\pi f_a$ (rad/sec)

Vectors and Matrices

$\{\ \}$ = 3 x 1 column vector

$[\ ]$ = 3 x 3 matrix

$[\ ]_i$ = matrix pertaining to ith isolator

$\left[\begin{array}{c|c} & \\ \hline & \end{array}\right]$ = partitioned matrix having 3 x 3 submatrices

$[\ ]^T$ = transpose of matrix

$[\ ]^{-1}$ = inverse of matrix

$[O]$ = null matrix (all the elements are zero)

$[A]$ = $1/4k_a[K]$ (See Eq. 74)

$[C]_i$ = inertial frame axis damping matrix for ith isolator

$[c]_i$ = principal axis damping matrix for ith isolator

$\{F\}$ = externally applied force

$[I]$ = mass moment of inertia matrix

$[K]$ = $\Sigma [K]_i$

$[K]_i$ = inertial frame axis stiffness matrix for ith isolator

$[k]_i$ = principle axis stiffness matrix for ith isolator

$[m]$ = mass matrix

$[P]$ = $\Sigma [R]_i [C]_i$

$[Q]$ = $\Sigma [R]_i [K]_i$

$[Q']$ = $\dfrac{1}{c(k_a - k_r)} [Q]$

$[R]_i$ = skew symmetric matrix corresponding to $\{r\}_i$

$\{r\}_i$ = position vector of the ith isolator

$\{T\}$ = externally applied torques

$[U]$ = unit matrix

$[V]$ = $\Sigma [R]_i [C]_i [R]_i^T$

$[W]$ = $\Sigma [R]_i [K]_i [R]_i^T$

$\{x\}$ = inertial frame coordinates; displacement vector of C.G. of the mass

$\{y\}$ = displacement vector of supporting structure

$\{\alpha\}$ = rotation vector for small motions about the C.G. of the mass

$\{\beta\}$ = rotation vector for small motions of the supporting structure

$\{\delta\}_i$ = displacement vector of the ith isolator

$\{\xi\}_i$ = principle axis coordinates for the ith isolator

$[\lambda]_i$ = transformation matrix of the ith isolator

INTRODUCTION AND SUMMARY

Inclined isolators have been used for many years to decouple translational from rotational motions of a piece of equipment supported by isolators. However, there are only two configurations adequately presented in the literature. In one configuration, decoupling is accomplished in a plane where the isolators are symmetrically located on each side of the center of gravity. In this situation only two of the translational motions are decoupled. In the

other configuration, the isolators are located symmetrically about a ring and the center of gravity of the equipment is assumed to be above the center of the ring. For these two configurations, the conditions necessary for decoupling as well as the decoupled natural frequencies are given in Reference 1. This paper presents the conditions for decoupling translation from rotation for a configuration in which the isolators are located at the corners of a rectangle in a horizontal plane. The center of gravity of the equipment is located arbitrarily with respect to the center of the rectangular pattern of the isolators (See Figure 1).
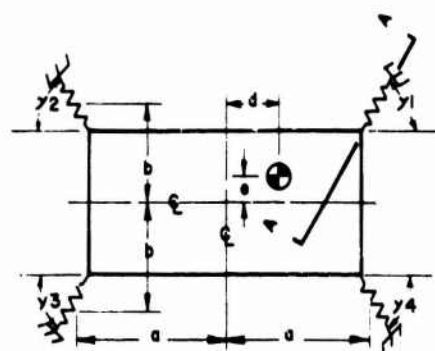
PLAN VIEW
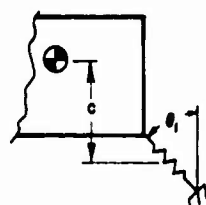
SECTION A-A

Figure 1: Schematic diagram showing isolator configuration

In the first part of the paper, the matrix formulation of the equations of motion are derived. By inspection of the matrix equations, it is quite apparent what the conditions for decoupling are. In order to simplify the decoupling conditions, it is assumed that the damping matrix is proportional to the stiffness matrix. This is a fairly common method used to represent damping, however, it is pointed out that it is probably not a very realistic representation of damping for elastomeric isolators. From the matrix formulation, a set of eight simultaneous scaler equations are derived as the conditions for decoupling translation from rotation. These equations, written in terms of each isolator's location with respect to the C.G. and it's three principal stiffnesses, are general and apply to

any number of different isolators in any arbitrary configuration.

The eight equations to be satisfied for decoupling are written for the particular configuration shown in Figure 1. For this situation it is also assumed that each of the four isolators has identical stiffness properties and that the two radial stiffnesses of an isolator are equal (i.e., when the isolator is not inclined its two horizontal stiffnesses are both equal to the radial stiffness k_r and its vertical stiffness is equal to the axial stiffness k_a). The equations for the decoupling condition are written in terms of the parameters a/b, c/b, d/a, e/b, k_a/k_r, γ_1, γ_2, γ_3, γ_4, θ_1, θ_2, θ_3, θ_4. The assumption of having identical isolators is based on the fact that it is easier to obtain identical isolators of given properties than it is to specify precisely what the properties of each isolator must be. The assumption of equal radial stiffnesses was made for two reasons: (1) to reduce the number of parameters in the study, and (2) it is quite common in practice. For a given geometry (i.e. a/b, c/b, d/a, and e/b) and a given stiffness ratio k_a/k_r, the eight equations are solved for the eight angles (i.e. γ and θ for each isolator). The angles γ and θ are essentially the Euler angles representing the orientation of the isolator. The third Euler angle is not necessary due to the assumption of having equal radial stiffnesses. Since the equations to be solved are a set of eight simultaneous transcendental equations, they are solved by digital computer using the Newton-Raphson method.

The computer program written in FORTRAN IV for General Electric Time Sharing Service, is presented along with a description of how to use it. Some results obtained from this program are presented in tabular form. Due to the large numbers of parameters, a complete graphical presentation covering reasonable ranges of all the parameters was beyond the scope of this paper. Besides determining the eight angles, the program also computes the three translational natural frequencies and their mode shapes. It is pointed out that the translational modes are decoupled from the rotational but not from each other.

Finally, it is assumed that the C.G. is located above the center of the rectangular pattern of the isolators (i.e. $d = e = 0$). For this configuration the assumption that all the γ's are equal and all the θ's are equal, results in reducing the eight equations to two equations and the number of parameters is reduced to five (i.e. a/b, c/b, k_a/k_r, γ, and θ). A complete graphical presentation is made for this situation including the three translational natural frequencies which are decoupled from each other as well as from the rotational frequencies.

93

MATRIX FORMULATION OF EQUATIONS OF MOTION

This section derives the equation of motion for a rigid body supported by isolators. The geometrical relationship of a single isolator to the center of mass of the rigid body is shown in Figure 2. The isolator is shown as a cylinder and it is assumed that the top surface is attached to the rigid body and the bottom to a supporting structure. It is assumed that the isolator is represented by three mutually perpendicular sets of a linear spring and viscous damper in parallel so that a stiffness and damping matrix in relation to the isolator's coordinates can be written as

$$[k]_i = \begin{bmatrix} k_1 & 0 & 0 \\ 0 & k_2 & 0 \\ 0 & 0 & k_3 \end{bmatrix}_i \qquad (1)$$

$$[c]_i = \begin{bmatrix} c_1 & 0 & 0 \\ 0 & c_2 & 0 \\ 0 & 0 & c_3 \end{bmatrix}_i \qquad (2)$$

The subscript i stands for the ith isolator. In order to represent the isolator stiffness and damping matrices in the inertial frame coordinates, these matrices are transformed using the transformation matrix relating the two coordinate systems (Ref. 2)

$$[\lambda]_i = \begin{bmatrix} \lambda_{11} & \lambda_{12} & \lambda_{13} \\ \lambda_{21} & \lambda_{22} & \lambda_{23} \\ \lambda_{31} & \lambda_{32} & \lambda_{33} \end{bmatrix}_i \qquad (3)$$

where an element λ_{ij} is the cosine of the angle between x_i and ξ_j. The transformed stiffness and damping matrices are

$$[K]_i = [\lambda]_i [k]_i [\lambda]_i^T \qquad (4)$$

$$[C]_i = [\lambda]_i [c]_i [\lambda]_i^T \qquad (5)$$

The position vector of the ith isolator's center of elasticity is given in terms of inertial frame coordinates as

$$\{r\}_i = \begin{Bmatrix} r_1 \\ r_2 \\ r_3 \end{Bmatrix}_i \qquad (6)$$
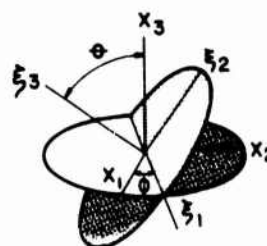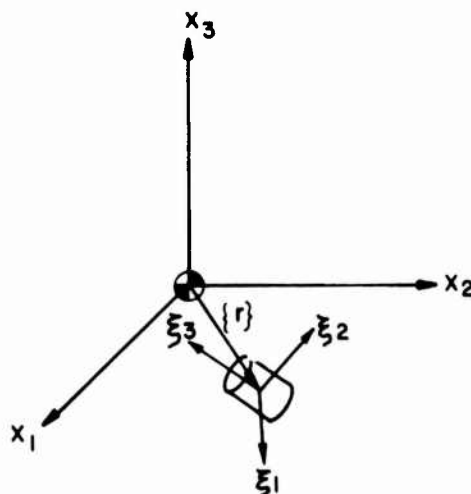
Figure 2: Relation of isolator to the inertial frame coordinates

and has a corresponding skew symmetric matrix defined as

$$[R]_i = \begin{bmatrix} 0 & r_3 & r_2 \\ r_3 & 0 & -r_1 \\ -r_2 & r_1 & 0 \end{bmatrix}_i \qquad (7)$$

The isolator deflection for small motions is related to the rigid body motion and supporting structure motion according to

$$\{\delta\}_i = \{x\} - \{y\} - [R]_i(\{\alpha\} - \{\beta\}) \qquad (8)$$

Where $\{x\}$ and $\{y\}$ are vectors representing translation of the rigid body and supporting structure, respectively, and $\{\alpha\}$ and $\{\beta\}$ are vectors representing small rotations of the

94

rigid body and supporting structure, respectively.

Letting $\{F\}$ and $\{T\}$ represent an externally applied force and torque, respectively, the rigid body equations of motion can be written as

$$[m]\{\ddot{x}\} = \sum_{i=1}^{n} \left[-[K]_i \{\delta\}_i - [C]_i \{\dot{\delta}\}_i \right] + \{F\} \tag{9}$$

$$[I]\{\ddot{\alpha}\} = \sum_{i=1}^{n} \left[[R]_i \left\{ -[K]_i \{\delta\}_i - [C]_i \{\dot{\delta}\}_i \right\} \right] + \{T\} \tag{10}$$

A dot over a variable indicates the first derivative with respect to time and two dots indicate the second derivative. The mass matrix is defined as

$$[m] = \begin{bmatrix} m & 0 & 0 \\ 0 & m & 0 \\ 0 & 0 & m \end{bmatrix} \tag{11}$$

where m is the mass of the rigid body and the inertia matrix is defined as

$$I = \begin{bmatrix} I_{11} & I_{12} & I_{13} \\ I_{21} & I_{22} & I_{23} \\ I_{31} & I_{32} & I_{33} \end{bmatrix} \tag{12}$$

where I_{ij} are the moments and products of inertia of the rigid body. The summation is taken over all the isolators where the total number of isolators is n.

Since the vector $\{\delta\}$ depends on both $\{x\}$ and $\{\alpha\}$, Eqs. (9) and (10) are coupled. These two equations can be written in partitioned matrix form. Noting that

$$[C]_i^T = [C]_i \tag{13}$$

$$[K]_i^T = [K]_i \tag{14}$$

$$[R]_i^T = -[R]_i \tag{15}$$

and using the following definitions

$$[C] \triangleq \sum_{i=1}^{n} [C]_i \tag{16}$$

$$[K] \triangleq \sum_{i=1}^{n} [K]_i \tag{17}$$

$$[P] \triangleq \sum_{i=1}^{n} [R]_i [C]_i \tag{18}$$

$$[Q] \triangleq \sum_{i=1}^{n} [R]_i [K]_i \tag{19}$$

$$[V] \triangleq \sum_{i=1}^{n} [R]_i [C]_i [R]_i^T \tag{20}$$

$$[W] \triangleq \sum_{i=1}^{n} [R]_i [K]_i [R]_i^T \tag{21}$$

the equations of motion (Eqs. (9) and (10)) can be written in partitioned matrix form as follows

$$\begin{bmatrix} [m] & [0] \\ [0] & [I] \end{bmatrix} \begin{Bmatrix} \{\ddot{x}\} \\ \{\ddot{\alpha}\} \end{Bmatrix} + \begin{bmatrix} [C] & [P]^T \\ [P] & [V] \end{bmatrix} \begin{Bmatrix} \{\dot{x}\} \\ \{\dot{\alpha}\} \end{Bmatrix}$$

$$+ \begin{bmatrix} [K] & [Q]^T \\ [Q] & [W] \end{bmatrix} \begin{Bmatrix} \{x\} \\ \{\alpha\} \end{Bmatrix} = \begin{bmatrix} [C] & [P]^T \\ [P] & [V] \end{bmatrix} \begin{Bmatrix} \{\dot{y}\} \\ \{\dot{\beta}\} \end{Bmatrix}$$

$$+ \begin{bmatrix} [K] & [Q]^T \\ [Q] & [W] \end{bmatrix} \begin{Bmatrix} \{y\} \\ \{\beta\} \end{Bmatrix} + \begin{Bmatrix} \{F\} \\ \{T\} \end{Bmatrix} \tag{22}$$

Eq. (22) is a general equation of motion for a rigid body supported by linear isolators and subjected to supporting structure motion and externally applied forces and moments.

CONDITIONS FOR DECOUPLING TRANSLATION FROM ROTATION

Referring to Eq. (22), if the matrices

$$[P] = [Q] = [0] \tag{23}$$

then all of the off-diagonal matrices of the partitioned matrices are null matrices. In this case, Eq. (22) can be written as two independent matrix equations as follows

$$[m]\{\ddot{x}\} + [C]\{\dot{x}\} + [K]\{x\} = [C]\{\dot{y}\} + [K]\{y\} + \{F\} \tag{24}$$

$$[I]\{\ddot{\delta}\} + [V]\{\dot{\delta}\} + [W]\{\delta\} = [V]\{\dot{\beta}\} + [W]\{\beta\} + \{T\} \tag{25}$$

A translation of the supporting structure, $\{y\}$, or a force acting through the center of mass, $\{F\}$, causes translation, $\{x\}$, but no rotation $\{\alpha\}$, of the rigid body. A rotation of the supporting structure, $\{\beta\}$, or a torque acting on the rigid body, $\{T\}$, causes rotation but no translation of the rigid body. Also, during free vibration, the translational motions x_1, x_2, and x_3 occur independently of the rotational motions α_1, α_2, and α_3.

If, for each isolator, the damping matrix can be expressed as

$$[c]_i = p[k]_i \qquad (26)$$

where p is a given constant for all the isolators, then

$$[C] = p[K] \qquad (27)$$

and

$$[P] = p[Q] \qquad (28)$$

In any case, if Eq. (28) is satisfied, the condition for decoupling translation from rotation is

$$[Q] = \sum_{i=1}^{n} [R]_i [K]_i = [0] \qquad (29)$$

Performing the matrix multiplication results in

$$\sum_{i=1}^{n} \begin{bmatrix} r_2 K_{31} - r_3 K_{21} & r_2 K_{32} - r_3 K_{22} & r_2 K_{33} - r_3 K_{23} \\ r_3 K_{11} - r_1 K_{31} & r_3 K_{12} - r_1 K_{32} & r_3 K_{13} - r_1 K_{33} \\ r_1 K_{21} - r_2 K_{11} & r_1 K_{22} - r_2 K_{12} & r_1 K_{23} - r_2 K_{13} \end{bmatrix}_i = [0]$$

$$(30)$$

Note that $Q_{11} + Q_{22} + Q_{33} = 0$ since $K_{ij} = K_{ji}$. Therefore, there are only eight independent equations to be satisfied. Eq. (30) was derived as the condition for decoupling under the assumption that the damping matrix is proportional to the stiffness matrix. In general, a set of second order differential equations can be written as

$$[M]\{\ddot{z}\} + [C]\{\dot{z}\} + [K]\{z\} = \{f\} \qquad (31)$$

Assuming Eq. (27) applies, this set of equations can be decoupled and written as a set of independent equations in terms of normal coordinates. The form of each of the equations is

$$M_n \ddot{Q}_n + pk_n \dot{Q}_n + k_n Q_n = F_n \qquad (32)$$

where the subscript n stands for the nth normal mode. The undamped natural frequency and fraction of critical damping associated with this equation are

$$\omega_n = \sqrt{\frac{k_n}{M_n}} \qquad (33)$$

and

$$\zeta_n = \frac{P\omega_n}{2} \qquad (34)$$

In this case, the fraction of critical damping is higher for the higher natural mode frequencies. However, this is at variance with what is commonly observed for elastomeric isolators Although in practice, it may not be precise to assume damping proportional to stiffness, this assumption is made here and Eq. (30) is taken as the condition for decoupling. (See Refs. 3 through 6 for a discussion of damping assumptions).

In order to obtain specific results, further assumptions are necessary. First it is assumed that each isolator has its k_1 and k_2 stiffness equal

$$[k]_i = \begin{bmatrix} k_r & 0 & 0 \\ 0 & k_r & 0 \\ 0 & 0 & k_a \end{bmatrix}_i \qquad (35)$$

With this assumption, the transformation matrix $[\lambda]_i$ can be written in terms of the Euler Angles φ and θ as shown in Figure 2 (Ref. 2). The third Euler angle is not necessary due to the symmetry assumed about the ξ_3 axis according to Eq. (35). Using the notation $C_\varphi = \cos(\varphi)$, $S_\varphi = \sin(\varphi)$, $C_\theta = \cos(\theta)$, and $S_\theta = \sin(\theta)$

$$[\lambda]_i = \begin{bmatrix} C_\varphi & -C_\theta S_\varphi & S_\varphi S_\theta \\ S_\varphi & C_\varphi C_\theta & -C_\varphi S_\theta \\ 0 & S_\theta & C_\theta \end{bmatrix}_i \qquad (36)$$

Combining Eqs. (4), (35), and (36), the transformed stiffness matrix for the ith isolator is

96

$$[K]_1 = \begin{bmatrix} k_r + S_\omega^2 S_\theta^2 (k_a - k_r) & -C_\omega S_\omega S_\theta^2 (k_a - k_r) & S_\omega C_\theta S_\theta (k_a - k_r) \\ -C_\omega S_\omega S_\theta^2 (k_a - k_r) & k_r + C_\omega^2 C_\theta^2 (k_a - k_r) & -C_\omega C_\theta S_\theta (k_a - k_r) \\ S_\omega C_\theta S_\theta (k_a - k_r) & -C_\omega C_\theta S_\theta (k_a - k_r) & k_r + C_\theta^2 (k_a - k_r) \end{bmatrix}_1 \qquad (37)$$

For the particular case depicted in Figure 1, the position vectors for each of the four isolators are given in Table I below.

TABLE I

Isolator	(1)	(2)	(3)	(4)
r_1	a-d	-a-d	-a-d	a-d
r_2	b-e	b-e	-b-e	-b-e
r_3	-c	-c	-c	-c

The angles γ_i shown in Figure 1 are related to the Euler angles ω_i as shown in Figure 3.
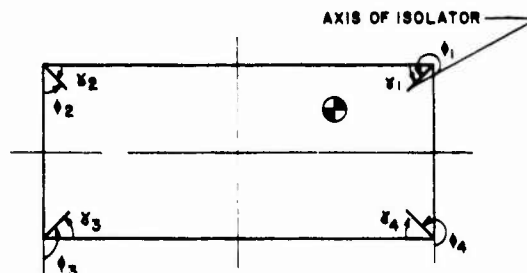
Figure 3: Relationship between γ and ω .

The angles γ_i are more convenient to use, since for the particular case where the center of mass of the rigid body is centered above the mount pattern (i.e. d = e = 0), setting all of the γ_i's equal results in a symmetrical arrangement. The two angles determining the orientation of each of the four isolators comprise eight unknowns to be solved for. Setting each element of the Q matrix, except Q_{33}, equal to zero comprises eight equations to be solved.

It is further assumed that each isolator is identical, except for its orientation, so that k_a and k_r are the same for each isolator. In this case, the $Q_{ij} = 0$ equations can be non-dimensionalized by defining

$$Q'_{ij} = \frac{Q_{ij}}{c(k_a - k_r)} \qquad (38)$$

$$\sigma = k_a/k_r \qquad (39)$$

$$A = a/c \qquad (40)$$

$$B = b/c \qquad (41)$$

$$D = d/c \qquad (42)$$

$$E = e/c \qquad (43)$$

The eight equations obtained from Eq. (30) using Eq. (37), Table I, and Figure 3 are given as

$$Q'_{11} = BS_1 - ES_2 - S_3 = 0 \qquad (44)$$

97

$$Q'_{12} = BS_4 - ES_5 - S_6 - \frac{4}{\sigma - 1} = 0 \qquad (45)$$

$$Q'_{13} = BS_7 - ES_8 - S_5 - \frac{4E}{\sigma - 1} = 0 \qquad (46)$$

$$Q'_{21} = AS_9 - DS_2 - S_{10} - \frac{4}{\sigma - 1} = 0 \qquad (47)$$

$$Q'_{22} = AS_{11} - DS_5 - S_3 = 0 \qquad (48)$$

$$Q'_{23} = AS_{12} - DS_8 - S_2 - \frac{4D}{\sigma - 1} = 0 \qquad (49)$$

$$Q'_{31} = BS_{13} - ES_{10} - AS_{14} + DS_3 - \frac{4E}{\sigma - 1} = 0 \qquad (50)$$

$$Q'_{32} = AS_{15} - DS_6 - BS_{15} + ES_3 - \frac{4D}{\sigma - 1} = 0 \qquad (51)$$

where the summations S_i are given as

$$S_1 = \sum_{24} C_{\gamma_i} C_{\theta_i} S_{\theta_i} \qquad (52)$$

$$S_2 = \sum_{23} C_{\gamma_i} C_{\theta_i} S_{\theta_i} \qquad (53)$$

$$S_3 = \sum_{24} C_{\gamma_i} S_{\gamma_i} S_{\theta_i}^2 \qquad (54)$$

$$S_4 = \sum S_{\gamma_i} C_{\theta_i} S_{\theta_i} \qquad (55)$$

$$S_5 = \sum_{34} S_{\gamma_i} C_{\theta_i} S_{\theta_i} \qquad (56)$$

$$S_6 = \sum S_{\gamma_i}^2 S_{\theta_i}^2 \qquad (57)$$

$$S_7 = \sum_{34} C_{\theta_i}^2 \qquad (58)$$

$$S_8 = \sum C_{\theta_i}^2 \qquad (59)$$

$$S_9 = \sum C_{\gamma_i} C_{\theta_i} S_{\theta_i} \qquad (60)$$

$$S_{10} = \sum C_{\gamma_i}^2 S_{\theta_i}^2 \qquad (61)$$

$$S_{11} = \sum_{24} S_{\gamma_i} C_{\theta_i} S_{\theta_i} \qquad (62)$$

$$S_{12} = \sum_{23} C_{\theta_i}^2 \qquad (63)$$

$$S_{13} = \sum_{34} C_{\gamma_i}^2 S_{\theta_i}^2 \qquad (64)$$

$$S_{14} = \sum_{34} C_{\gamma_i} S_{\gamma_i} S_{\theta_i}^2 \qquad (65)$$

$$S_{15} = \sum_{23} C_{\gamma_i} S_{\gamma_i} S_{\theta_i}^2 \qquad (66)$$

$$S_{16} = \sum_{23} S_{\gamma_i}^2 S_{\theta_i}^2 \qquad (67)$$

The summations are taken over the four isolators and the notation $\sum_{ij}$ indicates that terms i and j are negative (e.g. $\sum_{23} q_i = q_1 - q_2 - q_3 + q_4$). Eqs. (44) through (51) are solved by the Newton-Raphson method using a digital computer. The computer program is described in the next section.

The translational undamped natural frequencies, ω_n, are determined from Eq. (24) with the right hand side and the C matrix set to zero

$$[m]\{\ddot{x}\} + [K]\{x\} = 0 \qquad (68)$$

The K matrix is obtained by summing Eq. (37) for the four isolators. Using the definitions of the summations given by Eqs. (52) through (67) the K matrix can be written as

$$[K] = k_r \begin{bmatrix} 4 + S_{10}(\sigma-1) & S_3(\sigma-1) & -S_2(\sigma-1) \\ S_3(\sigma-1) & 4 + S_6(\sigma-1) & -S_5(\sigma-1) \\ -S_2(\sigma-1) & -S_5(\sigma-1) & 4 + S_8(\sigma-1) \end{bmatrix} \qquad (69)$$

The m matrix is just the mass m times the identity matrix. During free vibration of the nth mode, the acceleration is related to the displacement according to

$$\ddot{x} = -\omega_n^2 x \qquad (70)$$

where ω_n is the natural frequency in radians/second. In order to nondimensionalize equation (68), define

$$\omega_a^2 \overset{\Delta}{=} \frac{4k_a}{m} \qquad (71)$$

as the fictitious circular natural frequency. Thus

$$\nu \overset{\Delta}{=} \left(\frac{\omega_n}{\omega_a}\right)^2 = \left(\frac{f_n}{f_a}\right)^2 \qquad (72)$$

and divide the equation by ω_a^2. The frequencies are obtained by solving the eigenvalue problem given by

$$\Big[[A] - \nu[U]\Big]\{x\} = 0 \qquad (73)$$

98

where

$$[A] = \frac{1}{4\sigma} \begin{bmatrix} 4 + S_{10} (\sigma - 1) & S_3 (\sigma - 1) & -S_2 (\sigma - 1) \\ S_3 (\sigma - 1) & 4 + S_6 (\sigma - 1) & -S_5 (\sigma - 1) \\ -S_2 (\sigma - 1) & -S_5 (\sigma - 1) & 4 + S_8 (\sigma - 1) \end{bmatrix}$$ (74)

The three frequency ratios f_1/f_a, f_2/f_a, and f_3/f_a as well as their corresponding mode shapes are obtained as part of the computer output.

COMPUTER PROGRAM

The set of simultaneous equations (Eqs. (44) through (51), are solved using a computer program written in FORTRAN IV for General Electric Time Sharing Service. A listing of the program is given in the Appendix. The input to the program consists of eight numbers which are the values of a/b, c/b, d/a, e/b, k_a/k_r, Δ, N, and ϵ. The last three numbers are used for the numerical solution of the equations.

The Newton-Raphson method for solving a set of simultaneous equations (Ref. 7) requires the partial derivatives of each of the functions (i.e. the left side of Eqs. (44) through (51)) with respect to each of the variables (i.e. γ_1, γ_2, γ_3, γ_4, θ_1, θ_2, θ_3, and θ_4). In general if f_i stands for one of the functions and x_j stands for one of the variables, then the partial derivative of f_i with respect to x_j is approximated by

$$\frac{\partial f_i}{\partial x_j} \approx \frac{f_i (x_j + \Delta) - f_i}{\Delta}$$ (75)

where

$$f_i \triangleq f_i (x_1, x_2, \text{---} x_j \text{---} x_8)$$ (76)

$$f_i (x_j + \Delta) \overset{\Delta}{=} f_i (x_1, x_2, \text{---} x_j + \Delta \text{---} x_8)$$ (77)

and Δ is a small increment in the value of x_j.

In order to start the solution an initial guess must be made for the values of the eight variables. These are obtained from the solution to the problem assuming that the center of mass is located above the center of the mount pattern (i.e. d = e = o). The solution for this problem is given in the next section. The program then makes a revised estimate of the variables using the matrix of partial derivatives. This process is repeated until all of the functions in Eqs. (44) through (51) are

less than ϵ indicating that the solution has been found within the desired accuracy of ϵ. However, if the solution is not found within N iterations, the program prints out "No Solution".

If a solution is obtained, the program then determines the frequency ratios and mode shapes by solving the eigenvalue problem of Eq. (73). An example obtained from running the program is given below.

```
ANG            13:47EST      03/29/73

?*.5,1...1,.1,10...001,20,1.E-8
```

SOLUTIONS FOR C.G. ABOVE CENTER OF MOUNT PATTERN

GAMMA	THETA	F1/FA	F2/FA	F3/FA
80.372	37.903	0.331	0.656	0.813
58.533	8.723	0.325	0.339	0.990

SOLUTION 1

ISOLATOR	1	2	3	4
GAMMA	109.154	60.649	71.594	77.610
THETA	20.791	44.084	26.997	47.350

FREQUENCY RATIOS AND MODE SHAPES

	F1/FA	F2/FA	F3/FA
	0.3299	0.6233	0.8383
X(1)	0.9546	-0.2616	0.1428
X(2)	0.2546	0.9648	0.0659
X(3)	-0.1550	-0.0266	0.9876

SOLUTION 2

NO SOLUTION

For this case, a/b = 1.5, c/b = 1, d/a = 0.1, e/b = 0.1, k_a/k_r = 10, Δ = 0.001, N = 20, and $\epsilon = 10^{-8}$. For these parameter values there are two solutions for the C.G. above the center of the mount pattern. However, only the first solution led to a solution for the C.G. offset. Note that the value of γ for isolator 1 is greater than 90° so that this isolator is pointed away from the isolated mass. Also the mode shapes indicate that there is coupling between the x_1, x_2, and x_3 coordinates. In the solution for the C.G. above the center of the mount pattern, the natural frequencies f_1, f_2, and f_3

have mode shapes confined to the x_1, x_2, and x_3 directions, respectively. However, the coupling is not great and the three natural frequencies are quite close to those for the C.G. above the center of the mount pattern.

It may be possible to obtain a solution corresponding to the second solution for the C.G. above the center of mount pattern. For example, a solution could first be obtained for $d/a = 0.05$ and $e/b = 0.05$ and then use this solution as initial values for the case where $d/a = 0.1$ and $e/b = 0.1$. However, at the time of writing, this refinement has not been added to the program.

C.G. CENTERED ABOVE MOUNT PATTERN

For the special case where the center of mass of the rigid body is above the center of the mount pattern (i.e. $d = e = 0$), a symmetrical arrangement of the isolators is assumed so that

$$\gamma_1 = \gamma_2 = \gamma_3 = \gamma_4 = \gamma \qquad (78)$$

$$\theta_1 = \theta_2 = \theta_3 = \theta_4 = \theta \qquad (79)$$

In this case, every summation with subscripts (i.e. $\sum_{ij}$) in Eqs. (52) through (67) is zero. The set of eight simultaneous equations given by Eqs. (44) through (51) are reduced to the following two equations

$$Q'_{12} = BS_\gamma \, C_\theta \, S_\theta - S_\gamma^2 \, S_\theta^2 - \frac{1}{\sigma - 1} = 0 \qquad (80)$$

$$Q'_{21} = AC_\gamma \, C_\theta \, S_\theta - C_\gamma^2 \, S_\theta^2 - \frac{1}{\sigma - 1} = 0 \qquad (81)$$

By defining

$$T_\gamma \triangleq \tan (\gamma) \qquad (82)$$

$$T_\theta \triangleq \tan (\theta) \qquad (83)$$

Eqs. (80) and (81) can be written as

$$(B^2 + 1) \, T_\gamma^4 - AB (\sigma + 1) \, T_\gamma^3$$

$$+ [(A^2 + B^2) \, \sigma - 2] \, T_\gamma^2$$

$$- AB (\sigma + 1) \, T_\gamma + A^2 + 1 = 0 \qquad (84)$$

$$T_\theta = (A - BT_\gamma)\sqrt{1 + T_\gamma^2} \, / \, (1 - T_\gamma^2) \qquad (85)$$

These two equations are used to obtain the initial values for the variables γ_1 and θ_1 in the computer program. The natural frequencies are obtained from Eqs. (72), (73) and (74) noting that the summations $S_2 = S_3 = S_5 = 0$. In this case the translational modes are decoupled from each other and the three natural frequencies are given by

$$f_1/f_a = \sqrt{(C_\gamma^2 \, S_\theta^2 \, (\sigma - 1) + 1)/\sigma} \qquad (86)$$

$$f_2/f_a = \sqrt{(S_\gamma^2 \, S_\theta^2 \, (\sigma - 1) + 1)/\sigma} \qquad (87)$$

$$f_3/f_a = \sqrt{C_\theta^2 \, (\sigma - 1) + 1)/\sigma} \qquad (88)$$

Given the values of a/b, c/b, and k_a/k_r, Eqs. (84) through (88) are solved for the values of γ, θ, f_1/f_a, f_2/f_a, and f_3/f_a. In presenting the results graphically it is more convenient to plot k_a/k_r, θ, f_1/f_a, f_2/f_a, and f_3/f_a versus γ for given values of a/b and c/b. These results are presented in Figures 4 through 8. The parameter a/b takes on values of 1, 1.25, 1.5, 2, 2.5, and 3 and the parameter c/b has values of 0.1, 0.2, 0.5, 1, 1.5, and 2. Other than the case where $a/b = 1$ (i.e. a square mount pattern) there is a range of values of γ for which no solutions exist. This range is centered about $\gamma = 45°$. This situation can be more easily observed by solving Eq. (84) for the stiffness ratio σ as follows

$$\sigma = \frac{(B^2 + 1)T_\gamma^4 - ABT_\gamma^3 - 2T_\gamma - ABT_\gamma + A^2 + 1}{ABT_\gamma^3 - (A^2 + B^2)T_\gamma^2 + ABT_\gamma} \qquad (89)$$

Other than the case where $A = B$ (i.e. $a/b = 1$), $\sigma = \infty$ for $\gamma = 0°$, $90°$, $\tan^{-1}(a/b)$, and $\tan^{-1}(b/a)$. If the isolators are directed toward the C.G. in the plan view of Figure 1, then the angle $\gamma = \tan^{-1}(b/a)$. Since the stiffness ratio σ is infinite for this value of γ, the isolators should not be directed toward the C.G. For values of γ bracketed by $\tan^{-1}(b/a) < \gamma < \tan^{-1}(a/b)$, the stiffness ratio σ is negative and therefore unrealizable for positive stiffness springs.

C.G. CENTERED ABOVE SQUARE MOUNT PATTERN

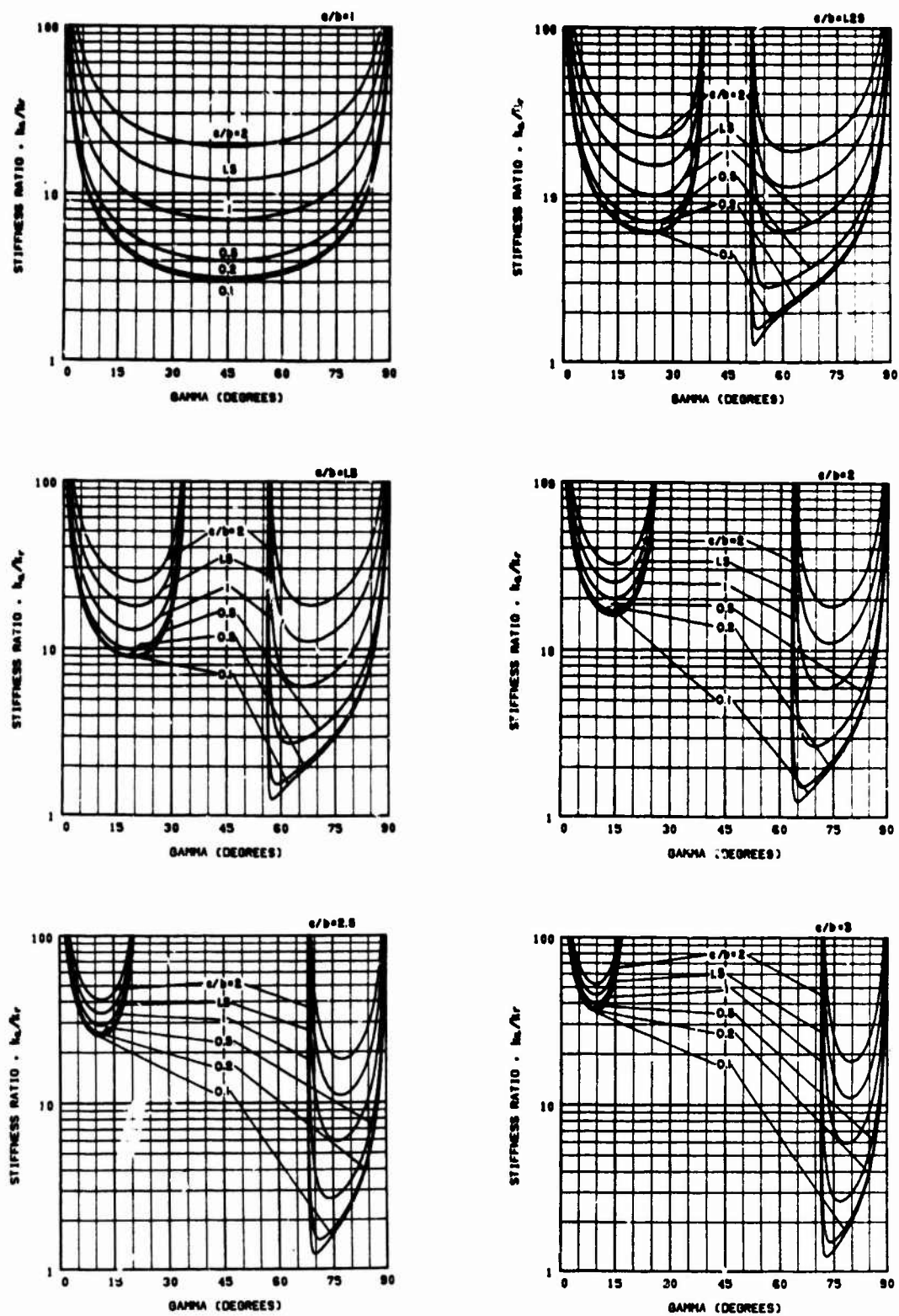For the case where $A = B$, it is seen from Eqs. (80) and (81) that for $\gamma = 45°$, the

Figure 4: Stiffness Ratio, k_a/k_r versus γ
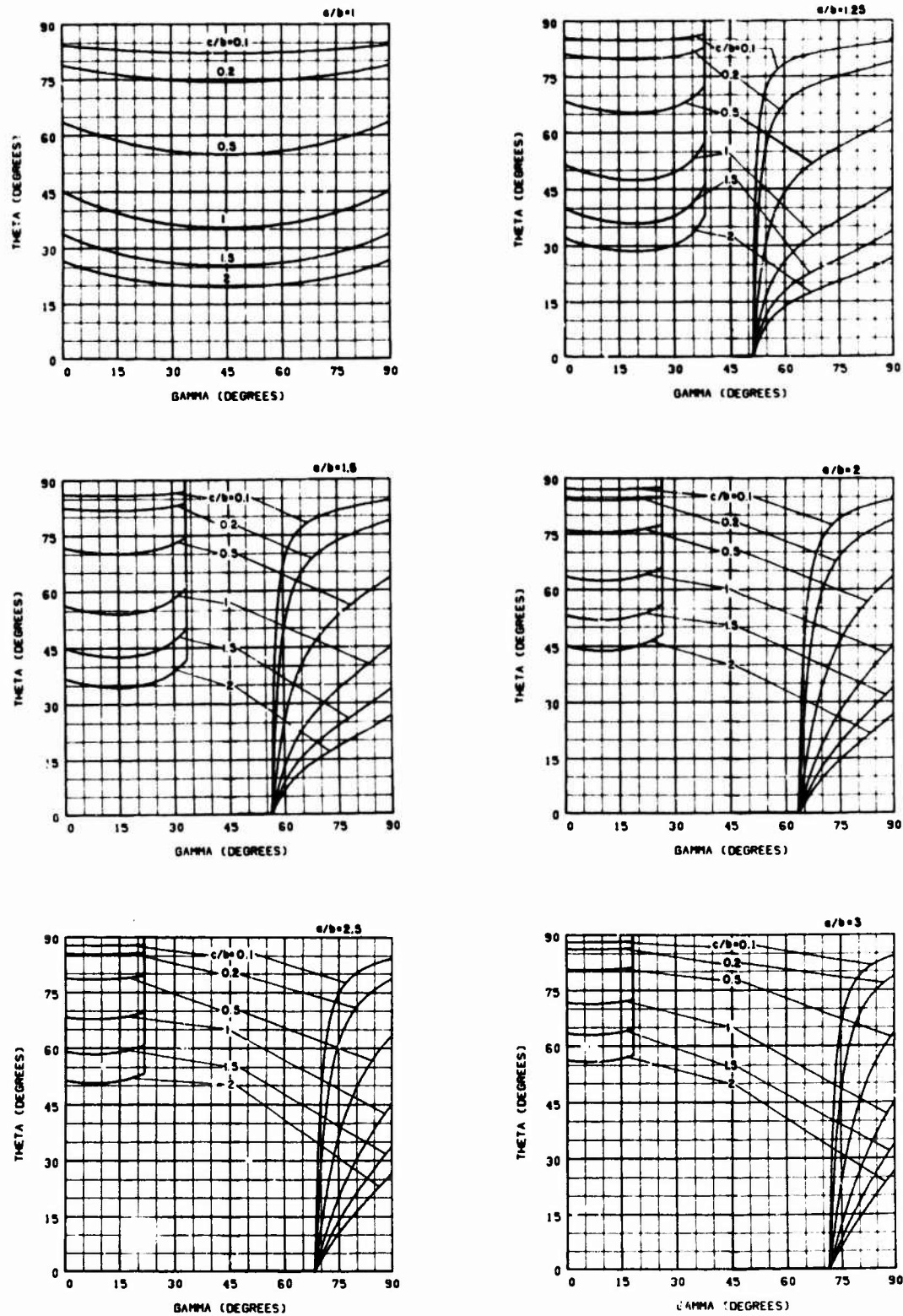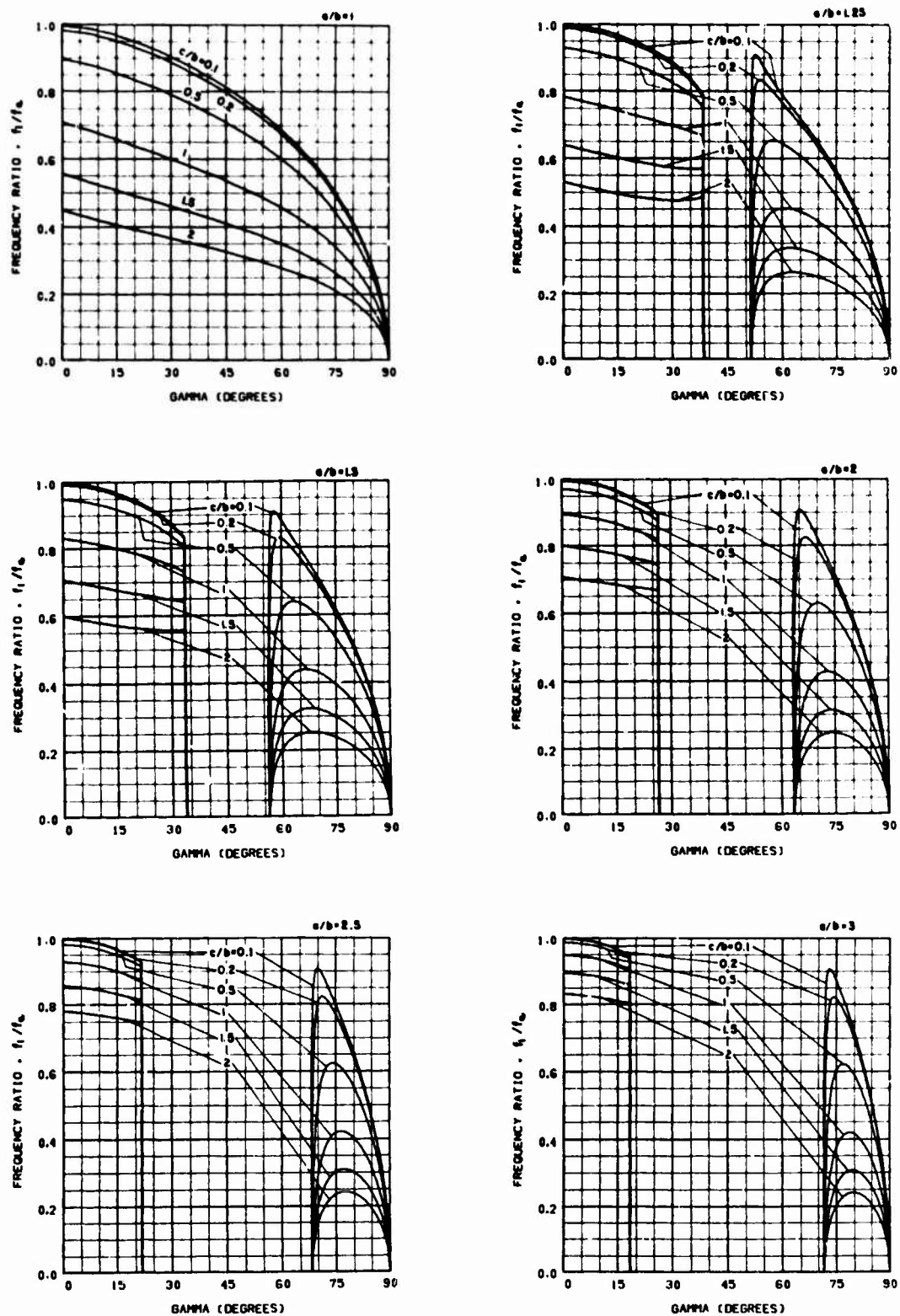
101

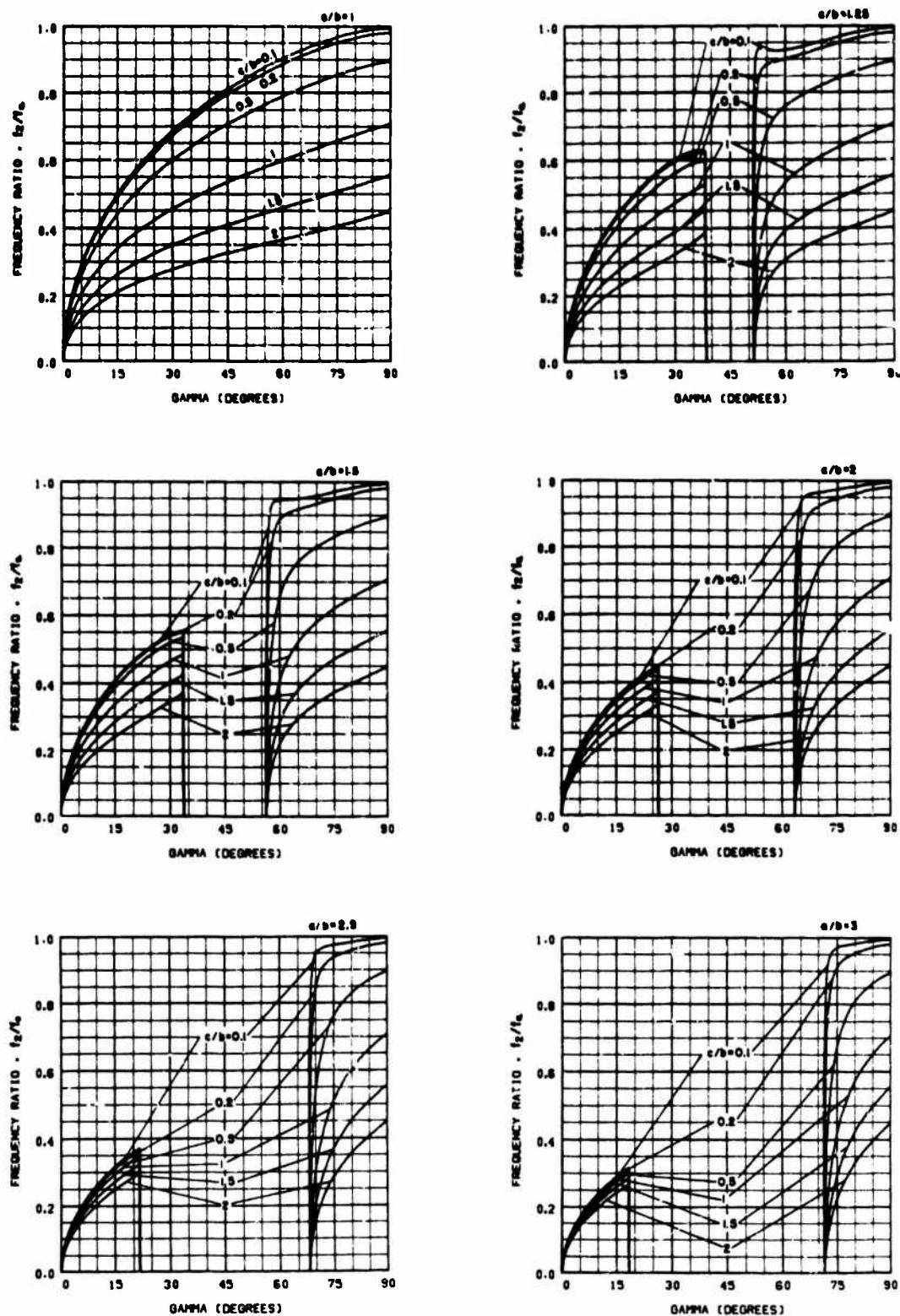Figure 5: Angle θ versus γ

Figure 6: Frequency Ratio, f_1/f_a versus γ
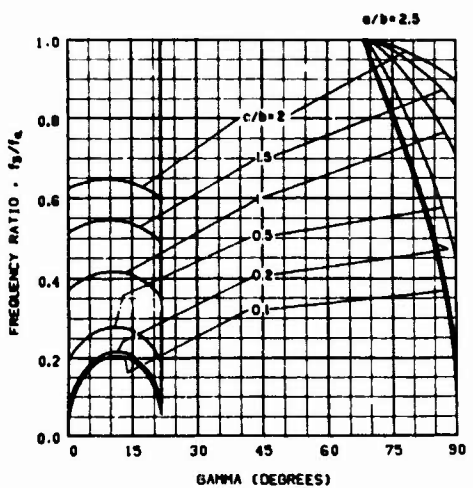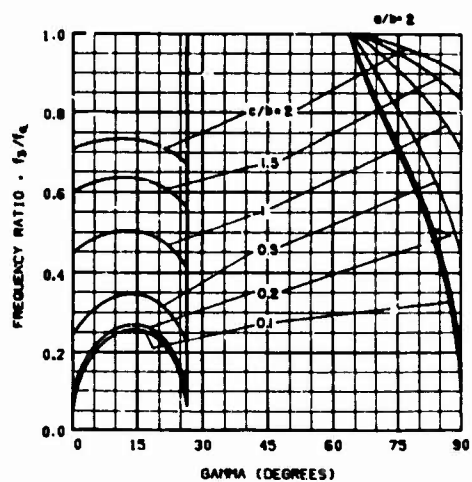
Figure 7: Frequency Ratio, f_2/f_a versus γ

104
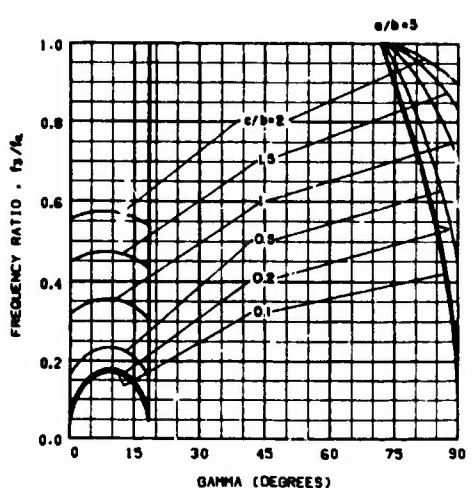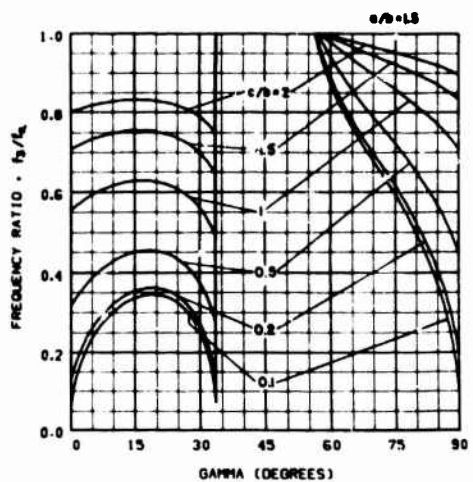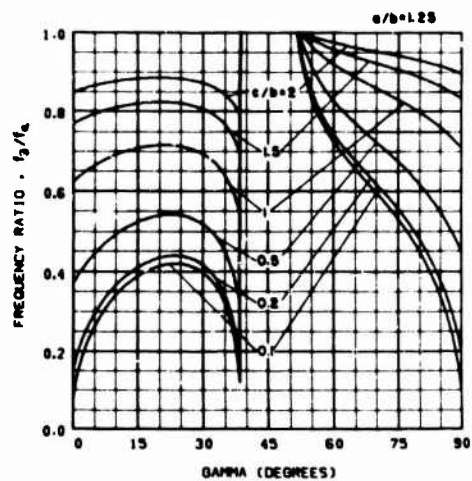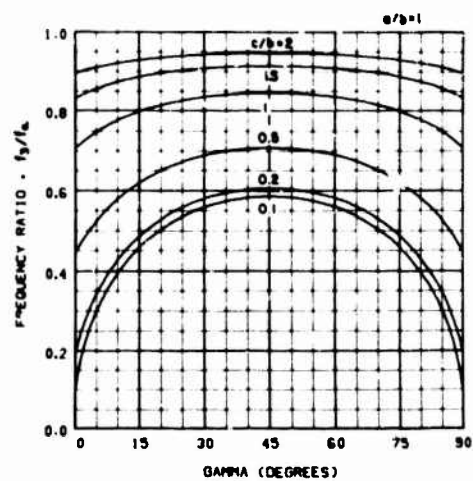
Figure 8: Frequency Ratio f_3/f_a versus γ

105

stiffness ratio σ and the angle θ are related according to

$$\sigma = \frac{2}{\sqrt{2}AC_\theta S_\theta - S_\theta^2} + 1 \tag{90}$$

On the graphs, the values that σ and θ approach as $\gamma \to 45°$ are determined from Eqs. (89) and (85) as

$$\sigma = 3 + 4/A^2 \tag{91}$$

$$\theta = \tan^{-1}(A/2) \tag{92}$$

These results are just a special case of the relation given by Eq. (90). However, if the values of σ and θ are chosen to satisfy Eq. (90) but not Eqs. (91) and (92), then there can be a large difference between these values and the proper values of σ and θ to achieve decoupling for a value of γ slightly different from $45°$. This is the situation that arises when all three natural frequencies are set equal.

When the three frequencies are set equal in Eqs. (86) through (88), the angles γ and θ can be solved for resulting in $\gamma = 45°$ and $\theta = 54° 44'$ (i.e. $T_\theta = \sqrt{2}$). Since $\gamma = 45°$, this is applicable only for the case where $a/b = 1$. With $\theta = 54° 44'$ Eq. (90) is satisfied for

$$\sigma = \frac{A + 2}{A - 1} \tag{93}$$

so that for any value of A greater than 1, a value of σ can be determined that will decouple the equations resulting in all three frequencies being equal and given by

$$f_i/f_a = \sqrt{\frac{A}{A + 2}} \qquad (i = 1, 2, 3) \tag{94}$$

If the further requirement is made that Eqs. (91) and (92) be satisfied then $A = a/c = b/c = 2$, $\sigma = 4$, and $f_i/f_a = .707$.

REFERENCES

1. Himelblau, H. Jr. and Rubin, S., "Vibration of a Resiliently Supported Rigid Body," in Shock and Vibration Handbook, Edited by C. M. Harris and C. E. Crede, McGraw-Hill, New York, 1961, Vol. 1, Chap. 3, pp. 27-29.

2. Goldstein, H., Classical Mechanics, Addison-Wesley, Reading, Mass., 1950, pp. 93-109.

3. Hurty, W. C. & Rubinstein, M. F., Dynamics of Structures, Prentice-Hall, Inc. Englewood Cliffs, N. J., 1964, Chap. 9.

4. Caughey, T. K., "Nonstationary Random Inputs & Responses", Random Vibration, Vol. 2 (S. H. Crandall, Ed.), MIT Press, Cambridge, 1963, Chap. 3.

5. Caughey, T. K. and O'Kelly, M.E.J., "Classical Normal Modes in Damped Linear Dynamic Systems," J. Appl. Mech., v. 32E, n. 3, Sept. 1965, pp. 583-588. (Discussion by Lin, Y. K., J. Appl. Mech., v. 33E, n. 2, June 1966, pp. 471-472).

6. Collins, J. D.; Hart, G. C., Hurty, W. C. and Kennedy, B., "Review & Development of Modal Synthesis Techniques", J. H. Wiggins TR 1073-1, May 1972.

7. Korn, G. A. and Korn, T. M., Mathematical Handbook for Scientists and Engineers, McGraw-Hill, New York, 1961, p. C34.

ANG   03/29/73

```
100     DIMENSION C(5),ZR(4),ZI(4),X(8,4),Y(8,1),EQ(5),F(8,1)
110    A          ,PDER(8),FF(16),SUM(3),S23(4),S24(4),S34(4),JS(4)
120    A          ,LABEL(8),AM(6),BM(3,3),TEMP(3),TEMP2(3)
130     DATA SP3/1.,-1.,-1.,1./,S24/1.,-1.,1.,-1./
140     DATA S34/1.,1.,-1.,-1./
145C READ PARAMETER VALUES
150 101 INPUT,ASB,CSB,DSA,ESB,SIGMA
160    A          ,DEL,NITER,ERR
165C SET CONSTANTS
170     A=ASB/CSB
180     B=1./CSB
190     D=DSA*A
200     E=ESB*B
210     N=*
220     C1=R**2+1.
230     C2=A*B
240     C3=A**2+B**2
250     C4=A**2+1.
260     Z=2./(SIGMA-1.)
270     C(1)=Z*C4
280     C(2)=2.*(1.+Z)*C2
290     C(3)=(2.+Z)*C3-2.+Z*
300     C(4)=C(2)
310     C(5)=Z*C3
315C COMPUTE GAMMA FOR CG ABOVE MOUNT PATTERN - EQ. (84)
320     CALL UBNNRC,N,ZR,ZI)
325C DETERMINE NUMBER OF SOLUTIONS
330     NJSOL=0
340     ISOL=0
350     PRINT I
360     DO 10 J=1,4
370     IF(ZI(J) .NE. 0.) GO TO 20
380     IF(ZR(J) .LE. 0.) GO TO 20
390     ISOL=ISOL+1
400     JS(J)=ISOL
410     TA=ZR(J)
420     TH=SQRT(1.+TA**2)*(A-B+TA)/(1.-TA**2)
425C GAMMA=AL , THETA=BE
430     AL=ATAN(TA)
440     BE=ATAN(TB)
450     CA2=COS(AL)**2
460     SA2=SIN(AL)**2
470     CB2=COS(BE)**2
480     SB2=SIN(BE)**2
490     SM1=SIGMA-1.
495C COMPUTE FREQUENCY RATIOS
500     FX=SQRT((1.+CA2*SB2*SM1)/SIGMA)
510     FY=SQRT((1.+SA2*SB2*SM1)/SIGMA)
520     FZ=SQRT((1.+CB2*SM1)/SIGMA)
525C PRINT RESULTS FOR CG ABOVE MOUNT PATTERN
```

ANG   03/29/73

```
530     PRINT 2,AL*57.3,BE*57.3,FX,FY,FZ
535C SET INITIAL VALUES OF VARIABLES FOR EACH SOLUTION
540     DO 30 I=1,4
550     X(I,J)=AL
560  30 X(I+4,J)=BE
570     GO TO 10
580  20 NJSOL=NJSOL+1
590     JS(J)=0
600  10 CONTINUE
610     IF(NJSOL .EQ. 4) GO TO 90
620     IF(D .EQ. 0. .AND. E .EQ. 0.) GO TO 100
625C LOOP THRU 4 POSSIBLE SOLUTIONS
630     DO 60 J=1,4
640     ITER=0
650     IF(JS(J) .EQ. 0) GO TO 60
655C PRINT SOLUTION NUMBER
660     PRINT 7,JS(J)
670     L=0
680     IL=1
685C SET SUMMATIONS TO ZERO
690 200 DO 40 I=1,16
700  40 S(I)=0.
710     DO 50 I=1,8
720     CA=COS(X(I,J))
730     SA=SIN(X(I,J))
740     CB=COS(X(I+4,J))
750     SB=SIN(X(I+4,J))
760     CA2=CA**2
770     SA2=SA**2
780     CB2=CB**2
790     SB2=SB**2
795C COMPUTE SUMMATIONS - EQS. (52) THRU (67)
800     S(1)=S(1)+S24(I)*CA*CB*SB
810     S(2)=S(2)+S23(I)*CA*CB*SB
820     S(3)=S(3)+S24(I)*CA*SA*SB2
830     S(4)=S(4)+SA*CB*SB
840     S(5)=S(5)+S24(I)*SA*CB*SB
850     S(6)=S(6)+SA2*SB2
860     S(7)=S(7)+S34(I)*CB2
870     S(8)=S(8)+CB2
880     S(9)=S(9)+CA*CB*SB
890     S(10)=S(10)+CA2*SB2
900     S(11)=S(11)+S24(I)*SA*CB*SB
910     S(12)=S(12)+S23(I)*CB2
920     S(13)=S(13)+S34(I)*CA2*SB2
930     S(14)=S(14)+S34(I)*CA*SA*SB2
940     S(15)=S(15)+S23(I)*CA*SA*SB2
950  50 S(16)=S(16)+S23(I)*SA2*SB2
960     F1=2.*Z
970     F2=E*F1
```

ANG   03/29/73

```
980     F3=D*F1
985C COMPUTE Q PRIME VALUES - EQS. (44) THRU (51)
990     EQ(1)=B*S(3))-E*S(2)-S(3)
1000    EQ(2)=B*S(4)-E*S(5)-S(6)-F1
1010    EQ(3)=B*S(7)-E*S(8)-S(5)-F2
1020    EQ(4)=A*S(9)-D*S(2)-S(10)-F1
1030    EQ(5)=A*S(11)-D*S(5)-S(3)
1040    EQ(6)=A*S(1)-O-D*S(R)-S(2)-F3
1050    EQ(7)=B*S(13)-E*S(14)-A*S(14)+D*S(3)-F2
1060    EQ(8)=A*S(16)-D*S(6)+B*S(15)+E*S(3)-F3
1070    IF(L .NE. 0) GO TO 201
1080    DO 202 K=1,8
1090 202 F(K,1)=EQ(K)
1100    GO TO (203,207),IL
1105C SET VARIABLE BACK TO ORIGINAL VALUE
1110 201 X(L,J)=X(L,J)-DEL
1115C COMPUTE PARTIAL DERIVATIVES
1120    DO 204 K=1,8
1130 204 PDER(K)=(EQ(K)-F(K,1))/DEL
1140 203 L=L+1
1150    IF(L .GT. 8) GO TO 205
1155C SET VARIABLE AHEAD BY DELTA
1160    X(L,J)=X(L,J)+DEL
1170    GO TO 200
1175C COMPUTE INVERSE OF PARTIAL DERIVATIVE MATRIX
1180 205 CALL MTINV(PD,8,8,LABEL)
1185C MULTIPLY VECTOR OF Q PRIME VALUES BY INVERSE
1186C OF PARTIAL DERIVATIVE MATRIX. SET RESULT IN Y VECTOR
1190    CALL MTMPY(O,PD,F,Y,8,8,1,N,8)
1195C COMPUTE NEW VALUES OF VARIABLES
1200    DO 206 K=1,8
1210 206 X(K,J)=X(K,J)-Y(K,1)
1230    L=0
1240    IL=2
1250    GO TO 200
1260 207 ITER=ITER+1
1270    IF(ITER .LE. NITER) GO TO 208
1275C IF ITERATIONS EXCEEDS NITER, PRINT "NO SOLUTION"
1280    PRINT 4
1290    GO TO 60
1295C ACCEPT SOLUTION IF ALL Q PRIME VALUES ARE LESS THAN ERR
1300 208 DO 209 I=1,8
1310    IF(ABS(EQ(I)) .GT. ERR) GO TO 203
1320 209 CONTINUE
1325C PRINT GAMMA AND THETA FOR EACH ISOLATOR
1330    PRINT 3,(X(I,J)+57.3,I=1,8)
1335C COMPUTE ELEMENTS OF MATRIX A - EQ. (74)
1340    AM(1)=4.+S(10)*SM1
1350    AM(2)=S(3)*SM1
1360    AM(3)=-S(2)*SM)
```

ANG   03/29/73

```
1370    AM(4)=4.+S(6)*SM1
1380    AM(5)=-S(5)*SM1
1390    AM(6)=4.+S(8)*SM1
1400    DO 210 I=1,6
1410 210 AM(I)=AM(I)/(4.+SIGMA)
1415C SOLVE EIGENVALUE PROBLEM - EQ. (73)
1420    CALL EIGI(AM,BM,3,0.,TE1'I,TEMP2,1,J)
1430    DO 211 I=1,3
1440 211 AM(I)=SQRT(AM(I))
1445C PRINT FREQUENCY RATIOS AND MODE SHAPES
1450    PRINT 6,(AM(I),I=1,3),((BM(I,K),K=1,3),I=1,3)
1460  60 CONTINUE
1470    GO TO 100
1480  90 PRINT 4
1485C GO TO THE NEXT CASE OR END
1490 100 PRINT 5
1500    INPUT,IDIR
1510    GO TO (101,102),IDIR
1520 102 STOP
1530   1 FORMAT(///" SOLUTIONS FOR C.G. ABOVE CENTER"
1540   6          " OF MOUNT PATTERN"//3X,"GAMMA",3X,"THETA"
1550   A          ,3X,"F1/FA",3X,"F2/FA",3X,"F3/FA")
1560   2 FORMAT(5F8.3)
1570   3 FORMAT(///" ISOLATOR",7X,"1",9X,"2",9X,"3",9X,"4"
1580   A          /" GAMMA",6X,4F10.3/" THETA",4X,4F10.3)
1590   4 FORMAT(/" NO SOLUTION")
1600   5 FORMAT(///" ANOTHER CASE(1=YES,2=NO)")
1610   6 FORMAT(///2X,"FREQUENCY RATIOS AND MODE SHAPES"//
1620   A          9X,"F1/FA",5X,"F2/FA",5X,"F3/FA",5X,3F10.4//
1630   A          3(" X(",I1,")",3F10.4)1
1640   7 FORMAT(///" SOLUTION",I2/1X,10("-")1
1650    END
```

DISCUSSION

Mr. Dickerson (Motorola): From your curves it looks like you get a tremendous number of possible solutions for any given set of assumptions. How does your computer program decide which one to print out for you?

Mr. Derby: The initial guess would be the answer I know is correct for the CG centered above the mount pattern and I just keep interating, using that as an initial estimate, to get the answer.

Mr. Dickerson: Do you get "the" answer or "an" answer?

Mr. Derby: "An" answer.

Mr. Dickerson: Do you have any confidence it is an answer you could go to press with and build equipment?

Mr. Derby: I think it is a correct theoretical answer. How good this is going to be for actually decoupling I don't know, because there are considerations such as damping, nonlinearities, and so forth.

SHOCK MITIGATION SYSTEM SUBJECTED TO THIRTEEN FEET OF VERTICAL GROUND MOTION – CANNIKIN EVENT[*]

Eugene C. Jackson
University of California, Lawrence Livermore Laboratory
Livermore, California 94550

Shock isolation of fragile equipment from severe three-dimensional ground motion induced by underground nuclear detonations at the Nevada Test Site requires special techniques for inexpensive, reliable performance. A much larger detonation, the Cannikin Event with a yield of less than 5 Mt, was detonated November 6, 1971 at Amchitka Island, Alaska. For this event a new system was designed to protect the diagnostic equipment from 15 feet of vertical ground motion. Nine trailers were shock mounted on this system. Actual ground upheaval was 13 feet. All data was recovered and all systems operated as planned. There was no damage to the shock mounted equipment or structures. The design, set-up, motion measurement program, and performance of this system are discussed.

INTRODUCTION

The Cannikin Event was a nuclear explosion of nominal yield less than 5 Mt detonated November 6, 1971, in an excavated chamber 5875 ft beneath the surface of Amchitka Island, Alaska. The primary purpose of this test was to confirm the new warhead design for the Spartan antiballistic missile.

Experimental data that indicated the performance of the warhead were recorded by fragile electronic equipment. To minimize signal degradation caused by extremely long signal cables and to reduce cable costs, the equipment was housed in trailers close to ground zero. Because the dynamic environment for Cannikin was predicted to be much more severe than any we had experienced during underground detonations at the Nevada Test Site (NTS), a new shock mitigation system was developed. This new system allowed us to locate the recording trailers 2000 ft from surface ground zero and resulted in a net savings of $550,000.

ENVIRONMENT

Ground motion induced by an underground nuclear detonation varies considerably, depending on the yield of the device, geology, and location of interest [1]. Practically all existing surface motion data have been recorded at NTS. Because the geologies of NTS and Amchitka are different, the surface ground motion estimates for the Cannikin Event were based on measurements from two smaller detonations at Amchitka: the Longshot and Milrow Events.

For Cannikin, the spall zone was predicted to extend 33,000 ft from surface ground zero. Within the spall zone the vertical surface motion is more severe than the horizontal motion. The vertical motion is characterized by an initial upward acceleration pulse followed by a -1 g ballistic period and then an upward impact acceleration when the spall gap closes. Horizontal acceleration pulses are usually less severe but, in a few cases, have equalled the vertical values on impact. Peak horizontal displacements occur after impact, which is well after the vertical peak displacements have been reached.

The capacity of an absorption type of shock isolation system in the vertical direction is primarily defined by the kinetic energy of the peak negative ground velocity (free-fall height). For Cannikin the estimated nominal peak vertical velocity and kinetic energy versus distance from surface ground zero is shown in Fig. 1 [2]. The shock isolation system that we developed for large events at NTS is applicable for estimated ground motions not exceeding 18 fps nominal and 24 fps maximum[†] [3]. For the Cannikin Event this system would have required a location 5500 ft from surface ground zero.

---

[*]Work performed under the auspices of the U.S. Atomic Energy Commission.

[†]For design purposes, nominal values (best estimate) are used with a safety factor; maximum values are used to check that the system has adequate reliability based on maximum credible energy.
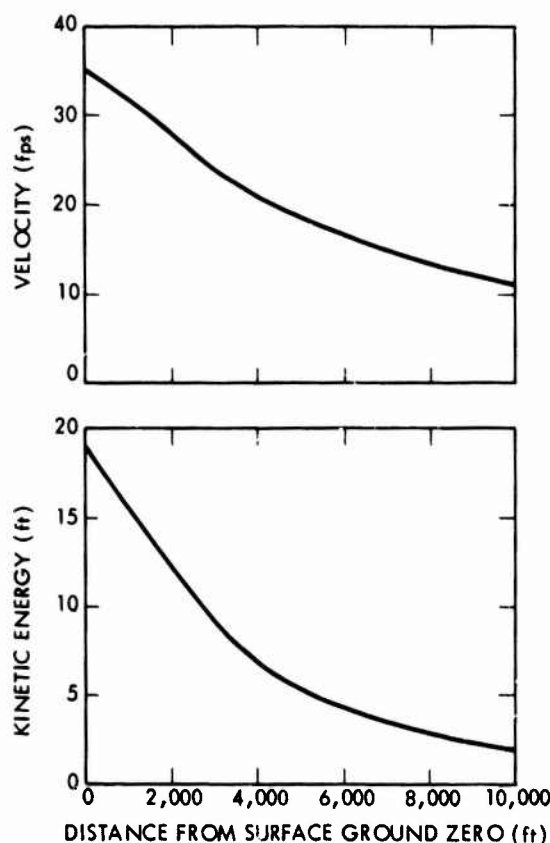
Fig. 1 - Estimated peak vertical surface ground
velocity and kinetic energy for
Cannikin Event

PERFORMANCE REQUIREMENTS

The purpose of the new shock isolation system was to circumvent any failures due to the shock environment and to recover all experimental data. Damage would be acceptable as long as it did not degrade the integrity of an experiment. All diagnostic systems required post-event checks. Therefore, all electronic equipment was required to operate after or through shock arrival time.

For maximum utility and mobility the recording systems were housed in nine truck-trailer vans. There were five 50-ft-long instrumentation trailers. One trailer contained oscilliscopes and tape recorders while the other four contained 250 oscilliscopes with cantilevered cameras (Fig. 2). There were two 30-ft- and one 50-ft-long instrument power trailers and a 20-ft mobile timing trailer. Previous experience and proof tests indicated that the fragility level for the timing, instrumentation, and power systems was 7 g minimum. At slightly higher accelerations various structural and operating failures begin to occur.

CONCEPTUAL DESIGN

For the Cannikin Event there were no critical post-event position or alignment requirements

On the other hand, the possibility of a subsidence crater limits close-in positioning of recording systems. The severe slope at the edge of the crater prohibits the use of reliable systems in this area. The estimated maximum crater radius for Cannikin was 1500 ft. A subsidence slump radius of 3000 ft was estimated. This value was scaled from observations of the Milrow Event. The possibility of a gentle slump did not pose a limiting condition.

To be safely outside a possible subsidence crater, a location 2000 ft from surface ground zero was chosen for the critical Cannikin recording systems. The nominal peak vertical ground motion values at this location were estimated to be 27 g initial acceleration with impact equal to or less than 35 g, 28 fps velocity, and 15 ft displacement [2]. The estimated maximum peak velocity was 31 fps. Since this location was near ground zero, peak horizontal displacements could be relatively low even though peak horizontal accelerations could equal the vertical values. This ground motion environment required that a new shock isolation system be developed.

Fig. 2 - Typical equipment inside an instrumentation recording trailer

for the trailers. This allowed us to design around the 3-dimensional ground motion environment by decoupling the horizontal shock components. The vertical isolation system could then be treated as a single-degree-of-freedom system Constant force versus displacement energy absorbers are desirable for maximum efficiency. Energy absorber deceleration set values are based on equipment fragility levels and a structural amplification factor of 1.75. This factor accounts for the elasticity of the shock mount structures, equipment mounting brackets, and the trailer structures.

The stroke requirements for the energy absorber are calculated by analyzing the constant force absorber characteristics and the time history profile of the ground motion. Figure 3 shows the idealized vertical ground motion and energy absorber response for nominal design conditions. The absorber stroke is best illustrated in the velocity curve. The area bounded by curves a, b, and d define the initial stroke. System rebound after initial stroke is shown by the offset of curve e from curve b. Final stroke (curve f) is determined by absorbing all of the kinetic energy at impact. The effect of the ground impact spike (curve c) is negligible. For the Cannikin design the total energy absorption stroke was calculated to be 67 in. for nominal and 82 in. for maximum conditions.

Variations in some parameters have large effects on absorber stroke and overall reliability. A 10% increase in peak initial acceleration has a small effect on the slope of curve a (Fig. 3) and the absorber stroke. On the other hand, a 10% variation in the peak velocity (offset of curve b) or absorber deceleration (slope of curve d) have large effects on the absorber stroke and, therefore, on system reliability.

One of the most important aspects of a shock mitigation system is the control and support of lateral forces. This is especially critical with a multidirection nonsymmetrical large displacement environment. Generally, the size of system structures is affected by the amount of isolator stroke. A nonsymmetrical system will have coupled modes of motion and therefore will require longer isolator strokes than an uncoupled system with the same degree of isolation. In an uncoupled system the resultant of the isolator forces must be directed through the center of mass of the body. For this use the trailers were mounted above the ground surface with provision for at least a 7-ft-vertical stroke. Under these conditions a continuously active symmetrical lateral shock isolator can be very complex. We have decoupled the lateral effects by making the continuously active forces very low and the relatively high forces inactive during the time of critical vertical motion.

The basic design characteristics are shown in Fig. 4. Several cross beams are solidly attached to the trailer. Each end of a beam con-

tains a guide in which a column is inserted. The column rests on a low-friction surface pad. The vertical-shock isolator is fully guided and can be either an extension (A) or a contraction type (B). Lateral constraint is provided by friction at the bottom of the column and by lateral tethers (T).
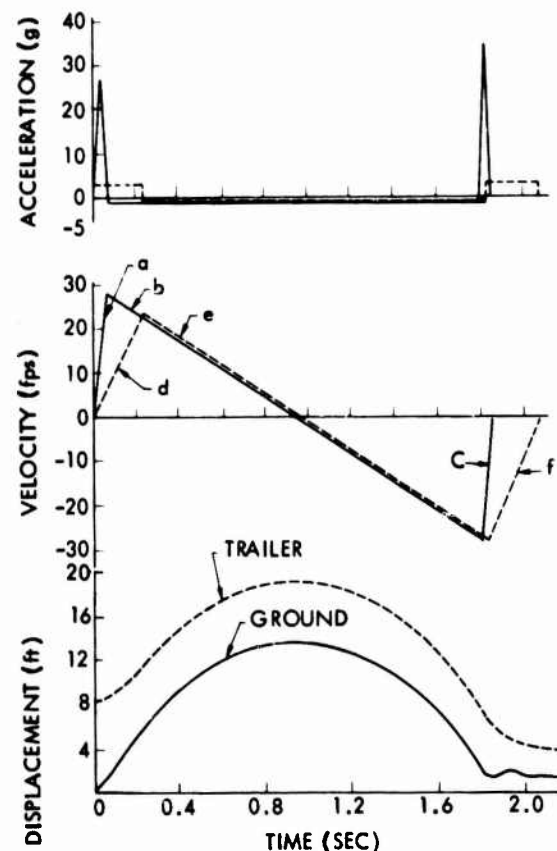

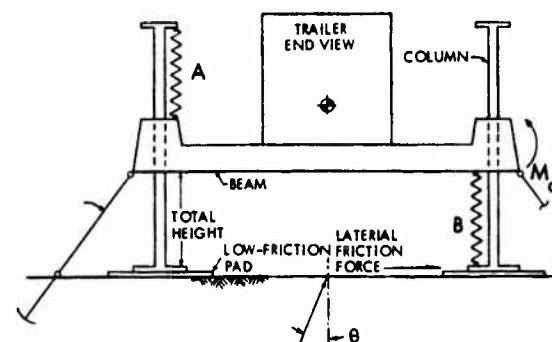Fig. 3 - Idealized vertical ground motion and energy absorber response

Fig. 4 - Characteristics of guided column shock isolation system

111

The initial acceleration pulse through the ground approaches the trailer at angle θ (between 15 and 45 deg from vertical). When the imposed acceleration level overcomes the energy absorber's set deceleration level, the energy absorber displaces and the lateral tethers loosen. At this time all lateral forces into the main body are limited by the low-friction pads. The coefficient of friction for this pad is 0.06, which limits the effective input force to an angle of about 4 deg from vertical. At the end of the initial absorption stroke (curve d Fig. 3) the shock isolation system rebounds from the ground and goes into a ballistic path completely decoupled from the ground (curve e). The shock isolation system impacts the ground shortly after the ground surface above the spall gap impacts (curve c). During the impact absorption stroke (curve f) the system remains on the low-friction pads and all tethers remain loose. This is followed by peak horizontal ground displacements; excessive trailer motion is limited by the tethers and high-friction pads.

Lateral loads from the friction pads are transferred to the bottom of the columns and tend to bend them. The resulting moments tend to bend the beam in the axial direction (M_a) and to twist it in the longitudinal direction. In most cases the twisting moment is transferred into the trailer structure by the box beam. In these cases the trailer structure is the primary longitudinal support.

Thus far the description applies both to our NTS universal guided column (UGC) system [1, 3] and to the system developed for the Cannikin Event. The NTS-UGC system uses a compressive type of crush material for vertical energy absorption (Fig. 4 item B). When crush materials are used, the energy absorber stroke must be limited to about 65% of the total height [1]. For the anticipated severe Cannikin environment a full-stroke energy-absorption system was desired; this would reduce the total height by one third, thereby reducing the column moment arm and most structures accordingly.

The full-stroke guided-column (FSGC) system developed for Cannikin uses an extension type energy absorber (Fig. 5). A constant-force columnar energy absorber (TOR-SHOK*) is used in the extension mode. A single stage of this device consists of two concentric tubes with a coil of ductile wire forced between them. The interference fit between the wire and the tubes is sufficient to prevent sliding and to force the wires to rotate. Rotation of the wires is similar to rotating the ring of a torus inside out. The resulting tensile and compressive strains are in the plastic range. Contracting or extending the tubes apart axially forces the wires to rotate many times. The repeated cyclic plastic strain-

---

*Reference to a company or product name does not imply approval or recommendation of the product by the University of California or the U.S. Atomic Energy Commission to the exclusion of others that may be suitable.
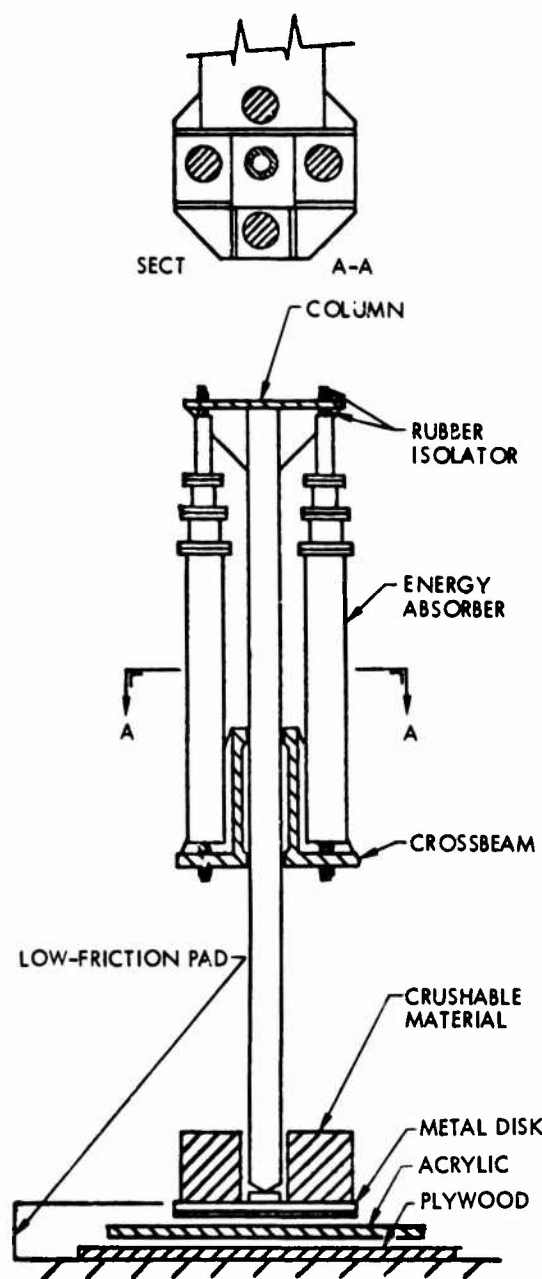
Fig. 5 - Characteristics of FSGC system

ing results in almost constant energy absorption per cycle of rotation (or inch of linear stroke) until eventual fatigue failure.

We tested individual absorbers statically and dynamically in both the extension and contraction directions before incorporating them into a shock isolation system. The tests indicated that the stroke and average deceleration values were uniform but that some vibration was present, especially in the contraction mode.

112

To use the full-stroke capability of the guided-column system, we attached the energy absorber between the top of the column and the beam (Fig. 5). Rubber isolators were used to isolate some of the 200- to 300-Hz vibration and to ensure that no bending moments were transferred into the energy absorber.

Before the system design was completed, a series of full-scale drop tests was conducted using a 30,000-lb trailer. Various load ratings and cluster arrays of energy absorbers were tested. At some locations the clusters were arranged to impart very high eccentric loadings into the columns. Drop heights were varied from 1 to 15 ft (Fig. 6). Through these tests we identified some component weaknesses and verified that the system would be reliable for the Cannikin Event. Details of the test program are discussed in Ref. 3.

SYSTEM SETUP FOR CANNIKIN

A typical FSGC shock isolation system for a 30-ft trailer is shown in Fig. 7. Because of the extreme height it is desirable to keep the center of mass as low as possible. Most trailers have road gear, fuel tanks, or other items that extend below the structural frame so that the minimum clearance to the ground is not controlled by the straight box beams of the shock isolation system.

Nylon webbing or rope tethers were arranged as shown in Fig. 7 to allow control of a pair of tethers failed completely. Earth anchors were conventional power installed screw anchors; torque readout during installation verified their holding capacity.

At the bottom of each column was a rigid polystyrene foam energy absorber and low-friction pad. A metal disk formed the main structural member of the low-friction pad (Fig. 5). The disk was attached to the bottom of the column by a simple pivot joint. About 30% of the disk bottom was covered with 10-mil-thick Teflon adhesive tape. The Teflon is loaded high enough to overcome its high friction properties at low load. An acrylic sheet under the disk is the low-friction rubbing surface and electrically isolates the trailer from the ground. During rebound and ballistic motion the acrylic sheet is centered to the disk by rubber straps. Laboratory- and full-size field tests consistently indicated a 0.06 coefficient of friction for this pad when it is clean. A slight amount of dirt can raise the coefficient to about 0.3. Therefore, the pad was completely enveloped in one polyethelene film and a second
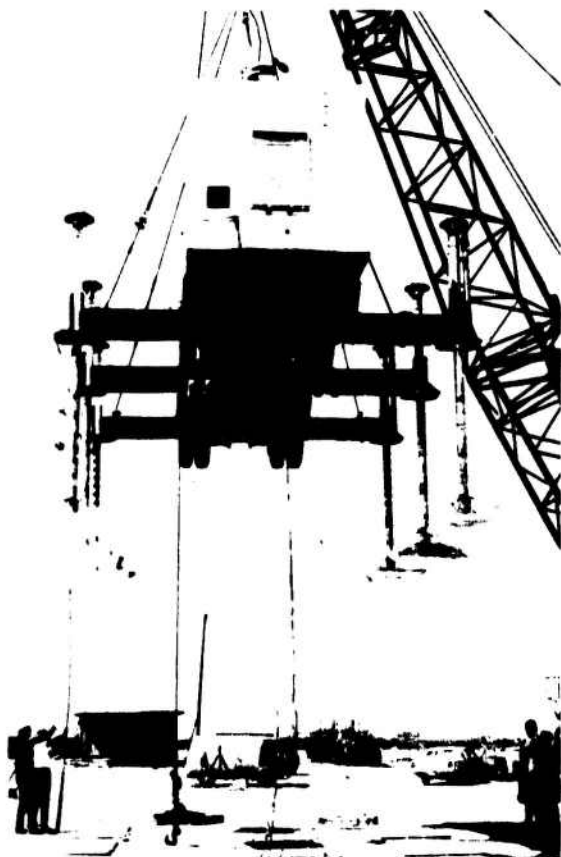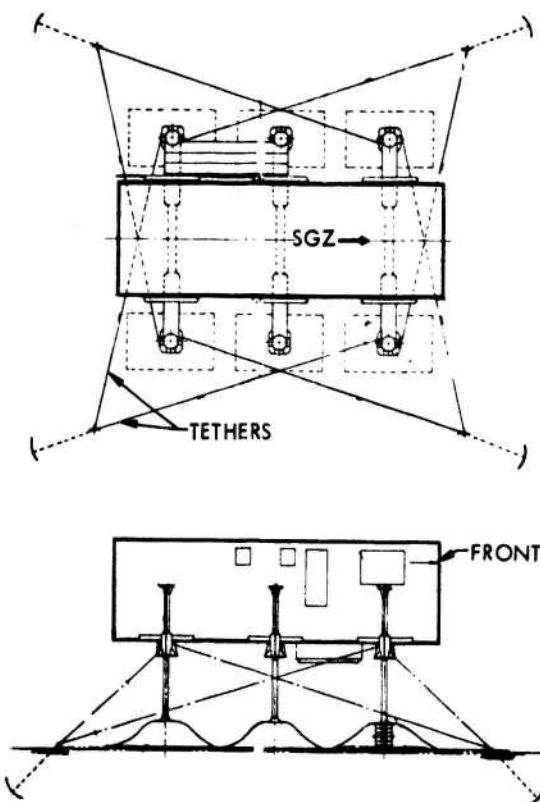

Fig. 6 - Prototype FSGC system rea for 15-ft drop test

Fig. 7 - Typical FSGC setup for a 30-ft trailer

113

film was draped over a larger area. Plywood sheeting formed a level base for the acrylic sheets and provided an intermediate friction surface (coefficient of friction about 0.3) for motion beyond the limits of the acrylic. During very severe horizontal displacement the disk slides off the plywood onto compacted soil where the coefficient of friction is about 0.5.

The TOR-SHOK energy absorbers are three-stage units with a minimum compressed length of 58.5 in. and an 8-ft minimum stroke. As installed for Cannikin their length was 70 in. Basic load ratings (third stage) varied from 6000 to 12,000 lb in increments of 1000 lb. Load ratings for the second and third stages were 95.5 and 91% respectively. Load tolerance was ±10% of the rated load. Each column could accommodate up to four energy absorbers with a total deceleration load capacity of 48,000 lb.

For a system to perform in a single degree of freedom manner, the center of isolator resistance must coincide with the system center of mass. The load ratings and appropriate distribution of the 196 energy absorbers (Fig. 8) required accurate weight and center of gravity measurement of the trailers with their shock isolation structures. The three power trailers had nonsymmetrical fuel tanks with capacities equal to about 8% of their gross weight. Estimated fuel capacities at the time of detonation were based on running time since the last refueling.

Part of our quality assurance program was to subject each energy absorber to a 1-in. stroke static compression and tension test on arrival at Amchitka. First-stage loads for each group averaged from 3 to 9% below the nominal first-stage ratings. The energy absorbers were then selectively redistributed to minimize the nonsymmetrical load distribution effects. The net results decreased the average deceleration levels by 10% in five trailers and between 3 and 8% in the remaining four trailers. Installation of additional foam pads required to regain the 10% degradation in absorption capacity was prevented by a severe storm. Two examples of the FSGC configuration prior to the event are shown in Figs. 9 and 10.

MEASUREMENT PROGRAMS

The Cannikin Event was the first application of the new shock isolation system. The environment was estimated to be three times more severe than previously experienced. Actual surface ground motion at the recording trailers and the performance of the new shock isolation system were measured with accelerometers, velocity gages, and motion pictures. The dynamic data were recorded on our portable data system [4]. This is a suitcase size, shock resistant, battery powered, tape recorder system, which was installed in one of the recording trailers. Instrumentation included a ground canister
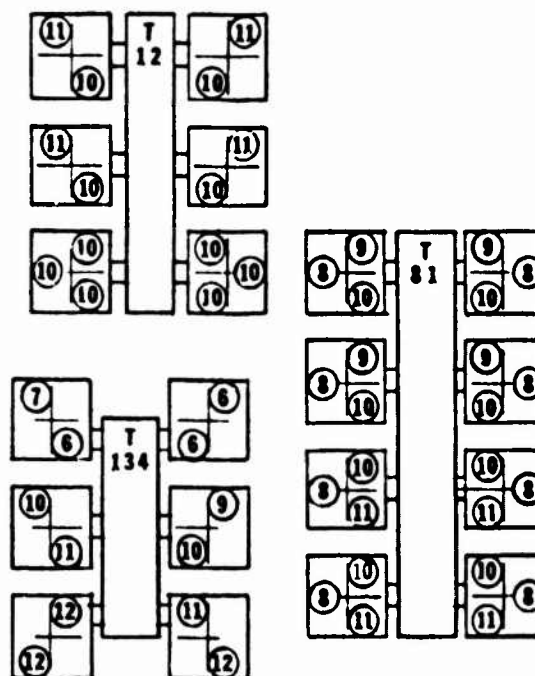
Fig. 8 - Energy absorber load rating distribution for three trailers

with a triaxial array of accelerometers and velocity gages buried 4 ft in native soil, a vertical accelerometer on each trailer, and an additional vertical or horizontal accelerometer on three trailers.

Instrumentation movie coverage is an important tool for analyzing multidirectional motion. Because of the severe environment the cameras must be located close up or at a great distance with resulting loss of resolution. Cameras in closeup locations must be shock resistant and will record only relative motions. We had four camera stations convering 6 fields of view at the Cannikin recording trailer park (Fig. 11). Seven 16 mm cameras with speeds between 64 and 250 fps were used. Camera station 1 was in a transportainer solidly mounted to the ground. Power for this station came from shock-mounted wet cell batteries. A special solid-state shock-resistant camera controller was used at this station. Cameras at stations 2, 3, and 4 were mounted on shock isolation structures; power was supplied by one of the shock mounted instrumentation power trailers. For displacement verses time analysis, the guide columns appearing in the closeup views were painted with 3-in.-wide color coded rings.

RESULTS

The overall condition of the recording trailer park is shown in Fig. 12. Conveniently,
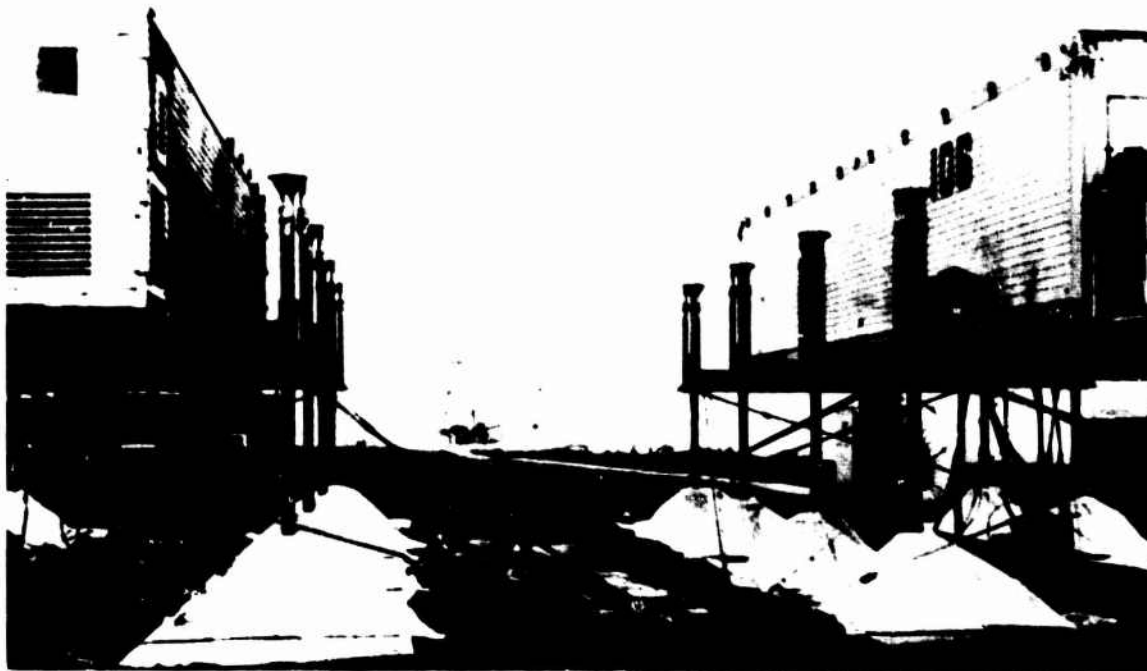
Fig. 9 - Two instrumentation trailers mounted on the FSGC system, view looking toward ground zero

Fig. 10 - Typical setup of FSGC system for Cannikin Event

Fig. 11 - Camera stations and fields of view for recording trailer park

the instrumentation trailers had moved from the collapsed raised boardwalk allowing easy safe entry into the trailers. All systems had operated as planned and we recovered 100% of the data.

One broken light fixture was the total damage in the nine shock mounted trailers. Nonoperational equipment, such as the four office trailers in the center of Fig. 12, were

damaged beyond repair. Only one surface ground crack extended under a shock mounted trailer.

The condition of a typical trailer is shown in Fig. 13. The mobile timing trailer, number 134, was tilted as shown in Fig. 14. Both measurement programs were completely successful. Acceleration data for all trailers, including 134, were in good agreement; the data averaged about 12% less than design conditions.

Fig. 12 - Recording trailer park after Cannikin detonation

The measured vertical motion of the ground and a typical trailer is shown in Fig. 15. The trailer accelerated at 2.5 g while the ground accelerated at 21 g peak. The trailer departed from the ground at about 300 msec after shock arrival while the ground was decelerating at -1.8 g. The ground was in a relative ballistic path for about 1.3 sec, but about 0.2 sec of this was at -1.8 g and the remainder was at -1 g. The trailer, on the other hand, was in a ballistic path at -1 g for about 1.4 sec. Impact in the ground was relatively low (11 g peak) and the trailer deceleration averaged 3 g.

Energy absorption strokes and final horizontal displacements of the trailers are summarized in Table 1. Except for trailer 134, the tilt in the longitudinal direction was negligible and the average tilt in the lateral

direction was 2%; one trailer tilted 8%. The average absorption stroke for each trailer was within 4% of the average for all trailers.

The vertical motion for trailer 134 was different. This trailer was very short (20 ft) and the most likely to tilt. Its motion was recorded by movie cameras. For the first 200 msec of the initial energy absorption stroke the trailer came straight down indicating that the center of gravity and shock isolator force coincided. The columns on the end of the trailer away from ground zero then froze. The remaining initial absorption stroke occurred at the four columns toward ground zero which induced a rolling motion into the trailer. This rolling motion continued while the trailer was in its ballistic path. The end of the trailer toward ground zero impacted first and all impact absorption occurred at the four columns toward ground zero. This trailer came to rest in a severe tilt, but the shock isolators did not bottom out. Average deceleration was 2.7 g and, except for one broken light fixture, there was no damage or operational loss. After disassembly each energy absorber on this trailer was tested statically. Two had load increase spikes of 25 and 55% in their stroke. These absorbers were located on opposite sides of the end of trailer 134 that froze up. Two absorbers were mounted at each column on this trailer so the effective load spikes would be much less.

During the vertical motion there was no relative horizontal motion between the trailer and the ground. After vertical impact, the trailers moved several feet from ground zero and then toward ground zero, finally coming to rest in the positions indicated in Table 1. None

Fig. 13 - Post-shot condition of a typical trailer

116

Fig. 14 - Post-shot condition of trailer 134

TABLE 1

CANNIKIN RTP Shock Isolation Displacements

Trailer	Vertical Absorption Stroke at Column (in.)			Final Horizontal Displacement (in.)	
	Left Side*	Right Side*	Average	Toward SGZ	Toward Right*
12	54.4	72.6	63.5	30	7
81	69.5	61.9	65.7	54	32
97	67.4	71.0	69.2	27	22
106	60.8	67.5	64.1	30	18
107	56.9	72.7	64.8	30	15
108	68.9	68.9	68.9	45	12
109	67.4	66.6	67.0	24	6
110	64.5	67.0	65.7	29	12
134	54.0	64.3	59.2	15	12

Average of all trailers except 134 = 66.1 in.

*Facing surface ground zero (SGZ)

of the anchors or nylon tethers failed. All horizontal motion occurred while the disks were on the low-friction pads, except at two places where the disks were half on the acrylic and half on the plywood pads.

There was good agreement between the actual absorption stroke values and the design. Trailer decelerations were low, as expected from pre-event testing. Large absorption strokes were avoided because the peak negative ground velocity was much less than the peak positive velocity. This effect was expected to occur but for conservatism it was ignored in the design analysis [2]. The accuracy of the ground motion predictions were verified by the dynamic motion data.

117
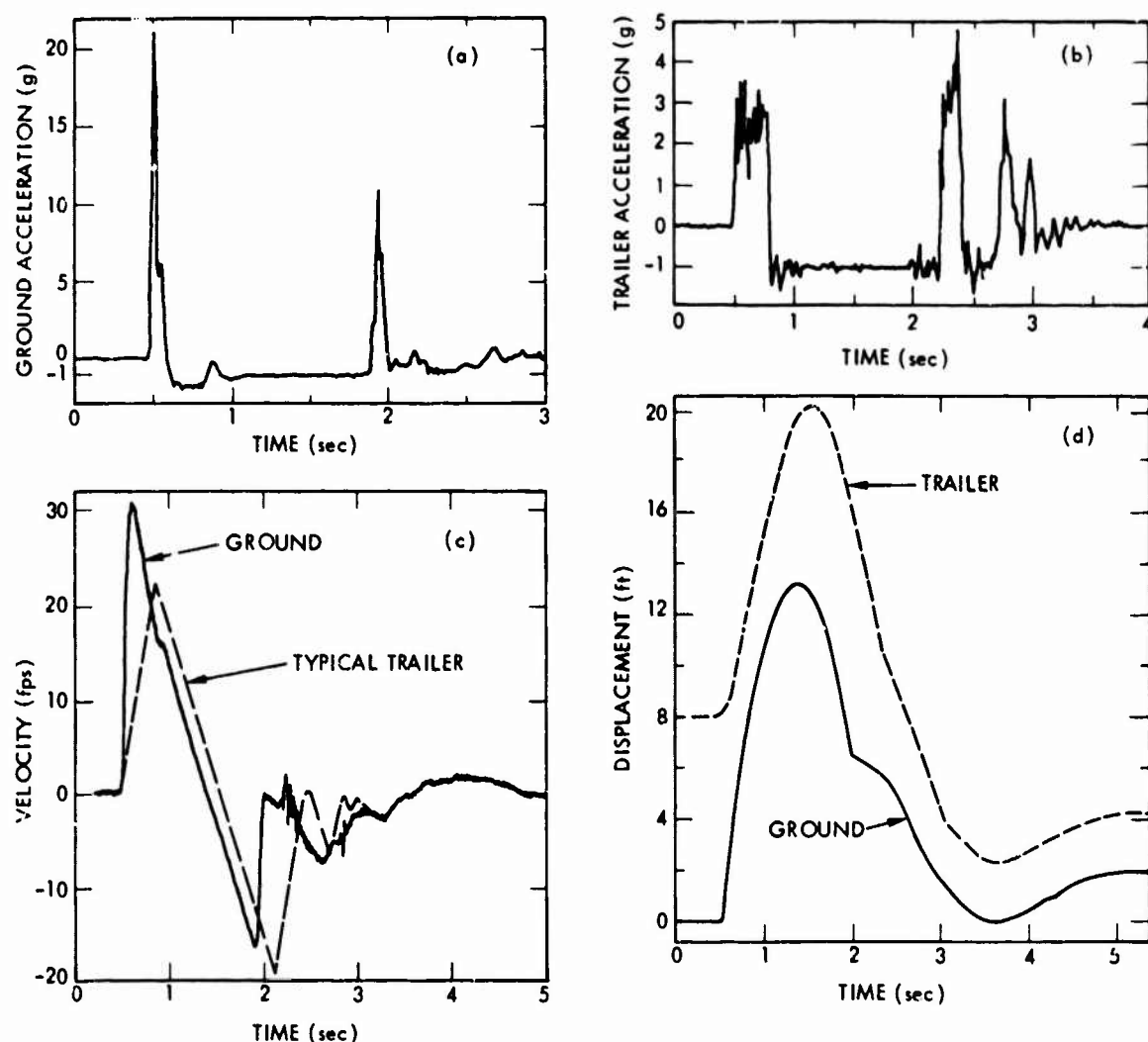
Fig. 15 - Measured vertical motion at recording trailer park during Cannikin Event.

Motion pictures showed many loose items flying into the air. Actually it was relative motion to the ground. This effect was primarily caused by the -1.8 g pulse during the first portion of the ground ballistic path.

Thirty-seven hours after detonation a subsidence slump occurred in the Cannikin area. This slump had a radius of 3000 ft but did not affect the recording trailers 2000 ft from ground zero.

REFERENCES

1. D. L. Bernreuter, E. C. Jackson, and A. B. Miller, "Control of the Dynamic Environment Produced by Underground Nuclear Explosives," U.S. Atomic Energy Commission Rept. CONF-700101, Vol. 2, pp. 979-993, May 1970

2. E. C. Jackson, "Operation CANNIKIN – Estimated Surface Ground Motion Effects," LLL Rept. UCID-15905, 1971

3. E. C. Jackson, A. B. Miller, and D. L. Bernreuter, "A Shock-Isolation System for 22 Feet of Vertical Ground Motion," The Shock and Vibration Bulletin, Bull. 42, Part 2, pp. 67-73, Jan. 1972

4. E. C. Jackson, "Portable Data System," LLL Rept. UCRL-73816, 1972

THE ACTIVE DAMPER -

A NEW CONCEPT

FOR

SHOCK AND VIBRATION CONTROL

Michael J. Crosby
Lord Corporation
Erie, Pennsylvania

and

Dean C. Karnopp
University of California - Davis
Davis, California

A new concept in shock and vibration isolation called the active damper is presented. The active damper is an externally control-lable force generator, where the force is developed by the rela-tive velocity of its attachment points. It provides isolation system performance which exceeds that of passive systems and approaches that of fully active systems, without significant ex-ternal power required. Computer simulation results demonstrate the performance of the active damper, compared to passive and fully active systems. Discrete sine wave and random disturbances were investigated for one and two degree of freedom systems. An elec-trohydraulic hardware implementation of the concept is described. Potential applications are discussed.

INTRODUCTION

In numerous applications, a mass is isolated from shock and vibration by interposing spring and damper elements between it and the disturbance. In such cases the mass, spring and damper elements act as a mechanical filter which attenuates the shock and vibra-tion energy reaching the mass. Typical systems of this type are vehicle sus-pensions, wherein springs and shock absorbers isolate the body of the vehi-cle from roadway disturbances. The use of rubber mounts, which are springs with inherent damping, to support sen-sitive equipment also utilizes this approach.

In the case of rigid bodies and linear springs and dampers, the solu-tions to the differential equations of motion are well known and isolation system design is straight forward. The design involves compromise between resonant amplification, high frequency attenuation, static and dynamic deflec-tion, and stability. Since the mass is usually predetermined, only the spring rates and damping coefficients can be specified in the design.

By utilizing nonlinear springs

and dampers, the forces they produce are functions of the relative displace-ment and velocity of their attachment points. This characteristic tends to limit their performance in many appli-cations.

To achieve greater system design flexibility and performance, active elements have been applied in isola-tion systems. In idealized form, an active suspension element is a control-lable force generator powered from an external energy source. Such devices can be programmed to produce forces which are functions of any desired system variable. By sensing system variables, such as absolute or rela-tive accelerations, velocities, or displacements and appropriately com-bining them, a command signal is devel-oped for the force generator. With such devices, isolation system perfor-mance is limited only by the amount of external power, the designer is willing to expend and system complexity.

An example of a simple active iso-lation system is the use of height controlled air bags for vehicle suspen-sion. Here the relative displacement

119

across the air spring is sensed. The
pressure in the air bag, is controlled
to maintain constant vehicle height.
The design flexibility achieved, is the
ability to lower dynamic spring rate
without excessive static deflection.

In the mounting of airborne equip-
ment, high performance pitch and roll
control has been achieved by using ac-
tive elements. They are controlled by
signals proportional to the absolute
angular accelerations of the equipment.

The primary limitation in the app-
lication of active elements to isola-
tion is the need for external power.
The problem is two fold. Where large
masses are to be isolated, the external
power requirements can easily become ex-
cessive. This is the case for high
performance vehicle suspension systems.

Secondly, the need for an external
power source requires the equipment to
generate the power or convert it to a
useable form. If the force generator
is to be hydraulically powered, pumps,
resevoirs, filters and valving would
be required. This auxiliary equipment
tends to increase isolation system weight
and decrease reliability.

Recognizing both the performance
benefits as well as the limitations of
active isolation elements, a new con-
cept in isolation was developed. This
concept involves the application of a
controllable force generator which does
not require significant external power.
Called an active damper, this device
produces a controllable force which is
derived from the relative velocity of
its attachment points. It, like the
externally powered active element, can
produce forces which are functions of
measured system variables which are
appropriately combined to form a com-
mand signal for the device. Since the
device does not utilize significant ex-
ternal power, its performance is more
limited than the fully active force gen-
erator.

This report describes the active
damper concept and some of its potential
applications. First, an idealized ac-
tive damper is defined. Its performance
is investigated analytically using com-
puter simulation and compared to that
of passive and fully active systems.
A prototype design of an electrohydrau-
lic active damper is then described
and its operation discussed. Potential
applications of the active damper are
finally presented.

SUMMARY AND CONCLUSIONS

The active damper is a new concept
in the control of shock and vibration.
It provides system performance inter-
mediate to that of a passive isolation
system and a fully active isolation
system.

The active damper is an externally
controllable force generator, where the
force is developed by the relative vel-
ocity of its attachment points. Essen-
tially a controllable energy dissipator,
it does not require significant external
power for its operation. Like the fully
active system, its output force is con-
trolled as a function of measured sys-
tem variables, such as velocities and
accelerations.

During portions of its operation
where the command force and available
force are in opposite directions, the
active damper is controlled to produce
essentially zero force. If the command
force exceeds the available force, the
active damper experiences a lock up
mode which transmits the maximum avail-
able force. Both of these conditions
degrade system performance relative
to a fully active system.

The performance of the active dam-
per in a single degree of freedom iso-
lation system was investigated by com-
puter simulation. The device was
controlled to generate a force propor-
tional to isolated mass velocity. The
results indicate that the system sig-
nificantly attenuated vibrational
inputs at and below the spring mass
natural frequency. The high frequency
performance was superior to a system
with a conventional damper. Overall
performance approached that of a fully
active system with isolated mass velo-
city feedback.

System performance in the pre-
sence of a random vibrational input
was favorable. It was significantly
better than a comparable passive sys-
tem and approached that of a fully
active system.

In a two degree of freedom, bounce/
pitch study, the active damper allowed
independent control of the two vibra-
tional modes. As in the case of the
single degree of freedom system, the
high frequency performance was signi-
ficantly better than the passive system.

A prototype design of an electro-
hydraulic active damper is presented.
The design utilizes conventional hy-
draulic components to implement the
active damper concept.

Results to date, suggest that the active damper can be successfully applied to achieve high performance vehicle suspensions and vibration and shock isolation systems. Impact cushioning and tuned absorbers are additional potential applications which have not been investigated as yet.

ANALYSIS OF THE IDEALIZED ACTIVE DAMPER

The active damper is a device which produces an instantaneously controllable force which is derived from the relative velocity of its attachment points. The device is shown schematically in Figure 1a.

In the figure, the velocities of the attachment points are indicated by $\overset{\circ}{X}$ and $\overset{\circ}{X}_o$, respectively. A relative velocity, $\overset{\circ}{X}_R$, is defined as follows:

$$\overset{\circ}{X}_R = \overset{\circ}{X}_o - \overset{\circ}{X} \qquad (1)$$

The force produced at the attachment points, F_{actual}, is derived from the relative velocity $\overset{\circ}{X}_R$ and is defined in the directions indicated.

The active damper is represented by a viscous damper symbol with an arrow which indicates an instantaneously variable damping force. The dashed line indicates that the damping force is controlled from a command signal, $F_{command}$. In general, the commanded force is a function of one or more time varying signals. These signals are normally obtained from measured system variables, such as displacements, velocities, accelerations or forces, which may be modified by appropriate signal conditioning.
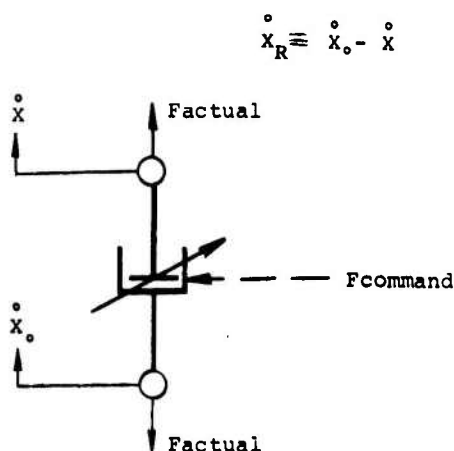
Although the basic damper symbol conventionally represents viscous damping, it is to be understood that any type of basic damping mechanism can be used. This would also include square law fluid throttling, friction, electro viscous, or electro mechanical implementations. The only requirement is that the basic mechanism be an energy dissipator, that is one which produces a force in phase with relative velocity.

The utilization of fully active systems allows the design of very versatile, high performance isolation systems, but the cost, complexity and weight of the required power sources has limited their widespread application. Therefore, the intent of the active damper is to approach the performance of fully active isolation devices without the need for external power.

Compared to fully active elements, the active damper has the following limitations:

1. The active damper can produce a force only when a relative velocity is present across the attachment points.

2. There will be time intervals when the direction of the available force from the active damper is opposite to the direction of the desired force. During these intervals the active damper must be controlled to produce zero force.

3. If the commanded force exceeds that which can be produced with a finite damping coefficient, the damper is controlled to a locked up or rigid link mode. In this mode, the maximum force which can be produced is limited to the inertial forces derived from accelerating the attached masses less the algebraic sum of other forces acting on the masses.

These conditions are illustrated in Figure 1b.

It should be noted that the active damper responds to a commanded force, not a commanded damping value. If the latter approach were used, the damping force would be a function of relative velocity. This would require that the controller sense relative velocity and adjust the damping value to compensate, in order to produce a desired force.

$$\overset{\circ}{X}_R \equiv \overset{\circ}{X}_o - \overset{\circ}{X}$$

Figure 1a

Active Damper Schematic
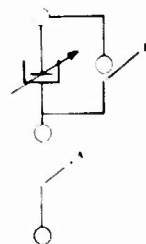
Mode	Constraint	A	B
Off	F Command and F Available in Opposite Direction	Open	Either
Lockup	F Command = F Available	Closed	Closed
On	Except as Above	Closed	Open

Figure 1b

Active Damper Modes

In general, the application of the active damper is similar to that of fully active devices. This may be illustrated by comparing its performance to that cf fully active devices in representative isolation systems. Further comparison with passive isolation devices demonstrates that the active damper provides performance intermediate between passive and fully active systems.

A single degree of freedom system illustrates the relative performance of passive, active and active damper isolation.

Passive Isolation

A conventional passive isolator is shown in Figure 2. It consists of a spring and viscous damper which support the mass to be isolated.

Writing the equations of motion and taking the Laplace transform yields the transfer function relating the motion of the mass, X, to the motion of the base, X_o. This transfer function follows:

$$\frac{X}{X_o} = \frac{BS + K}{MS^2 + BS + K} \tag{2}$$

Here S is the independent variable in the Laplace transformed equation. For frequency response analyses, S is replaced by $j\omega$ where $j = \sqrt{-1}$ and ω represents the frequency in radians/second. The undamped natural frequency of this system is $\sqrt{K/M}$ and the damping ratio is $B / 2\sqrt{KM}$. Plotting the amplitude ratio, X/X_o, versus frequency, ω, on log-log paper gives the familiar transmissibility plot, Figure 3.

For this plot, the undamped natural frequency is unity and various damping ratios from 0.1 to 2.0 are shown. In general, the figure indicates attenuation of the output amplitude

above the resonant frequency, an amplification at resonance and unity gain at low frequencies. In the isolation or attenuation region, the slope of the curve becomes asymtotic to minus one. The isolation region can be extended by decreasing the spring stiffness, K, or by increasing the mass, M. Since the mass is usually predetermined, the designer selects K to yield the desired natural frequency. The constraint on K is the initial displacement of the spring due to the weight.

Control of the resonant amplitude is achieved by the damper. This reduction is accompanied by decreased isolation above resonance in the isolation region. If no damping were present, the amplitude at resonance would be infinite. The high frequency amplitude would be asymtotic to a slope of minus two, giving superior isolation there. Thus, the selection of damping is a design compromise.
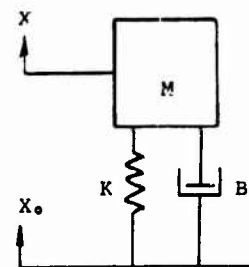

Figure 2

Passive Isolator
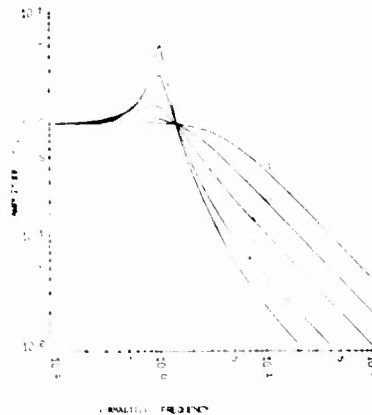
122

Figure 3

Amplitude Response - Passive Isolator

Active Isolator

A typical active isolator is shown in Figure 4. It is represented by an idealized controllable force generator and a conventional spring. Here the force generator is controlled by an isolated mass acceleration signal and velocity signal generated by integrating the acceleration signal. The acceleration and velocity gains are k_1 and k_2 respectively. The integration is represented by the $1/s$ term.

Writing the equations of motion and taking the Laplace transform gives the transfer function of the active system.

$$\frac{X}{X_o} = \frac{K}{(M + k_1)S^2 + k_2 S + K} \qquad (3)$$

As is evident by the equation, the undamped natural frequency is given by $\sqrt{K/(M + k_1)}$. Since k_1 can be arbitraily selected to a positive or negative value, the system natural frequency can be adjusted to any desired value. Positive k_1 will produce a low natural frequency and increase the isolation region. Thus K can be selected to produce the desired static deflection.

The damping ratio of the active system is given by $k_2/2 \sqrt{(M+k_1)K}$ Thus, any desired damping ratio can be achieved by selecting an appropriate value of k_2. It should be noted that the numerator of the transfer function is a constant. Therefore the high frequency amplitude is asymptotic to a slope of minus two. Thus the use of the active isolator allows

control of resonant amplitude without compromising high frequency performance. Figure 5 shows typical transmissibility plots for the active isolator with various damping ratios.

The active system allows for the design of higher performance isolation systems. The penalty of course, is the requirement for external power to generate the controllable force and the complexity and cost of this equipment.
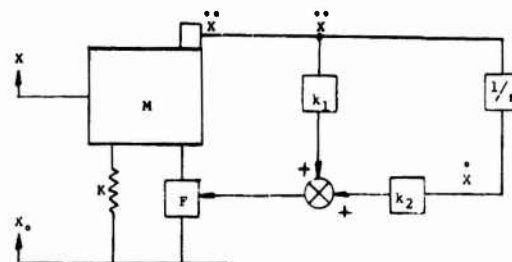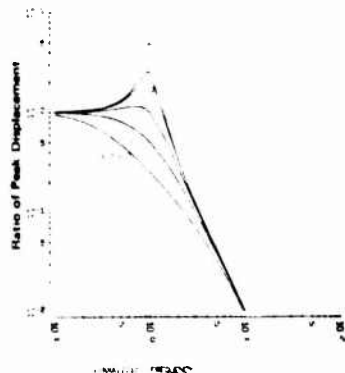

Figure 4

Active Isolator

123

Figure 5

Amplitude Response - Active Isolator

Active Damper

Figure 6 illustrates the application of the active damper to single degree of freedom isolation. As in the case of the fully active isolator, the velocity and acceleration of the isolated mass are measured. The active damper is commanded to produce a force proportional to the sum of these signals.

Due to the limitations of the active damper as previously discussed, we expect its performance to approach, but not equal, that of the fully active system.

An example of the results obtained from computer simulation of the active damper as shown in Figure 6 follows. In this example the effect of mass velocity feedback is investigated. The acceleration gain, k_1, is set equal to zero. The velocity gain, k_2, is set to the value which would give the indicated system damping ratio in the equivalent fully active system.

Figure 7 shows time history plots of the displacements and velocities of the base and mass, and the damper output force, F_D. Also shown is the total suspension system force, F_S, which is the algebraic sum of the spring and damper force.

In Figure 7a the velocity feedback gain, k_2, is set to give a system damping ratio of 1.00. The base displacement input frequency is equal to 0.5 times the system natural frequency.

The plot of damper force versus time shows that the damper turns off twice during each cycle. This indicates that the relative velocity across the damper is in a direction opposite the command force, that is, a force proportional to body velocity, $\dot{X}$.

The velocity plot shows that $\dot{X}$ and $\dot{X}_0$ are equal during portions of the cycle. This indicates the lock up condition, resulting from commanding a force higher than that available from the active damper.
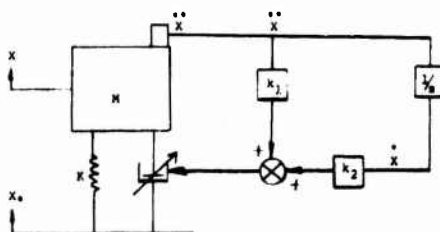

Figure 6

Active Damper Isolation

The bottom plot shows the somewhat nonlinear mass displacement, due to the nonlinear force generated by the active damper.

It also indicates the attenuation of the displacement even though the excitation is below the resonant frequency.

Figure 7b shows the operation of the same system at 1.5 times resonant frequency. Here the damper ~ e is zero during portions of the cycle but no lock up occurs as evidenced by the velocity plots. The displacement plot shows significant attenuation of the base induced disturbance.

To investigate the operation of the active damper in this system, several damping ratios and excitation frequencies were examined. The ratio of the output displacement to input displacement are plotted versus frequency for various damping ratios in Figure 8.

As shown, the performance of the active damper approaches that of the fully active isolation system as shown in Figure 5. For the higher damping ratios, the base disturbance is attenuated below and through system resonance. Furthermore, the high frequency attenuation has a slope of minus two which gives superior isolation in this region to that of the passive isolation system.
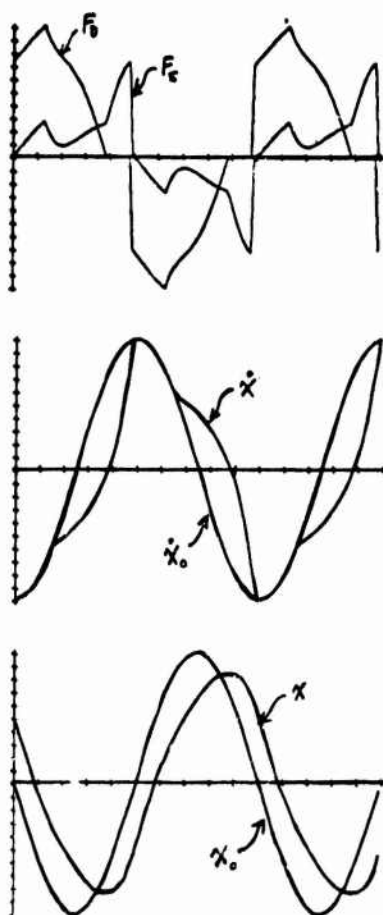
FREQ RATIO = 0·50
DAMP RATIO = 1·00

FREQ RATIO = 1·50
DAMP RATIO = 1·00

Figure 7a

Active Damper Simulation Results
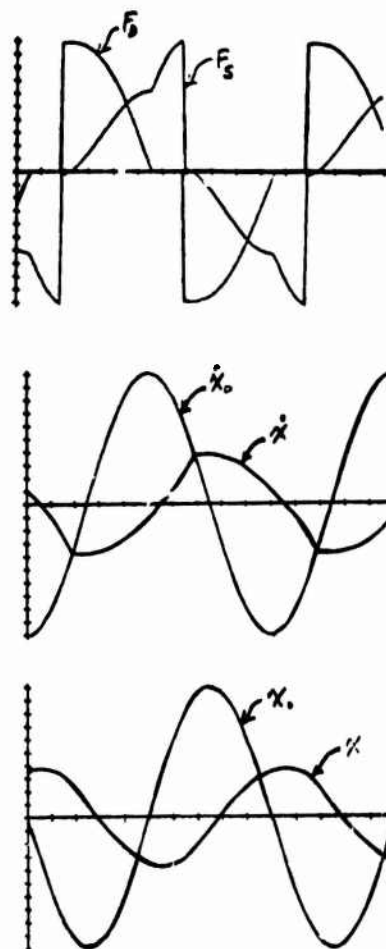
Figure 7b

Active Damper Simulation Results

125

The attenuation at and below resonance gives the system characteristics similar to that of a lower natural frequency isolator, which is highly desirable. This is achieved without reducing spring rate which is favorable from a static deflection point of view.

In Figure 9, the displacement amplitude ratios of the passive system are compared to that of the fully active and active damper systems with body velocity feedback. It shows the superior isolation of the active damper and fully active systems. It also indicates that the active damper system approaches the fully active system in performance.

Active Damper with Random Input

In many applications, an isolation system is subjected to random disturbances. The performance of the active damper subjected to a typical roadway disturbance was investigated and compared to a conventional passive isolator and a fully active isolator with velocity feedback.

To perform these studies a random base displacement was generated and used to excite a computer simulation of the isolation systems. Figure 10 shows the power spectral density plot of the input disturbance. It is representative of a typical roadway input.

Figure 8

Amplitude Response - Active Damper

Figure 9

Amplitude Response Comparison

126

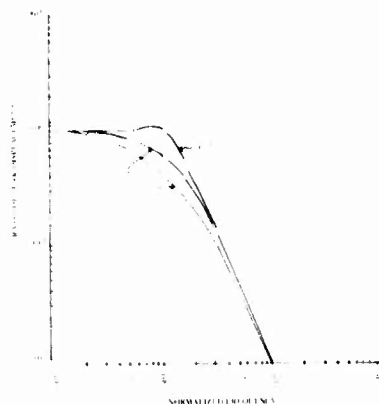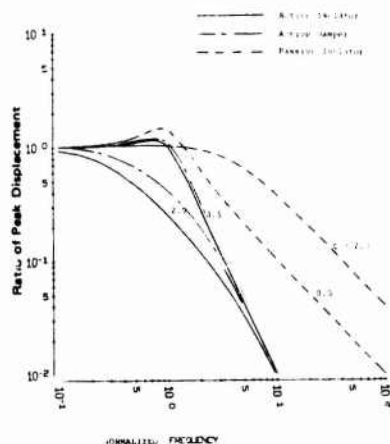The resulting power spectral density of the acceleration of the isolated mass for the various systems with a damping ratio of 0.5 are shown in Figure 11a. These were obtained by analyzing the time history plots of the mass acceleration as obtained from the computer simulation. The natural frequency of all systems was 1.0 Hz.
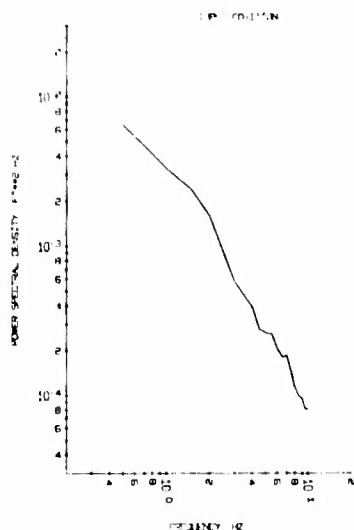
Figure 10

Power Spectral Density - Base Displacement
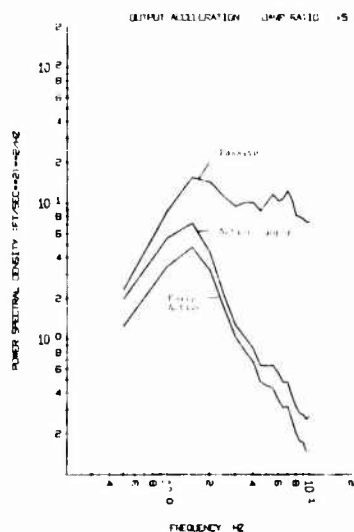
Figure 11a

Power Spectral Density -

Isolated Mass Acceleration
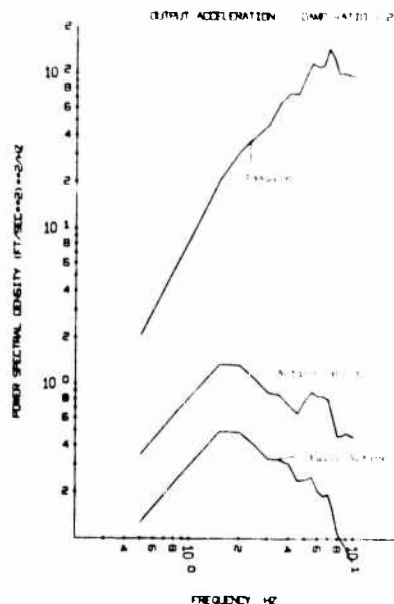
Figure 11b

Power Spectral Density -

Isolated Mass Acceleration

As shown in Figure 11a, the performance of the fully active and active damper systems is superior to the passive system at all frequencies. This effect is most pronounced at frequencies above system resonance. Here the passive isolator damper transmits significant accelerations to the isolated body since it produces forces proportional to relative velocity.

The performance of the active damper approaches that of the fully active system. The nonlinear characteristics of the active damper tend to increase the disturbance energy at high frequencies as compared to the fully active system, however. The performance of the active damper through resonance is similar to that of the fully active system but is somewhat degraded.

Figure 11b presents body accelerations for the same input disturbance with the system damping ratio set at 2.0. Here the high frequency performance of the passive system is seriously degraded. The fully active and active damper system are again comparable. The high frequency degradation of the active damper is somewhat more pronounced. The apparent decrease in system natural frequency for both active systems is evidenced

127

by their excellent low and mid-frequency isolation performance. A further illustration of the performance of these systems subjected to the random disturbance is given in Figure 12. The base displacement versus time is the dashed line. The position of the isolated mass is given for the passive, fully active and active damper systems. The body velocity feedback is set for a damping ratio of 2.0. The natural frequency of each system is 1.0 Hz.

body to the input disturbance, X_0. The spring rates and geometry give a heave natural frequency of 1 Hz. and a pitch natural frequency of 4 Hz. Selection of passive dampers to give a heave damping ratio of 0.25, gives a pitch damping ratio of 1.00 as determined by geometry. As indicated by Figure 14 the high frequency response has a slope of minus one due to the passive dampers responding to relative velocity.
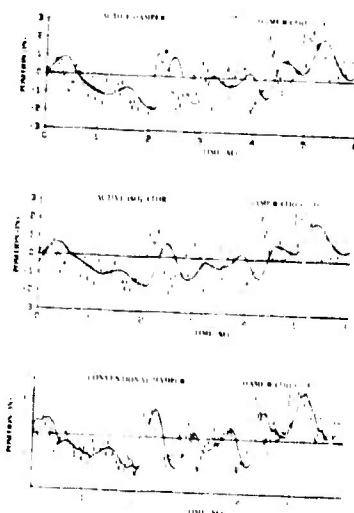
Figure 12

Displacement Time Histories

Two Degrees of Freedom Isolation

The active damper can be applied as an isolator in systems with multiple degrees of freedom. For example, a two degree of freedom pitch/heave system is shown in Figure 13. The pitch is designated by the angle θ and the heave by Z, the vertical displacement of the mass center of gravity. In general such a system would have disturbances through both isolators, but for simplicity a single input disturbance, X_0 is illustrated.

In this example the active dampers are controlled to generate forces proportional to a combination of body vertical and angular velocities as indicated in Figure 13. In this manner the damping of the pitch and heave modes can be independently controlled by adjusting k_1 and k_2. Excellent high frequency isolation is obtained since the dampers do not produce forces proportional to relative velocity.

In Figure 14 are compared the amplitude ratio of the point X on the

The fully active and active damper system gains were selected to give unity damping ratio for both pitch and heave modes. As before, the active damper approaches but does not equal the performance of the fully active system. As in the case of the single axis system, significant attenuation is achieved through the resonance region. The high frequency isolation follows a slope of minus two.

128
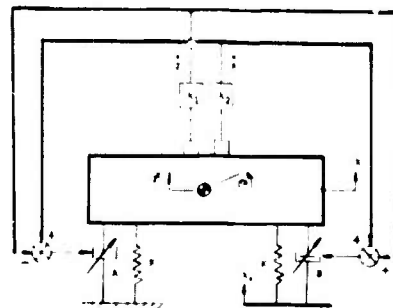
Figure 13

Two Degree of Freedom

Active Damper Isolation System
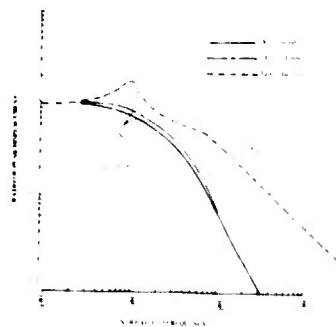
Figure 14

Two Degree of Freedom Amplitude Response

Hardware
Implementation

The active damper concept requires a controllable force generator where the force is derived from relative velocity of the attachment points. The device must be an energy dissipator or damper to insure that external power need not be supplied to vary its coefficient.

One of the criteria in selecting an appropriate damping mechanism is the ability to readily control its damping properties. Another, is the availability of materials and components for its construction.

Fluid damping is a prime candidate on both counts. A great deal of prior art exists, which utilizes throttled fluid as a damping mechanism. This art includes shock absorbers for vehicle suspensions, hydraulic decelerators and similar devices.

The addition of suitably controlled valving to these devices provides the essential elements of the active damper.

Figure 15 is a schematic representation of an active damper using these elements. A piston and cylinder with an integral accumulator is used to generate mechanical force from hydraulic pressure. The pressure is externally controllable through a pair of pressure relief valves as indicated. The upper valve controls damper force in tension. The lower valve regulates the output force in compression.

To illustrate the operation of the device, assume the relative velocity of the attachment points is decreasing the distance between them. This tends to force fluid from the lower chamber, through the external conduits to the upper chamber.

129

Figure 15

Electrohydraulic Active Damper Schematic

If a compression force is commanded, a control force proportional to the desired force is applied externally to the stem of the lower poppet valve. Zero external control force is simultaneously applied to the upper poppet valve.

The weak poppet valve spring, aided by the increased pressure in the lower chamber closes the upper valve. The lower valve opens to that area such that the pressure drop across the valve times the valve area equals the external command force. The poppet valve spring rate is assumed negligible.

Since the pressure drop across the lower valve is applied acrossed the piston, the output force is proportional to the applied command force. Specifically, it is amplified by the ratio of piston area to valve area.

For constant command force, the output force is independent of the relative velocity of the end points. If this velocity increases, the poppet valve assumes that area required to maintain the desired pressure drop.

In general, the command force will be a function of measured system variables, and will vary accordingly as a function of time. As the command force is modulated, the output force will follow proportionally.

If a tension force is commanded, the external force on the lower valve is made zero and an external force is applied to the upper valve. With the attachment points distance decreasing,

the upper valve remains closed. The lower valve opens fully, producing essentially zero pressure drop and zero output force from the damper.

This is the case previously discussed, where the damper produces zero output force if the commanded valve is opposite to that attainable for the existing relative velocity.

With the relative velocity of the attachment points in the opposite direction the process reverses. In this case, the lower valve remains closed. The upper valve controls the output force when tension is commanded. If compression is commanded, the upper valve opens producing essentially zero output force.

If the relative velocity is at any time insufficient to produce the required flow to achieve the commanded pressure drop, the controlling valve reaches the fully closed position. Then both valves remain closed and the lock up case occurs. Here the damper is transmitting the maximum possible force which is less than that commanded. At that time when the damper can again achieve the commanded force, the controlling valve re-opens and controls the output force.

In summary, the active damper illustrated in Figure 15, controls the throttling of fluid produced by relative velocity of the attachment points. It utilizes small forces and displacements of the poppet valves to control the amplified forces and displacements of the piston. It will produce commanded forces in tension or

130

compression if possible. If the relative velocity is in the wrong direction, it provides essentially zero force. If a force is commanded which exceeds that available, it locks up, providing maximum available force for that interval.

Figure 16 illustrates a breadboard version of this concept. Here, commercially available pressure relief valves are used. The pressure relief setting of these valves is electrically controllable from an external signal. They produce a pressure drop proportional to the applied voltage, as illustrated. Diode networks direct the command signal to the proper valve to achieve either tension or compression forces.

The controller accepts measured system variable inputs and produces a single output voltage proportional to desired damper force. For example, the controller could consist of an adjustable gain for the isolated mass velocity signal. This was one of the cases investigated analytically. In general, the controller would consist of gain, summing and filter elements operating on appropriately selected system variables.

Although the active damper illustrated is electrically controlled, in certain cases direct hydromechanical control is possible. For example, a spring, mass and damper could be used to sense isolated mass acceleration or velocity and directly control pressure relief valves. Fluid connections between dampers could be utilized with appropriate valving to control pitch and roll modes directly. The optimum hardware implementation is of course dependent on the specific application.

APPLICATIONS

The active damper represents a new class of components for application in shock and vibration isolation systems. Utilization of devices of this type can provide system performance intermediate to passive and fully active systems. Broad application catagories include vehicle suspension, vibration and shock isolation, impact cushioning, and tuned absorbers.

Vehicle Suspension

In vehicle suspension, the active damper can be used in parallel with conventional springing to attain increased isolation and stability. For example, by appropriate use of active dampers, significant attenuation of vibration and shock can be attained at and below the spring-mass natural frequency. As demonstrated analytically, this improvement can be obtained without sacrificing high frequency performance. Achieving increased isolation through active dampers allows the designer to use stiffer springing, which increases pitch and roll stability and minimizes static deflection. As demonstrated in the two degree of freedom analyses, independent control of bounce and pitch modes, is also possible with active dampers.

Suspension systems which require multiple feedback loops to achieve the required performance might use an electrohydraulic active damper. Vehicle velocities and accelerations could be measured and appropriately filtered to generate the command signal.

Suspensions requiring only isolated mass vertical velocity or acceleration feedback could utilize a self
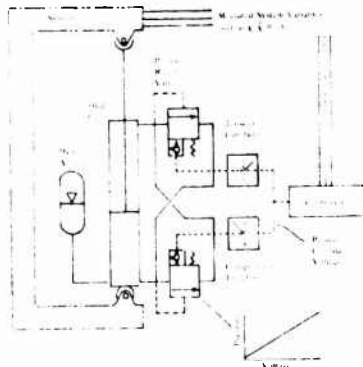

Figure 16

Breadboard Active Damper System

131

contained hydromechanical active damper. This type of device would be similar to a conventional damper in external configuration and installation.

Vibration and Shock Isolation

Performance benefits attainable with active dampers in vibration and shock isolation systems are similar to those described under vehicle suspensions. Increased vertical isolation and independent pitch and roll control are possible by using active dampers with a variety of spring elements.

Pitch and roll control of self leveling pneumatic spring isolation is a probable application. A decrease in apparent natural frequency of rubber mounted equipment is another probable use of active dampers.

In general, vibration and shock isolation systems will require a large range in active damper capacity. Typical specific applications include isolation of precision avionics and reconnaissance equipment, operator seating, helicopter rotors, and large bases and platforms.

Impact Cushioning

Since the active damper is a controllable energy dissipator, it should provide a high degree of design flexibility in impact cushioning systems. Current hydraulic decelerators have predetermined nonlinear damping versus stroke characteristics. This allows for uniform deceleration of a known mass with known initial velocity. Some devices are manually adjustable to utilize the entire stroke and thereby minimize deceleration forces for a specific mass and initial velocity.

The active damper, being externally controllable, could be automatically adjusted to minimize deceleration forces where the mass and initial velocity are unknown. This feature could be highly desirable for such application as dock fendering and material handling. The use of the active damper in impact cushioning has not been investigated to date.

Absorbers

The active damper should introduce additional flexibility to the design of tuned vibration absorbers. By connecting the active dampers in series with springs attached to the absorber mass, it should be possible to automatically vary the absorber

resonance. Since the active damper includes a zero force and lock up mode, as well as the controllable force mode, it can act as a variable stiffness linkage to control the effective spring rate of the absorber. This type of application has not been investigated to date.

132

Mr. Snowdon (Pennsylvania State University)
Would the system be confused if you were dealing, for example, with an input comprised of two predominate frequencies, one very low and one very high with roughly 180 degrees of separation. Is this automatically taken care of or would it present problems for the isolator?

Mr. Crosby: We did some studies with two sine wave inputs and the system was able to take care of it. I think, in the limit, the random excitation is probably the limiting case. If it can perform under random, it should be able to handle any multiplicity of single sinusoidal inputs.

Mr. Masur (Radiation, Inc.): What motions are you encountering? Looking at the picture that you had of the little isolator, it looked as if you had to have quite a bit of motion in order to get any amount of force to work with your isolator.

Mr. Crosby: In the linear case it was independent of the motion and we modeled this such that during the time it was turned on, it was linear. In other words, it was independent of the amplitude. We didn't really get down to worrying about making an orifice-type control where you get very small motions, so that if you are on the low part of the square law curve, you are going to have low forces out. If you're going to design a device for very low motions, you might go to a viscous flow and control, or maybe its an electro-mechanical device or even a controllable Coulomb friction device. There's a great deal of flexibility in the implementation of the basic concept. I think you have to tailor the specific actuation device to the problem. Is it large or small motion. What kind of an environment is it in? You would have to study those cases individually.

Mr. Masur (Radiation, Inc.): All those curves you have shown us, were they of an actual isolator or were they just some hypothetical calculations that you did?

Mr. Crosby: In this particular case, the curve that we have shown are from the nonlinear computer simulation studies. We are in the process of developing some breadboard and prototype electrohydraulic devices and are hopeful that, at the next meeting we will be able to present some good experimental data.

Mr. Paladino (Naval Ship Systems Command): We in the Navy have been interested in these active systems. Just how would you propose to handle your phase and response to a frequency and amplitude that you are interested in bucking out, and still have your sensor be immune to all other forms of vibration that you are not interested in? Is your response time fast enough with this servo system?

Mr. Crosby: The hardware that we are looking at right now, is on the order of 15 Hz response, that is with the electrohydraulic implementation. If you go to smaller, like reconnaisence type applications, you might be able, using electromagnetic devices, to get this higher response. If you are dealing with very large structures, such as you might have on shipboard, you might be down lower than that. It depends upon the specific implementation. In terms of the ability to control certain frequencies and reject other frequencies, you can use that same electrical filtering device. You could use, with a fully active system, an electrically controlled thing. You could use filtering. We have not really investigated the use of band-pass filters for this device, although this is something we should investigate.

VIBRATION CHARACTERISTICS OF SKIN-STRINGER STRUCTURES

J. P. Henderson
Air Force Materials Laboratory
Wright-Patterson AFB, Ohio 45433

Results of transfer matrix analysis of the vibrations
of flat and curved skin-stringer structures are presented
in the form of resonant frequencies, mode shapes, moment
distributions, and the forced response of damped structures.
The response of a five panel laboratory specimen is com-
pared with a 56 panel complete structure, and theoretical
predictions for the response of flat structures are compared
with experimental data. In addition, the effects of cir-
cular curvature on the resonant frequencies and mode shapes
in a five panel structure are discussed.

INTRODUCTION

One of the most commonly used types
of aircraft construction is the skin-
stringer structure. A typical fuselage
of this type consists of a thin metal
skin stiffened in one direction by heavy
frames and by lighter stringers normal
to the frames. In recent years consid-
erable effort has been applied to
analysis of both the forced and free
vibration of this type of structure.
This effort has been prompted by con-
cern over the response of structures to
acoustic excitation and the resulting
fatigue problems, as well as interior
noise problems caused by the vibrating
structure acting as an acoustic source.
Efforts to reduce these problems through
more sophisticated design procedures
and the efficient utilization of damping
materials require detailed information
on the frequencies of maximum response
and the distributions of the dynamic
strains and displacements.

Several recent papers have discussed
the development of analytical techniques
for predicting vibration response of
this type of structure. Most recently,
advances in the application of transfer
matrix analysis have made it possible
to analytically evaluate the effects of
circular and noncircular curvature in
the structure [1,2,3], stringer-width
[4], stringer stretching [2], and the
effect of tuned viscoelastic dampers

on the response of skin-stringer struc-
tures [2].

It is the purpose of this paper to
discuss the vibrational characteristics
of skin-stringer structure predicted by
these analytical techniques and compare
these results with some recent experi-
mental measurements. No attempt will
be made to present the detailed mathe-
matics involved in transfer matrix
analysis, since discussions of this type
of analysis are available in other pub-
lications [1-5]. Instead it is intended
to present a review of resonant fre-
quencies, modes shapes, moment distri-
butions, and forced frequency response
functions that can be expected in this
type of structure.

Validity of the Analysis

Although the details of the analy-
sis will not be presented here, it is
appropriate to review the assumptions
of transfer matrix analysis and to dis-
cuss how the mathematical model relates
to real aircraft structures. The most
important assumption in this type of
analysis is that the vibrational charac-
teristics of the panels in a complete
structure can be reasonably predicted by
considering rows of panels, stiffened
by stringers, and supported on the edges
by stiff parallel frames which are ass-
umed to act as simple supports. Although
such a row of panels certainly does not

135

represent all the properties of an aircraft fuselage, there is experimental evidence indicating that these assumptions can lead to quite useful engineering predictions of the vibrations occuring both in laboratory specimens [6] and real aircraft structures [7, 8], particularly if the frames are spaced farther apart than the stringers. Applying this boundary condition assumption and assuming that the steady state motion of the structure varies harmonically with time, the displacements and forces of primary interest can be expressed as:

displacement in x direction
$$u = \sum_{n=1}^{\infty} \tau_n(s) \cos \frac{n\pi x}{b} e^{i\Omega t}$$

displacement in s direction
$$v = \sum_{n=1}^{\infty} \psi_n(s) \sin \frac{n\pi x}{b} e^{i\Omega t}$$

displacement in z direction
$$w = \sum_{n=1}^{\infty} \phi_n(s) \sin \frac{n\pi x}{b} e^{i\Omega t}$$

rotation about x axis
$$\beta = \sum_{n=1}^{\infty} \frac{d\phi_n}{ds}(s) \sin \frac{n\pi x}{b} e^{i\Omega t}$$

bending moment
$$M_s = \sum_{n=1}^{\infty} \bar{M}_n(s) \sin \frac{n\pi x}{b} e^{i\Omega t}$$

Kirchhoff shear
$$V_s = \sum_{n=1}^{\infty} \bar{V}_n(s) \sin \frac{n\pi x}{b} e^{i\Omega t}$$

where $V_s = Q_s + \dfrac{dM_{sx}}{dx}$

in-plane tension
$$N_s = \sum_{n=1}^{\infty} \bar{N}_{s_n}(s) \sin \frac{n\pi x}{b} e^{i\Omega t}$$

and

in-plane shear
$$N_{sx} = \sum_{n=1}^{\infty} \bar{N}_{sx_n}(s) \cos \frac{n\pi x}{b} e^{i\Omega t} \quad (1)$$

Figure 1 shows the sign convention assigned to these displacements and forces.

The transfer matrix analysis of curved structures is formulated by determining the relationship between the state vector at some arbitrary initial location in the structure, for example $s = s_0$, and the state vector at any
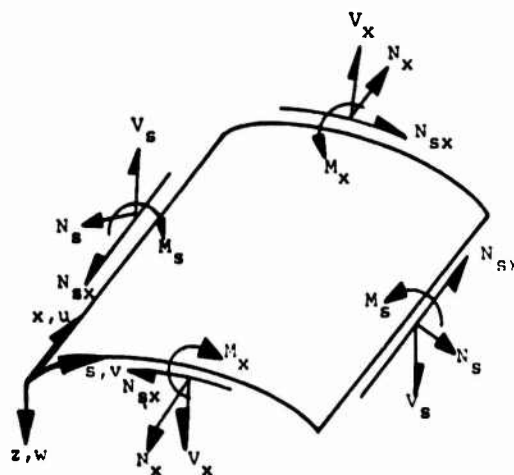
other loaction, $s = s_1$.

Figure 1. Sign Convention for Curved Panels.

This state vector of displacements and forces at any point in the shell can be defined for a given frequency Ω as:

$$\{Z_n(s)\} = \{\tau(s), \psi(s), \phi(s), \bar{\beta}(s), \bar{M}(s),$$
$$\bar{V}(s), \bar{N}_s(s), \bar{N}_{sx}(s)\}_n \quad (2)$$

where it is understood that the $\{\ \}$ indicate a column vector. The elements in this state vector are complex valued when damping is present in the structure. A non-dimensional state vector can also be defined as:

$$\{Z_n(s)\} = \left\{ \frac{\tau}{h}, \frac{\psi}{h}, \frac{\phi}{h}, \bar{\beta}, \frac{\bar{M}h^2}{D}, \frac{\bar{V}h^2}{D}, \frac{-\bar{N}_s h^2}{D}, \right.$$
$$\left. \frac{\bar{N}_{sx}h^2}{D} \right\}_n \quad (3)$$

where the functional notation indicating dependence on s has been omitted for simplicity, but is still implied. Nomenclature is defined in Table 1.

Provided that there are no externally applied forces between s_0 and s_1, the basic transfer matrix relationship is of the form

$$\{Z_n(s_1)\} = {}_1[T_n]_0 \{Z_n(s_0)\} \quad (4)$$

136

where $_1[T_n]_0$ is an 8 by 8 transfer matrix which has a unique value at each frequency Ω. This transfer matrix is the chain product of field transfer matrices $[U_n]$, representing transfer across a shell segment, and stringer tranfer matrices $[P_n]$.

Derivation of each type of transfer matrix is described in reference [2] along with methods of formulating the analysis of the forced vibration of a row with a moderate number of curved panels and with arbitrary boundary conditions at each of the rows. Complete shells, with a large number of panels arranged in a periodic manner have been analyzed by formulating a difference equation relationship from the basic transfer matrices (9).

Response of Segments of Structures Compared with Complete Shells

It is interesting to compare the calculated response of a typical laboratory specimen, such as the five panel segment of curved shell shown in Figure 2, with the response of a corresponding complete shell with 56 identical panels as shown in Figure 3. The calculated nondimensional displacement response of the center point of five panel segment is shown in Figure 4, for the case in which the structure is excited by a harmonic force f distributed along a line in the middle of the structure, where

$$f(x,\Omega) = F \sin \frac{\pi x}{b} \, e^{i\Omega t} \qquad (5)$$
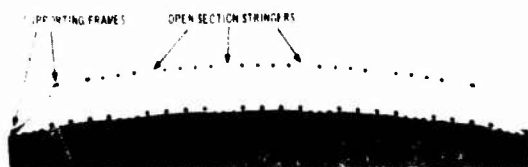
Figure 2. Five Span Curved Skin-Stringer Laboratory Test Specimen.

Inherent structural damping of the riveted structure was modeled by assuming complex stiffness, with a loss factor $n_p = .05$, in the stringer. Damping in the panels was not accounted for. This approach seems reasonable, since most of the inherent structural damping is due to the riveted joints and not hysteresis in the materials (10, 11). The value of stringer loss factor was selected to approximate typical overall damping as measured in actual structures [4]. The three response peaks correspond to symmetric

modes for which n = 1 in equation (1); that is, in the frequency range shown, there is no response in modes with node lines parallel to the frames.

Table 1

DIMENSIONS AND PROPERTIES OF STRUCTURES
used in calculations presented in Figures 12-19.

Young's Modulus $E = 10.5 \times 10^6$ Lb/in^2

Poisson's ratio $\nu = 0.3$

distance between frames $\quad b = 14$ in.

skin thickness $\quad h = .050$ in.

distance between stringers $\quad a_1 = 2\ell_c = 6$ in.

stringer area $\quad A = .2200$ in.^{2}

stringer dim* $\quad A_z = 0.4117$ in.

stringer dim* $\quad C_z = 0.7912$ in.

mass density $\quad \rho = .101/386$ Lb·sec^2/in^4

STRINGER MOMENTS OF INERTIA:

transverse $I_\eta = 3.5831 \times 10^{-2}$ in^4

in plane $I_\xi = 3.5433 \times 10^{-2}$ in^4

polar (mass) $J_A = 2.6939 \times 10^{-5}$ Lb·sec

TORSION CONSTANTS

St. Venant $\quad C = 4.2083 \times 10^{-4}$ in^4

warping $\quad Cwa = 1.1928 \times 10^{-2}$ in^6

flexural rigidity $D = \dfrac{Eh^3}{12(1-\nu^2)}$

radius of curvature $\quad a = $ as specified (in.)
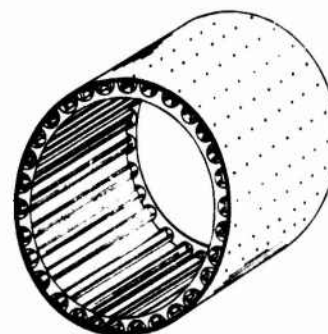
*Refer to [2] for details

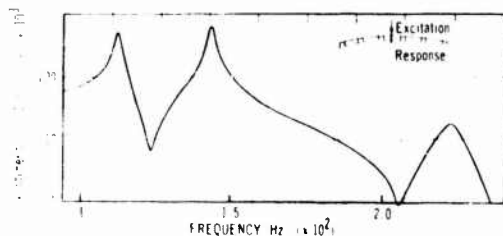Figure 3. 56 Span Complete Skin-Stringer Structure.

137

Figure 4. Frequency Response of
Five Span Segment (ref 1)

Typically, there is an anti-symmetric
mode between every two symmetric modes
but these do not appear in Figure 4
due to symmetry of the excitation.

For comparison, the response of a
complete ring of 56 curved panels,
with the same dimensions, stringers,
and damping as used in the five panel
segment, has been calculated by Mc-
Daniel [1]. The response in the
center of the panel, where the excitation
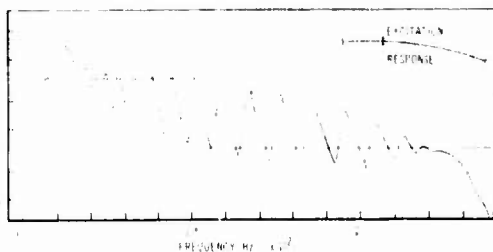is applied, is shown in Figure 5.

Figure 5. Frequency Response of 56
Span Complete Structure
([1]).

The question naturally arises as to
whether or not the response of a finite
length laboratory specimen is represen-
tative of the complete, fuselage-like,
structure. It is apparent from Figures
4 and 5 that the modal density of the
response of the complete structure is
much higher than found in the finite
length specimen, and that the response
peaks to a given excitation are higher
in the smaller structure. Figures 6 and
7 show some of the calculated undamped
normal modes and normalized moment dis-
tributions for each structure. Mode
shapes and moment distributions excited
in the smaller structure are typical
of those found in the complete structure.
These typical response modes are useful
in testing the effectiveness of vibra-

tion damping techniques.

Comparison of Analytical and Experi-
mental Results

Another question that can be
raised when studying the results of
analytical studies is whether or not
the analysis predicts behavior typical
of real structures. Recently, response
calculated by transfer matrix analysis
of a flat, five panel, skin stringer
laboratory specimen was compared with
the results of carefully conducted
laboratory measurements [4]. Table 2
shows a comparison of resonant frequen-
cies predicted analytically for the
symmetric modes in a flat structure
and those measured experimentally in
the laboratory. The analysis used to
obtain these results takes into account
the finite width of the stringer. Other
analysis, employing different assump-
tions as to the interaction between the
stringer and skin near the stringer,
did not agree as well with experimental
results [4].

A comparison between analytically
predicted and experimentally measured
frequency displacement response func-
tions is shown in Figures 8-10. The
theoretical response curves are for a
unit harmonic force applied at the
center point of the structure. In the
experiment the structure was excited by
a small electromagnetic shaker with a
very light moving element in order to not
unduly mass load the structure. Since
the excitation force could not be
measured without mass-loading the struc-
ture in these experiments, the experi-
mental results were arbitrarily normal-
ized for comparison with the theory.

As in the previous example, damping
was analytically modeled by assuming
complex stiffness in the stringer. How-
ever, in the analytical results shown
in Figures 8-10, damping due to bending
of the stringer ($n_b = 0.1$) had to be
made three times as large as the damping
due to torsion of the stringer ($n_t =
0.0333$).

While these particular assumed
loss factors in bending and torsion
were chosen in an attempt to approxi-
mate the experimentally measured modal
damping, there does appear to be some
rational explanation for the stringers
dissipating more energy in bending than
in torsion. In investigations of the
response of typical aircraft structures,
Ungar [10] attributed damping in a
riveted joint to be primarily due to
normal movements between the skin and
the stringer, which would be predominant
in the stringer bending mode. In addi-

138

tion, Mead [11] has pointed out that
acoustic damping of structures will be
higher when adjacent panels are in
phase. An increase in the damping of
the stringer bending modes over the
stringer torsion modes can be noted in
the experimental results shown in
Figures 8-10.
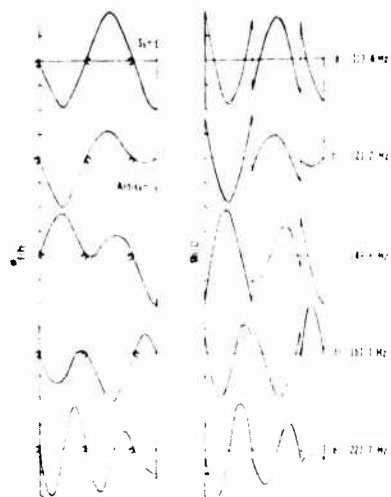
Figure 6. Free Vibration Normal
Modes and Moment Distributions
for Five Span Structure (ref[1]).
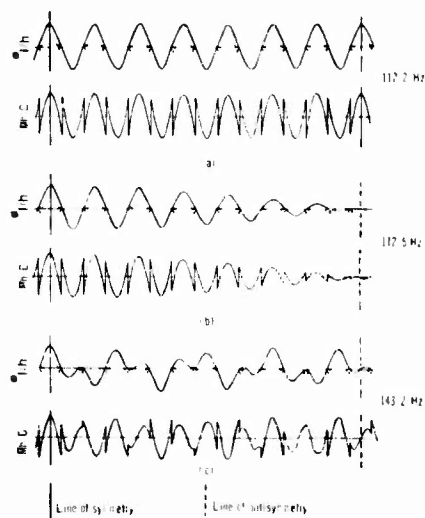
Figure 7. Free Vibration Normal
Modes and Moment Distributions for
56 Span Complete Structure (ref [1]).

For example the resonant amplification
factor Q measured at the center of
panel 3 was about 50 for the first mode
in which the stringer is twisting and

about 25 for the third symmetric mode
in which the stringers are primarily
bending.
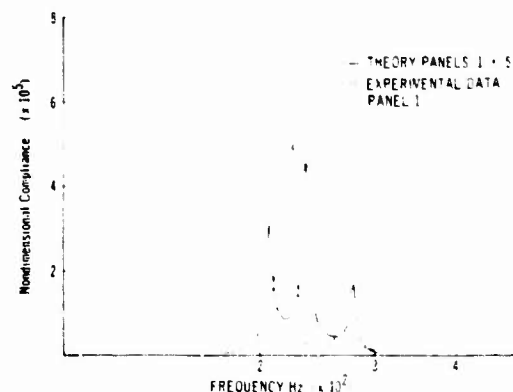
Figure 8. Comparison of Experimen-
tally and Analytically determined
Frequency Response of Panel 1 of
a Flat Structure.
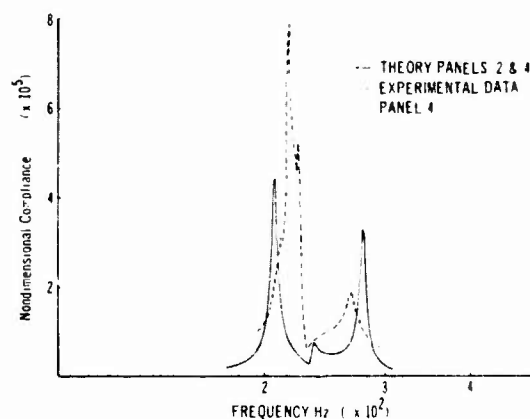
Figure 9. Comparison of Experimen-
tally and Analytically Determined
Frequency Response of Panel 4 of
a Flat Structure.

However, the relative importance of
these modes in sonic fatigue consider-
ations can vary depending on the
spatial distribution of the excitation.
For instance, the third symmetric mode
might be more efficiently excited by
a turbulent boundary layer with small
values of scale of turbulence.

Figure 10. Comparison of Experimentally and Analytically Determined Frequency Response of Panel 3 of a Flat Structure.

Effects of Curvature

Resonant frequencies in typical flat skin-stringer structures have been shown by Lin [2, 12] to occur in periodically spaced frequency bands. The mode shape usually associated with the lower bound of the first frequency band is characterized by adjacent panels vibrating out of phase with each other and string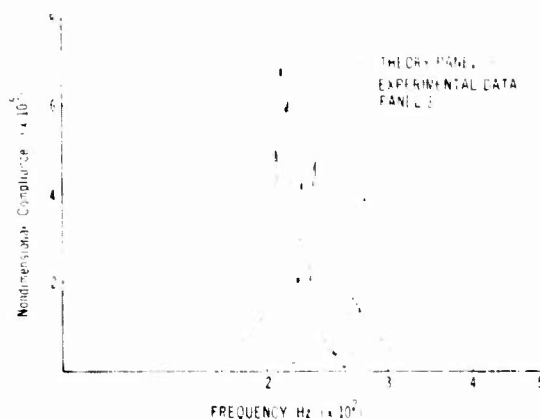ers undergoing primarily torsional displacements, as shown for the first "stringer twisting" mode in Figure 11. The mode shape corresponding to the upper bound of the first band, called the "stringer bending" mode is characterized by adjacent panels vibrating in phase and the stringers undergoing primarily bending deformations. Mode shapes corresponding to the lower and upper bounds of the second band, for which $n = 1$, are likewise characterized by stringer twisting and stringer bending as shown in Figure 11. Other bands, having additional node lines parallel to the stringers, are at higher frequencies. For structures consisting of a large number of panels there were a large number of resonant frequencies in each band and the frequency response of the structure exhibited "filter band" characteristics in response to the imposed excitations. These analytical predictions have been confirmed experimentally [2].

Results of specific numerical calculations of the effects of curvature on the distribution of undamped resonant frequencies and normal modes are shown

FIRST STRINGER TWISTING MODE

FIRST STRINGER BENDING MODE

SECOND STRINGER TWISTING MODE

SECOND STRINGER BENDING MODE
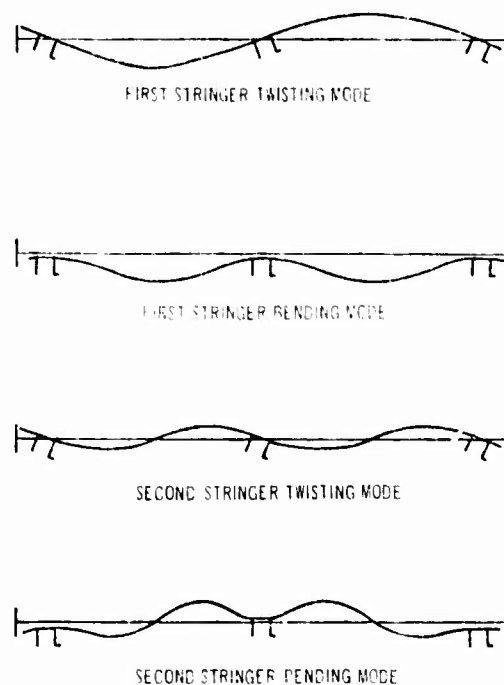
Figure 11. Limiting Modes (ref.[2]).

206.7 Hz

235.4 Hz

278.5 Hz

493.4 Hz

548.4 Hz
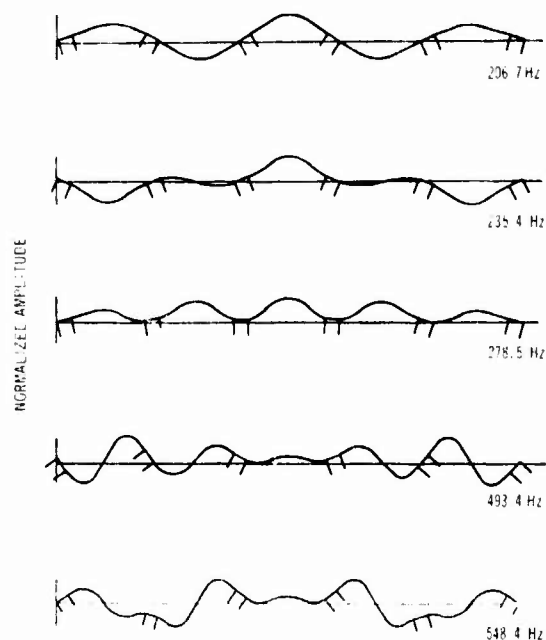
Figure 12. Symmetric Normal Modes Flat Structure, $n = 1$.

140

TABLE 2

CURVATURE (IN.)	SYMMETRIC MODES				
	MODE 1	MODE 2	MODE 3	MODE 4	MODE 5
25	257.8(HZ)	346.6	459.4	512.7	670.8
50	215.6	267.7	442.0	532.5	551.6
72	208.4	249.1	391.9	503.0	539.9
100	205.6	240.8	346.6	495.3	541.0
125	204.8	237.8	324.7	494.0	542.0
150	204.6	236.3	311.8	493.1	542.9
175	204.5	235.5	303.5	492.9	543.5
FLAT	206.6	235.4	278.5	463.4	548.4
EXP. (FLAT)	214	225	269		
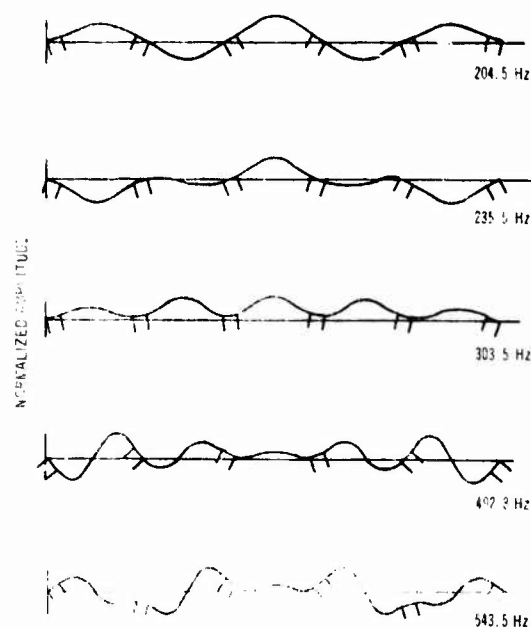
Figure 13. Symmetric Normal Modes,
a = 175", n = 1.

The particular structures investigated,
which have the dimensions and material
properties shown in Table 1, representing
laboratory specimens used in damping
tests. All structures were identical ex-
cept for radius of curvature which
ranged from infinity (or flat) to 25".
Each structure was considered to have
five identical panels and six identical
stringers. Stringer end conditions
were assumed at the ends of the rows of
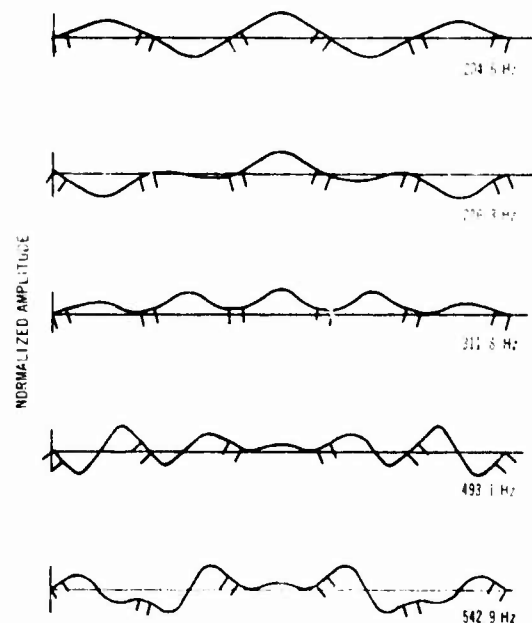
Figure 14. Symmetric Normal Modes,
a = 150", n = 1.
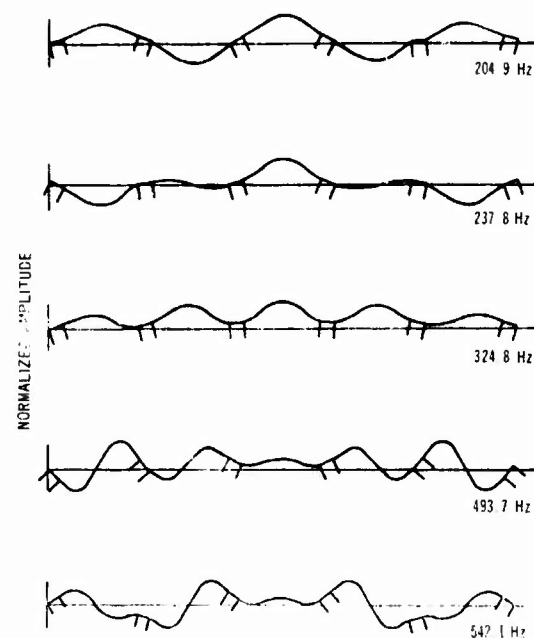
Figure 15. Symmetric Normal Modes,
a = 125", n = 1.

141
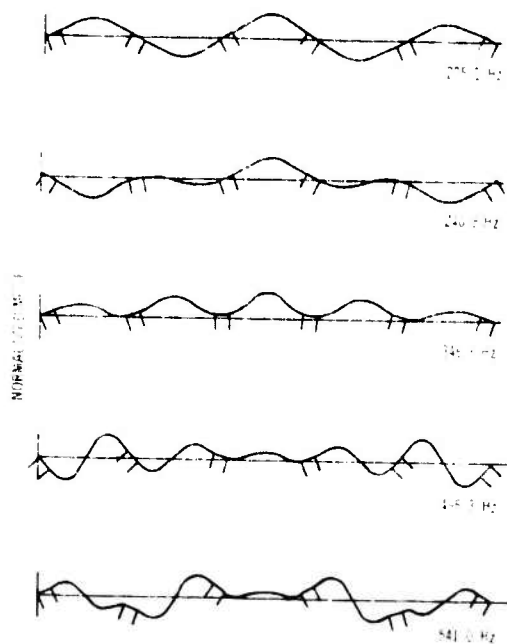
Figure 16. Symmetric Normal Modes, a = 100", n = 1.
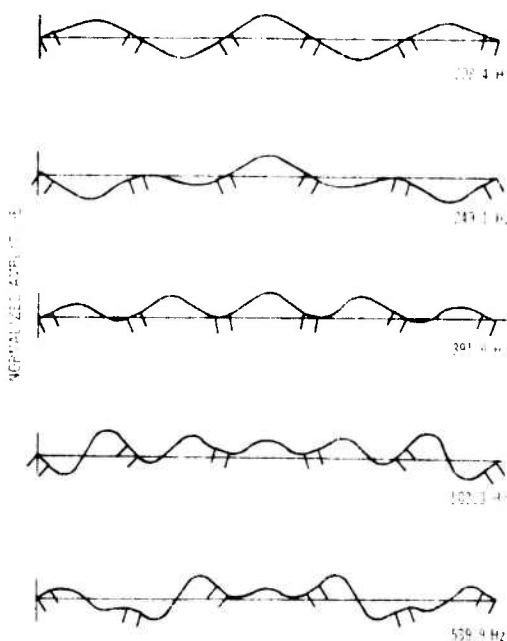
Figure 17. Symmetric Normal Modes, a = 72", n = 1.
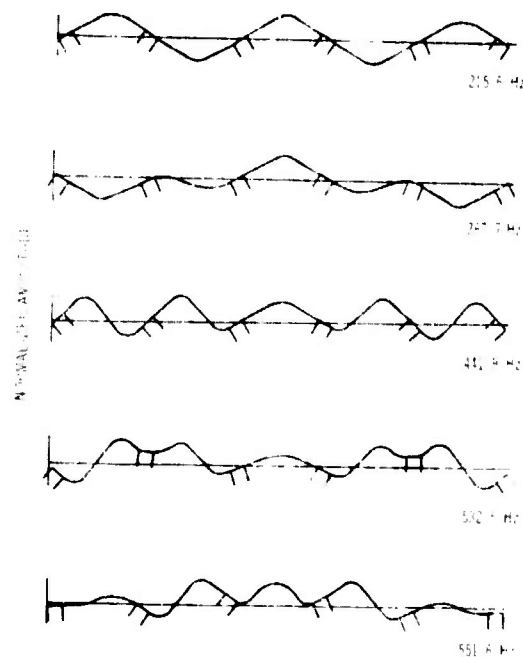
Figure 18. Symmetric Normal Modes, a = 50", n = 1.
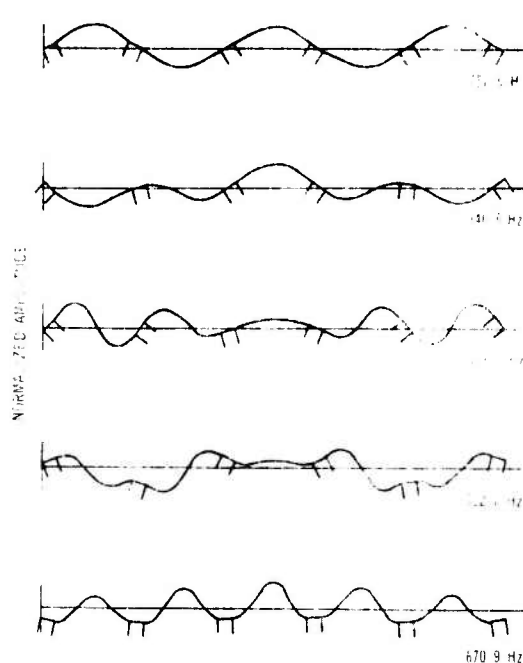
Figure 19. Symmetric Normal Modes, a = 25", n = 1.

142

Although only the first five symmetric normal modes, for which n = 1, are shown, important changes in the dynamic behavior of these structures can be noted. It is apparent that the stringer twisting mode, which is the lowest frequency mode considered for all structures, is only slightly affected by increasing curvature. This can be explained physically by realizing that the out-of-phase motion of adjacent panels tends to cancel out membrane deformations and forces in the curved structures. On the other hand, the stringer bending mode, which is the third symmetric mode in the flat structure, has all panels vibrating in phase and is associated with high membrane deformations and forces in curved structures. This is manifested in the rapid rise in resonant frequency with slight increases in curvature, and the gradual change in mode shape to a mode with node lines parallel to the stringers. The well defined, periodically spaced, frequency bands observed in flat structures appear to spread out and lose their significance as curvature increases. Resonant frequencies for these structures are tabulated in Table 2.

It is interesting to note that the resonant frequencies tabulated in Table 2 exhibit what, at first sight, appears to be peculiar behavior. Note that the calculated resonant frequencies of some of the modes appear to decrease slightly for small increases in curvature in the nearly flat panels. At first the author thought this was an error in the analysis and spent many hours looking for a sign error in a small term in the analysis or in the computer program. Although the possibility of such an error still exists, it appears that this behavior is due to coupling between the membrane forces and the bending forces in the flat plate. The analysis used is based on eighth order shell theory and of course considers both bending and in-plane forces and displacements. Normally, in a flat panel, the in-plane effects are decoupled from the bending effects. However, in these skin-stringer structures, the stringer, which is attached to the panel at a point different from its shear center or centroid, couples the in-plane and bending effects even in the flat case. If the terms in the stringer transfer matrix representing this coupling are removed the resonant frequencies monotonically increase with an increase in curvature. The small increases in resonant frequencies in the flat cases are accompanied by increases in the in-plane forces in the panel. Apparently this behavior reflects the great in-plane stiffness of a flat structure. These small changes in resonant frequency are not significant from an engineering standpoint since they are about 1% of the resonant frequency, and it would be very difficult to experimentally confirm this behavior since the differences in frequency are less than the typical specimen to specimen deviations in this type of structure.

SUMMARY

Some results of transfer matrix analysis of the vibration characteristics of typical skin-stringer structures have been presented in this paper. It has been shown that investigations of five panel laboratory specimens can produce useful information on typical modes and frequencies but will not reproduce the modal densities of larger structures. Furthermore, it has been demonstrated that transfer matrix analysis can reasonably predict the resonant frequencies and damped response of typical specimens if the finite width of the stringer is considered and the damping in the stringer terms is carefully chosen. Increasing the curvature in this type of structure has been shown to result in a gradual change of mode shapes and resonant frequencies until eventually the well defined frequency bands, characteristic of flat structures, lose their significance. Hopefully, the paper has given the reader a better physical understanding of the types of response behavior present in skin-stringer structures, and more specifically the effects of curvature and other structural parameters on these phenomena. The analytical techniques discussed can be further applied to such problems as that of designing efficient damping treatments for use in skin-stringer structures.

ACKNOWLEGEMENT

REFERENCES

1. Henderson, J.P. and McDaniel, T.J., "The Analysis of Curved Multi-Span Structures", J. Sound and Vibration, Vol. 8, No. 2, pp. 203-219, 1971.

2. Henderson, J.P., "Vibration Analysis of Curved Skin-Stringer Structures Having Tuned Elastomeric Dampers", AFML-TR-72-240, Oct. 1972.

3. McDaniel, T.J. "Dynamics of Non-Circular Stiffened Cylindrical Shells", J. Sound and Vibration, Vol. 23, No. 2, 1972.

4. Henderson, J.P. and Nashif, A.D., "The Effects of Stringer Width and Damping on the Response of Skin-Stringer Structures", Journal of Engineering for Industry, pp. 159-166, February 1972.

5. Lin, Y.K. and Donaldson, B.K., "A Brief Survey of Transfer Matrix Techniques with Special Reference to the Analysis of Aircraft Panels", J. Sound and Vibration, Vol. 10, No. 1, pp. 103-143, 1969.

6. Lin, Y.K., "Free Vibrations of Continuous Skin-Stringer Panels", J. Appl. Mechanics, Vol. 27, No. 4, pp. 669-676, 1960.

7. Clarkson, B.L. and Ford, R.D., "Experimental Study of the Random Vibrations of an Aircraft Structure Excited by Jet Noise", Wright Air Development Division Report, WADD Tech. Report 61-70, 1961.

8. Clarkson, B.L. and Ford, R.D., "The Response of a Typical Aircraft Structure to Jet Noise", J. Royal Aero. Society Vol. 66, p. 31, 1962.

9. Henderson, J.P. and McDaniel, T.J. "The Analysis of Curved Multi-Span Structures", J. Sound and Vibration Vol. 8, No. 2, pp. 203-219, 1971.

10. Ungar, E., "Vibrational Energy Losses at Joints in Metal Structures", Shock and Vibration and Associated Environments, Bulletin No. 33, Part IV, DoD, Research and Engineering pp. 189-199, March 1964.

11. Mead, D.J., "The Effect of Certain Damping Treatments on the Response of Idealized Aeroplane Structures Excited by Noise", AFML-TR-65-284, Air Force Materials Laboratory, Wright-Patterson AFB, Ohio, pp. 12-23, August 1965.

12. Lin, Y.K., McDaniel, T.J., Donaldson, B.K., Vail, C.F., and Dwyer W.J., "Free Vibration of Continuous Skin-Stringer Panels with Non-Uniform Stringer Spacing and Panel Thickness", Air Force Materials Laboratory Report, AFML-TR-64-247, Part I, 1965.

DISCUSSION

Mr. O'Leary (Boeing Vertol): Is this transfer matrix technique like a Myklested associated matrix or is it like a finite element approach? Can you say in a couple of words?

Mr. Henderson: The transfer matrix technique is a technique in which you define a state vector. In the case of the curved structure, there are four displacements and four forces. If you know the state vector at the edge of one panel, you define what it would be at the other edge of the panel. You can work across panels and stringers in this manner. It does include distributed mass and distributed stiffness. Now, some of the early transfer matrix techniques used a Myklested type of approach where they lumped mass along lines and so forth. This particular approach is a distributed mass approach and it is not directly related to a finite element technique. It requires less computer time than a finite element approach would.

Mr. O'Leary: How effective are the boundary conditions on a particular part you are investigating? If you take a portion out of a wing or a fuselage, obviously the boundary conditions of that edge where you assumed the state vector have some influence on the frequencies.

Mr. Henderson: You can put arbitrary boundary conditions on the edges of the panels. The one overriding restriction in the analysis is the fact that you have to make it a one dimensional analysis and you have to have the simple supports on the frames. As a matter of fact, it is very convenient in a transfer matrix analysis to put elastic boundary conditions in the ends of your panels. Say you have a stringer at the end of your panel, you just put a transfer matrix across that stringer. It is very easy to incorporate different boundary conditions at the ends of the panels using the transfer matrix technique.

MATERIALS FOR VIBRATION CONTROL IN ENGINEERING

A. D. Nashif

University of Dayton
Dayton, Ohio

Design data on the damping properties of a number of materials have been measured and are presented as functions of both temperature and frequency. The selected materials are typical of those which can be utilized collectively to reduce vibrational amplitudes and noise levels in resonating structural systems over an extremely wide temperature range typically from -200°F to 2000°F.

INTRODUCTION

Many of the resonant noise and vibration problems which severely affect present day technology and which have not all be resolved by means of conventional vibration and noise control techniques, are highly amenable to resolution by proper use of materials which dissipate large amounts of energy under cyclic strain deformation. It is clear that future application of this vibration control technology, utilizing damping materials, depends critically on the existence of a highly sophisticated and broad data base concerning the damping properties of materials having high damping capability at various points in the temperature range -200°F to +2000 °F. This wide temperature range arises because practical vibration and noise problems can occur under widely varying environmental conditions, ranging from deep space at temperatures as low as -200°F, through general industrial vibration problems, which occur near room temperature, as in appliances, through problems associated with internal combustion engines and transmissions at temperatures around 200°F to 300°F, to problems associated with engine exhaust systems and gas turbines at temperatures up to 2000°F. What is even more remarkable than the width of this temperature range, however, is the variety of materials available for use within it, including elastomers between -200°F and +500 °F, plastics from +200°F to 400°F or so, and enamels between +600°F and +2000°F. The reason for establishing data for a variety of different materials, to cover such an extremely wide temperature range, is the fact that good damping materials exhibit high damping properties only in a relatively narrow temperature range,

known as the transition region which is illustrated in Figure 1.
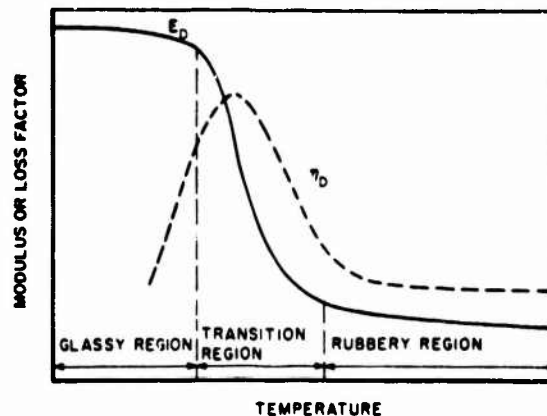
Figure 1. Variation of the properties of a typical damping material with temperature.

This paper, therefore, will outline and quantify the damping behavior of some typical materials, which have been evaluated up to the present time for damping applications in the above temperature ranges, including elastomers, plastics, and enamels. This data will be the first step toward providing the designer with information needed for practical application of damping to real problems in the future.

MEASUREMENT TECHNIQUES

Vibrating beam tests were conducted to obtain the damping properties presented in this paper, because such tests can provide reliable damping data over wide temperature and frequency ranges.

145

The damping material was either coated on a metal beam or sandwiched between two metal beams, as shown in Figure 2. Externally coated beam specimens were used to measure the damping properties of stiff materials, where the real part of Young's modulus ranged in value from 10^3 to 10^7 psi, while the sandwiched beam specimens were used for relatively soft materials with Young's moduli under 10^4 psi. The damping properties were computed from the results of tests conducted on both damped and undamped beams as follows, using the procedures described for data reduction.

(a) Oberst beam specimen

(b) Modified Oberst beam specimen

(c) Sandwiched beam specimen
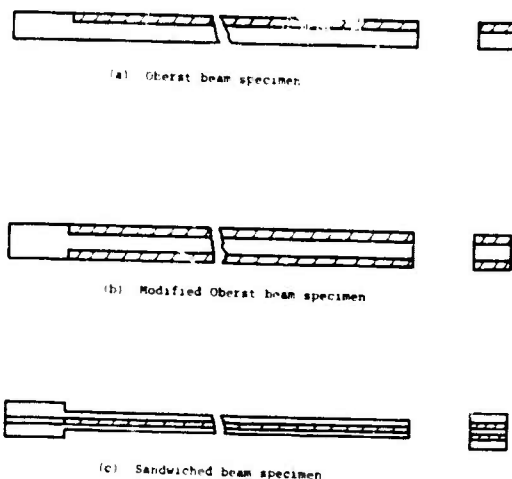
Figure 2. Beam Specimens

Coated Beam Tests

This technique was developed by Oberst [1] for measuring the extensional complex modulus properties of materials. The material is coated on one side of the beam, and the composite beam is then subjected to a sinusoidal force of fixed amplitude by means of a driver and the response obtained by means of a pickup transducer, as illustrated in Figure 3. From the response spectra of the beam, both modal frequency and half-power bandwidth can be measured for each mode of vibration. The loss factor η_D and the real part of Young's modulus E_D of the material can then be calculated by using the following equations:

$$(\omega_n/\omega_{1n})^2(1+h_r\rho_r) =$$

$$\frac{1+2\ E_r h_r(2+3h_r+2h_r^2) + E_r^2 h_r^4}{1 + E_r h_r},$$

$$\eta/\eta_D =$$

$$\frac{E_r h_r(3+ 6h_r+ 4h_r^2+ 2E_r h_r^3+ E_r^2 h_r^4)}{(1 + E_r h_r)(1+ 4E_r h_r+ 6E_r h_r^2+ 4E_r h_r^3+ E_r^2 h_r^4)}$$
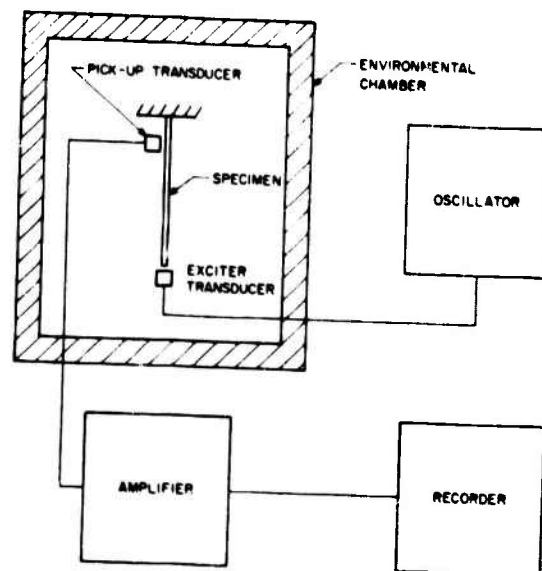
Figure 3. Schematic diagram of experimental beam setup.

A modification of this technique [2], designed to simplify the data reduction and get a good understanding of the error magnification factors, is obtained by coating the beam on both sides with the damping material. The resulting equations for such symmetric beams are:

$$E_D = \frac{[(\omega_n/\omega_{1n})^2(1+2h_r\rho_r) -1]E_1}{8h_r^3 + 12h_r^2 + 6h_r},\ \text{and}$$

$$\eta_D/\eta = 1 + \frac{E_1}{(8h_r^3 + 12h_r^2 + 6h_r)\ E_D}$$

Sandwiched Beam Tests

By this technique, the material is sandwiched between two identical metal beams and tests are conducted in a similar way to the coated beam tests. The equations used for this technique are based upon those developed by Ross, Kerwin and Ungar [3] for a three-layer damped system and modified for a simple symmetric sandwiched beam [4,5]. An

146

iteration process is needed to compute the damping properties of materials by these equations because they are coupled. An early attempt has been made [6] to uncouple these equations in order to simplify the data reduction. Another simpler form of these uncoupled equations is presented here:

$$G_D = \frac{(A-b)^2 - 2(A-B)^2 - 2A\eta^2}{(1-2A+2B)^2 + 4(A\eta)^2}$$

$$\frac{h_1 h_1 h_D}{\eta} \eta \quad , \text{ and}$$

$$\eta_D = \frac{A\eta}{A-B-2(A-B)^2 - 2(A\eta)^2}$$

where:

$$A = (\omega_n/\omega_{1n})^2 (2+\rho_r h_r)(B/2) \quad \text{and}$$

$$B = \frac{1}{6(1+h_r)^2}$$

Data Reduction

It should be noted that all the above equations contain terms that are essentially functions of small differences between large numbers, which may lead to large error magnifications [1, 2, 6]. A number of different beam geometries were used for each material in order to overcome this difficulty. The experimental setup illustrated in Figure 3 was used for measuring the damping properties of materials up to 500°F. Above this temperature, the specimen was placed inside a furnace on top of the shaker... the shaker and the furnace. The damping properties of the material were then obtained by measuring the driving point force and acceleration.

For all materials, and for each mode of vibration, the frequency and the loss tangent of the composite beam were measured at each temperature in order to verify that reliable data was obtained. Using values from the graphs, and the appropriate equations above, the real part of the modulus, and the loss factor, of each material were then calculated and cross-plotted against frequency at a number of different temperatures at regular intervals. It was necessary to go through this somewhat tedious procedure because damping materials are both

frequency and temperature sensitive. All experimentally determined values of the real part of the modulus and the loss factor were then plotted on one master graph for each material by using the temperature-frequency superposition principle [7]. These master graphs were then used, to plot the damping properties of each material in a usable form, as shown in Figures 4 to 11.

DISCUSSION

Although many materials have good damping capabilities in the range from -200°F to 2000°F, only four materials were selected for this paper because they are typical of what is available for four important temperature ranges covering "low", "room", "medium high", and "high temperatures".

Figures 4 and 5 represent the real part of Young's modulus and the loss factor, respectively, of a natural rubber [8] as a function of both frequency and temperature. This material is typical of many elastomers such as silicones, butyl, and acrylonitrile-butadiene rubber, which have high damping capabilities in the range from -200°F to about 50°F. Such a capability makes these materials very effective when utilized in constrained or sandwich treatments near their transition region because of the extremely high loss factor, as can be seen in Figure 5. In addition, these materials are very useful as links for tuned damping devices when they are utilized in their rubbery region because of the small variation of the modulus values with temperature, as can be seen in Figure 4.

The second material evaluated was 3M-467 adhesive [9] which is typical of many pressure sensitive transfer adhesives that have their optimum damping in a temperature range... at this condition, this material has its optimum damping, see Figures 6 and 7, at room temperature. This makes it applicable for many industrial vibration and noise problems, when utilized in a shear configuration.

For vibration and noise problems which occur at moderately high temperatures, such as heat insulation, internal combustion engines, and others, plastic materials are candidates for providing good damping capabilities in a range from 200°F to 400°F. Figures 8 and 9 show the damping properties of one of these materials, namely a high impact polystyrene [10].

Finally, for high temperature app-

lications such as in exhaust systems, engine housings and after-burners, vitreous enamels can provide high damping capabilities up to 2000°F.
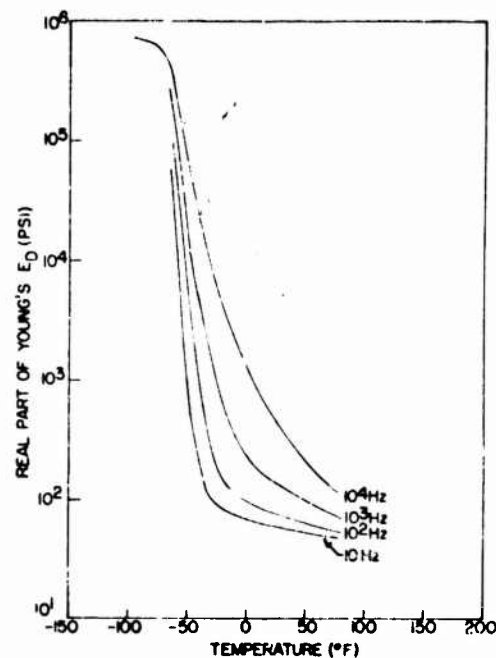
Figure 4. Variations of the real part of Young's modulus with temperature and frequency for Natural Rubber.

Figure 6. Variations of the real part of shear modulus with temperature and frequency for 3M-467 adhesive.

Figure 5. Variations of the loss factor with temperature and frequency for Natural Rubber.
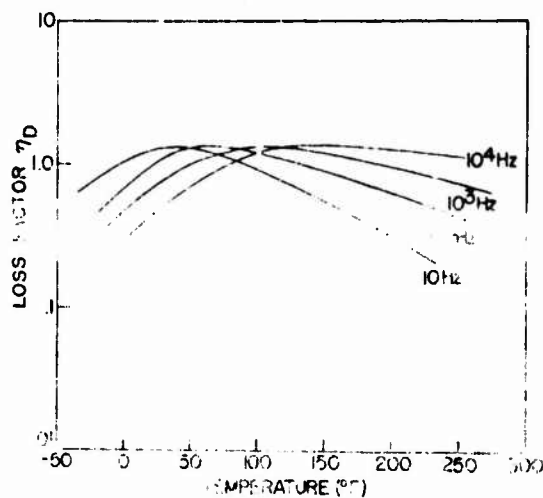
Figure 7. Variations of the loss factor with temperature and frequency for 3M-467 adhesive.
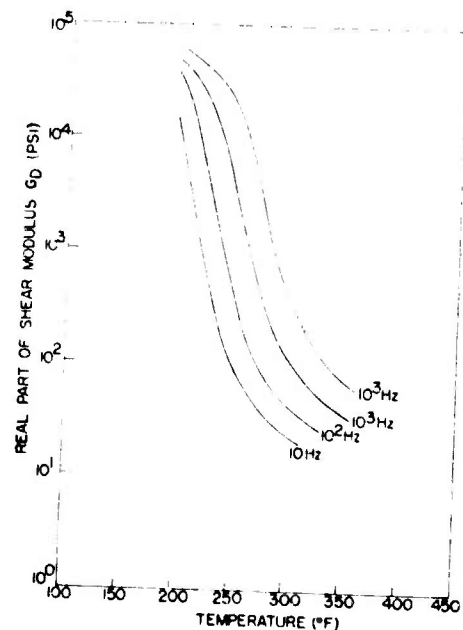
Figure 8. Variations of the part of shear modulus with temperature and frequency for High Impact Resistant Polystyrene Plastic.

Figure 9. Variations of the loss factor with temperature for High Impact Resistant Polystyrene Plastic

Results for a typical example of one of these enamels are shown in Figure 10 and 11 [11]. Such materials can be utilized in a free layer damping configuration because of their high modulus

and loss factor, as can be seen from the above figures. It can also be seen from these figures that such a material can provide good damping over a wide temperature range, which is usually well below its firing temperature.

Figure 10. Variations of the real part of Young's Modulus with temperature and frequency for Chicago Vitreous Enamel #325

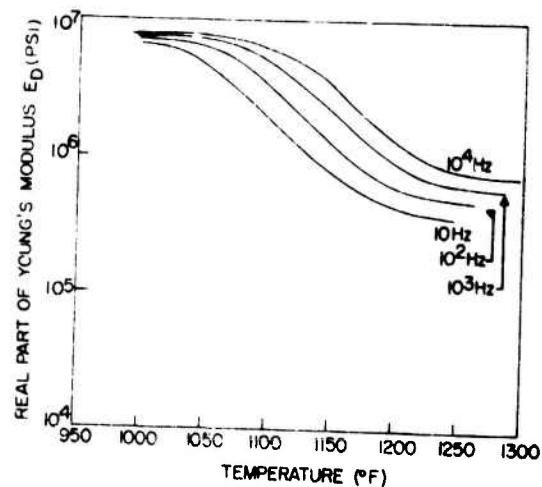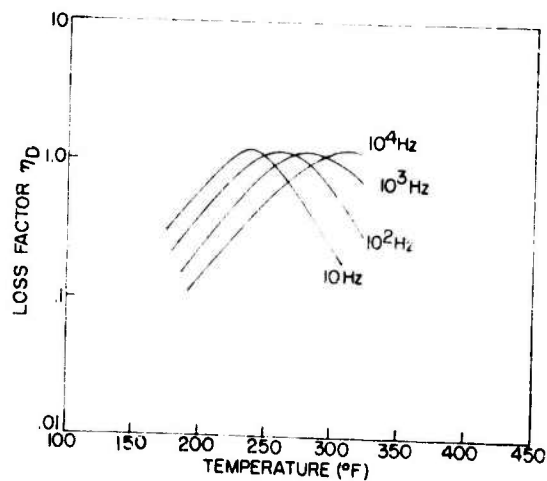Figure 11. Variations of the loss factor with temperature and frequency for Chicago Vitreous Enamel #325.

149

CONCLUSIONS AND RECOMMENDATIONS

Examples of damping materials which collectively cover a temperature range from -200°F to 2000°F have been discussed in this paper along with complex modulus data to enable designers to utilize such materials for resonant vibration and noise problems. However, at the present time, there is no knowledge of good damping materials in a small region within this extremely wide temperature range. This is the region between 400°F and 600°F, where most elastomeric damping materials leave off and enamel damping materials take over. Future work is needed in this area to evaluate and/or develop new damping materials for this gap. Possibly low melting temperature glasses might be an answer.

ACKNOWLEDGEMENTS

REFERENCES

1. Oberst, H. and Frankenfeld, K. "Uber die Dampfung dunner Bleche durch festhaltende Belage", Acustica, 1952 Vol. 2, pp. 181-194, (1954).

2. Nashif, A.D. "New Method for Determining Damping Properties of Viscoelastic Materials", Shock and Vibration Bulletin 36, Part 4, pp. 37-47, (1967).

3. Ross, D., Kerwin Jr. E.M., and Ungar E.E., Damping of Plate Flexural Vibrations by Means of Viscoelastic Laminae", Structural Damping, J.E. Ruzicka, Ed., ASME, New York (1959).

4. Braunisch, H. "Schwingungsgedampfte dreischichtige Verbundsysteme", Acustica, Vol. 22, pp. 136-144, (1969/70).

5. Roscoe, A.S. III, Thomas, E.V., and Blasingame, W., "Measurements of Complex Shear Modulus of Viscoelastic Materials by Mechanical Impedance Methods", Shock and Vibration Bulletin 35, Part 7, pp. 267-274, (1966).

6. Abdulhadi, F. "Determination of Damping Properties of Soft Viscoelastic Materials", Shock and Vibration Bulletin 41, Part 2, pp. 133-139, (1970).

7. Ferry, S.D., Viscoelastic Properties of Polymers, New York, John Wiley and Sons Inc. (1961).

8. Manufactured by Lord Manufacturing Co., Erie Pa.

9. Manufactured by 3M-Co., St. Paul, Minn.

10. Manufactured by Impact Plastic Co., New Jersey.

11. Manufactured by Chicago Vitreous Co., Chicago, Ill.

SYMBOLS

a_n	Characteristic number of the nth mode
E_1	Young's modulus of metal beam
E_D	Young's modulus of damping material
E_r	E_D/E_1
G_D	Shear modulus of damping material
h_1	Thickness of metal beam
h_D	Thickness of damping material
h_r	h_D/h_1
ℓ	Length of beam
η	Loss factor of composite beam
η_D	Loss factor of damping material
ρ_1	Density of metal beam
ρ_D	Density of damping material
ω_n	Natural frequency of nth mode of composite beam
ω_{1n}	Natural frequency of nth mode of metal beam

DISCUSSION

Mr. Platus (Mechanics Research): Did you consider in looking at the temperatures, the temperature rise due to energy dissipation in the damping materials themselves? How do you control temperatures? Is this a problem?

Mr. Nashif: In this particular measuring technique it is not a problem, because in all vibrating beam techniques you have to keep it at low force input so you can stay in the linear range of the material. In that linear range there is very little heat dissipated. If we were using a different technique, like a resonance technique or an impedance technique and trying to put high strain into the material, then we have to control temperature and that gets to be a problem. When using tuned dampers with large deformations, you have to consider it in designing the dampers so you can tune it for the right temperature range with consideration of heat build-up.

Mr. Platus: Have you determined fatigue properties for any of these materials or does it become a problem

Mr. Nashif: No, we have not determined the fatigue life of these materials. In our applications we haven't had any problem.

Mr. Forkois (Naval Research Laboratory): There are problems of fatigue, then internal friction which under resonant conditions can destroy the material, particularly a low modulus material like solid polyurethane. We also have the problem of creep with other materials. Have you considered this in some of your analyses?

Mr. Nashif: As a matter of fact we did go through that. On our first application of a tuned damper, we made the tuned damper and didn't pay much attention to the tensil strength of the material. It came apart in two seconds. At that time we had to go back and find another material with much higher tensil strength which still wasn't good enough until we added quite a bit of carbon black filler. This increased the tensil strength enough so it would withstand the environment. That is why I mentioned that, for tuned damping devices, you have to restrict yourself to silicone materials, natural rubber, butyl rubber and rubbers which have a much higher tensil strength.

Mr. Forkois: I do know that internal friction can raise the temperature quite high. I imbedded thermocouples inside the rubber material and got excessive temperature rises. Have you done this too?

Mr. Nashif: We have done some work on that, because whenever we apply these damping materials for tuned dampers, we have to worry about the effect of the strain on the changes in the modulus and the loss factor. This becomes very difficult because of high strain. Your material is changing because of the strain effect and also the temperatures building up quite rapidly. You have two effects simultaneously. We have some data on that, but not very much.

Mr. Henderson (Materials Lab WPAFB): This comment is relative to the last two questions. We have conducted fatigue investigations on some of these materials, specifically the pressure sensitive materials. Some of the work done by Whittier years ago at the University of Minnesota does indicate that you can take these materials to very high strains. I think he went up to 10 million cycles with no indications of fatigue damage. The other thing to keep in mind on typical surface treatments that he is talking about here is that our viscoelastic-elastic layers are often about 0.002 inches thick and they are on a metal structure. We do not get heat buildup in the viscoelastic layer, because the metal structure dissipates that heat very rapidly.

151

VISCOELASTIC EPOXY SHEAR DAMPING CHARACTERISTICS

C. V. Stahle, A. T. Tweedie, and T. M. Gresko
General Electric Company, Space Division
Valley Forge, Pennsylvania

An experimental study evaluating the shear damping characteristics of a number of viscoelastic epoxy compounds is presented. The basic epoxy compound (SMRD 100F50) is castable, has low outgassing properties, and a low density compared to other viscoelastic materials. To further explore this class of materials, a series of formulations were selected to determine the effects of stiffness, crosslinking in the base resin, plasticizer, filler material, and combinations of plasticizer and filler material. A high damping Butyl rubber compound was also evaluated for comparison with the epoxy compounds.

A steel block was attached to a shaker through a shear layer of the material. The peak quadrature response relative to the input motion was used to determine the storage modulus, loss modulus and loss factor. Comparison of the measured response with that determined using complex and viscous damping models indicates that reasonable accuracy can be obtained with either representation.

The results show that a loss factor on the order of 1.5 can be obtained for more than two orders of magnitude variation in storage modules. The addition of filler material to the base resin increases the stiffness without degrading the loss factor whereas crosslinking provides high stiffness but lowers the loss factor. The comparison of measurements on two samples having the same formulation indicates that variations on the order of 30 percent in the modulus can be expected with present methods of compounding. A hypothetical example using a constant shear layer thickness shows the filled materials to be the most effective.

INTRODUCTION

As a result of a previous investigation of high-damping space-compatible materials, a viscoelastic epoxy material, SMRD 100, was found to have an exceptionally high loss factor. It was used as the outer layer of a two-layer damping treatment that effectively reduced the dynamic magnification factor of a relay panel of the NASA-Goddard Space Flight Center Earth Resources Technology Satellite as reported in Ref. 1. The basic viscoelastic epoxy compound is castable, has low outgassing properties, and a low density compared to other viscoelastic materials. Although a considerable amount of literature exists regarding the damping characteristics of a number of elastomeric compounds (e.g., Ref. 2), little information appears to be available on viscoelastic epoxy materials.

To further explore this class of materials, an experimental study evaluating the shear damping characteristics of a series of variation of the basic SMRD 100 viscoelastic epoxy compound was performed. The effects on damping of stiffness, crosslinking in the base resin, plasticizer, filler material, and combinations of filler material and plasticizer were investigated. A high-damping Butyl rubber was also evaluated for comparison with the viscoelastic epoxy compounds.

The following sections describe the material formulations selected, the method used to determine the material shear damping loss factor and the resulting relation between stiffness and loss factor for the formulations evaluated. Predicted results using viscous and complex damping representations are compared with measured responses. Finally, some considerations in selecting the material that maximizes the effective damping are mentioned.

MATERIAL FORMULATIONS

The material formulations selected for experimental evaluation are shown in Table 1. As indicated in the table, the materials can be placed in seven groups according to purpose. Nearly all the materials listed are variations of the basic resin formulation used in the original SMRD 100F50 which

TABLE 1
Material Formulations

Group	Purpose	Test Specimen Number	Formulation Number	Hardness Shore A	Al$_2$O$_3$ σ_i	Plasticizer σ_i	Description
I	Damping and	A	10	68			Clear Damping Compound
	Stiffness	B	12	50			Clear Damping Compound
	Variation of	C	11	43			Clear Damping Compound
	Base Resin	DD	12	50			Duplicate B
		EE	11	50			Duplicate C
		FF	24	- -			Softer than B or C
		II	25	40			Softer than B or C
II	Crosslinking	G	SMRD 100	60			Crosslinked Clear Compound
	Effect	I	SMRD 104	90			Crosslinked Clear Compound
III	Plasticizer	HH*	20	40		5	Plasticized C
	Effect	GG*	22	35		15	Plasticized C
IV	Effect of Alumina	D	16	85	120		Alumina Filler
	Filler	E	15	60	120		Alumina Filler in C
		F	13	50	120		Alumina Filler in B
		H	19	-	175		More Filler in B
V	Effect of Micro-sphere Filler	J	SMRD 100F50	50			Microspheres 12 percent
VI	Effect of Filler	JJ	26	55	110	9	Filler and Plasticizer
	and Plasticizer	KK*	27	37	110	15	Filler and Plasticizer
VII	Control	K		50			Butyl Rubber

*Not tested because of bond failure

was used in the ERTS spacecraft. The resin in this compound is a flexible epoxy resin and the filler is silica microspheres in about 12 percent by weight. (The 50 designation refers to the nominal Shore A hardness.)

The test specimens are designated by letters and used various formulations as indicated in the table. The specimens were made and tested at two different times. The single letters designate the initial specimens and the double letters indicate the specimens made at a later date.

Group 1 consists of seven samples of the clear base resin with slight variations in the formulation to alter the damping and stiffness characteristics. The hardness measurements, ranging from 68 to something less than 40 for sample FF, indicates that this series gave a range of materials on the soft side. Because of the viscoelastic nature of these materials, it was found that hardness measurements are subject to a wide degree of variation between samples and between operators. The hardness is not a very adequate measurement and should only be considered as indicative of trends. Included in this group are two duplicate specimens which were selected to evaluate the consistency of the formulations.

Group II samples were made to investigate the effect of adding a crosslinker to the base resin. It was thought that the crosslinker, besides stiffening the resin might change the overall character of the damping. The two samples used existing formul-

ations which were originally developed for sterilizable conformal coating application.

In Group III, plasticizer was added to the formulation used for Specimen "C" The materials turned out softer as expected. They also failed to bond firmly to the test fixture so that they could not be tested. Because of the inherently good bonding characteristics of epoxy, the bond surfaces were not etched and no special care was taken in preparing the surfaces. This combined with the fact that the plasticizer seems to interfere with bonding, as also indicated by Specimen KK, prevented the effect of plasticizer alone to be evaluated.

Alumina filler was added to samples in Group IV. The alumina is much cheaper than the microspheres and is of a finely divided granular nature rather than spheres A range of hardnesses of the base resin with filler was chosen to survey the effect of the filler. The filler led to a harder formulation with the same base resin (compare C and E in Table 1). The addition of 55 percent more filler in H seems to have moved it somewhat toward the softer side as compared to F. This may be with the variability of the measurement or the optimum point of filler addition may have been past. That is, as filler is added, some point is reached where the mechanical properties of the compound peak and then fall off. Samples of the alumina filler resins were cast in 6 x 6 x 1/8 in. molds. These showed good uniformity with only very narrow bands (< 1/16 in.) at the top and bottom indicating settling of the filler.

154

The combination of filler and plasticizer was made in Group V. Unfortunately, the sample KK with 15 percent plasticizer came unbonded and could not be tested. JJ which is a plasticized F was found to be very flexible.

The original compound investigated for spacecraft use was included in Group VI. The SMRD 100F50 was designated as specimen J. The expense and difficulty in handling the microspheres does not make this formulation a good choice where weight is not an overriding concern. The microspheres tend to float, giving a variation in density across a casting.

Butyl rubber, the Group VII material, was used as a control. The sample had one slotted surface which was subsequently tested with the slots in the direction of applied motion.

All of the formulations were cured for 16 hours at 275°F. No attempt was made to determine optimum cure time and temperature or to add catalysts to speed the cure. The cure could probably be speeded up somewhat.

A number of other formulations of castable flexible resins were tried and discarded as being too bouncy in a steel ball drop test. All together, about 25 different formulations were tried.

TEST SPECIMEN DESCRIPTION

Each test specimen consisted of a steel block and an aluminum base plate sandwiching a layer of damping material as shown in Fig. 1. The viscoelastic damping material was cast in place between the block and base plate with a thickness of 0.090 in. and a rectangular area 3 in. by 2 in. Small samples of the material were cast and cured separately to enable the hardness to be evaluated. The butyl rubber specimen was bonded to the block and base plate using Eastman 910. The steel block was 3 in. by 2 in. by 2.44 in. high and weighed 4.14 pounds. The block simulated the inertial loading of an application being considered at that time.
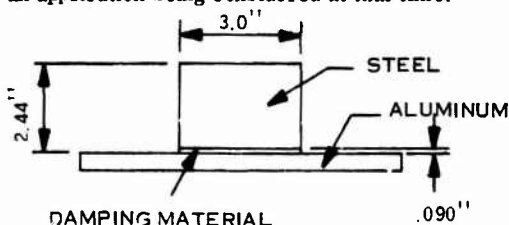

Fig. 1 - Test specimen

The test specimens were compact and easily transportable to the test area where they were mounted to a slip plate.

TEST ARRANGEMENT AND PROCEDURE

Each specimen was mounted horizontally to an MB C-150 driven Team Table and vibrated at 5 g's from 20 to 2500 Hz at the rate of two octaves per minute. The specimens were shaken, one at a time, in a direction so as to shear the damping material along the length of the shear area (Fig. 2).
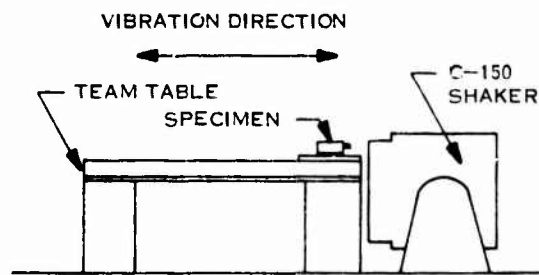
Fig. 2 - Test arrangement

An accelerometer attached to the front face of the specimen measured the response of the steel block. The input acceleration was controlled by an accelerometer mounted to the edge of the baseplate. Initial tests indicated that no resonant effects occurred in the 2500 Hz range. On-line response plotting of the quadrature and coincident response components relative to the base acceleration was accomplished using a Spectral Dynamics Model 109 Co-Quad Analyzer. The total response was also plotted after processing it through a SD101 tracking filter. Thus, three plots of response were obtained from each specimen which were subsequently used to determine the damping characteristics of the materials.

COMPLEX AND VISCOUS DAMPING REPRESENTATION

The results of previous investigations of the damping characteristics of viscoelastic materials of the type investigated in this paper have shown that a complex modulus representation is the most desirable in that it minimizes the frequency dependence of the damping [2]. However, in some applications it may be desirable to use a viscous representation because of the ease with which it can be combined with other elements in a system. The differences and errors resulting from these two types of representation were examined as part of this investigation.

As indicated in the previous section, the test specimen consisted of a steel block attached to a base plate through a shear layer of damping material and excited by base motion. Because of the dimensions of the block and the relatively high

155

compression stiffness of the damping material, the test specimen can be represented analytically as a single degree of freedom system (Fig. 3). For complex damping, the response of the system relative to the base motion is:

$$\frac{X}{Y} = \frac{[(1 - \beta^2) + \eta^2] - i(\eta\beta^2)}{(1 - \beta^2)^2 + \eta^2}$$ (1)

where $\beta = \dfrac{\omega}{\omega_\eta}$ and η is the loss factor of the damping material.

Fig. 3 - Analytical models of test specimen
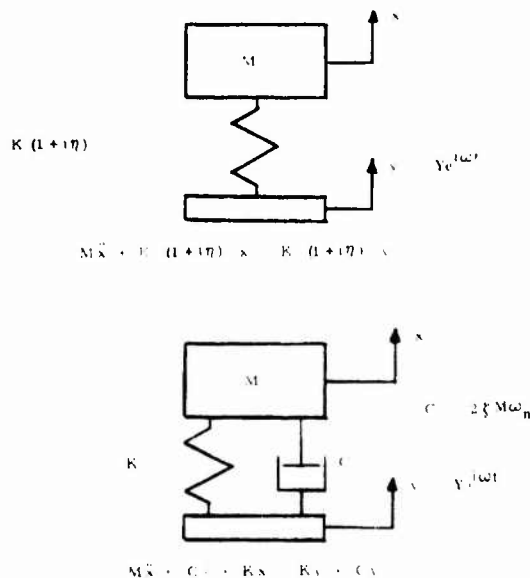
The quadrature and coincident response are:

$$A_Q = \frac{\eta\beta^2}{(1 - \beta^2)^2 + \eta^2}$$ (2)

$$A_C = \frac{(1 - \beta^2) + \eta^2}{(1 - \beta^2)^2 + \eta^2}$$ (3)

Differentiating the quadrature response with respect to β and setting it equal to zero defines the value of β and A_Q at which the quadrature response peaks:

$$\beta_{QP} = (1 + \eta^2)^{1/4}$$ (4)

$$A_{QP} = \frac{\eta \ 1 + \eta^2}{2 + 2\eta^2 - 2\sqrt{1 + \eta^2}}$$ (5)

Solving equation (5) for η in terms of A_{QP}, gives

$$\eta = \frac{4 A_{QP}}{4 A_{QP}^2 - 1}$$ (5a)

This equation allows η to be evaluated from the maximum quadrature response. The quadrature response has a well-defined peak for high damping materials whereas the total response peak is poorly defined. Once η is determined, the natural frequency and hence the real part of the shear modulus can be determined from equation (4). This completely defines the theoretical response of the system.

Using a similar approach for viscous damping, the following relations are determined:

$$A_Q = -\frac{2\zeta\beta^3}{(1 - \beta^2)^2 + (2\zeta\beta)^2}$$ (6)

$$A_C = \frac{(1 - \beta^2) + (2\zeta\beta)^2}{(1 - \beta^2)^2 + (2\zeta\beta)^2}$$ (7)

$$\beta_{QP} = [(2\zeta^2 - 1) + 2\sqrt{\zeta^4 - \zeta^2 + 1}]^{1/2}$$ (8)

Where β_{QP} is solved for a particular ζ value and substituted in equation (6) to obtain A_{QP}.

Figures 4 and 5 show comparison between the theoretical curves for complex and viscous damping and the actual test curves for specimen A. The ζ and η values used for the theoretical curves were chosen to obtain the same peak quadrature value. The comparison for specimen A is typical of the results obtained. It will be noted that the total response does not exhibit a well-defined resonant peak for these high damping materials, making quadrature response measurement a necessity.

Comparing total response curves, it can be seen that the complex damping curve has a closer proximity to the test curve than does the viscous curve. This is also true when comparing the coincident component curves (Figs. 4c and 5c). Although the complex damping curve drops below zero prematurely, it does show a negative value whereas the viscous curve does not. A comparison of the quadrature curves (Figs. 4b and 5b) shows that the viscous damping curve is more representative than the complex damping curve, especially for the high frequency range. Thus, in summary, the complex damping curves seem to fit the coincident component and the total response test results, while the viscous curve seems closer to the quadrature test results.

The complex damping model and its equations will be used for the remaining portions of this paper.
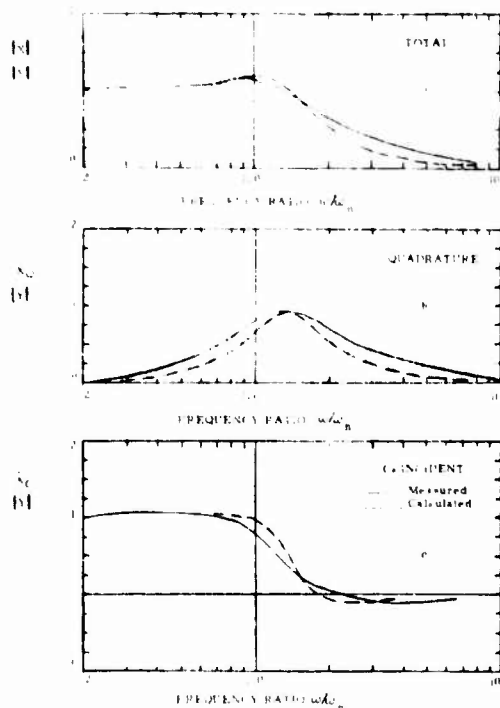
Fig. 4 - Comparison of complex model response
with experimental results, Specimen A

However, these comparisons indicate that reason-
able accuracy can be obtained with either represen-
tation. Neither model shows a clear advantage over
the other.

EXPERIMENTAL RESULTS AND DISCUSSION

The experimental measurements and specimen
characteristics determined using the complex
damping relations are summarized in Table 2.
Basic measurements are the magnitude and fre-
quency of the peak quadrature response, X_Q, and
f_{qp}. From these measurements, the loss factor of
the material, η, and the resonant frequency of the
specimen, f_n, were derived. The table shows that
results were obtained for resonant frequencies that
varied from approximately 100 Hz to 2000 Hz. The
percent error in the calculated maximum dynamic
amplification factor, Q_C, as determined from the
η and f_n values and the maximum measured dynam-
ic amplification, Q_A, is also shown. The peak
quadrature response used to derive the loss factor
shows a variation that is well within the measure-
ment accuracy and should provide a good measure
of η. The percent error in the dynamic magnifi-
cation provides an indication of the accuracy of the
complex damping representation. The average
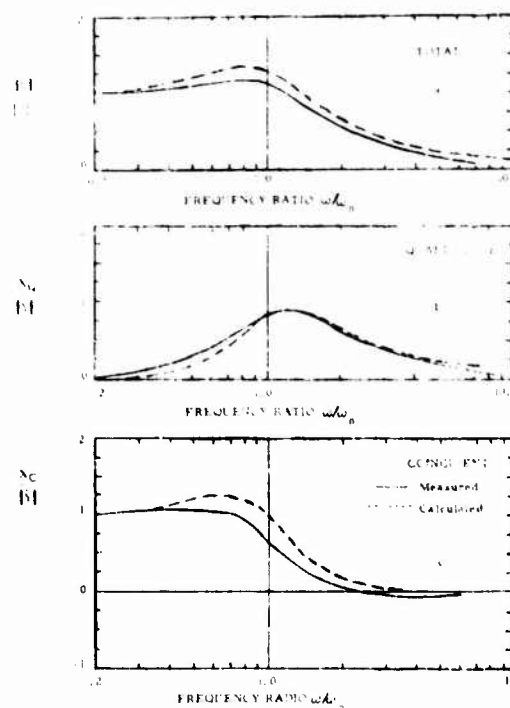
Fig. 5 - Comparison of viscous damping model
response with experimental results, Specimen A

error is approximately 6 percent with approximate-
ly half the data falling above or below the average.
The maximum error was approximately 15 percent
and was for the stiffest most lightly damped speci-
men, i. Tests at twice the excitation level showed
no significant nonlinear effects.

Table 3 summarizes the loss factor, shear
storage modulus, and shear loss modulus deter-
mined from the experimental data. The storage and
loss modulus were determined using the relations:

$$\text{Storage Modulus} = G' = M \left(2 \pi f_n\right)^2 \left(\frac{t}{A}\right) \quad (9)$$

$$\text{Loss Modulus} = G'' = \eta G' \quad (10)$$

where t is the thickness (0.090 in.) and A is the area
(6 in.^{2}) of the shear layer. The loss factor and loss
modulus are plotted as a function of the storage
modulus in Figs. 6 and 7 for the various materials.
Examination of the results relative to the purposes
of the groups tested indicates the following:

Base Resin - A relatively wide range of stiffnesses
was obtained through variations in the base resin
without degrading the loss factor. The loss factor

157

TABLE 2
Summary of Measurements and Comparison of Calculated and Measure Total Response

Group	Purpose	Test Specimen No.	Formulation	η	A_{qp}	f_{qp} (Hz)	f_r (Hz)	Q_C	Q_A	Percent Error
I	Damping &	A	10	1.49	.939	485	362	1.20	1.1?	6.2
	Stiffness	B	12	1.69	.876	350	250	1.16	1.15	0.9
	Variation	C	11	1.58	.908	565	415	1.19	1.09	8.0
		DD	1?	1.10	1.13	570	467	1.55	..7	6.2
	Results	EE	11	1.24	1.04	590	467	1.28	1.17	9.6
		FF	24	1.82	.846	135	93.7	1.14	1.18	3.4
		11	25	1.27	1.03	255	200	1.27	1.25	1.7
II	Crosslinking Effect	G	SMRD	0.179	5.53	1790.	1775	5.67	5.?5	0.5
		1	SMRD 104	0.126	7.75	2100.	2091	7.94	9.40	15.1
IV	Alumina	D	16	0.489	2.16	1680.	1592.	2.28	2.12	7.5
	Filler	E	15	1.50	1.01	880.	686.	1.26	1.16	8.2
	Effect	F	13	1.33	1.00	1000.	775.	1.25	1.13	10.6
		H	19	1.18	1.07	740.	594.	1.31	1.20	9.2
V	Effect of Microsphere Filler	J	SMRD 100F50	1.08	1.13	780.	642	1.36	1.31	3.8
VI	Effect of Plasticizer & Filler	JJ	26	1.12	1.12	315.	257	1.34	1.27	5.3
VII	Control	K	Butyl	0.694	1.60	300.	272.	1.75	1.75	0.

TABLE 3
Material Stiffness and Damping Characteristics

Group	Purpose	Test Specimen No.	Formulation	Hardness	Loss Factor η	Shear Storage Modulus (psi)	Shear Loss Modulus (psi)
I	Damping &	A	10	68	1.49	$.83 \times 10^3$	1.24×10^3
	Stiffness	B	12	50	1.69	.40	.67
	Variation of	C	11	4?	1.58	1.08	1.71
	Base Resin	DD	12	50	1.10	1.39	1.5?
		EE	11	50	1.24	1.39	1.72
		FF	24	--	1.82	.06	.10
		11	25	40	1.27	.25	.32
II	Crosslinking Effect	G	SMRD 100	60	.18	20.0	3.58
		:	SMRD 104	90	.13	28.0	3.53
IV	Alumina Filler Effect	D	16	85	.49	16.1	7.87
		E	15	0	.50	..99	?.89
		F	.?	3?	1.?3	?.??	?.?7
		H	19	--	1.18	2.24	2.64
V	Effect of Microsphere Filler	J	SMRD 100F50	90	1.08	2.62	2.8?
VI	Effect of Plasticizer & Filler	JJ	26	55	1.12	.42	47
VII	Control	K	Butyl	50	.65	.?7	.32

does not appear to be affected by the storage modulus although there may be a slight tendency for the loss factor to be lower for the stiffer formulations.

Repeatability - The duplicate specimens indicated reasonable repeatability although something affected one specimen. The two Formulation No. 11 specimens, C and EE, displayed approximately 28 percent variation in loss factor and storage modulus but almost identical loss modulus. Although the 28 percent variation includes experimental error, this appears to be the degree of repeatability that can be expected with the present method of compounding. If larger quantities were made, the criticality of weighing the ingredients would be reduced and better repeatability should result. On the other hand, the
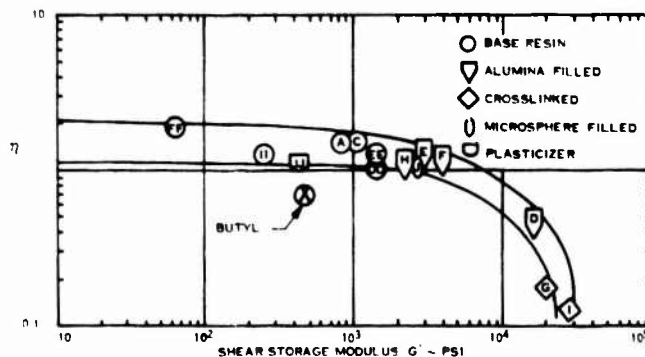
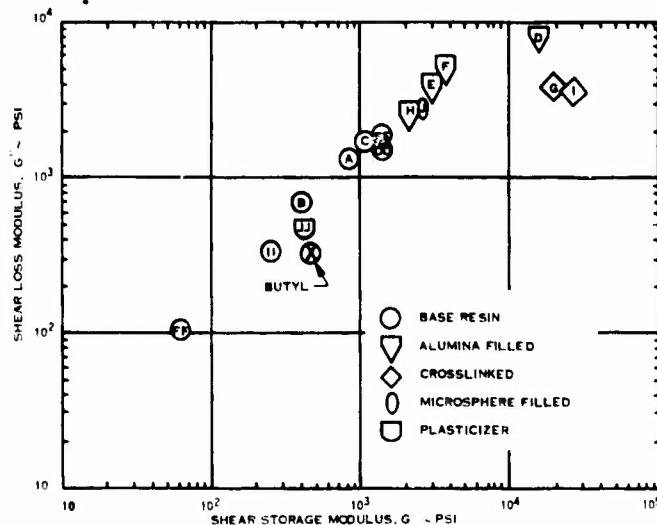Fig. 6 - Variation in loss factor with shear storage modulus

Fig. 7 - Variation in shear loss modulus with shear storage modulus

B specimen, which was duplicated by DD, did not cure properly. When torn apart, material B indicated good bonding to both surfaces of the test specimen. However, the resin in the fixture was very soft and tacky as indicated by the low value of the storage modulus. It was softer than the "hockey puck" cured along with the B specimen. The B specimen resin may have become contaminated somehow. At any rate, the large variation in storage modulus (approximately 3 1/2:1) and loss factor (approximately 1 1/2:1) is not considered representative of the degree of repeatability that can be obtained.

Crosslinking - The crosslinker resulted in a large increase in the storage modulus but did not provide a comparable increase in the loss modulus. The net effect was a significant degradation of the loss factor. Although these materials may be useful if high stiffness with only moderate damping is required, other materials appear to provide superior characteristics.

Filler - The addition of filler, either alumina or silica microspheres, was found to increase damping as well as stiffness. Both the storage modulus and loss modulus were increased over that of the base resin. The loss factor remained high for most of the compounds being only slightly less than that of the base resin compounds. The microsphere filler was not as effective as the alumina filler. However, on a weight basis, the microsphere material, SMRD 100F50, is comparable to the alumina-filled compounds. Because the specific gravity of the microsphere-filled material is only 0.7 compared to 1.2 for the alumina-filled material, the microsphere-filled material provides an equivalent loss modulus of 4800 on an equal weight basis. Therefore, all the materials provide a high effective loss modulus.

Plasticizer and Filler - The addition of plasticizer to the filled material does not appear attractive. The primary effect of the plasticizer is to lower the storage and loss modulus, roughly proportionally. Although the loss factor remained reasonably high,

159

the damping quality of the material is reduced which in many applications is undesirable.

Butyl Rubber Control - Viscoelastic epoxy materials show an order of magnitude increase in the loss modulus and double the loss factor of the Butyl rubber used as a control. As a rubber compound, the Butyl specimen is relatively stiff (50 Durometer) and has a high loss factor. At room temperature the Butyl specimen characteristics do not compare favorably with those of the viscoelastic epoxy materials; however, the Butyl comparison may be more favorable at a lower temperature.

The damping characteristics of the materials tested in this study fall within the banded region of Fig. 6. This banded area indicates the range of parameters that can be readily obtained with variations of the present formulations. The graph indicates that roughly three orders of magnitude variation in storage modulus can be obtained, but that the loss factor will deteriorate for the stiffer materials. The "best" materials appear to be the filled materials in that they provide a high loss factor and a relatively high stiffness.

MATERIAL APPLICATION

Although it is difficult to generalize, the examination of the merits of the various materials applied as a shear layer to a single degree of freedom system indicates the factors that must be considered. The system that will be considered is shown in Fig. 8. It is a simple spring mass system excited by base motion. A shear layer of damping material represented by $K_D (1 + i\eta)$ is added in parallel to the undamped support spring, K. It will be assumed that the allowable shear strain is the same for the various damping materials. The objective is to determine the amount of the various damping materials required to provide a desired dynamic magnification factor, Q.

Using the notation of the previous sections, the system loss factor (η_s), and magnification factor (Q) are:

$$\eta_s = \left(\frac{K_D}{K + K_D}\right)\eta \qquad (11)$$

$$Q = \frac{(\eta_s^2 + 1)^{1/2}}{\eta_s} \qquad (12)$$

A convenient measure of the amount of damping material is A/t where A is the shear area of the damping layer and t is the thickness. Based on the assumption of a constant allowable shear strain for the various materials, the layer thickness will be
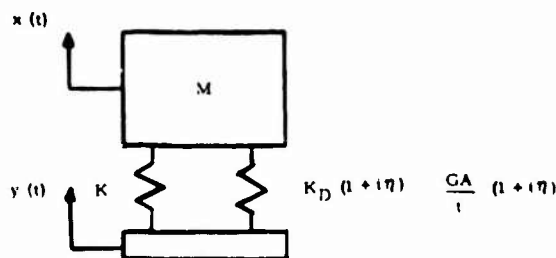

Fig. 8 - Analytical model of typical system

the same for all materials for a particular dynamic magnification factor. Therefore, a material which minimizes A/t will provide the smallest shear area design. This ratio can be generalized by dividing by the spring constant of the system. Substituting GA/t for K_D in equation (11) and solving, the parameter describing the "amount of damping material is found to be:

$$\frac{A}{tK} = \frac{1}{G\left(\dfrac{\eta}{\eta_s} - 1\right)} \qquad (13)$$

Examination of this equation indicates several limiting conditions. If $\eta >> \eta_s$, the controlling parameter is simply $G\eta$, the loss modulus of the damping material. As the desired system loss factor approaches the material loss factor, very large amounts of damping material are required. It becomes impossible to provide the desired system damping when $\eta \leq \eta_s$.

Also of interest, is the shift in system resonant frequency from the original resonant frequency, f_0. This can be expressed as:

$$f/f_0 = \left[1 + G\left(\frac{A}{tK}\right)\right]^{1/2} \qquad (14)$$

Using these equations and the values of G and η for selected materials from Table 3, the curves shown in Figs 9 and 10 were obtained. The curves show the variation in parameters A/tK and f/f_0 as a function of the system dynamic magnification factor. As indicated previously, low values of A/tK are desired in that this provides the smallest damping material area. The curves show the filled materials to be the best. Although not evident from the previous curves, the "D" material is better than the other filled materials for Q values greater than roughly 4, while the "F" material which has a considerably higher loss factor, is best for the very low Q range. The unfilled base resin, as indicated by the curve for Specimen C, requires 3 to 4 times the area of the best filled materials while the Butyl requires 20 times the area. The crosslinked material
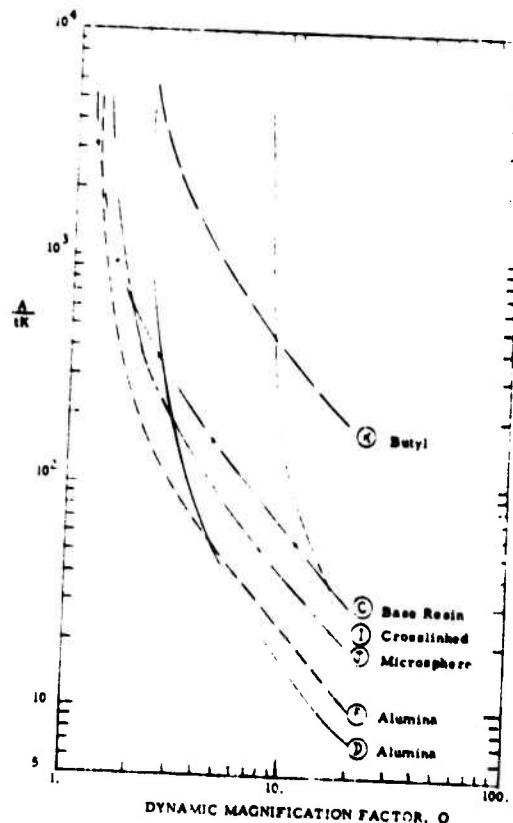
Fig. 9 - Variation in area parameter with
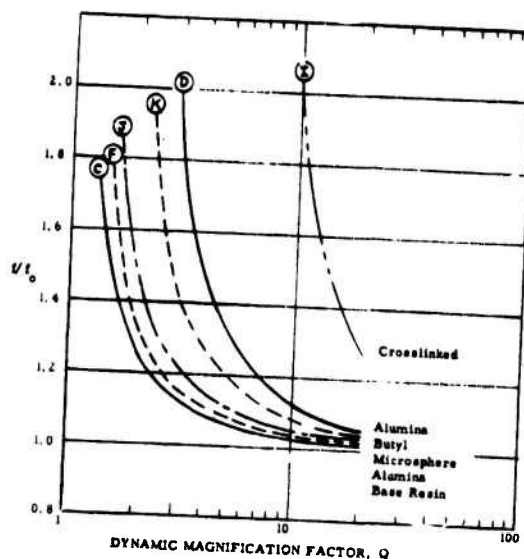dynamic magnification factor

Fig. 10 - Variation in system resonant
frequency with dynamic magnification factor

requires more than 3 times the area of the best fill-
material for the Q's of interest and has a large stiff-
ening effect. Because of the high loss factors of the
filled materials, they provide a relatively small in-
crease in resonant frequency for dynamic magnifica-
tions on the order of 10 but would provide 20 to 40
percent increase in the resonant frequency if lower
dynamic magnifications are required.

Although the trends and limitations indicated in
this example aid in understanding the factors in-
volved in applying damping materials, practical ap-
plications involve many other considerations. How-
ever, these viscoelastic epoxy materials provide
high loss factors which can be used effectively to
limit resonant responses through proper application.

CONCLUSIONS

Based on the results of this investigation, the
following conclusions are made:

1. Viscoelastic materials having loss factors more
than twice that of Butyl rubber are available for a
range of stiffnesses varying by more than two orders
of magnitude.

2. The experimental technique and the complex
damping representation used for the material evalu-
ation enabled the damping and stiffness character-
istics of the materials to be measured and modeled
with an average error of 6 percent.

3. Either complex damping or viscous damping can
be used to represent the material characteristics
with reasonable accuracy.

4. Formulations having additional crosslinking de-
grade the damping of the material.

5. The addition of filler material to the formula-
tions increases the stiffness without significant de-
gradation of the loss factor and provides the highest
loss modulus of the materials tested.

6. The addition of plasticizer to the formulations
reduces the stiffness without degrading the loss
factor.

7. Using current methods of compounding, the
material characteristics are repeatable within ap-
proximately 30 percent.

REFERENCES

1. Stahle, C. V. and Tweedie, "A Layered Visco-
elastic Epoxy Material for Vibration Control,"
Shock and Vibration Bulletin 42, Pt 4, Jan. 1972.

2. Jones, D. I. G., "Damping Treatments for
Noise and Vibration Control," Sound and Vibra-
tion, July 1972.

DISCUSSION

Mr. Nashif (University of Dayton): I think the reason the butyl rubber didn't show up as good as your material is because apparently your material is optimized at room temperature, while butyl rubber is optimized at zero degrees fahrenheit. At that temperature it has as high a damping or as high a loss factor as the material you have developed. I think for a better comparison you should have picked a room temperature optimized material to compare with. Do you have any comments on that?

Mr. Stahle: When we were doing this testing we hadn't looked into the temperature characteristics of the material. I have since become very much aware of the fact that there is a transition temperature range where the materials show up as much better. I was aware of what it was for the butyl. It was a material used in this particular application, and we put it in as a control. However, I have the feeling the loss factors that this class of materials has at this transition temperature, which is apparently room temperature, is relatively high. I wonder if you would comment on that.

Mr. Nashif: It is about as high as most of the materials optimized at room temperature.

Mr. Stahle: Is it higher or is it just as high?

Mr. Nashif: It is as high. Most materials at their optimum are usually between one and 1.4 in loss factor. The problem is to find where that optimum is so you can match it with the environment that the material is going to be used for.

Mr. Henderson (Materials Laboratory WPAFB): If I understood your slide correctly, you were using the mass on the shear layer as a means of deriving your material properties. Is this correct?

Mr. Stahle: That is correct.

Mr. Henderson: Did you take any measurements to find out if your block was rotating? Your center of mass of the block was much higher that your shear layer and we have found in some of our previous tests that this can sometimes give a lot of rotation in that block. Did you put accelerometers in various locations on the block or what?

Mr. Stahle: No, we did not. The characteristic as indicated by the quadrature total response show a single resonant peak. The shear layer itself was rather thin and also the length of the shear layer was fairly large. I presume the rotational motion did not effect the results, however, we did not measure this. The accelermeter was at the center of the block. We had no indication of a second resonance.

VISCOELASTIC DAMPING IN FREE VIBRATIONS
OF LAMINATES

S. Srinivas
NAS Post-Doctoral Resident Research Associate
NASA Langley Research Center
Hampton, Virginia 23365

(U) In this paper a parametric study of free vibrations of viscoelastic laminates has been carried out using a three-dimensional analysis. Three-layer laminates with a viscoelastic core of the standard linear solid type are studied numerically. The most important parameters affecting damping are the relaxation parameter of the core, intermodular ratio, and the standard linear solid parameter. Also, damping is not always a monotonic function of intermodular ratio or the relaxation time of the core.

Thin-plate theory yields highly inaccurate estimates of damping, whereas an approximate laminate theory, in which displacements are assumed to be piecewise linear across the thickness and transverse shear deformations are taken into account, evaluates the damping very accurately.

INTRODUCTION

(U) Damping in laminates has been studied by DiTaranto and McGraw [1] and Abdulhadi [2]. In both studies, transverse shear stresses in the outer layers and bending stresses in the core were neglected. Such simplifications lead to inaccuracies when the core material does not have a relatively low modulus. Classical thin-plate theory, when applied to laminates, also leads to errors when the laminate is thick and the core is of relatively low modulus material. The purpose of the present paper is to study the damping characteristics of viscoelastic laminates under free vibrations by means of an exact three-dimensional analysis, in which no simplifying assumptions other than small deformations and linear stress-strain law are made. The laminates are simply supported on all sides. The complex frequencies of free vibration, whose real parts correspond to oscillations and imaginary parts correspond to damping, are evaluated for three-layer laminates with viscoelastic cores and elastic outer layers. The influences of various parameters on damping are investigated and the significant parameters are identified. Since the simple support conditions simulate the nodes in wave propagation in infinite laminates, the results presented are readily applicable to infinite laminates.

A general, three-dimensional analysis is very complicated, except perhaps for simple configurations such as simply supported rectangular laminates. When three-dimensional analysis is impossible or impractical from a computational standpoint, approximate theories must be used. With this in mind, an assessment of some of the approximate theories (those of Abdulhadi [2], Srinivas [3], and the classical thin plate) is made by comparing their results with the exact results presented herein.

NOMENCLATURE

a, b	Length and width of laminate
h_j	Thickness of j-th layer
G_1, G_3	Shear modulus of outer layers 1 and 3
$\bar{G}_2$	Complex shear modulus of the core
K	Bulk modulus of the core
k	Bulk modulus parameter of the core = K/μ
m, n	Integers used in trigonometric expansion of displacements and stresses in x and y directions, respectively
$[(mh_1/a)^2 + (nh_1/b)^2]$	Modal parameter
t	Time

u, v, w	Displacements in x, y, z directions, respectively
α	Standard linear solid parameter
G	Intermodular ratio $= G_1/\mu$

γ Relaxation parameter $= \left[\dfrac{G_1}{\rho_1 h_1^2}\right]^{1/2} \tau$

λ_d Damping coefficient $= \left[\dfrac{\rho_1 h_1^2}{G_1}\right]^{1/2} \Omega_d$

λ_r Oscillation coefficient $= \left[\dfrac{\rho_1 h_1^2}{G_1}\right]^{1/2} \Omega_r$

μ	elastic shear modulus of the core
ν_j	Poisson's ratio of the j-th layer
ρ_j	Mass density of the j-th layer
τ	Relaxation time of the viscoelastic core
Ω	Complex frequency of vibration
Ω_r, Ω_d	Real and imaginary parts of frequency Ω

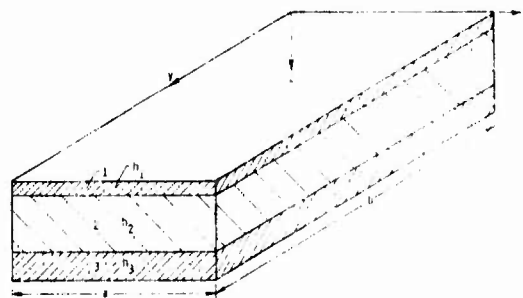Coordinate system and dimensions are given in Fig. 1.

Fig. 1. Three-layer laminate

ANALYSIS

The governing differential equations and the stress-displacement relations of linear small deformation theory for free vibrations of viscoelastic bodies are the same as those for elastic bodies [4], except that the bulk modulus K, shear modulus G, and frequency Ω are complex for viscoelastic bodies. Thus, viscoelastic laminates are formally analyzed much as elastic laminates are. In this paper, the

analysis of simply supported elastic laminates [5] is adapted to viscoelastic laminates and is briefly described in the Appendix. The analysis is applicable to multilayer laminates and no restriction is needed about the type of viscoelastic material.

The mode shape is trigonometric in the (x, y) plane and is of the form,

$$w(x,y,z) = W(z) \sin(m\pi x/a) \sin(n\pi y/b)$$

The time dependence of displacements and stresses in a freely vibrating viscoelastic laminate is of the form

$$\xi(x,y,z,t) = \Xi(x,y,z)e^{-\Omega_d t}(B \sin \Omega_r t + C \cos \Omega_r t) \quad (1)$$

where, ξ and Ξ correspond to any stress or displacement. B and C are arbitrary constants and Ω_r and Ω_d are the real and imaginary parts of the complex frequency Ω and correspond to oscillation and damping, respectively.

The characteristic equation defining the frequencies is given in the Appendix. This transcendental characteristic equation can be solved to yield an infinite set of frequencies for given material properties and modal parameter $\left[(mh_1/a)^2 + (nh_1/b)^2\right]$. Of this infinite set of frequencies, the one contributing most to the response under a transverse load is called the primary flexural frequency. In this paper only primary flexural frequencies are presented because they are the most important in transverse vibration and flexural response problems.

For numerical investigations three-layer laminates with elastic outer layers and viscoelastic core of standard linear solid type have been considered. For a standard linear solid, the bulk modulus is a real constant, but the shear modulus is complex and frequency dependent:

$$\overline{G} = \mu(1 + i\tau\Omega)/(1 + i\alpha\tau\Omega) \quad (2)$$

where α is the standard linear solid parameter and τ is the relaxation time. The relaxation time is a measure of the damping capacity of the viscoelastic material. The standard linear solid would correspond to an elastic material when either $\alpha = 1$ or $\tau = 0$. In such a case $\overline{G} = \mu$, a constant, and for this reason μ is referred to as the elastic shear modulus.

164

NUMERICAL RESULTS

In the numerical investigations, greater importance was attached to the properties of the core, since it is the damping agent. In order to keep the volume of results within reasonable limits, the two outer layers were made identical and their properties, in general, held constant while the core properties were varied systematically.

The ratio of the shear modulus of the outer layers to the elastic shear modulus of the core is referred to as the intermodular ratio ($\beta = G_1/\mu$). Also, three nondimensional parameters — the relaxation parameter of the core λ, the damping coefficient λ_d, and the oscillation coefficient λ_r — are defined as

$$\gamma = \left(\frac{G_1}{\rho_1 h_1^2}\right)^{1/2} \tau; \quad \lambda_d = \left(\frac{\rho_1 h_1^2}{G_1}\right)^{1/2} \Omega_d;$$

$$\lambda_r = \left(\frac{\rho_1 h_1^2}{G_1}\right)^{1/2} \Omega_r.$$

γ, λ_d, and λ_r are linearly related to τ, Ω_d, and Ω_r, respectively.

Six different laminates (see Table 1) were chosen for numerical investigation. A wide range of γ's (3 to 3000) and β's (1 to 100) have been considered. For example, for a three-layer laminate with 1/8-inch-thick aluminum outer layers, γ of 3 and 3000 correspond to core relaxation times of 0.0000105 and 0.0105 second.

TABLE 1
Properties of Laminates

Number of layers: 3
Outer layers (1 and 3): Elastic and identical
Core (layer 2): Standard linear solid, $h_2/h_1 = 8$

Laminate	α	ρ_1/ρ_2	k	ν_1
A	0.1	5	2	0.3
B	0*	5	2	0.3
C	0.5*	5	2	0.3
D	0.1	10*	2	0.3
E	0.1	5	5*	0.3
F	0.1	5	2	0.2*

Laminate A is considered the reference laminate. In the other laminates, of the material properties α, ρ_1/ρ_2, k, and ν_1 only one is different from those of laminate A. The differing property is indicated by an asterisk (*).

In Fig. 2, the damping and oscillatory coefficients are plotted against the relaxation parameter. In Fig. 3, the damping and the oscillatory coefficients are plotted against intermodular ratio for different relaxation and modal parameters. In Fig. 4, the dai in oscillatory coefficients obtained by appr. mate theories — classical thin-plate theory, sandwich plate theory [2], and refined laminate theory [3] * — are compared with exact values.

DISCUSSION

a. Damping

Figure 2 indicates that damping does not monotonically increase with relaxation parameter. The range in which the damping coefficient decreases with increase in γ is a function of α and β. Damping starts decreasing when the bending energy in the core begins to dominate over the shear energy in the core. Also, at low values of γ the damping coefficient is nearly independent of α and β. At high values of γ, both α and β have a significant influence on the damping coefficient.

Figure 3 indicates that the damping coefficient does not decrease monotonically with increasing intermodular ratio (that is, decreasing shear modulus of the core). This is due to the way in which bending and shear energies in the core vary. With increasing β, bending energy in the core decreases while the shear energy increases initially, then decreases later. In the range from zero to the value of β for which λ_d is minimum, the bending energy in the core predominates over the shear energy. For β's greater than this minimum, the shear energy in the core predominates over the bending energy. The damping coefficient λ_d has a maximum in the range of β greater than β (for λ_d minimum). This maximum corresponds to maximum shear energy. The β for which λ_d is a minimum and the β for which λ_d is a maximum differ for different γ's, but are not strong functions of the other core properties.

*Reference [3] deals with elastic laminates and has been adapted here to viscoelastic laminates.
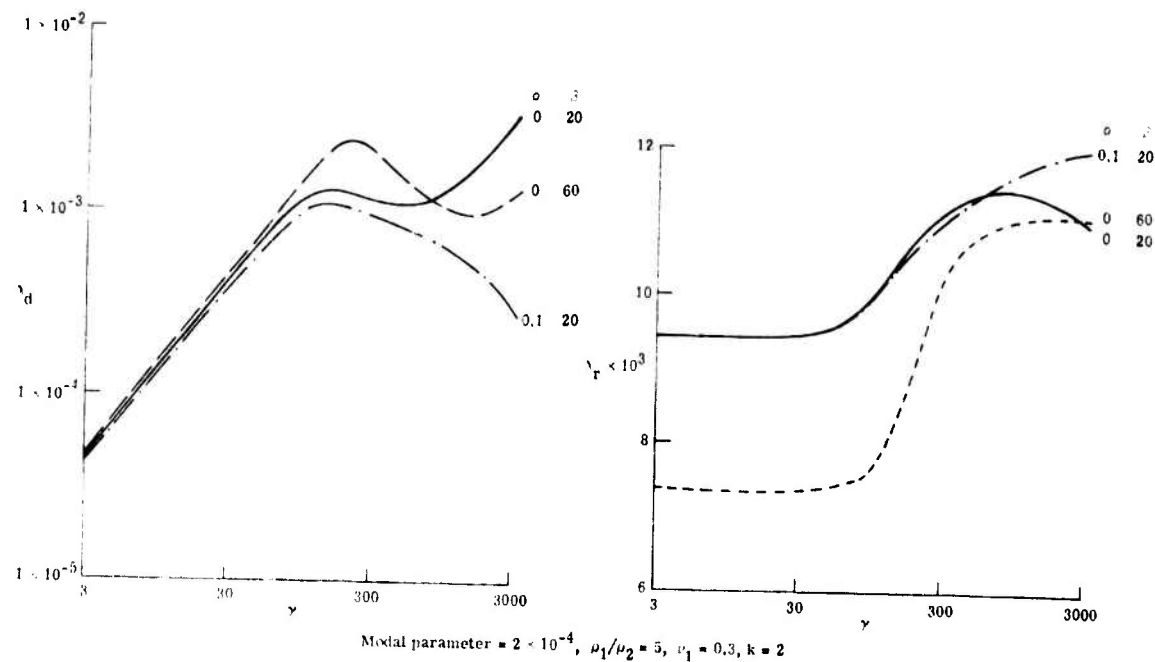
165

Fig. 2. Variation of the damping (λ_d) and oscillation (λ_r) coefficients with the relaxation parameter (γ)
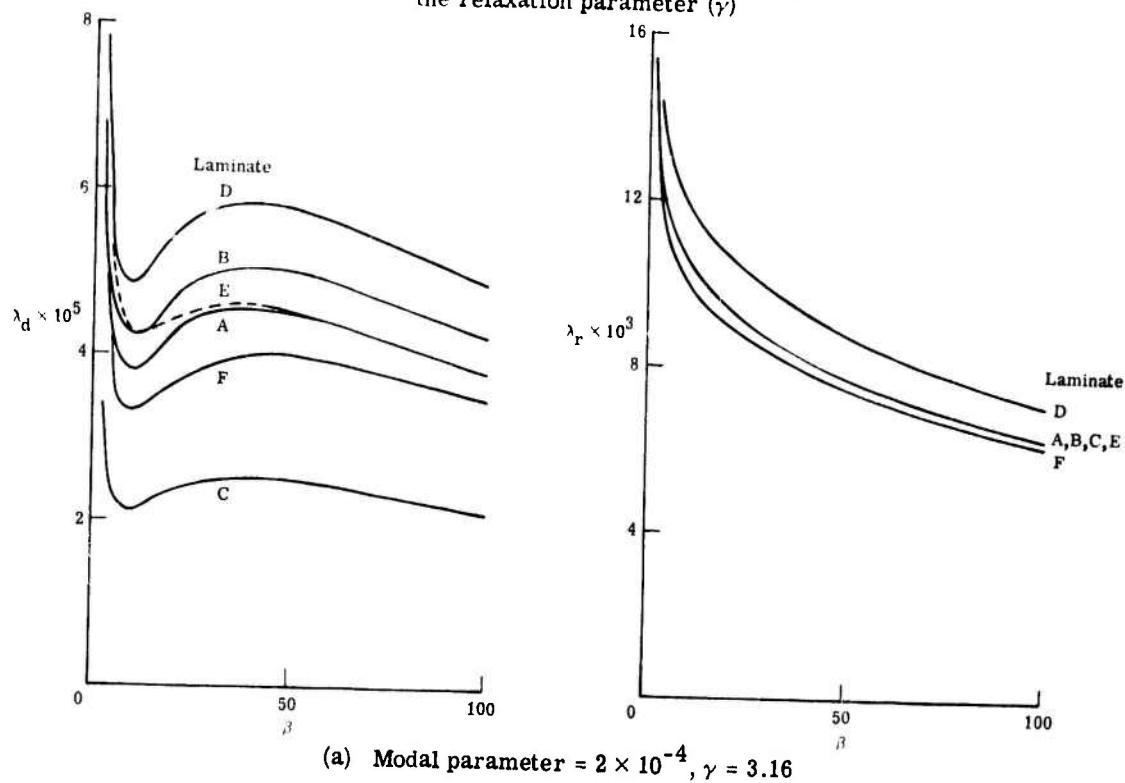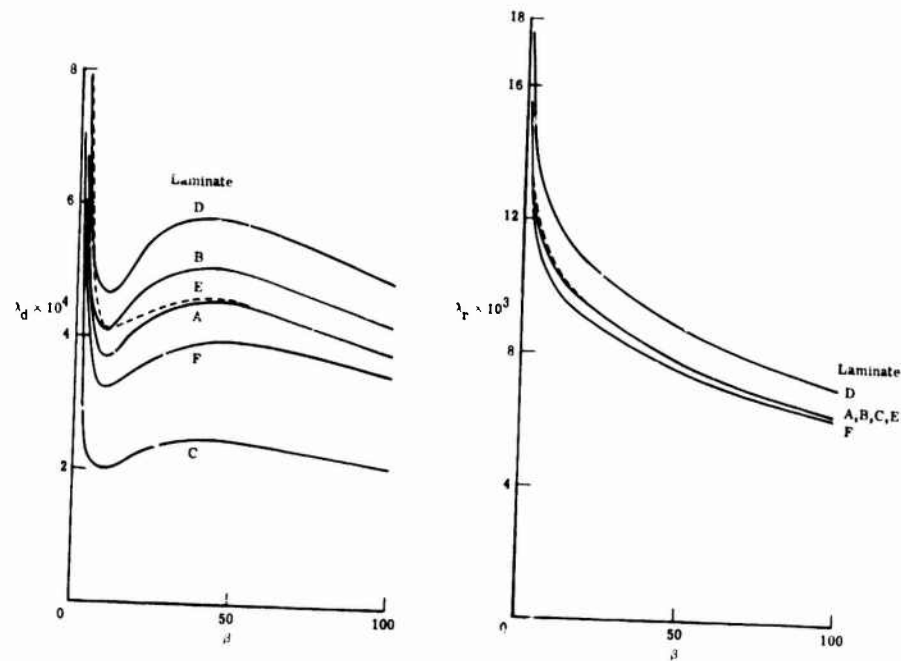

(a) Modal parameter = 2×10^{-4}, $\gamma = 3.16$

Fig. 3. Variation of damping (λ_d) and oscillation (λ_r) coefficients with the intermodular ratio (β)
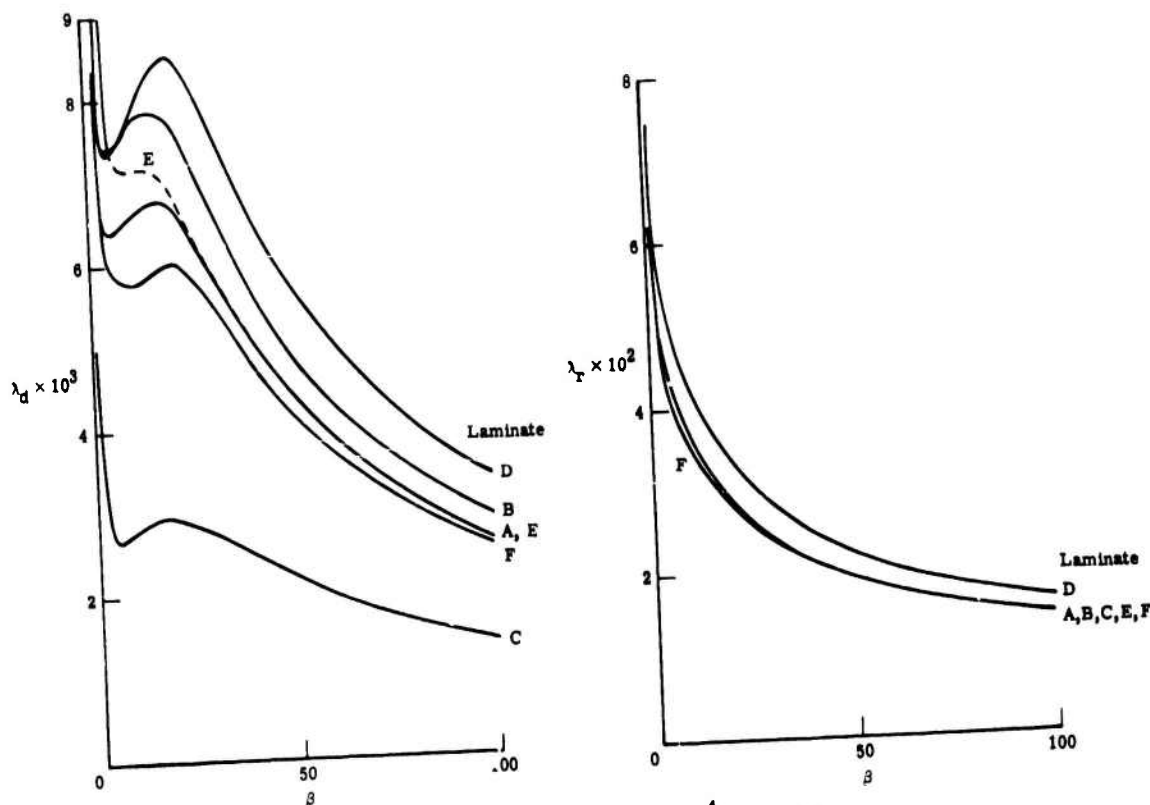
166

(b) Modal parameter = 2×10^{-4}, $\gamma = 31.6$
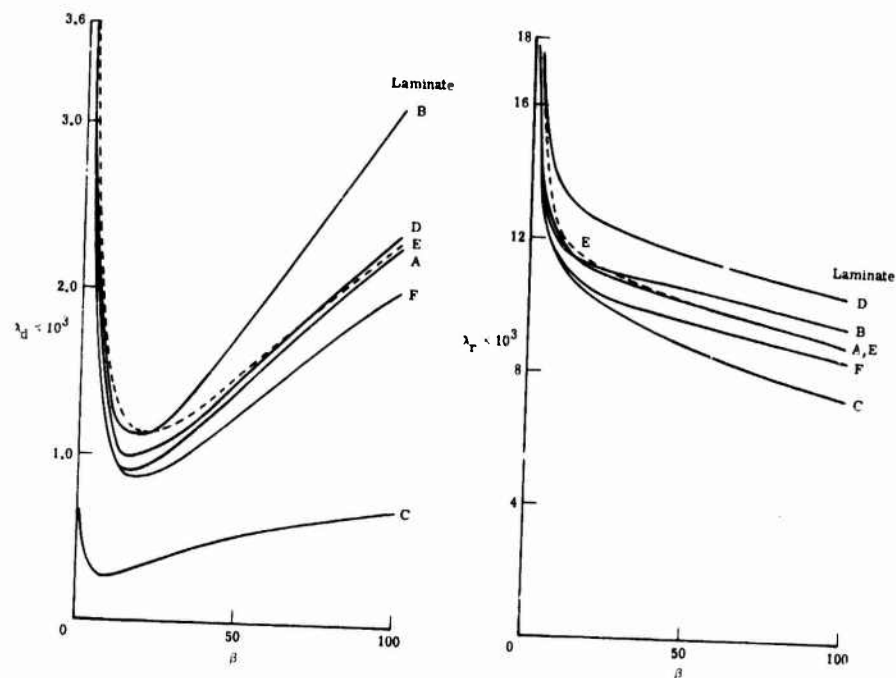
Fig. 3. Continued

(c) Modal parameter = 2×10^{-4}, $\gamma = 316$

Fig. 3. Continued

(d) Modal parameter $= 8 \times 10^{-4}$, $\gamma = 31.6$

Fig. 3. Concluded

As shown by the curves A, B, and C in Fig. 3, the damping decreases as the standard linear solid parameter α increases, and the influence of α on damping depends only slightly on β.

The influence of the bulk modulus parameter $(k = K/\mu)$ on damping is very small, except at low values of the intermodular ratio (refer to curves A and E).

A decrease in the density of the core, relative to the outer plies, increases damping (compare curves A and D). However, the ratio λ_d/λ_r, which is a measure of the decrease in amplitude between successive peaks of oscillation, does not change significantly.

A decrease in Poisson's ratio of the outer plies ν_1 decreases the damping (see curves A and F). Damping, as well as the ratio λ_d/λ_r, increase as the modal parameter increases (compare Figs. 3(b) and 3(d)).

b. Oscillation

Figure 2 indicates that with increasing γ, λ_r remains almost constant up to a certain γ, then increases rapidly, then flattens out or has a maximum with a subsequent decrease. The rapidity of increase as well as the subsequent behavior with an increase in γ is a function of both β and α.

Figure 3 indicates that the oscillation coefficient λ_r decreases monotonically with an increase in β.

The parameter α has negligible influence on λ_r at lower values of γ, but at higher values of γ and β, λ_r decreases with an increase in α (see Fig. 3). In general, the value of λ_r is higher for a viscoelastic laminate than it is for an elastic laminate ($\alpha = 1$ for core). The bulk modulus parameter (k) has an insignificant influence on λ_r. A decrease in Poisson's ratio of the outer plies (ν_1) reduces λ_r slightly. The

168

oscillation coefficient increases with increase in the value of modal parameter (compare Figs. 3(a) and 3(d)).

c. Approximate Theories

Thin-plate theory yields highly erroneous values (see Fig. 4), especially when the intermodular ratio is high. It underestimates

damping and overestimates the oscillatory coefficient, with the error in the damping parameter being greater than the error in the oscillation parameter. Also, thin-plate theory does not indicate the true trend in the variation of damping with respect to the variation in the intermodular ratio or relaxation parameter.
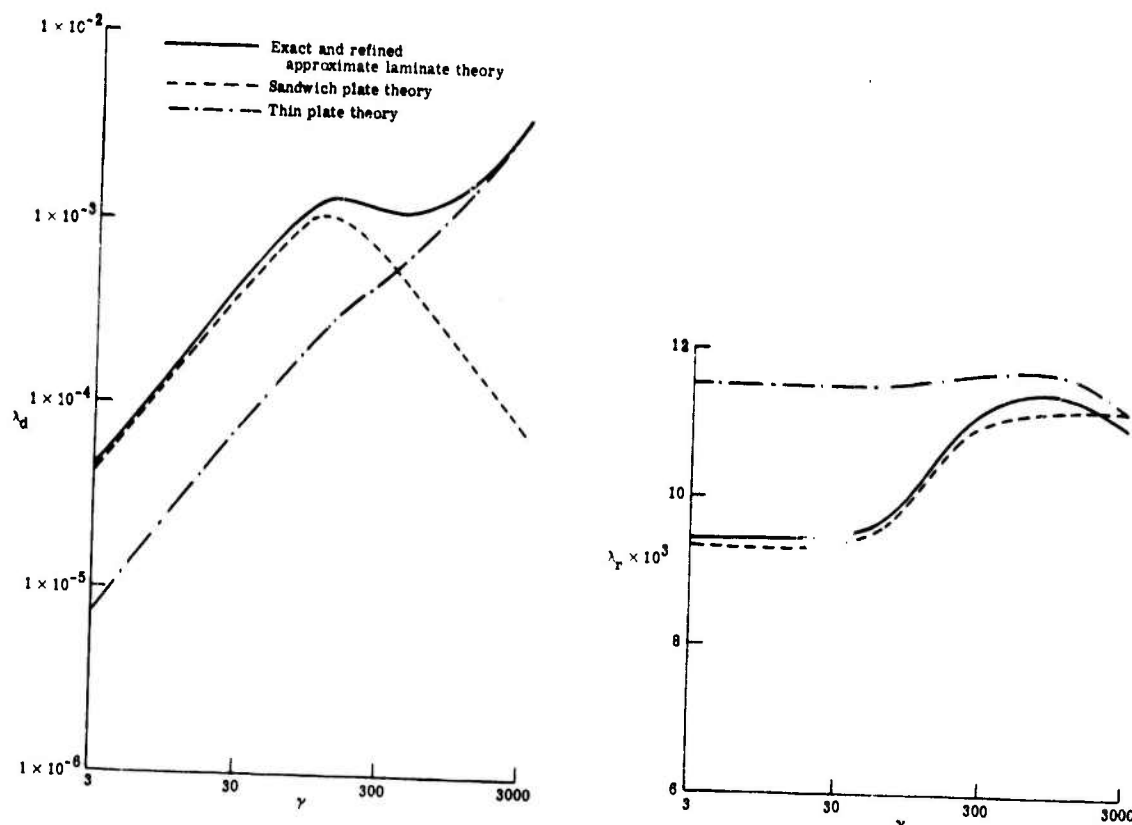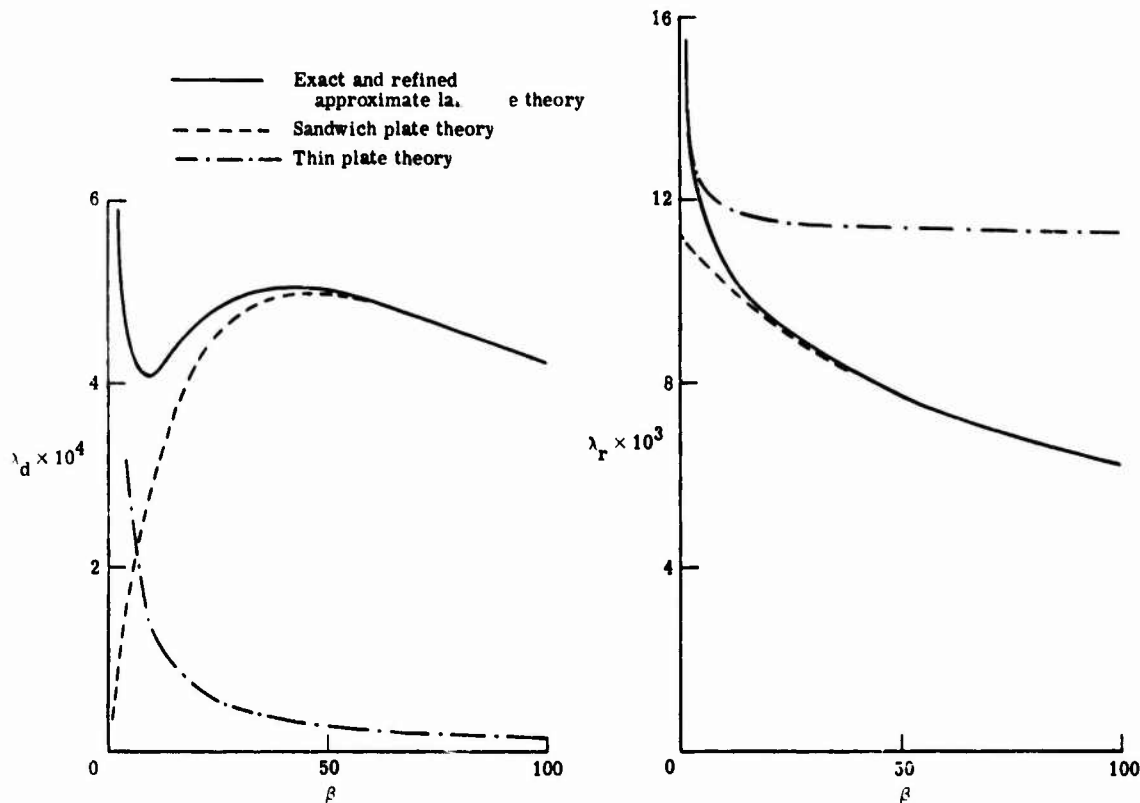

(a) Laminate B, modal parameter = 2×10^{-4}, $\beta = 20$

Fig. 4. Comparison of results from approximate and exact theories

In the refined approximate laminate theory [3] the displacements u and v are assumed piecewise linear across each of the plies and w is assumed constant across the thickness. Taking into account the effects of transverse shear deformations and rotary inertia, the governing differential equations, $(3 + 2 \times \text{No. of plies})$ in number, are derived through variational considerations. Both λ_r and λ_d obtained using this analysis could not be distinguished from the exact curves in Figs. 2 to 4. The reasons for such a high degree of accuracy are: (1) the true distribution of displacement across the thickness is nearly piecewise linear (found from three-

dimensional analysis), and (2) the transverse shear deformations and bending stresses in the core are taken into account.

Results obtained using the "sandwich plate" theory [2] are plotted in Fig. 4. This theory yields accurate results for low to moderate values of γ when the intermodular ratio is high; but at high values of γ, results become inaccurate. At lower values of β, the results are highly erroneous. This is because the influence of the bending stiffness of the core, which is neglected, is substantial at lower values of β. At higher values of β, the bending stiffness of the core is low; thus, neglecting it does not affect the results.

(b) Laminate B, modal parameter $= 2 \times 10^{-4}$, $\gamma = 31.6$

Fig. 4. Concluded

CONCLUDING REMARKS

In this paper, a parametric study of free vibrations of viscoelastic laminates was carried out using three-dimensional analysis. Numerical results were presented for three-layer laminates with elastic outer layers and viscoelastic cores of the standard linear solid type. The various parameters involved are the relaxation parameter of the core, the inter-modular ratio, the standard linear solid parameter, Poisson's ratio of the outer layers, density ratio, and ratio of bulk modulus to elastic shear modulus of the core. Of these, the most significant parameters influencing damping are the relaxation parameter of the core, intermodular ratio, and the standard linear solid parameter. The damping was not, in general, a monotonic function of either the intermodular ratio or the relaxation parameter of the core.

The thin-plate theory, when applied to viscoelastic laminates, is highly erroneous, especially when estimating damping. The sandwich plate theory of Ref.[2] yields accurate results only for high values of inter-modular ratio and moderate values of the relaxation parameter. The refined approximate laminate theory of Ref. [3], in which in-plane displacements are assumed piecewise linear across the thickness and transverse shear deformations and rotary inertia are taken into account, yields highly accurate values of damping and oscillatory parts of the frequency for all values of intermodular ratio, relaxation parameter, and modal parameter. Furthermore, as this approximate theory is far simpler than the exact three-dimensional analysis, it can be used profitably in the analysis of laminates for which three-dimensional analysis is either impossible or impractical from a computational standpoint.

REFERENCES

1. R. A. DiTaranto and J. R. McGraw, "The Free Vibratory Bending of Damped Laminated Plates," ASME Paper No. 69-vibr-68.

170

2. F. Abdulhadi, "Transverse Vibrations of Laminated Plates With Viscoelastic Layer Damping," The Shock and Vibration Bulletin, Bull. 40, Part 5, pp. 93-104, 1969.

3. S. Srinivas, "A Refined Analysis of Thick Anisotropic Laminates," Report AE 283S, Department of Aeronautical Engr., Indian Institute of Science, Bangalore, India, 1971.

4. Y. C. Fung, Foundations of Solid Mechanics, Ch. 15, Prentice-Hall, New Jersey, 1965.

5. S. Srinivas, C. V. Joga Rao, and A. K. Rao, "An Exact Analysis for Vibration of Simply Supported Homogeneous and Laminated Thick Rectangular Plates," J. Sound and Vibration, Vol. 12, pp. 187-199, 1970.

APPENDIX

THREE-DIMENSIONAL ANALYSIS

In the exact three-dimensional analysis of laminates, each layer of the laminate is treated as a homogeneous plate. In addition to the boundary conditions, the conditions of continuity and equilibrium at the interfaces are also satisfied. The governing differential equations of linear, small-deformation theory of viscoelasticity for free vibrations are [4],

$$
\begin{aligned}
\nabla^2 \bar{u}_j + \frac{1}{1-2\bar{\nu}_j} \frac{\partial}{\partial x}\left(\frac{\partial \bar{u}_j}{\partial x} + \frac{\partial \bar{v}_j}{\partial y} + \frac{\partial \bar{w}_j}{\partial z}\right) + \frac{\rho_j \Omega^2 \bar{u}_j}{\bar{G}_j} &= 0 \\
\nabla^2 \bar{v}_j + \frac{1}{1-2\bar{\nu}_j} \frac{\partial}{\partial y}\left(\frac{\partial \bar{u}_j}{\partial x} + \frac{\partial \bar{v}_j}{\partial y} + \frac{\partial \bar{w}_j}{\partial z}\right) + \frac{\rho_j \Omega^2 \bar{v}_j}{\bar{G}_j} &= 0 \\
\nabla^2 \bar{w}_j + \frac{1}{1-2\bar{\nu}_j} \frac{\partial}{\partial z}\left(\frac{\partial \bar{u}_j}{\partial x} + \frac{\partial \bar{v}_j}{\partial y} + \frac{\partial \bar{w}_j}{\partial z}\right) + \frac{\rho_j \Omega^2 \bar{w}_j}{\bar{G}_j} &= 0,
\end{aligned}
\qquad (A1)
$$

where subscript "j" refers to the j-th layer. $\bar{\nu}_j$ and $\bar{G}_j$ are the complex Poisson's ratio and complex shear modulus. $\bar{u}_j, \bar{v}_j,$ and $\bar{w}_j$ are complex and the actual displacements $u_j, v_j,$ and w_j are given by the real parts $\bar{u}_j e^{i\Omega t}, \bar{v}_j e^{i\Omega t},$ and $\bar{w}_j e^{i\Omega t},$ respectively. The differential equations for elastic materials are the same as (A1) except that in the elastic case $\bar{\nu}_j$ and $\bar{G}_j$ are real constants. Thus, the analysis for viscoelastic laminates is formally identical to that for elastic laminates. The analysis of simply supported elastic laminates is available in Ref. [5] and is adapted here to simply supported viscoelastic laminates. The analysis is briefly described below.

The displacements are chosen as

$$
\begin{aligned}
\bar{u}_j &= \phi_j\,(Z)\,\cos\,(m\pi x/a)\,\sin\,(n\pi y/b) \\
\bar{v}_j &= \psi_j\,(Z)\,\sin\,(m\pi x/a)\,\cos\,(n\pi y/b) \\
\bar{w}_j &= \chi_j\,(Z)\,\sin\,(m\pi x/a)\,\sin\,(n\pi y/b)
\end{aligned}
\qquad (A2)
$$

Substituting these in Equations (A1) and simplifying, a set of three homogeneous coupled ordinary differential equations is obtained. Solution of these equations yields expressions for $\phi, \psi,$ and χ. Making use of stress-displacement relationships, expressions for stresses can be obtained. The simple support boundary conditions are automatically satisfied by the present solution because of the form of variation of stresses and displacements in the x and y directions. Satisfying the stress-free conditions on exterior lateral surfaces and the interface conditions, the characteristic equation is obtained. Solution of this transcendental characteristic equation yields the frequencies of free vibration.

The characteristic equation for a three-layer laminate is

$$\begin{vmatrix} \left[L\left(0,1\right)\right]_1 & \left[0\right] & \left[0\right] \\ \left[L\left(H_1,\overline{G}_1\right)\right]_1 & \left[L\left(H_1,-\overline{G}_2\right)\right]_2 & \left[0\right] \\ \left[J\left(H_1,1\right)\right]_1 & \left[J\left(H_1,-1\right)\right]_2 & \left[0\right] \\ \left[0\right] & \left[L\left(H_2,-\overline{G}_2\right)\right]_2 & \left[L\left(H_2,\overline{G}_3\right)\right]_3 \\ \left[0\right] & \left[J\left(H_2,-1\right)\right]_2 & \left[J\left(H_2,1\right)\right]_3 \\ \left[0\right] & \left[0\right] & \left[L\left(H_3,1\right)\right]_3 \end{vmatrix} = 0$$

where,

$$\left[L(Z,q)\right]_j = q \begin{bmatrix} 2g^2 r_j & -2g^2 r_j & 0 & 0 & \left(r_j^2+g^2\right) & \left(r_j^2+g^2\right) \\ \left(r_j^2+g^2\right)M & \left(r_j^2+g^2\right)M & Nr_j & -Nr_j & 2Ms_j & -2Ms_j \\ \left(r_j^2+g^2\right)N & \left(r_j^2+g^2\right)N & -Mr_j & Mr_j & 2Ns_j & -2Ns_j \end{bmatrix} \left[f\right]_j$$

$$\left[J(Z,q)\right]_j = q \begin{bmatrix} r_j M & -r_j M & N & N & M & M \\ r_j N & -r_j N & -M & -M & N & N \\ g^2 & g^2 & 0 & 0 & s_j & -s_j \end{bmatrix} \left[f\right]_j$$

$\left[f\right]_j$ is a diagonal matrix with diagonal terms,

$$\left[\exp(r_j Z), \exp(-r_j Z), \exp(r_j Z), \exp(-r_j Z), \exp(s_j Z), \exp(-s_j Z)\right],$$

where

$$r_j = \left\{ g^2 - \lambda^2 \left(\frac{\rho_j}{\rho_1}\right) \left(\frac{G_1}{\overline{\overline{G}}_j}\right) \right\}^{1/2}$$

$$s_j = \left\{ g^2 - \lambda^2 \left(\frac{1-2\overline{\nu}_j}{2-2\overline{\nu}_j}\right) \left(\frac{\rho_j}{\rho_1}\right) \left(\frac{G_1}{\overline{\overline{G}}_j}\right) \right\}^{1/2}$$

$g^2 = (\text{modal parameter}) \times \pi^2$

$\lambda = \lambda_r + i\lambda_d$

$Z = z/h_1$; $H_1 = 1$, $H_2 = (h_1 + h_2)/h_1$, $H_3 = (h_1 + h_2 + h_3)/h_1$

$M = m\pi h_1/a$, $N = n\pi h_1/b$.

172

The Poisson's ratio $\bar{\nu}_j$ can be expressed in terms of bulk modulus and shear modulus as

$$\bar{\nu}_j = \frac{3\bar{K}_j - 2\bar{G}_j}{2(3\bar{K}_j + \bar{G}_j)}$$

OPTIMUM PASSIVE SHOCK ISOLATION FOR

UNDERGROUND PROTECTIVE STRUCTURES*

David L. Platus
Mechanics Research, Inc.
Los Angeles, California

This study was oriented toward configuration and hardware approaches
for achieving near-optimum performance of six-degree-of-freedom passive
shock isolation systems for underground protective structures. Design
goals were established and preferred isolation systems were selected
and evaluated for three cases of geometry, attach conditions, and
input motions.

INTRODUCTION

Considerable attention has been given to
optimization techniques for active and passive
shock isolation. An extensive treatment of the
subject is presented by Sevin and Pilkey [1],
including an annotated bibliography. The pres-
ent paper is oriented toward configurations and
hardware approaches for achieving near-optimum
performance of passive isolation systems for
underground protective structures.

Previous optimization studies of active and
passive shock isolation using a single-degree-
of-freedom model, notably those of Liber and
Sevin [2], led to the conclusion that, for many
input wave forms, a constant-force isolator pro-
vides the best possible solution in the trade-
off between shock attenuation and rattlespace.
Here, rattlespace denotes the maximum displace-
ment of the isolated article relative to the
base.

Klein [3] studied active and passive three-
degree-of-freedom coupled planar systems and
developed the "Optimum Shock Isolation Theorem".
According to this theorem, for rectangular
objects subjected to translational shock inputs,
optimum performance can always be obtained with-
out rotation of the isolated object. Two impor-
tant conclusions follow. First, the results
obtained from optimizing a single-degree-of-
freedom active system are directly applicable to
any multi-degree-of-freedom active system of
rectangular geometry and rattlespace limits.
Second, an isolation system whose force center
coincides with the center of mass of the iso-
lated object is the optimum configuration for
any passive system. Thus, a system of isolators

which provides constant-force behavior in the
direction of relative motion, and whose force
center coincides with the center of mass of the
isolated object, could, theoretically, provide
optimum shock isolation for many input wave
forms.

The objective of the present investiga-
tion [4] was to predict the performance of six-
degree-of-freedom passive shock isolation sys-
tems of "potentially commercially available"
shock isolators suspending rigid objects. The
systems were to be designed to minimize rattle-
space requirements for specified maximum allow-
able accelerations transmitted to the isolated
objects. Input motions were to be consistent
with those expected to result from nuclear deto-
nations, and the allowable transmitted motions
were to be consistent with the assumed capabil-
ity of electronic equipment. The term "poten-
tially commercially available" as used in this
study implies that, as a minimum, preliminary
development of key features of the isolators
must have been completed.

Isolation system dead space can also influ-
ence the total size of a facility and the
improvement that can be made in existing facil-
ities. Although the primary purpose of this
study was to minimize rattlespace, attention was
also given to minimizing isolation system dead
space in the selection of preferred isolators
and isolation system configurations.

SPECIFIC REQUIREMENTS

Three cases of geometries, weights, and
attach constraints were specified as shown in
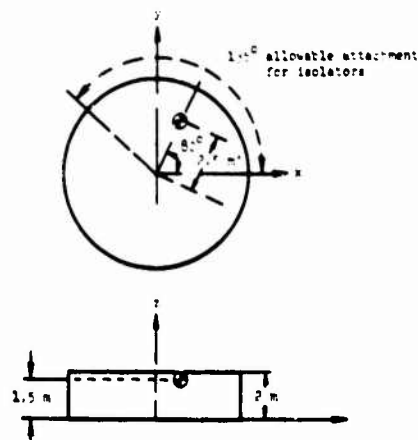Figures 1 to 3. The maximum allowable
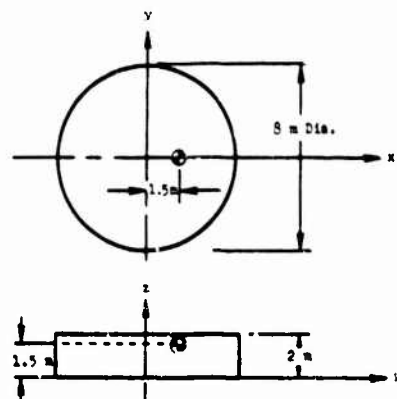
Weight = 10,000 kg

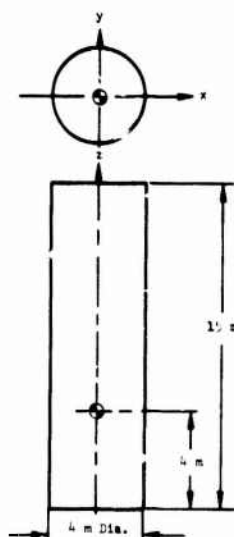Attach Conditions: Isolators can attach anywhere on the isolated object and anywhere on the surrounding facility.

Figure 1. Case I Geometry, Weight, and Attach Conditions

Weight = 40,000 kg

Attach Conditions: No isolators can attach to the top surface of either the isolated object or the surrounding facility, and only compressive loads can be applied to the isolated object.

Figure 2. Case II Geometry, Weight and Attach Conditions

Weight = 10,000 kg

Attach Conditions: Isolators can only attach at the top of the isolated object and within a 135° segment of the lateral surface.

Figure 3. Case III Geometry, Weight, and Attach Conditions

accelerations for any point on the isolated articles were specified as ± 1.58 g vertical and ± 4.74 g horizontal. The systems were required t, withstand several possible cases of input motions, as illustrated in Figure 4.

SPECIFIC DESIGN OBJECTIVES

Specific design objectives were established which guided the selection of isolators and configurations for passive shock isolation systems of interest. These are summarized as follows:

1. Provide constant-force, double-acting, energy-dissipative force-displacement behavior.

2. Provide omnidirectional force-displacement behavior in azimuth.

3. Maintain the isolation system force center as close to the cm as possible.

4. Provide sufficient energy-storage load-stroke behavior in order to passively restore the isolated object to its initial position in the presence of gravity.

5. Minimize "dead space" required for the isolators.

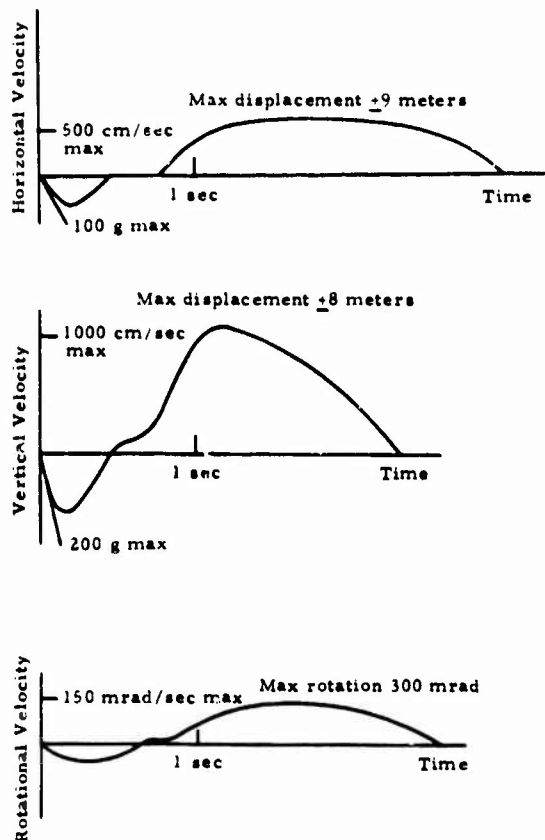6. Minimize the generation and transmission of high-frequency motions.

Figure 4. Typical Input Waveforms

acting system.

From the foregoing examples, it is apparent that, in general, constant-force double-acting energy-dissipative behavior is closer to optimum than constant-force single-acting energy-dissipative behavior or constant-force energy-storage behavior. For many wave forms, it can be shown that constant-force double-acting energy-dissipative behavior will provide the true optimum or "best possible" solution.
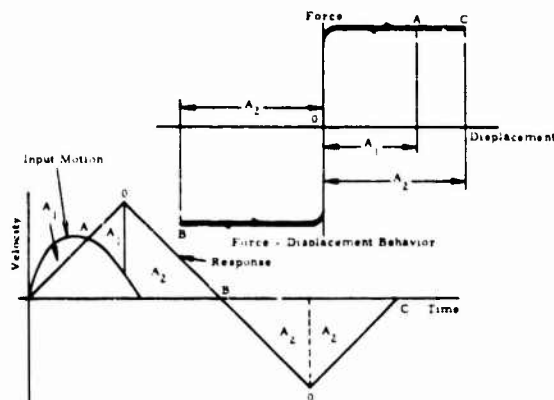
Figure 5. Response Solution for Constant-Force Spring (Energy-Storage) Behavior

Constant-force behavior can result from springs (energy-storage) and dampers (energy-dissipative). Also, dampers can be single-acting (resistance in one direction) or double-acting (resistance in both directions). The influence of these characteristics is illustrated in Figures 5 to 9, in terms of response solutions for single-degree-of-freedom systems. For the spring behavior of Figure 5, the required rattlespace is area A_2. Figure 6 shows the improvement which results from single-acting energy-dissipative behavior. Here the required rattlespace is also area A_2, but is considerably less than that of Figure 5. A further reduction in required rattlespace is shown in Figure 7 for double-acting energy-dissipative behavior. The required rattlespace is now area A_1. Figures 8 and 9 show the trade-off in rattlespace for single-acting and double-acting energy-dissipative behavior, using an input velocity pulse with the characteristic reversal of the specified motions. The required rattlespace is area A_2, but is considerably less for the double-
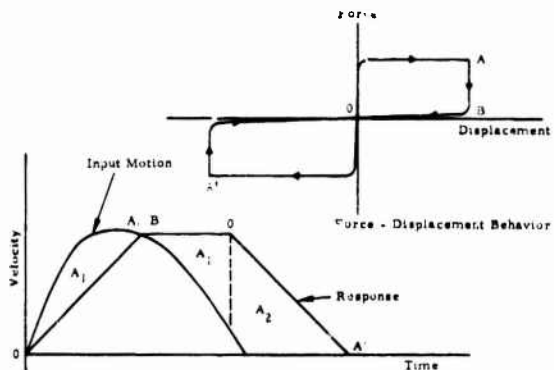
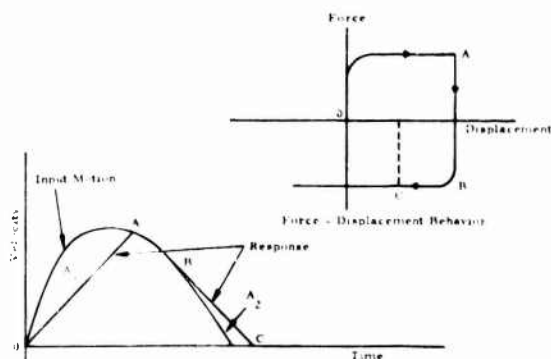Figure 6. Response Solution for Constant-Force Single-Acting Energy-Dissipative Behavior

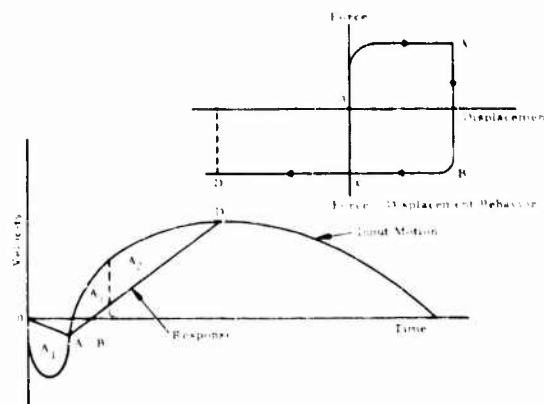Figure 7. Response Solution for Constant-Force Double-Acting Energy-Dissipative Behavior

Figure 9. Response Solution for Double-Acting Energy-Dissipative Behavior
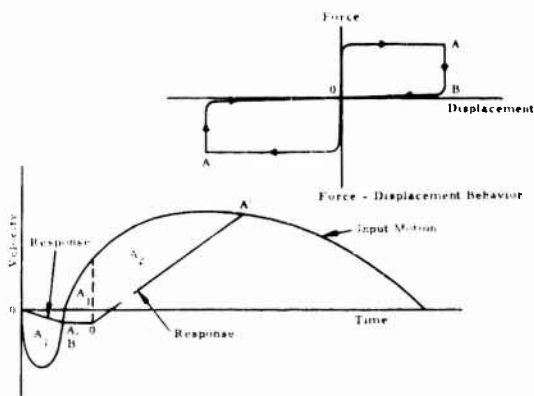

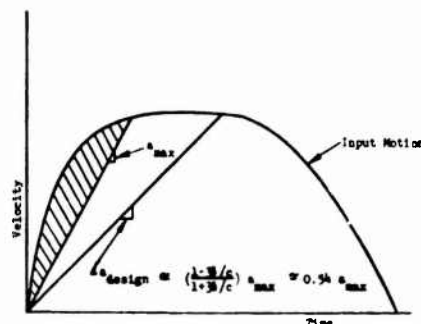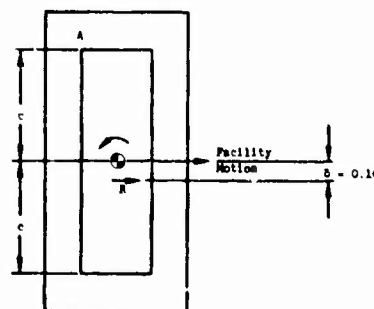Figure 8. Response Solution for Single-Acting Energy-Dissipative Behavior

The effect of translational-rotational coupling on required rattlespace is illustrated in Figure 10 for the case of horizontal input motion. The isolation system force center is eccentric to the cm by an amount $\delta = 0.1\ c$. The resulting rotation produces two effects. First, points at the bottom of the object experience greater acceleration than the cm, so the maximum allowable acceleration of the cm must be reduced, causing an increase in required rattlespace. Second, the horizontal acceleration at point A, which establishes the rattlespace, is further reduced causing a further increase in required rattlespace. For the geometry and waveform shown, the design acceleration is shown [4] to be approximately 0.54 a_{max}. The

Figure 10. Effect of Translational-Rotational Coupling on Required Rattlespace

178

resulting rattlespace is close to three times the "best possible" solution corresponding to the shaded area in Figure 10.

SELECTION OF PASSIVE ISOLATORS

Three types of passive isolators potentially capable of meeting the specific design requirements were identified as liquid spring-shocks, MRI Shock Isolators, and flexible plastic foams.

Liquid springs and shock absorbers are of interest because of their high efficiency, design versatility, and advanced state of development [5, 6]. A unique and attractive form of metering in liquid shock absorbers is the Orivis head concept manufactured by Taylor Devices, Inc. [6]. Three types of Orivis heads are illustrated in Figure 11, and a typical force-stroke curve for a liquid spring-shock with a Type 3 Orivis head is illustrated in Figure 12. All three heads are double-acting. Single-acting energy-dissipative behavior can be achieved with check valves.

MRI Shock Isolators are mechanical devices which convert linear motion to rotary motion and drive efficient constant-torque rotary energy absorbers through one-way ratchet-type or viscous clutches. Relatively weak springs provide restoration. An MRI Shock Isolator for use in a cable-actuated system is illustrated in Figure 13.

A cable passes over a pulley which is connected to a shaft through a one-way ratchet clutch. The cable attaches to a spring mounted on the isolated object, which provides restoration. The shaft drives a constant-torque energy absorber which is connected to the isolated object through a viscous clutch. Under rapid motion which extends the cable, the viscous clutch and the ratchet clutch lock. The constant-torque energy absorber is driven, providing energy-dissipative constant-force resistance to the cable. Under rapid motion which tends to shorten the cable, the ratchet clutch releases and the restoration spring reels in the extra cable. Under subsequent extension of the cable, the ratchet clutch locks and the rotary energy absorber is again driven to provide constant resistance to the cable. Thus, sets of single-acting cable isolator units mounted on opposite sides of the isolated object provide double-acting behavior for the isolation system. After a shock, energy in the displaced springs restores the system through the viscous clutches.

Plastic foam isolators have been investigated for underground protective structures [7] and offer advantages as well as disadvantages compared with other passive isolators [4]. They were given only limited attention in this investigation but further investigation is recommended.
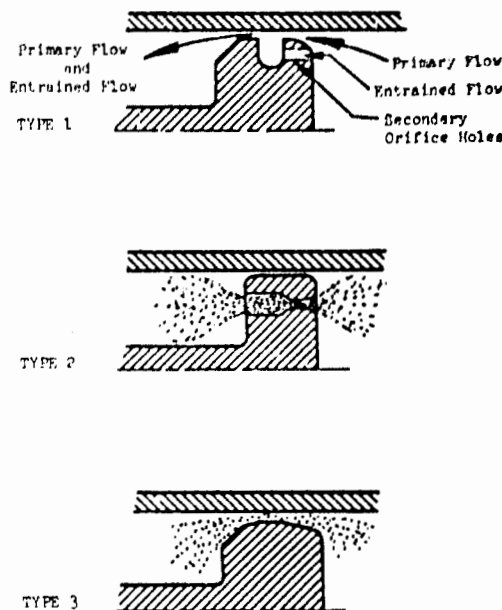

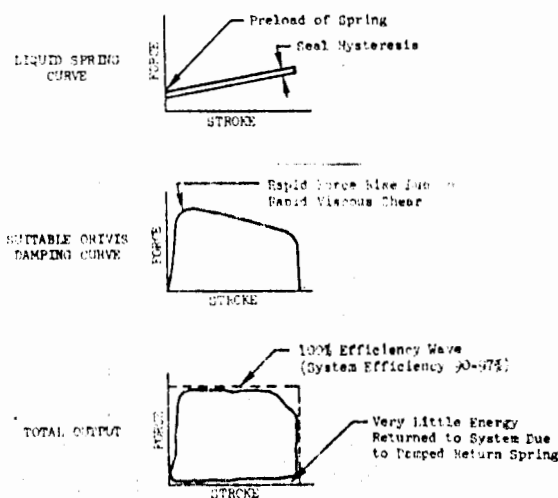Figure 11. Three Types of Orivis Heads Used in Taylor Liquid Spring-Shocks [6]

Figure 12. Force-Stroke Curve for a Liquid Spring-Shock with Type 3 Orivis Head Arresting an Impacting Object [6]
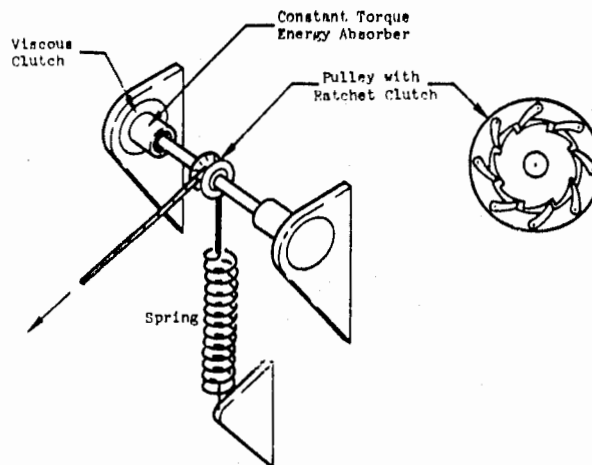
179

BEST AVAILABLE COPY

Figure 13. MRI Shock Isolator for Cable System

PREDICTION OF ISOLATION SYSTEM PERFORMANCE

The isolator model used in this study is shown in Figure 14.

F represents a constant-friction (Coulomb) damper, c a viscous damper, K a linear spring, and δ the initial spring deflection. The energy-dissipation elements F and c can be selected to act in either one direction or both directions so the isolator can be made single-acting or double-acting with respect to damping.

This model was selected to represent either liquid spring-shocks or MRI Shock Isolators. It is a good representation of MRI Shock Isolators, but only approximates liquid spring-shocks. The major source of inaccuracy is the use of a velocity-independent constant-force element and a linear viscous damper. Although the liquid spring-shocks of interest do exhibit constant-force behavior for a particular stroking velocity history, variation in the velocity history can alter the constant-force behavior.

A computer program, called OPSHK, was written to solve for the response of a rigid object suspended on a set of isolators of the type shown in Figure 14 and subjected to the input motions of the type shown in Figure 4. The isolators may attach anywhere on the suspended object or the surrounding facility. The program treats large-displacement behavior. Output is in the form of tables and line printer plots of relative displacements and velocities and absolute accelerations of specified points on the suspended object.

The program was originally written to handle a set of isolators, each having one end pinned to the suspended object, and the other end pinned to the surrounding facility. Only axial loads are transmitted by the isolators, in a direction established by the end points. An option was added to handle the condition where one or two horizontal isolators attach to a fitting which rides on a low-friction vertical rail at the facility wall.
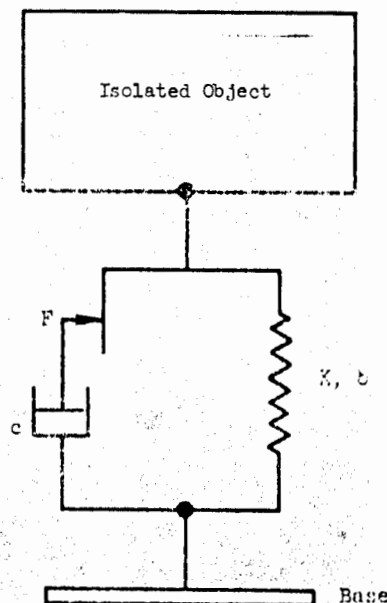

Figure 14. Isolator Model

180

SELECTION OF PREFERRED SYSTEMS

Preferred isolation systems for the three cases of interest have the following common features:

- Liquid spring-shocks are used as the principle isolator elements for providing constant-force energy-dissipative load-stroke behavior, as well as the energy-storage behavior required for restoration.

- Sets of isolators distributed around the isolated article provide omnidirectional horizontal force-displacement behavior required in azimuth, and minimize translational-rotational coupling in the horizontal plane.

- A set of vertical rails connect the horizontal isolators to the facility walls and decouple the horizontal and vertical motions.

The designs of Cases I and III use compact cable-driven rotary isolators employing ball-screws and liquid spring-shocks as illustrated in Figure 15. These isolators handle the large vertical motions without substantially increasing the total space required beyond the rattle-space itself. The ball-screws efficiently convert rotary motion to linear motion, and can be efficiently back-driven permitting the use of smaller liquid spring-shocks than otherwise be required. Ball-splines, not shown in the figure, resist the torques applied to the ball-nut.

Case I

The preferred system for Case I is illustrated in Figures 15 to 17. Preloaded single-acting liquid spring-shocks are used in the vertical system in order to maintain tension on the cable and follow the motion of the isolated object when the cable tends to go slack. The up-load units also support the isolated object and restore the system following a shock.

The horizontal isolation system consists of two sets of rail-mounted, double-acting liquid spring-shocks. The use of double-acting isolators helps to minimize coupling from rail friction since friction forces are produced on opposite sides of the object, proportional to the horizontal forces transmitted to the rails. The moments from these friction forces approximately cancel each other.

The spring-shocks connect to the isolated object and to the shoe assemblies through spherical bearings, in order to minimize bending loads. Because of these bearing connections stabilizer springs are added to react vertical loads on the shoes from friction, shoe inertia, and vertical components which may result from rotation of the horizontal

isolators. An alternate means for providing stability is to tilt pairs of top and bottom isolators attached to a common shoe.
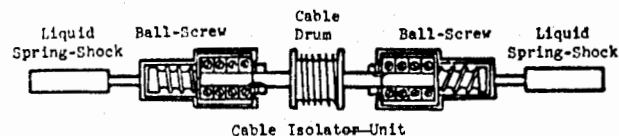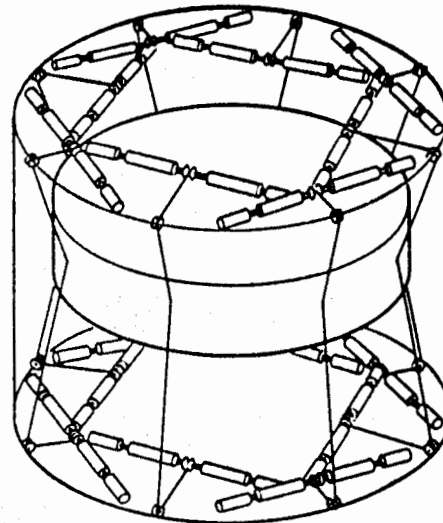

Figure 15. Case I Vertical Isolation System and Cable Isolator Unit

In addition to the primary isolation system illustrated in Figures 15 to 17, impact limiters are required to attenuate relatively low-velocity impacts between the isolated object and the facility walls; or within the primary isolators as they "bottom out" prior to impact between the object and the facility walls. The energy associated with these impacts is a small fraction of that absorbed by the primary system. Relatively small plastic foam or elastomeric pads should be adequate.

The preferred horizontal isolation system of Figure 17 is believed to be equally efficient and mechanically superior to an earlier approach, shown in Figure 18, which was used for the performance evaluation.

Because of the offset cm, isolator force levels in both the vertical and horizontal systems vary as a function of isolator location in order to minimize translational-rotational coupling.

Case II

The preferred system for Case II is illustrated in Figures 19 to 21. The system is made up of the following key elements.
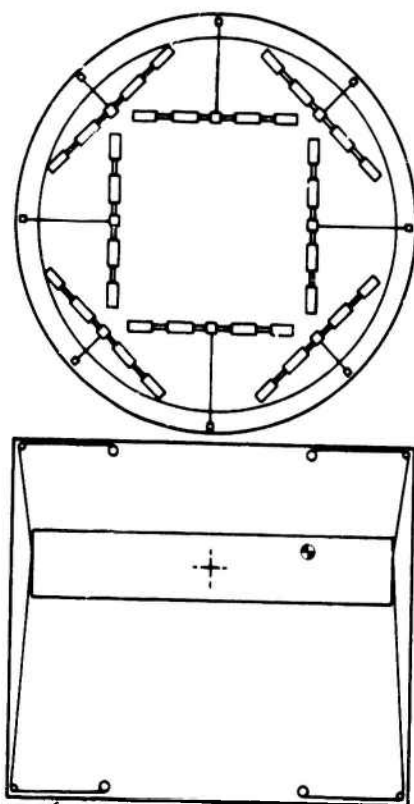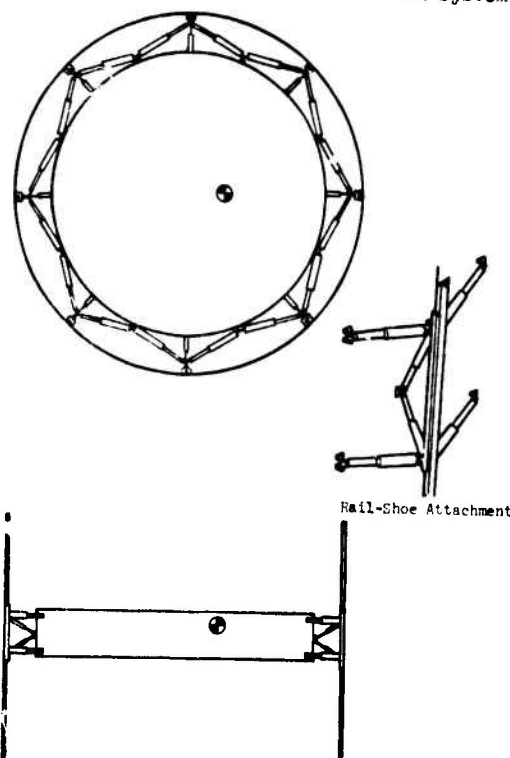
Figure 16.   Case I Vertical Isolation System

Rail-Shoe Attachment

Figure 17.   Case I Horizontal Isolation System
and Rail-Shoe Attachment

Strap maintains vertical constraint,
permits lateral motion
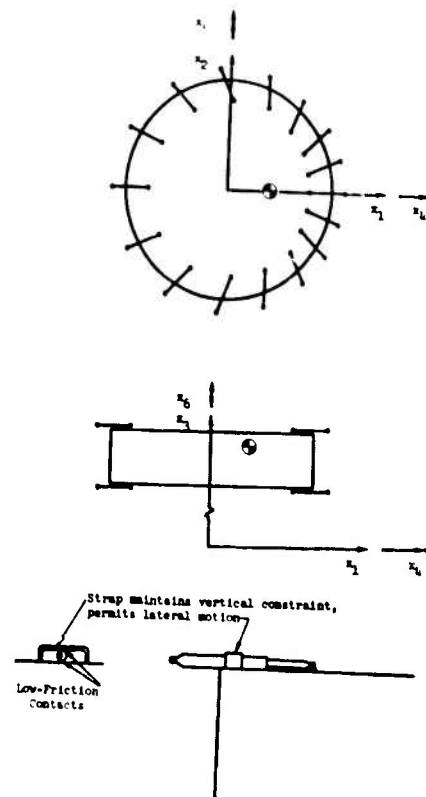
Low-Friction
Contacts

Figure 18.   Case I Horizontal Isolation System
Used in Parameter Study

- A structural "can" to support the iso-
  lated object and apply only compressive
  loads. This may be in the form of a
  truss with local cushions at the con-
  tact points.

- Vertical isolators consisting of two
  sets of single-acting liquid spring-
  shocks connected to the facility
  through cable-pulley systems. The
  liquid spring-shocks are integral with
  the support truss. One set handles
  upward loads; the other set handles
  downward loads.

- Horizontal isolators consisting of sets
  of double-acting liquid spring-shocks
  connected to shoe assemblies which ride
  on low friction vertical rails, as in
  Case I.

The horizontal isolators are arranged in
four rings at different vertical locations,
symmetrically spaced with respect to the cm.
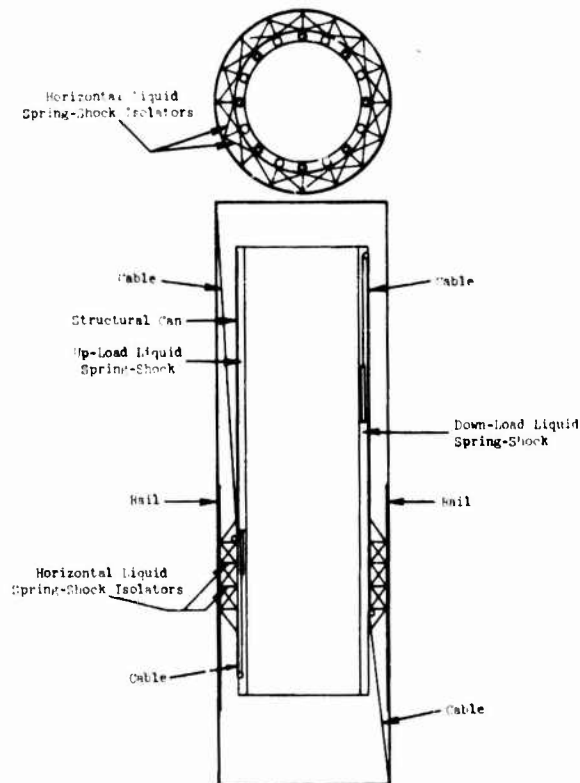Alternate rings are staggered circumferentially

Figure 19. Case II Shock Isolation System

to provide a more omnidirectional system and to reduce translational-rotational coupling in the horizontal plane. Stabilizer springs are used for stability, as in Case I.

The configuration of the vertical isolators takes advantage of the large vertical dimension of the isolated object. Cable-pulley systems are used which require two sets of single-acting struts operating only in tension. An additional pulley is used to bring the cable into the isolated object near the cm. This minimizes translational-rotational coupling from the cable loads as the article is displaced horizontally. The extra pulley also keeps the cable inboard of the network of horizontal isolators.

As in Case I, impact limiters are required to attenuate relatively low-velocity impacts.

It is expected that the Case II system could be simplified by using considerably fewer

isolators, with little reduction in performance. The emphasis in this study was on developing systems to achieve best possible performance. Further trade-off studies should be performed.

Case III

The preferred system for Case III, illustrated in Figure 22 is similar to that of Case I. It differs because of the attach constraints which prohibit attaching isolators on the sides, except for a 135° sector, and on the bottom. Therefore, all of the cables from the vertical isolators and the top ring of horizontal isolators attach at the top periphery of the isolated article. A partial ring of horizontal isolators attaches at the sides near the bottom, within the 135° sector, in order to balance, to the extent possible, the coupling moments produced by the other isolators.

183

Figure 20. Case II Vertical Isolation System

Figure 21. Case II Horizontal Isolation System

Outside of
135° Sector

Within
135° Sector
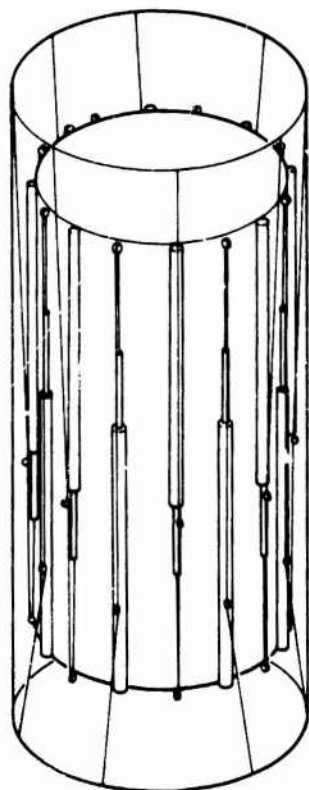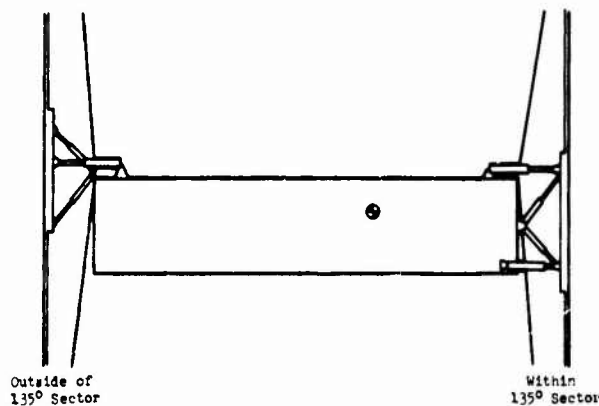
Figure 22. Case III Isolation System

PERFORMANCE EVALUATIONS

Results of parametric evaluations for the three systems are shown in Table 1, which summarizes the maximum responses for the isolator parameters which are closest to optimum. Also shown for comparison are the theoretical optimum solution and the maximum accelerations and displacements for the input motions. The isolator parameters and methods for their selection are presented in Reference 4.

The optimum solution is based on single-degree-of-freedom vertical and horizontal models of the uncoupled systems, using a constant-force, double-acting, energy-dissipative isolator model. The rotational inputs were found to have negligible effect on the solution using a technique developed to determine near-optimum solutions with planar translational and rotational inputs [4]. The present solution can be shown to be the best possible for the horizontal and the top rattlespace values, even considering active systems without "esrly warning" [2], although active systems could reduce the bottom rattlespace at the expense of the top rattlespace.

Figure 23 compares the results for Case I with the theoretical optimum and the maximum

input displacements. Also included in the solution envelope is an allowance for isolator dead space. Results for Case II are very similar to those of Case I. The parametric evaluations of Case III were too limited to be conclusive, but indicate achievable performance close to Cases I and II.

FURTHER DESIGN CONSIDERATIONS

Near-optimum performance can be achieved based on the models used in the performance

184

TABLE 1
Results of Parametric Evaluations

System	Maximum Response				
	Vertical			Horizontal	
	Accel.	Rattlespace (cm)		Accel.	Rattlespace
	(g's)	Top	Bottom	(g's)	(cm)
Case I	1.55	146	333	3.79	38.6^1 (57.4^2)
Case II	1.48	147	320	4.48	26.9^1 (62.5^2)
Case III	2.5	158	381	4.4	44
Optimum Solution	1.58	141	267	4.74	24.6
Facility Motions	200	900	900	100	800

[1] Initial peak response.

[2] Total response which could be reduced to very nearly the initial peak response using low-velocity impact limiters.
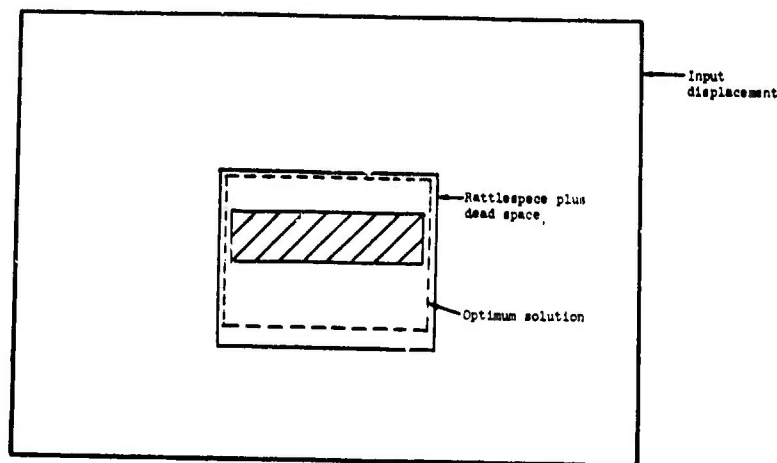

Figure 23. Case I Optimum Solution, Achievable Rattlespace Plus Dead Space, and Maximum Input Displacements

evaluations. It is recognized that these models are somewhat idealized, and important potential problems associated with real hardware require further investigation. The more significant potential problems are as follows:

- Seal friction in vertical liquid spring isolators causing "dead band" or uncertainty in equilibrium position of restored system.

- Overshoot in the isolation system force and reduction in performance, due to unloading or reduced loading in top vertical isolator cables from inertia of isolation system components.

- Manufacture of practical liquid spring-shocks with behavior characteristics approaching those of the preferred isolators.

185

- Friction in rail-shoe assemblies and other attachment hardware.

- High-frequency effects.

- Treatment of low-velocity impacts.

A discussion of these problems is presented in Reference 4.

CONCLUSIONS

Passive shock isolation systems appear promising for achieving near-optimum performance in underground protective structures subjected to severe motions from nuclear detonations. Specific design goals have been developed for guiding the selection of isolators and configurations, and several promising design concepts have been identified.

ACKNOWLEDGEMENT

The author wishes to acknowledge Dr. G. H. Klein, Project Consultant, and Mr. R. E. Curtis, who developed the computer program, for their valuable contributions to this study. Gratitude is also expressed to Captain Paul Smith, Air Force Project Officer for his helpful guidance and assistance.

REFERENCES

1. E. Sevin and W. D. Pilkey, "Optimum Shock and Vibration Isolation," SVM-6, The Shock and Vibration Information Center, Naval Research Laboratory, Washington, D. C., 1971.

2. T. Liber and E. Sevin, "Optimum Shock Isolation Synthesis," Shock and Vibration Bulletin, No. 35, Part 5, pp 203-215, Feb. 1966.

3. G. H. Klein, "Optimization of Linear, Nonlinear and Active Multi-Degree-of-Freedom Shock Isolation Systems," Ph.D. Dissertation, University of California, Jan. 1971.

4. D. L. Platus, G. H. Klein, R. E. Curtis, "Investigation of Optimum Passive Shock Isolation Systems," AFWL-TR-72-148, Feb. 1973.

5. L. L. Boulden, "Hydraulic Shock Absorbers," Machine Design, pp 140-144, Nov. 11, 1971.

6. D. P. Taylor, "Application of the Hydraulic Shock Absorber to a Vehicle Crash Protective System," Society of Automotive Engineers, Mid-Year Meeting, Montreal, Que., Canada, June 7-11, 1971.

7. W. A. Voltz, "Application of Polyurethane Foam to Shock Isolation of Large Silo-Based Missiles," Shock and Vibration Bulletin, No. 36, Part 2, Jan. 1967.

Mr. Curtis (Hughes Aircraft Company):
You had a slide showing various responses.
During your paper you were talking in terms of
displacements, but the curves were labeled
velocities for the ordinates.

Mr. Platus: I didn't have time to develop
this graphical solution. This is developed in
a paper by Lieber and is also described in the
monograph by Sevin and Pilkey. I think the
confusion is that I was referring to areas
between the curves. We're on a velocity time
plot and the area under a velocity time history
is displacement. The area under the input curve
is input displacement; the area under the re-
sponse curve is response displacement; the
area between the two curves is the relative
displacement. When I talked displacement I
was referring to these areas.

Mr. Kalinowski (IIT Research Institute):
When you showed the physical model we saw many
isolators, yet your mathematical model only
showed one. Were they all similar to that?
How many unknown parameters do you have to
optimize?

Mr. Platus: The isolator model shown was
a general model of all of the isolators. It
involved a constant force element for the
constant force damper, the linear dashpot
element, a spring constant and a damping
constant. There were four elements for each
isolator.

Mr. Kalinowski: How many isolators?

Mr. Platus: There were 16 isolators going
around the top and 16 around the bottom. So
there are 32 in the horizontal and then another
16, 8 vertical and 8 horizontal That gives
you a rough idea of the total number. There
was essentially no optimization done, optimal
synthesis or anything like that. It was pretty
clear how one had to adjust the isolator para-
meters almost at the outset. The parameter
study involved making some good guesses, running
the program, and then looking at the results.
The final report on the study, not the written
paper gives a pretty extensive description as
to how the isolator parameters were selected.

Mr. Kalinowski: The one thing you really
don't know for sure is what the input is in
this type of problem. I realize you were
given the waveforms ahead of time, but there
is a great amount of uncertainty as to what
the waveform is. This is due to the soil-
structure interaction problem involved with
what ever this item ties into. How sensitive
do you think this would be to variations on
the input waveform that you did assume?

Mr. Platus: It is true that there is
uncertainty in the input motions. In our study
things were simplified because they were given
to us. However, the fact that we are consid-
ering basically a constant force system makes
the response somewhat insensitive to the input
motions. The isolation system characteristics
pretty well fix the maximum response of the
isolated object. In this case, we're limiting
the object response to some specific accelera-
tion. So we tailor the force levels that the
isolator is to provide, essentially this con-
stant force behavior. Let's say the input
motions are a little more severe so that these
areas shown in single-degree-of-freedom solutions
are a little larger. The consequence will be
that we will perhaps underestimate the maximum
displacement or rattle space. This is where
the uncertainty is, not in the acceleration
response of the article. If there is some
uncertainty as to what the worse waveforms are
one could allow for a little more severe wave-
form in terms of a slightly greater displace-
ment. In other words, just design some addition-
al displacement into the system.

Mr. Kalinowski: You haven't actually tried
it for different waveforms to see what the
response would be?

Mr. Platus: No. For this study we had
one waveform corresponding to air-induced motion
and two others corresponding to direct-induced
motions, and then they were phased differently.
All in all there were about four different
waveforms that had to be satisfied. It was
simple to run through the computer solutions,
test all of them and then pick out the one
that required the maximum displacement. That
then becomes the rattle space requirement.
There is a little bit of an iterative proced-
ure because the sizing and the configuration of
the isolators depends on what kind of displace-
ment you have to contend with.

INFLUENCE OF AN ABSORBER ON MACHINE TOOL VIBRATION

Otto Susolik
The Timken Company, Canton, Ohio

The influence of an oil squeeze film type of a damped vibration absorber on the dynamic behavior of a machine tool (surface grinding machine) has been investigated as part of a project. Several procedures for testing and evaluating the vibrational parameters of the grinder were applied. Substantial improvement due to the absorber was observed and is presented herein as values of dynamic stiffness, damping ratio, maximum negative real vector component, and on Gain-Phase plots indicating chatter resistance.

INTRODUCTION

The ever increasing demand for higher quality machine tool work accentuates the need for reducing dynamic weakness of structures. Dynamic weakness combined with the influence of the cutting process causes chatter instability. The suppression of chatter and improvement of dynamic behavior leads to better quality products, higher production rates and a more favorable machine stiffness-to-cost ratio.

One effective remedy for improving the performance of a machine is the incorporation of vibration dampers. In recent years, especially, new evaluation methods have aided in proper design and reliable installation of absorbers [1, 2, 3, 4].

In this investigation a damped vibration is ... than all ... ... spring ... ... on ... ... ing machine at the point of maximum deflection amplitude; namely the drive motor case at the rear of the spindle. Generally, it should be located at a position where a vibration node will not develop at any critical speed at which the absorber is expected to be effective.

The design utilized an auxiliary mass in parallel with the main force loop, attached by an adjustable spring to the original system. The damper consisted of an aluminum cylindrical housing about 8 inches long and 5 inches in diameter. A steel cylinder weighing about 12 pounds was inserted into the housing and held by a flexible steel bar. The small gap between the cylinder and housing was filled with a specific amount of damping fluid which dissipated the vibration energy. The goal was to

suppress the most dangerous mode of vibration by tuning the natural frequency of the absorber mass to the resonant mode and then by damping the device. The design and optimization of the absorber will be described elsewhere.

After the absorber tuning and damping was optimized, its effect on the relative tool deflection and on the total vibration mode shape was evaluated by several procedures. The evaluation was expected to be done in a simplified manner without performing time consuming and costly cutting tests.

TEST PROCEDURES

Four different experimental test procedures have been applied to analyze the machine tool behavior and the effect of the added absorber:

1. tuning procedure

2. ... ve tool motion measurement

3. vector component measurement

4. vibration mode measurement.

The procedures were based on a frequency response method using an automatic mechanical impedance measuring system [5, 6]. To obtain the results in the convenient form of a transfer function an instrumentation package called the Transfer Function Analyzer (hereinafter denoted by TFA) was used.

The transfer function values, defined as displacement to force ratio (compliance), are not dependent on force magnitude and are applicable for any force situation arising on the machine tool within the assumed linearity limits.

A sketch of the surface grinding machine investigated is shown in Figure 1. The indica-ted main force loop was composed of elements [illegible] in the transmission of cutting [illegible] actions of the tool and workpiece. [illegible] system of interest was centered around the spindle unit equipped with a direct drive [illegible]
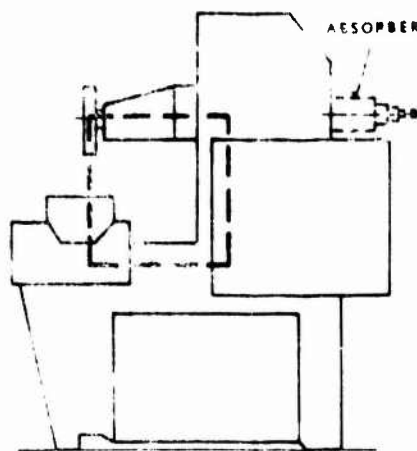
locations on the structure where deflections were measured during the mode shape investiga-tion are indicated in the picture with numbers 1 and 2 respectively.

An exciter head was located on the machine table. The exciter applied a vibrating force to the structure to simulate a cutting force.

Figure 1 - Grinding Machine with Main
Force Loop

Figure 3 - Exciter Location and Relative
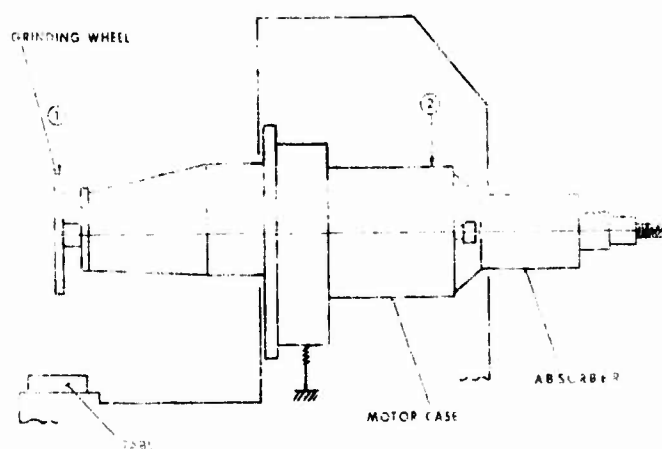Tool Motion Measurement

Figure 2 - Significant Locations on Spindle Compartment

Figure 2 shows the spindle compartment with the vibration absorber attached. The ab-sorber was mounted in place of the motor rear cover using six bolts. Two of the significant

The situation is shown in Figure 3. A displace-ment transducer was attached to the side of the exciter head to measure the tool relative motion (X_W).

INSTRUMENTATION

The electro-hydraulic exciter produced a sinusoidally alternating force through the dynamic range of 10 to 1000 Hz. The dynamic force F was maintained by a feedback control loop consisting of a quartz force transducer, charge amplifier, electronic control device and auxiliary static balance circuit (Figure 4).

20 lb. p-p acted with the frequency from 10 Hz through 700 Hz. On the ordinate the tool motion is expressed as the relative displacement amplitude, x_w, measured by an inductive transducer between the wheel and table (workpiece).
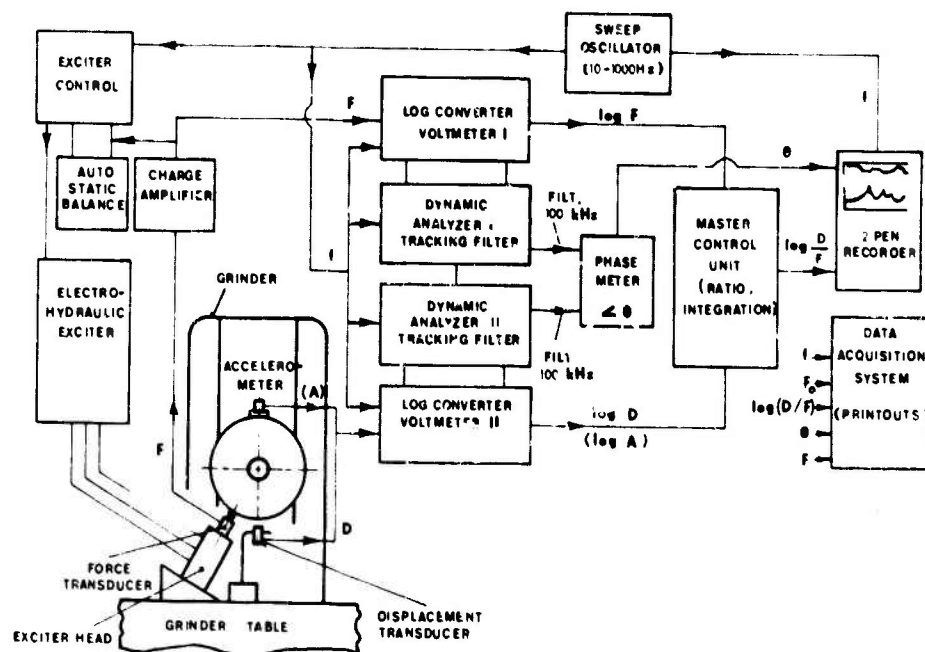

Figure 4 - Simplified Block Diagram

The Transfer Function Analyzer contained two tracking filter analyzers, sweep oscillator and phase meter. In procedures 3 and 4 the Vector Component Analyzer was also incorporated. The vibration was measured in both an absolute and relative manner by accelerometer and inductive transducers respectively.

EVALUATION CONCEPT

A continuous elastic system, consisting of elements such as beams, plates, etc., displays very complicated frequency response with different vibration modes more or less coupled. The response of the investigated grinder, plotted on Bode-type diagram, displayed nine significant resonances, if we consider as significant any resonance peak accompanied by at least a 30° phase shift (Figure 5). The Bode diagram as used in this paper is the display of log amplitude ratio and phase angle, each plotted versus log frequency. The dynamic force of

As can be seen the first vibration mode of approximately 80 Hz-frequency had the highest compliance and thus the lowest dynamic stiffness. The other modes had considerably smaller compliances; e.g., the second one was only 2/5 of the first one.

The first mode was the matter of our concern in the damping effort. For analytical purposes this mode was considered as a system having a single degree of freedom and isolated from other modes. After the vibration absorber was mounted, the model under consideration was transformed into one having two degrees of freedom. The added mass changed the dynamic response and the new system displayed two compensating resonances.

Optimization was achieved when both resonant peaks on the response curve were brought to the same level and depressed to the lowest possible compliance value [7].
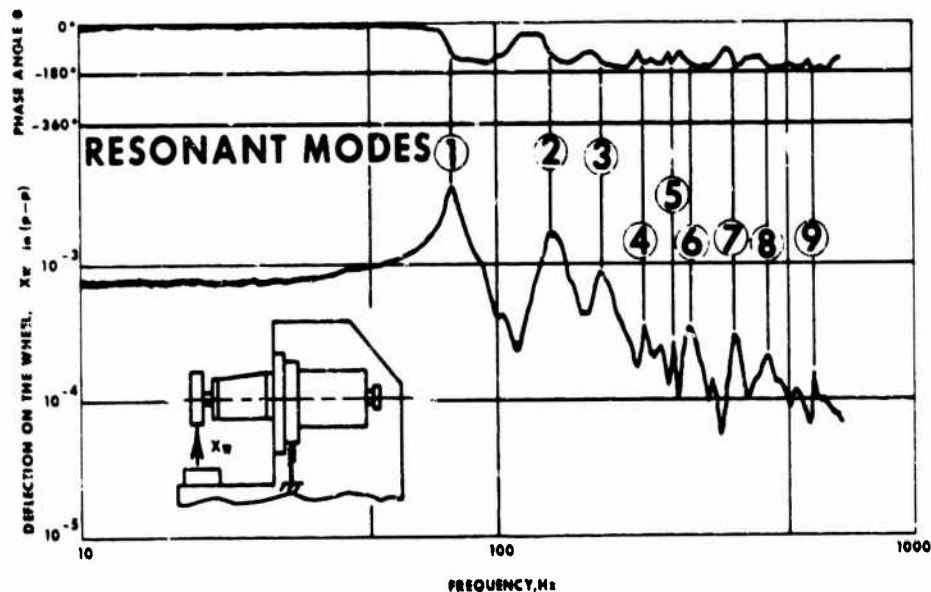
191

Figure 5 - Frequency Response of the Grinder (Original Design)

TUNING PROCEDURE

By proper choice of the spring constant of the absorber, obtained by changing the thickness and the length of spring bar, the amplitudes of the compensating resonant peaks on the frequency response curve of the main mass (Y_1 values measured on motorcase, location 2 in Figure 2) were adjusted to equal heights.

The damping amount was experimentally determined by adding the oil in small increments into the absorber cylinder. During the damping process it was necessary to occasionally readjust the spring constant after the increased damping disturbed the peak heights balance. When the damping was too high there appeared only one resonance. The second mass became coupled with the first one and two degrees of fraedom changed into the former single degree; however, now with increased mass and correspondingly lower resonant frequency.

The amount of energy absorbed by the shearing process in the absorber was influenced by the amount and type of damping fluid used. Common mineral oils of lower viscosity were used. To gain more experience with damping fluids the absorber was tuned with four different oils. The tuning procedure was finished when both balanced peaks were brought to the lowest possible level but they still stayed observable on the diagram.

In Figure 6 an example of the tuning processes performed is shown. The curves were obtained by the TFA in transfer function form as values Y_1 but were rearranged to show normalized values of the amplitude ratio X_1/X_0. These values correspond to K_1/Y_1, where K_1 is the static stiffness at position 2. Approximately twenty diagrams such as these were needed to tune the damper with a specific oil.

Experimental results showed that the optimum amplitudes Y_1 reached with particular oils were between 2.5×10^{-5} and 3.9×10^{-5} in/lb or, if expressed non-dimensionally as X_1/X_0 values, between 1.6 and 2.4. The spread depended upon the fineness of the tuning process; i.e., on the selection of the increments and number of bar turns in readjusting the spring constant. Further improvement in the tuning could be achieved by adding smaller oil increments and shortening the changes in the mass positioning. However, the improvement would be relatively small in proportion to the number of necessary test runs and excessive time consumption.

RELATIVE TOOL MOTION MEASUREMENT

Relative motion between the tool and workpiece is the decisive measure of quality of a machine performance. Its value influences the surface deficiencies on the product and is the measure of chatter.
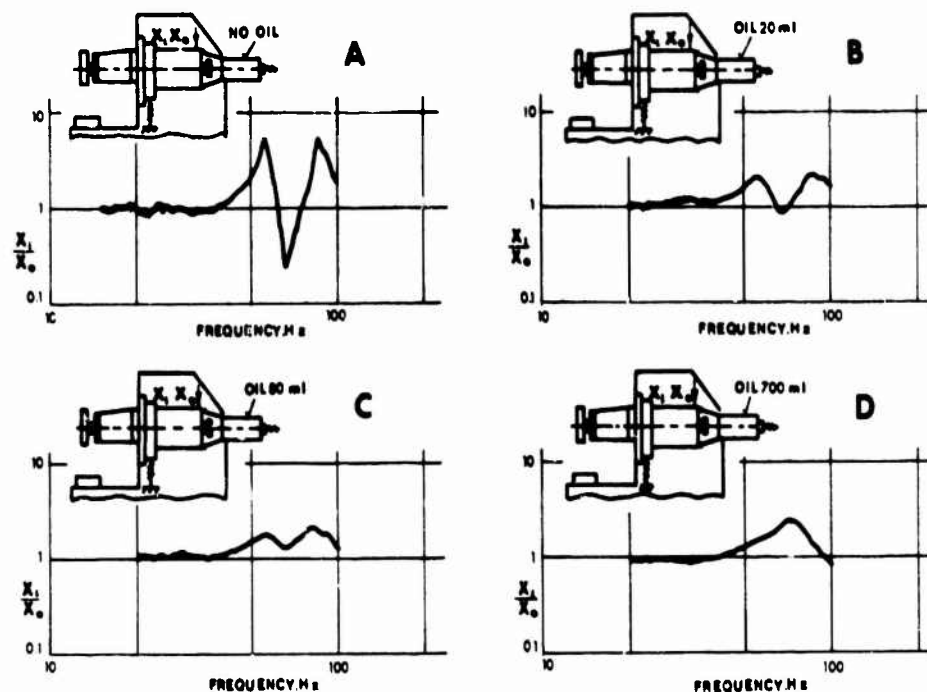
192

Figure 6 - Tuning Diagrams

Motion between the workpiece and tool was measured in the chip thickness direction which is perpendicular to the table as shown in Figure 3. The relative vibration displacement was expressed as dynamic compliance (value Y_W measured on the wheel, place 1 in Figure 2) by the TFA and plotted on Bode-type diagrams.
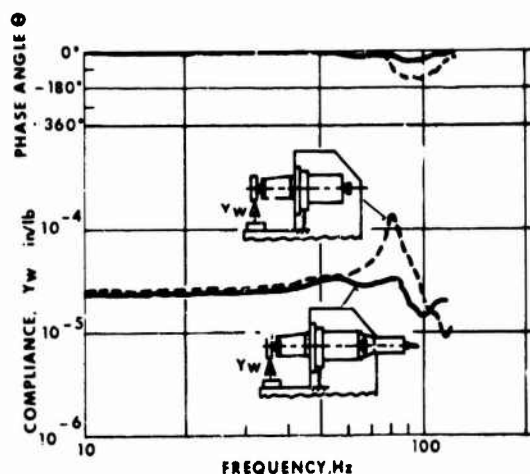
Figure 7 compares the motion of the spindle wheel of the original grinder design (dashed line) with the motion of the adapted machine (solid line) showing the effect of the added optimum tuned absorber. The resonant peak was lowered which caused the compliance to improve 4.4 times. The lower slope of the phase angle plot indicates a substantial increase in damping.

The related parameter, minimum dynamic stiffness (the stiffness at the resonant frequency), was increased in the same manner since its value is determined by inversion of the compliance.

MAGNIFICATION FACTOR

Another performance parameter, often apparent in practice, is the dynamic magnification factor κ. It is defined as the ratio of the maximum dynamic amplitude of a system point (grinding wheel), when the system is subjected to a harmonic force, to the deflection of that point when the force is applied very slowly, as a static force.

Zero frequency deflections or static deflections were estimated from compliance values taken at very low frequency where the slope of the recorded curve approached zero (2.7×10^{-5} in/lb).

Figure 7 - Influence of Absorber on Relative Tool Vibration

193

In the comparison shown in Figure 7 the magnification factor has the value of 1.18 for grinder with absorber as compared with the value of 5.2 for original grinder design.

GAIN-PHASE RELATIONSHIP

Compliance data are further presented in the form of a gain-phase plot to provide a comparison of the chatter onset circumstances on the machine with and without the absorber, Figure 8.

The gain is plotted on the ordinate axis and is defined as the absolute value of the ratio of structure displacement in the uncut chip-thickness direction to the exciting force applied in the direction of the resultant cutting force which in our case is displacement compliance. The phase angle is plotted as the abscissa and is the angle between the foregoing displacement and applied force which is derived in our case after subtracting the preset angle value used according to instrumentation practice.
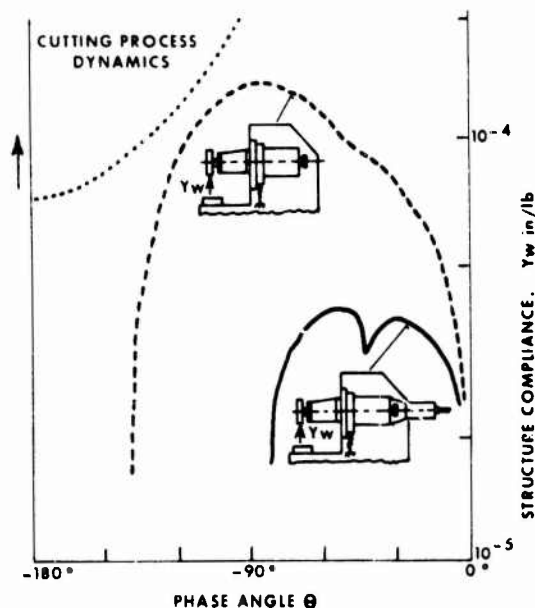

Figure 8 - Gain-Phase Plots as Chatter Onset Indication

The second part is needed to form a conclusion about chatter onset, and is a plot of the critical cutting loci derived from the analysis of the closed-loop representation of the chatter mechanism. For evaluation purposes

the mutual configuration of both plots is observed. If the gain phase plot representing the machine structural dynamics does not intersect the other curve defined by cutting dynamics then the system is absolutely stable at all cutting conditions and will resist chatter [8].

However, the estimation of critical cutting loci is rather complicated and would have required extensive cutting tests which were beyond the scope of the project. For purposes of comparison the effect of the absorber is observed through the changes in the structure portion of the gain-phase plot while the cutting conditions in compared cases stay unchanged. The curve of the cutting process dynamics as shown in Figure 8 is an example approximating the cutting conditions. The scale for this curve (on the left side) will be different from the compliance scale.

The shape of the comparative curve in the right hand corner of Figure 8, representing the conditions with the absorber, reveals that the tuning here was not quite perfect as shown by different peak levels. Nevertheless, it is obvious that the distance between the borderline of the critical cutting loci and structural gain-phase plot had substantially increased after the absorber was mounted and thus the danger of initiating chatter was considerably reduced. Even if the grinding condition became less favorable, which would lower the position of the upper curve (dotted line), it is very improbable that intersection would occur. The system with the absorber incorporated is expected to be stable at severe cutting conditions and will resist chatter vibration occurring in the observed range.

VECTOR COMPONENT MEASUREMENT

The third test procedure provided plots of two vector components of the relative vibration motion between the tool and table. In addition, Nyquist polar diagrams were also obtained.

The coincident component plots contain the damping information [9]. Two plots are compared in Figure 9. The dashed line represents the original machine, the solid line the adapted machine with the absorber.

The damping ratio ζ was computed from peak-and-notch frequencies ω_a and ω_b using the equation:

$$\zeta = [(\omega_a/\omega_b)^2 - 1]/[(\omega_a/\omega_b)^2 + 1]$$

The damping ratio for the original grinder design was thus obtained as $\zeta = 0.075$. However, under the strong influence of the absorber the resonant peaks sank so low that no significant resonance had developed and in some cases with particular oils the coincident curve did not cross the zero line. The estimation of ζ from peak-and-notch readings gave only approximate

information under these conditions. For comparison sake the damping ratio was evaluated between 0.21 and 0.23 and the damping improvement was by a factor of approximately three.
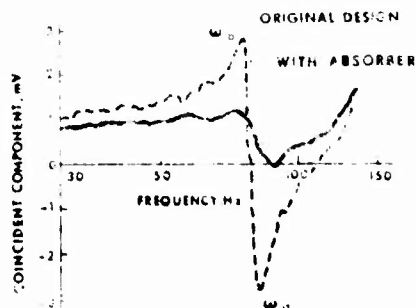

Figure 9 - Coincident Component Plots

The quadrature component plot was used for exact determination of the resonant frequency, specifically for the mode shape procedure. The peak on the plot was very steep and sharply pointed giving an accuracy of the resonant frequency value within 2 Hz. This sensitivity was substantially higher than the previous overall response plots allowed.

The amplitude of the quadrature resonant peak represented a maximum relative displacement between the tool and workpiece with less influence from non-resonant modes [9]
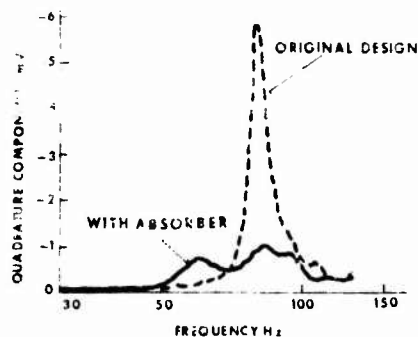

Figure 10 - Quadrature Component Plots

In Figure 10 the results obtained from the original machine are compared with results

from the adapted machine with the absorber. This is an improvement of 9 times.

Polar diagrams indicated the machine chatter resistance by estimating the maximum negative real vector component [10]. The smaller this value, the higher the dynamic stability displayed by the machine structure.

The experimental Nyquist polar diagrams are displayed in Figure 11.

The diagrams were recorded with the coincident component driving the vertical direction (ordinate) of the recording pen and the quadrature component driving the horizontal direction (abscissa). Nyquist diagrams enable reading of the phase in any of the four quadrants; however, the frequency, becoming parametric instead of coordinate, is not screened. To offset this disadvantage a display of frequency was additionally superimposed on our diagrams by rearranging the two pen recorder. For convenience of reading the auxiliary frequency plots were shifted out of the polar curve areas.
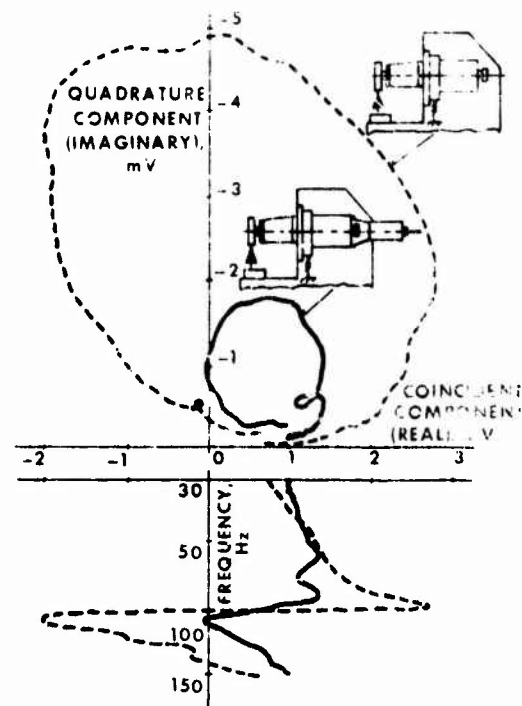

Figure 11 - Influence of Absorber on Nyquist Polar Plots

The machine of original design displayed the maximum negative real component of -2 mV compared to the value from the machine with the absorber which displayed -0.05 mV. In that kind of evaluation improvement of 40 times indicates a substantial increase in chatter resistance.

MODE SHAPE MEASUREMENT

For vibration mode shape measurement the vector component technique using the vector Analyzer was applied. Evaluating the quadrature component values of the absolute vibration displacements along the machine force loop provided adequate mode shape measurements.

Excitation frequency was locked and held at a constant value during the measurement. Vibration data were obtained by moving the accelerometer from one significant place to another. To obtain enough data for a detailed and reliable deflection picture thirty-eight significant places were selected and measured along the machine profile shown in Figure 2. Some additional places were investigated during higher modes when the deflection pattern became more sophisticated.

The observed value of quadrature component was read from the Analyzer scale for each accelerometer placement. From these data the mode shape pictures of the vibration modes were constructed.

due to the absorber effect was 5.8 times.

After the comparative mode patterns of the first mode were evaluated the analysis was expanded to include higher modes as well. The reason for this enlargement was not only to obtain supplementary data about the machine performance through the entire practical dynamic range but, at the same time, to check whether the absorber worsened the overall dynamic behavior.

In the theoretical evaluation of damping by a dynamic absorber in the literature [1] an additional effect was discussed. Not only was the absorber effective in suppressing the resonance to which it was tuned but its damping was also observable in suppressing the resonances that occurred at higher frequency modes, while it had little effect on the peaks below the absorber frequency.

In our investigations the absorber significantly suppressed the resonance of concern but no remarkable and steady differences at higher frequency modes were observed. The absorber influence on higher modes was negligible.

CONCLUSIONS

Four test procedures were developed and applied to evaluate the effect of a specially designed damped vibration absorber on the

DEFLECTION SCALE 10^{-3} in
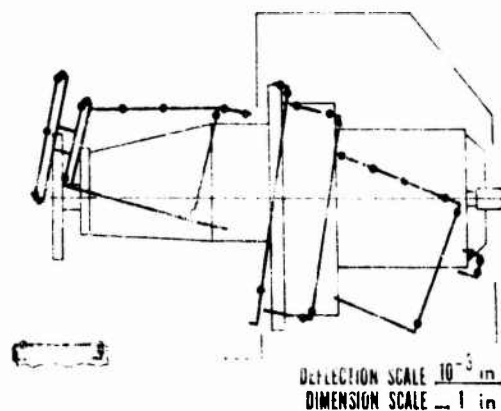DIMENSION SCALE _ 1 in

Figure 12 - Vibration Mode Shape of the Original Machine

Figures 12 and 13 demonstrate in the first mode deflection picture the difference between the original design of the machine tool and the adapted machine tool with the absorber.

The Deflection Scale calibrates the vibration motion. The Dimension Scale relates to the overall size of the machine.

Consideration should be given to the location No. 1 on the wheel where the improvement

dynamic behavior of a surface grinding machine; this was accomplished without conducting time consuming and costly cutting tests.

The applied frequency response method using the Transfer Function Analyzer provided satisfactory information about the absorber performance.

DEFLECTION SCALE $\underline{10^{-3} \text{ in}}$
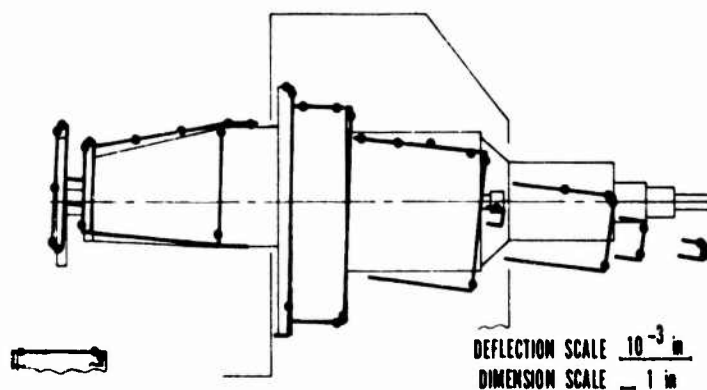DIMENSION SCALE $\underline{\quad 1 \text{ in}}$

Figure 13 - Vibration Mode Shape of the Machine with Absorber

The following parameters were evaluated:

Static and dynamic stiffnesses,

Magnification factors,

Damping ratios,

Maximum wheel deflections,

Vibraticn mode shapes,

Chatter resistance indications.

A comparison of the numerical values describing the differences between both machine tool design is reviewed in Table 1.

It is evident from this tabulation that substantially improved dynami. characteristics occurred after the absorber was mounted. One of the most significant improvements, it can be pointed out, was that the dynamic stiffness rose 4.4 times. In addition, increased chatter resistance was indicated by the Gain-Phase plots which showed a 40 times decrease in the maximum negative real vector component.

This investigation has shown the application of a tunable absorber and the evaluation of specially developed testing method. to give favorable results. It is entirely feasible to apply this type of design improvement and analysis to other machine tools.

197

TABLE 1

REVIEW OF EXPERIMENTAL RESULTS

Test Procedure	Compared Parameters	Grinder Design		Improvement, in 100%
		Original, Without Absorber	With Absorber	
Relative Tool Displacement	Max. Dynamic Compliance	1.4×10^{-4} in/lb	3.2×10^{-5} in/lb	4.4
	Min. Dynamic Stiffness	7,150 lb/in	31,500 lb/in	4.4
	Max. Magnification Factor	5.2	1.18	4.4
Vector Component Technique	Max. Relative Displacement Between Tool and Workpiece	-5.8 mV	-1.0 mV	5.8
	Damping Ratio	0.075	(0.230)	~3
	Max. Negative Real Vector Component	-2.0 mV	-0.05 mV	40
Mode Shapes	Max. Absolute Deflection on Grinding Wheel in Radial Direction	1.96×10^{-4} in	3.3×10^{-5} in	5.8
	Max. Absolute Deflection on Grinding Wheel in Axial Direction	1.05×10^{-4} in	1.3×10^{-5} in	8

REFERENCES

1. J. C. Snowden, "Vibration of Cantilever Beams to Which Dynamic Absorbers are Attached," J. Acc. Soc. Am., Vol. 39, No. 5, 1966.

2. S. A. Tobias, "Machine Tool Vibration," J. Wiley & Sons, New York, New York, 1965.

3. R. S. Hahn, "Metal Cutting Chatter and its Elimination," Trans. ASME, Vol. 75, 1953.

4. G. Sweeney, S. A. Tobias, "Survey of Basic Machine Tool Chatter Research," Int. J. Mach. Tool Des. Res., Vol. 9, No. 3, 1969.

5. G. W. Long, J. R. Lemon, "Structural Dynamics in Machine-Tool Chatter, Contribution to Machine-Tool Chatter Research-2," Trans. ASME, Paper No. 64 - WA/Prod-12.

6. W. R. Shapton, I. E. Morse, D. M. Wood, et al., "Dynamic Machine Tool Testing," Final Tech. Report, University of Cincinnati, 1969.

7. J. Ormondroyd, J. P. Den Hartog, "The Theory of the Dynamic Vibration Absorber," Trans. ASME, Vol. 50, 1928.

8. H. E. Merritt, "Theory of Self-Excited Machine Tool Chatter," ASME Paper No. 64-WA/Prod-13.

9. C. C. Kennedy, C. D. P. Pancu, "Use of Vectors in Vibration Measurement and Analysis," J. Aeronaut. Sc., Vol. 14, No. 11, 1947.

10. J. Tlustý, M. Poláček, "Beispiele der Behandlung der selbsterregten Schwingungen der Werkzeugmaschinen," Vogel Verlag, Würzburg, 1957.